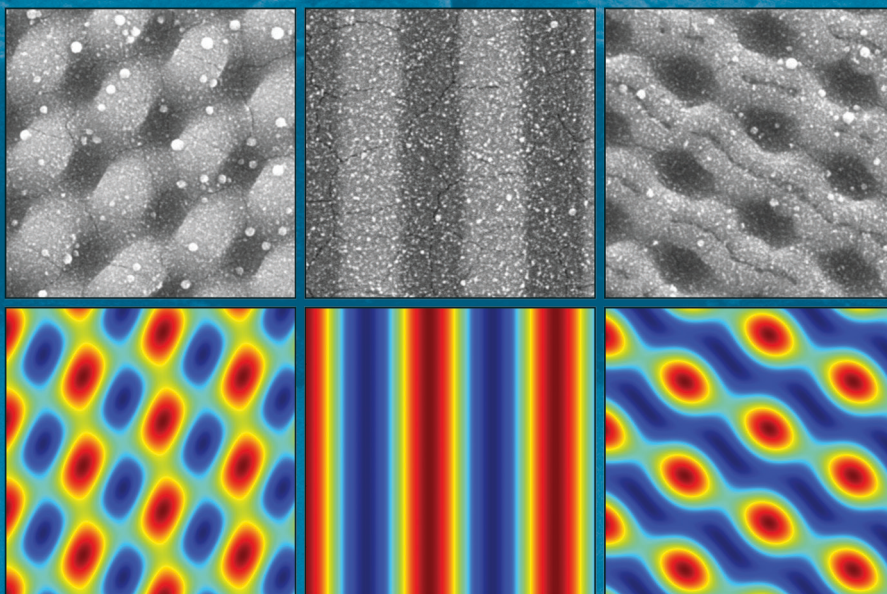


# Light Trapping by Light Treatment

Direct Laser Interference Patterning for the Texturing of Front Contacts in Thin-Film Silicon Solar Cells

Tobias Dyck



Energie & Umwelt /  
Energy & Environment  
Band / Volume 359  
ISBN 978-3-95806-208-5





Forschungszentrum Jülich GmbH  
Institute of Energy and Climate Research  
IEK-5 Photovoltaics

## **Light Trapping by Light Treatment**

### **Direct Laser Interference Patterning for the Texturing of Front Contacts in Thin-Film Silicon Solar Cells**

Tobias Dyck

Schriften des Forschungszentrums Jülich  
Reihe Energie & Umwelt / Energy & Environment

Band / Volume 359

---

ISSN 1866-1793

ISBN 978-3-95806-208-5

Bibliographic information published by the Deutsche Nationalbibliothek.  
The Deutsche Nationalbibliothek lists this publication in the Deutsche  
Nationalbibliografie; detailed bibliographic data are available in the  
Internet at <http://dnb.d-nb.de>.

Publisher and  
Distributor: Forschungszentrum Jülich GmbH  
Zentralbibliothek  
52425 Jülich  
Tel: +49 2461 61-5368  
Fax: +49 2461 61-6103  
Email: [zb-publikation@fz-juelich.de](mailto:zb-publikation@fz-juelich.de)  
[www.fz-juelich.de/zb](http://www.fz-juelich.de/zb)

Cover Design: Grafische Medien, Forschungszentrum Jülich GmbH

Printer: Grafische Medien, Forschungszentrum Jülich GmbH

Copyright: Forschungszentrum Jülich 2017

Schriften des Forschungszentrums Jülich  
Reihe Energie & Umwelt / Energy & Environment, Band / Volume 359

D 82 (Diss. RWTH Aachen University, 2016)

ISSN 1866-1793  
ISBN 978-3-95806-208-5

The complete volume is freely available on the Internet on the Jülicher Open Access Server (JuSER)  
at [www.fz-juelich.de/zb/openaccess](http://www.fz-juelich.de/zb/openaccess).



This is an Open Access publication distributed under the terms of the [Creative Commons Attribution License 4.0](https://creativecommons.org/licenses/by/4.0/),  
which permits unrestricted use, distribution, and reproduction in any medium, provided the original work is properly cited.

# Abstract

To further increase the energy conversion efficiency of thin-film silicon solar cells, the minimization of reflection losses by effective light trapping is essential. Light trapping is achieved by introducing textured surfaces in the layer stack of a solar cell. The incoming light is scattered at the textured interfaces, the light paths within the absorber layer are enhanced and the chance of absorption rises. This work aims to develop an industrial feasible laser-based process for the texturing of the aluminium-doped zinc oxide (ZnO:Al) layer used as front contact in solar cells. While wet chemical etching of the ZnO:Al is an established process for the texturing, a laser-based process offers higher flexibility and controllability of texture scattering properties. Accordingly, the light trapping can be engineered to fit the needs of a solar cell.

Within this work, five laser-based processing techniques are evaluated for their applicability to texture ZnO:Al layers in an industrial environment. The direct writing of textures is capable of producing the right feature sizes and is highly flexible. However, it has strong demands on the experimental setup and requires long processing times. Refocusing the laser light by a particle lens array as well as laser-induced chemical etching also lack the industrial feasibility due to the complex processing setup. The creation of laser-induced periodical surface structures (LIPSS) by ultra-short pulse lasers promises small feature sizes with a simple setup. However, the flexibility of feature sizes and shapes is limited. Only direct laser interference patterning (DLIP) is capable of producing a large variety of adjustable textures with right-sized features while being able to cover large areas in reasonable amounts of time with an industrial feasible processing setup.

To further investigate DLIP processing, a highly flexible three-beam interference setup was designed and implemented. Within the setup, the beam properties of the three partial beams can be adjusted completely independently. By controlling power, polarization and angle of incidence of the individual beams, the intensity distribution within the overlapping volume is adjusted. This intensity distribution then translates to a topography on the ZnO:Al sample. With one single laser pulse, hundreds of thousands strictly periodic micrometer and submicrometer-sized features are created. The general geometry of the features can be varied and the spatial periodicity can be adjusted deliberately and continuously. The electrical properties of the ZnO:Al remain nearly unchanged and although there is a minor

loss in transparency, the incident light is diffracted into distinct and adjustable patterns.

Fully functional thin-film silicon solar cells are manufactured on exemplary DLIP textures without growth limitations or adhesion problems. Whereas these unoptimized solar cells show better light trapping behavior than untextured cells, they do not fully reach the level of cells optimized for and deposited on the established wet etched reference texture.

In order to improve and optimize DLIP processing, the variety of producible textures as well as their potential light trapping capabilities are described by an extensive model. By mimicking the propagation of the beams through the various optical components, the influence of the experimental setup on the beam properties is determined and the corresponding intensity distribution in the interference volume is calculated. From this intensity distribution the energy intake in the material, the subsequent heat diffusion within the material as well as the resulting ablation is modeled. Consequently, the model is capable of predicting the expected surface texture for a given set of experimental setup parameters.

Furthermore, a scalar model for an expected light trapping efficiency of a given texture is adapted to the use on laser textured surfaces. Accordingly, a light trapping efficiency can be assigned to each modeled texture and its potential performance in a solar cell can be evaluated. Hence, the best achievable texture within the limits of the experimental setup is determined by an optimization algorithm. Likewise, the general potential of DLIP processing is evaluated. It is revealed that solar cells deposited on optimized DLIP-textured front contacts are expected to yield higher efficiencies than cells on standard wet chemical etched front contacts. Especially DLIP with multi-pulse processing and/or pulse durations in the subnanosecond regime shows the potential to improve light trapping efficiencies far beyond the ones of state-of-the-art textures.

# Contents

<b>Abstract</b>	<b>i</b>
<b>1 Introduction</b>	<b>1</b>
<b>2 Fundamentals</b>	<b>5</b>
2.1 Solar Cells . . . . .	5
2.1.1 Thin-Film Silicon Solar Cells . . . . .	5
2.1.2 Light Management and Textured Interfaces . . . . .	9
2.1.3 Phase Model . . . . .	11
2.2 Lasers . . . . .	15
2.2.1 Properties of Laser Light and Beams . . . . .	15
2.2.2 Laser-Material Interaction . . . . .	26
<b>3 Devices and Methods</b>	<b>29</b>
3.1 Devices and Methods for Characterization . . . . .	29
3.1.1 Laser Characterization . . . . .	29
3.1.2 ZnO:Al Characterization . . . . .	32
Topography . . . . .	32
Electro-Optical Properties . . . . .	34
3.1.3 Solar Cell Characterization . . . . .	35
3.2 Devices and Methods for Laser Treatment . . . . .	35
3.2.1 Laser Sources . . . . .	36
Rofin1064 . . . . .	36
Rofin532 . . . . .	37
Rofin355 . . . . .	37
TruMicro5050 . . . . .	38
TruMicro5000 . . . . .	39
Powerlite8020 . . . . .	39
3.2.2 Beam Guiding . . . . .	44
Structuring System . . . . .	44
Scanner Lab Jack Setup . . . . .	45
Interference Setups . . . . .	46
3.3 Computational Devices . . . . .	46
Genetic Algorithm for Global Optimization . . . . .	47

<b>4</b>	<b>Process Comparison</b>	<b>51</b>
4.1	Direct Writing . . . . .	52
4.2	Laser-Induced Chemical Etching . . . . .	53
	4.2.1 Experimental Procedure . . . . .	53
	4.2.2 Results and Discussion . . . . .	54
4.3	Particle Lens Array . . . . .	57
	4.3.1 Experimental Procedure . . . . .	57
	4.3.2 Results and Discussion . . . . .	58
4.4	Laser-Induced Periodical Surface Structures . . . . .	60
	4.4.1 Experimental Procedure . . . . .	60
	4.4.2 Results and Discussion . . . . .	61
	Low Spacial Frequency LIPSS (LSFL) . . . . .	61
	High Spacial Frequency LIPSS (HSFL) . . . . .	62
	4.4.3 Speed Considerations . . . . .	64
4.5	Two-Beam Direct Laser Interference Patterning . . . . .	65
	4.5.1 Experimental Procedure . . . . .	65
	4.5.2 Results and Discussion . . . . .	66
4.6	Conclusion . . . . .	69
<b>5</b>	<b>Three-Beam Direct Laser Interference Patterning (DLIP)</b>	<b>73</b>
5.1	Experimental Setup . . . . .	73
	5.1.1 Layout of Experimental Setup . . . . .	75
	5.1.2 Adjustment and Calibration of Laser Beam Properties . . . . .	79
	5.1.3 Setup Parameters . . . . .	81
5.2	Interference Pattern . . . . .	82
	5.2.1 Simulate Interference Model ( <i>SINT</i> ) . . . . .	82
	5.2.2 Exemplary Pattern . . . . .	84
5.3	Surfaces Textures . . . . .	89
	5.3.1 General Features of DLIP Textures . . . . .	89
	5.3.2 Control of Texture . . . . .	92
	5.3.3 Ablation Process . . . . .	96
5.4	Modeling Ablation . . . . .	100
	5.4.1 Ablation Model . . . . .	100
	Ablation without Heat Diffusion . . . . .	100
	Ablation with Heat Diffusion . . . . .	102
	5.4.2 Determination of Material Properties . . . . .	105
	Optimization . . . . .	105
	Reliability of Optimization Results . . . . .	107
	Comparison of Model and Experiment . . . . .	109
	5.4.3 Virtual Laser Interference Patterning ( <i>VLIP</i> ) . . . . .	111
5.5	Summary . . . . .	113
<b>6</b>	<b>Application in Solar Cells</b>	<b>115</b>

---

6.1	Macroscopic Texturing . . . . .	115
6.1.1	Stitching of Laser Spots . . . . .	116
6.1.2	Electro-Optical Characterization . . . . .	120
6.2	Solar Cells . . . . .	123
6.2.1	Deposition of Tandem Solar Cells . . . . .	124
6.2.2	Characterization of Solar Cells . . . . .	125
6.3	Conclusion . . . . .	132
<b>7</b>	<b>DLIP Potential</b>	<b>135</b>
7.1	Light Trapping Efficiency . . . . .	135
7.1.1	Calculation of $LTE$ and $LTE_{\text{eff}}$ ( $PyLTE$ ) . . . . .	136
7.1.2	Comparison with Solar Cells . . . . .	137
7.1.3	Discussion . . . . .	139
7.1.4	Conclusion . . . . .	140
7.2	Influence of Setup Parameters on Light Trapping Efficiency . . . . .	141
7.2.1	Periodicity and Total Power . . . . .	142
7.2.2	Partial Beam Power . . . . .	144
7.2.3	Partial Beam Polarizations . . . . .	145
7.2.4	Angle of Incidence . . . . .	146
7.2.5	Conclusion . . . . .	147
7.3	Global Optimization of Setup Parameters . . . . .	148
7.4	Outlook . . . . .	151
7.4.1	Two Pulse Processing . . . . .	152
7.4.2	Short Laser Pulse Durations . . . . .	154
7.4.3	Conclusion . . . . .	156
7.5	Summary . . . . .	157
<b>8</b>	<b>Summary and Outlook</b>	<b>159</b>
	<b>Bibliography</b>	<b>163</b>
	<b>List of Tables</b>	<b>I</b>
	<b>List of Figures</b>	<b>III</b>
<b>A</b>	<b>Appendix</b>	<b>VII</b>



# 1 Introduction

Solar cells are a convenient way of directly converting solar energy into electrical energy. Only an area smaller than the size of Germany covered with solar panels would suffice to supply the whole world's need of electrical energy<sup>1</sup>. Ever since the first solar cell was developed in 1876 [1], the types of solar cells have diversified. While the classical crystalline Silicon (c-Si) p-n junction solar cells today still hold the largest share of the solar cell market, various other types of solar cells like inorganic, organic or perovskite thin-film solar cells have emerged and evolved. Thin-film silicon solar cells promise a cost- and material-effective alternative to classical wafer-based c-Si cells, due to the thinner layers and the large area manufacturing process. Compared to many other thin-film technologies, they yield the advantage of only using abundant non-toxic materials. However, the energy conversion efficiencies of thin-film silicon solar panels still fall behind the established efficiencies of c-Si panels as well as the theoretical efficiency limit [91].

To further improve the efficiency of thin-film silicon solar cells, the probability of absorption of incident light needs to be enhanced. Only absorbed light can be converted to electrical power. Using thicker absorber layers is not favored due to higher material consumption and higher degradation of thicker layers [112]. By elongating the light path in the thin absorber layers, however, the likelihood of absorption can be enhanced without increasing material consumption. Such optical optimization of solar cells is often referred to as "light trapping". By internal reflections at the adjacent interfaces, the light can be "trapped" in the absorber layer until it is absorbed. Such light trapping is generally achieved by introducing textured interfaces in the layer stack of a thin-film silicon solar cell. The incoming light is scattered at the textured interfaces, the light paths are elongated and the light trapping abilities are enhanced. A common way of introducing the textures is by texturing the surface of the front contact layer which is the very first layer deposited during the production process. Because of the almost conformal growth of the subsequently deposited layers, all other interfaces are also textured. An established approach for the texturing is the wet chemical etching of a layer of aluminium-doped zinc oxide (ZnO:Al) which is then used as front contact.

---

<sup>1</sup>Assuming a total conversion efficiency of 10%, an averaged solar irradiation power of 1000 kWh/m<sup>2</sup>a and a total power demand of 2.7 TW [77].

This thesis aims to find laser-based alternatives for the texturing of the ZnO:Al front contact layer. While the wet chemical etching is a well established and efficient way to scatter the incoming light, it does not provide high flexibility concerning the texture's feature sizes and shapes and hence, their scattering abilities. A laser-based process, however, could offer a better control over the resulting texture's topography. By deliberately adjusting the texture's feature sizes and shapes, the detailed scattering properties of the layer can be manipulated and thus, the light trapping abilities can be controlled. Such engineering of light trapping abilities could even be used to adapt a texture to the needs of a specific type of solar cell. Apart from the advantages concerning flexibility and control, a laser-based process generally is vacuum compatible and thus, applicable in-line in the production process of thin-film silicon solar cells. Hence, time and energy consuming vacuum breaks could be avoided. Current laser system's output powers ensure industrial relevant processing speeds [61], while laser processes in general also offer a cleaner alternative to chemical processes. For these reasons, this thesis aims to find a laser-based alternative to the chemical etching, to investigate its potential and to deliver a proof of concept for its applicability in the manufacturing of thin-film silicon solar cells.

After introducing some fundamental concepts (**Chapter 2**) and specifying the devices and methods used throughout the thesis (**Chapter 3**), a comparison of various laser-based processes is presented in **Chapter 4**. The processing techniques of direct writing, laser-induced chemical etching, refocusing by particle lens arrays, creation of laser-induced periodical surface structures and direct laser interference patterning are compared and evaluated for their potential use to texture ZnO:Al. Apart from the demands on functionality, the evaluation of the different processes focuses on industrial applicability. The texturing by direct laser interference patterning (DLIP) proves to be the most promising process due to its high flexibility, potentially simple experimental setup and possible scalability to large areas.

For these reasons, DLIP processing is further investigated in **Chapter 5**. A highly flexible experimental setup for three-beam DLIP is designed. It is capable of producing a large variety of different intensity pattern and thus, textures in ZnO:Al. Parallel to the experimental setup, an extensive theoretical model is developed. The model mimics the propagation of the beams through the setup, calculates the intensity pattern in the interference volume and models the ablation process. Consequently, it can be used to predict the ZnO:Al topography after the laser treatment in dependence of given experimental adjustments.

To insure applicability of the DLIP-textured layers in solar cells, the patterning of macroscopic areas and the manufacturing of thin-film silicon solar cells on DLIP-textured layers is investigated in **Chapter 6**. Layer stacks of tandem

solar cells are deposited on selected DLIP textures. The resulting solar cells are characterized for their functionality and compared to state-of-the-art references.

To better grasp the potential of a certain DLIP texture, **Chapter 7** introduces a computable quantity, which is a measure for the light trapping efficiency of a given texture. After demonstrating the correlation of calculated values with experimentally measured light trapping abilities, the best achievable texture within the limits of the given experimental setup is determined by means of an optimization algorithm. Finally, an outlook is provided highlighting the potential of DLIP texturing by loosening the constraints of the experimental setup and broadening the perspectives to a more global picture.

A schematic outline of the thesis is depicted in Fig. 1.1.

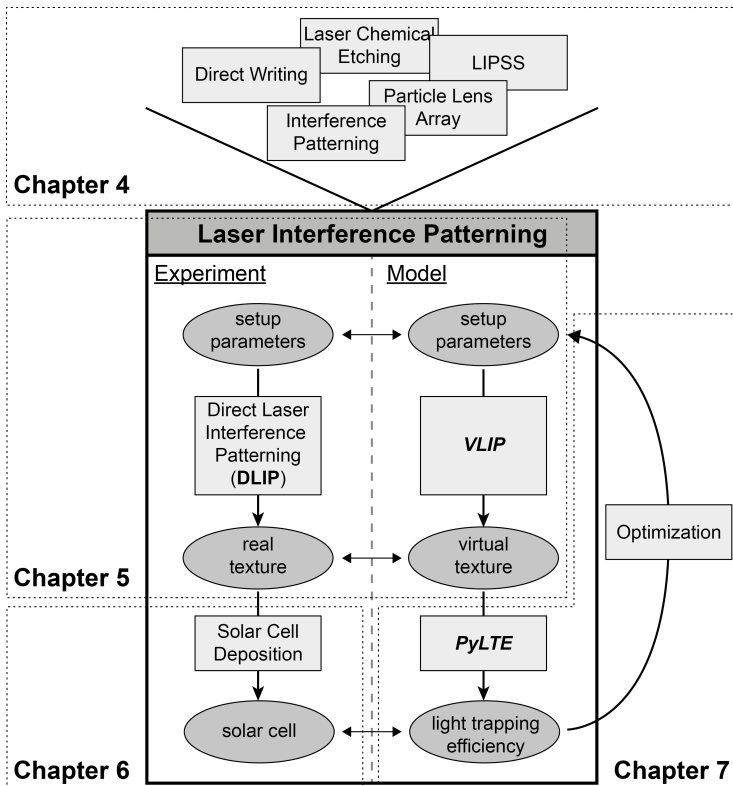


**Figure 1.1** Schematic outline of the contents of this thesis and the corresponding chapters.



## 2 Fundamentals

The following chapter presents a rough overview of the background of some of the concepts used throughout the thesis. The first section deals with topics related to solar cells. After a short introduction to thin-film silicon solar cells and their characteristic properties, the concept of light management within a solar cell is introduced. The section closes with a theoretical model which is capable of predicting the light trapping abilities of a given surface textured when used in a thin-film silicon solar cell. The second section in this chapter deals with topics related to lasers and their properties. Whereas the first subsection focuses on the properties of laser light, laser beams and the control of such, the second subsection presents the physical basics to describe absorption of laser light as well as heat diffusion in materials.

### 2.1 Solar Cells

#### 2.1.1 Thin-Film Silicon Solar Cells

A solar cell is a device that converts the energy of light into electrical energy by means of the photovoltaic effect. A thin-film silicon cell is a special type of solar cell. It consists of various thin layers of hydrogenated amorphous (a-Si:H) and/or micro-crystalline silicon ( $\mu\text{c-Si:H}$ ) which are deposited on a carrier material. The carrier material can be glass, but due to the thin and unbrittle layers also plastic foils can be used to build flexible solar cells [65, 105]. In contrast to "classic" crystalline silicon (c-Si) solar cells, no silicon wafer is needed. The silicon is deposited on the carrier from the gas phase. Due to the production process and the thin layers, thin-film silicon solar cells offer a cost- and energy-effective alternative to crystalline solar cells. However, the energy conversion efficiencies of thin-film silicon solar cells remain well below the level of wafer-based cells. An illustration of a simple single-junction a-Si:H solar cell along with its schematic band structure is depicted in Fig. 2.1.

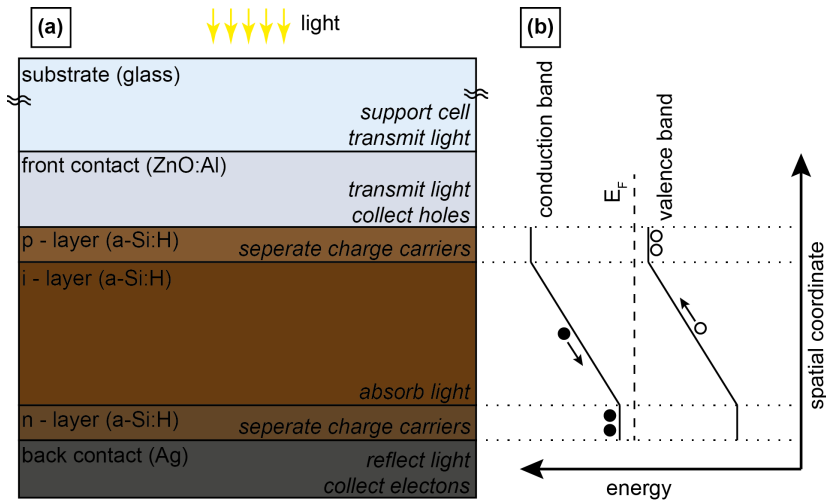


**Figure 2.1** Single-junction a-Si:H solar cell (illustration). (a) Exemplary layer stack: Materials used for each layer are stated in parenthesis. On the right hand side of each layer, the task of the layer is described. (b) Schematic band structure: By introducing the doped p- and n- layers, an intrinsic electrical field builds up which is used to separate the charge carriers and transport them to the contact layers.

**Layer Stack and Operation Principle** The light enters through the glass carrier and passes through the transparent but conductive front contact layer. It is then absorbed in the absorber layer and creates a charge carrier pair. The charge carriers are separated by an intrinsic electrical field and are transported to the contact layers. The electrical field is induced by introducing thin n- and p-doped layers on each side of the actual absorber layer to form a PIN-diode. The thickness of the whole layer stack is on the order of single micrometers. In order to effectively absorb a broader spectral range of the sun-light, multi-junction cells can be used. A tandem solar cells consists of two PIN-junctions (two solar cells) made of material with different micro structures (e.g. a-Si:H and  $\mu\text{c-Si:H}$ ) stacked on top of each other<sup>1</sup>. This yields the advantage that each cell can be optimized for a smaller spectral range and thus, the solar spectrum can be absorbed more efficiently by minimizing thermalization losses. However, the design of a multi-junction solar cell is more complicated, due to the fact that the individual cells are connected in series and need to be current matched to insure maximum power output. Exemplary layer stacks of tandem solar cells are depicted in later parts of the thesis (Fig. 2.4 and Fig. 6.6 (a)).

<sup>1</sup>These are referred to as top and bottom cell.

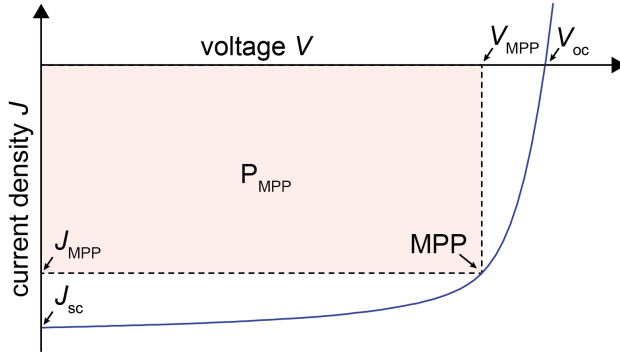


**Figure 2.2** Exemplary J-V characteristics of solar cell.

**Characteristic Properties** A solar cell can be characterized by various measurements and quantities. However, the most common description is made by measuring the current-voltage characteristics (J-V characteristics<sup>2</sup>) of the solar cell under illumination. An exemplary J-V curve is depicted in Fig. 2.2. The intersects of the curve with x- and y-axis correspond to the open-circuit voltage  $V_{oc}$  and short-circuit current density  $J_{sc}$ . While the  $J_{sc}$  is a measure for how effective the incoming light is absorbed in the absorber layers, the  $V_{oc}$  contains information about how well the charge carriers are separated. Ideally the solar cell is operated at the point of maximum power output (MPP). The fill factor  $FF$  is a measure of how well the device performs for given  $J_{sc}$  and  $V_{oc}$  and can be calculated by

$$FF = \frac{J_{mpp} V_{mpp}}{J_{sc} V_{oc}}. \quad (2.1)$$

The energy conversion efficiency of the solar cell  $\eta$  is expressed by the ratio of the electrical output power at the maximum power point  $P_{MPP}$  to the power of the incident light  $P_{in}$

$$\eta = \frac{P_{MPP}}{P_{in}} = \frac{FF}{V_{oc} J_{sc}} P_{in}. \quad (2.2)$$

To investigate the functionality of the solar cell spectrally resolved, the external quantum efficiency can be used. The external quantum efficiency is wavelength dependent and describes the fraction of the incoming photons that lead to charge carrier pairs at the contacts of the solar cell:

$$EQE(\lambda) = \frac{n_e(\lambda)}{n_{ph}(\lambda)}. \quad (2.3)$$

<sup>2</sup>To eliminate the influence of the total solar cell area  $A_{sc}$ , the electrical current  $I$  is normalized to the current density  $J = I/A_{sc}$ .

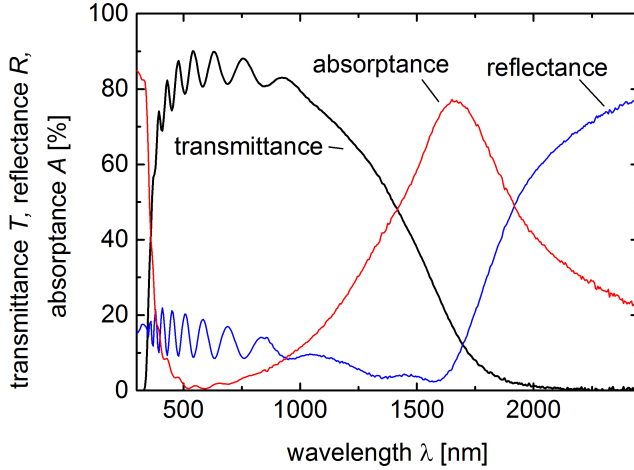


**Figure 2.3** Optical spectra of a  $h_{\text{TCO}} \approx 800$  nm thick layer of aluminium doped zinc oxide (ZnO:Al) as used for the experiments throughout this thesis: Due to the band gap of  $E_g = 3.4$  eV, ZnO:Al is highly absorbing below  $\lambda_{E_g} = 365$  nm. In the visible range, it is mainly transparent. Close to the plasma frequency at  $\lambda_p \approx 1700$  nm, the absorbance rises. Beyond, ZnO:Al becomes highly reflective.

With the number of incident photons  $n_{\text{ph}}$  and the number of electrons at the contact  $n_e$ . For further reading on solar cells and their characterization, please refer to [66, 83, 106]. For details about the measurement procedures as used in this thesis please refer to Sec. 3.1.3.

**ZnO:Al Front Contact** For the front contact layer of the solar cell, a highly transparent and conductive material (TCO)<sup>3</sup> is used. Common TCOs are tin-doped indium oxide ( $\text{In}_2\text{O}_3:\text{Sn}$ ), fluorine-doped tin oxide ( $\text{SnO}_2:\text{F}$ ) and aluminium-doped zinc oxide (ZnO:Al). As TCO for the front contact layer in thin-film silicon solar cells, mainly ZnO:Al or  $\text{SnO}_2:\text{F}$  are used [15, 68]. As  $\text{SnO}_2:\text{F}$  can be grown intrinsically textured, there is no urgent need for an additional texturing of the layers. Consequently, the work in this thesis focuses on the texturing of polycrystalline ZnO:Al layers.

<sup>3</sup>The abbreviation stems from Transparent Conductive Oxide but is used for all kinds of transparent and conductive materials.

Crystalline ZnO is a compound semiconductor with a direct band-gap of  $E_g = 3.4\text{ eV}$  [75]. Consequently it is transparent for visible light. By doping ZnO to degeneracy, the electrical conductivity is augmented. The ZnO:Al used for the experiments in this thesis is deposited by a radio-frequency sputtering process which leads to a growth in crystalline, columnar grains with an approximate grain size of  $d_{\text{grain}} = 40\text{ nm}$  to  $50\text{ nm}$  [8]. The layer thickness of a such typical ZnO:Al film used as front contact is  $h_{\text{TTCO}} \approx 800\text{ nm}$ . The sheet resistance of such a layer is on the order of  $R_{\square} = 3.5\ \Omega$ . An exemplary optical spectrum is depicted in Fig. 2.3. Due to the band-edge at around  $\lambda_{E_g} \approx 360\text{ nm}$ , the layer is strongly absorbing light below that wavelength<sup>4</sup>. In the visible range the transmittance is on the order of 80 %. Due to constructive and destructive interferences in between reflections from the flat glass–ZnO:Al and ZnO:Al–air interface, Fabry–Pérot interference fringes can be observed. From approx.  $\lambda \approx 1000\text{ nm}$  to longer wavelengths, the ZnO:Al layer becomes more absorbing. This is due to the exciting of the quasi-free electrons in the conduction band and damping of the oscillation by interaction with the ionic lattice. For smaller wavelengths the light cannot couple to the electron gas due to the high frequencies. The absorptance reaches its peak value at the wavelength corresponding to the plasma frequency at  $\lambda_p \approx 1700\text{ nm}$ . For even longer wavelengths, the light can perfectly couple to the electron gas and the ZnO:Al behaves like a metal and becomes highly reflective.

## 2.1.2 Light Management and Textured Interfaces

In order to improve the solar cells light harvesting behavior and efficiency, the control of light propagation into the cell and within the cell is essential. This control and guidance of light in the cell is often referred to as light management. Two main aspects of light management are the tasks to bring the light into the solar cell (by light in-coupling) and then keep it within the absorbing layer (by light trapping) until it is absorbed. A possible way to accomplish these tasks is by introducing textured interfaces into the solar cell.

**Light In-Coupling** Light in-coupling refers to minimizing the reflection of incoming light at the front contact–p-layer interfaces before the light even reaches the first absorbing layer (see left ray in Fig. 2.4 (a) ). This can be either achieved by anti-reflection coatings taking advantage of interference effects of incoming and reflected wave or by surface textures with very small feature sizes. Textures with feature sizes smaller than the wavelength of the incoming light, cannot be "resolved" by the light. The light only "sees" a gradual change of material and an associated gradient of refractive indices. A smooth transition of refractive indices,

---

<sup>4</sup>The exact band gap energy  $E_g$  depends on the charge carrier concentration.

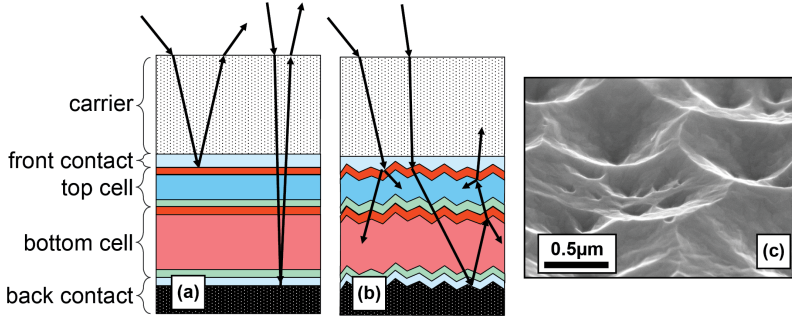


**Figure 2.4** Light management (illustration) and texture-etched ZnO:Al (SEM image [70]): Textured interfaces reduce reflection losses of solar cell. By introducing a gradient of refractive indices, the in-coupling of the light into the solar cell is improved (light in-coupling: left rays in (a) and (b)). By scattering the light, the light paths in the absorber layer are enhanced and the chance of absorption increases. (light trapping: right rays in (a) and (b)). (c) SEM image of topography of typical texture-etched ZnO:Al layer as used for the manufacturing of thin-film silicon solar cells.

however, can be interpreted as a stack of many flat layers with only small changes of refractive index between two adjacent layers. For the same materials, such layer stack reveals a lower total reflectance than the one of a single interface. The amount of reflected light at a flat interface of materials with different refractive indices can be described by the Fresnel equations. For perpendicular incidence the reflectance is given by

$$R = \left| \frac{n_1 - n_2}{n_1 + n_2} \right|^2. \quad (2.4)$$

With the refractive indices  $n_1$  and  $n_2$  of the first and second layer respectively. This reflectance decreases for decreasing  $|n_1 - n_2|$ . Even the increasing amount of interfaces and the corresponding additional reflections are overcompensated by the reduction of each of the single reflections. Consequently, textured interfaces with feature sizes smaller than the wavelength of the incoming light can reduce reflection and improve light in-coupling.

**Light-Trapping** Some of the light incident on the solar cell can also be reflected by passing through the absorbing layer, reflect at the back contact, passing through the layer again and leave the cell without being absorbed. To prevent such reflection losses, either the absorption properties of the absorbing material (here a-Si:H or  $\mu\text{-Si:H}$ ) need to be enhanced or the path the light travels within the absorbing

layer needs to be elongated. A longer propagation path<sup>5</sup> (light path) within the absorbing material increases the chance for absorption. One way to elongate the light path is by using thicker absorber layers. However, thicker a-Si:H layers show a stronger degradation due to the Staebler–Wronski effect [94]. Another option is to keep the layer thickness as thin as possible but elongating the light path by scattering the light into large angles (see right ray in Fig. 2.4 (b)) [9, 14, 87]. This concept is known as "light trapping" because for very large angles the light can be trapped within the absorbing layer due to internal total reflection. The scattering of light is generally achieved by introducing textured interfaces into the solar cell's layer stack. By texturing the TCO front contact and conformal deposition of the remaining layers on top of it (superstrate configuration), all interfaces within the layer stack can be textured. After Yablonovitch [108] developed a statistical model to determine the maximum theoretical gain of light intensity in the absorber layer by randomizing the incoming light, first optically enhanced a-Si:H solar cells were developed in 1983 [25]. From then on, various light trapping schemes have been developed [9, 84]. Apart from random texture, also periodic structures have been proven to show good light trapping abilities [39, 57, 76, 97].

**Texture-etching of ZnO:Al** To introduce textured interfaces in a solar cell, texture-etching of the polycrystalline ZnO:Al layers has become a standard approach and has been investigated thoroughly [9, 47, 68]. While other TCOs like SnO<sub>2</sub>:F can be grown intrinsically textured, the radio-frequency sputtered ZnO:Al grows comparatively flat. By submerging the substrate consisting of a glass carrier and the ZnO:Al film into a bath of  $\sigma_{\text{HCl}} = 0.5\%$  hydrochloric acid (HCl), the surface is textured. After an etch time of approx.  $t_{\text{etch}} \approx 30$  s a crater like texture can be observed on the surface of the ZnO:Al layer (see Fig. 2.4 (c)). However, the detailed etching behavior depends on the exact deposition conditions of the ZnO:Al layer [18, 53, 55].

### 2.1.3 Phase Model

In order to be able to judge the potential light trapping abilities of a given texture, the so called "phase model" is used. The model calculates the light trapping efficiency *LTE* for a given texture. This *LTE* is a scalar value between 0 and 1 which has been validated to correlate with the solar cell efficiency for thin-film silicon solar cells. The model is based on a theoretical approach to describe light

---

<sup>5</sup>Please keep in mind that due to the thin layer thicknesses and feature sizes the detailed propagation of electro-magnetic waves in the solar cell compound is better described by wave-optics – if not rigorous solution of the Maxwell equations. Nevertheless, the simple model of geometric optics provides a comprehensive and good approximation of the underlying processes.

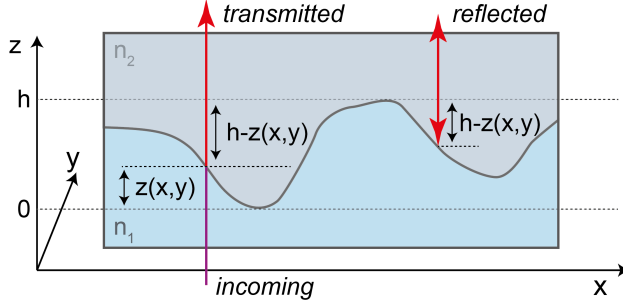


**Figure 2.5** Illustration of phase change due to different lengths of propagation paths in different media with refractive indices  $n_1$  and  $n_2$ . Light beam on the left is entering from the bottom and is propagating through a textured interface. Beam on the right is entering from the top and is being reflected at the textured interface.

scattering at rough surfaces by Harvey et al. [45] and has been adapted and validated to predict transmission through textured TCOs as used in thin-film silicon solar cells in theory and experiment [13, 28, 35, 90]. It was developed further to also predict reflection and hence, give a measure for the light trapping abilities of a given texture when used in a solar cell [11, 52]. Recently, it has been used to evaluate different textures for their potential application in thin-film silicon solar cells [12].

In the following paragraphs, the working principle of the phase model is described. In the framework of this thesis, the phase model was implemented as a module in the *Python* programming environment which is referred to as *PyLTE*.

**Phase Difference** For the calculations, normal incidence of the incoming light is assumed. For each point in the  $x, y$  plane, the change of phase for a light beam propagating through the textured interface is calculated in dependence of the layer thickness  $z(x, y)$  at that same point (see Fig. 2.5). The phase difference  $\Delta\phi^T$  in dependence of the refractive indices of the textured surface's adjacent layers  $n_1$  and  $n_2$  as well as the wavelength of the incoming light  $\lambda$  is calculated by

$$\Delta\phi^T(x, y) = \frac{2\pi}{\lambda}(n_1 - n_2)z(x, y). \quad (2.5)$$

Whereas it is assumed that the beam enters from the side of layer 1.

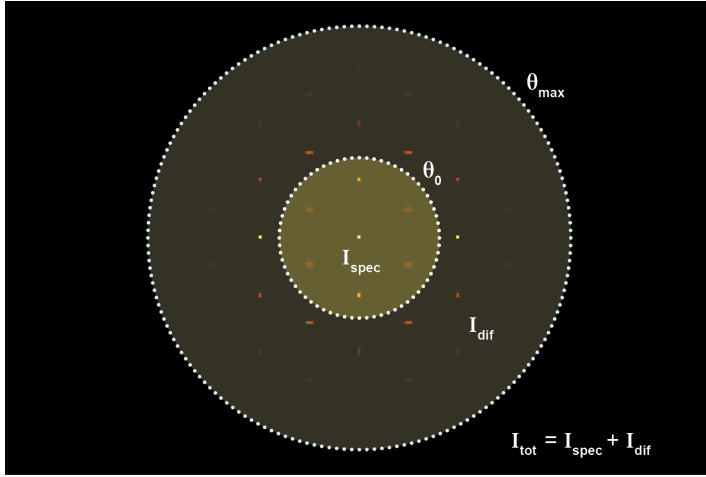


**Figure 2.6** Exemplary angular intensity distribution: The total intensity of the transmitted light  $I_{\text{tot}}$  is divided into the specular part  $I_{\text{spec}}$  and diffuse part  $I_{\text{diff}}$ .

Similarly, the change of phase for a light beam entering from the side of layer 2 which is being reflected at the textured interface can be calculated by

$$\Delta\phi^{\text{R}}(x, y) = 2 \cdot \frac{2\pi}{\lambda} n_2 (h - z(x, y)). \quad (2.6)$$

**Angular Intensity Distribution** From the phase differences  $\Delta\phi^{\text{T,R}}(x, y)$  an Angular Intensity Distribution  $AID(\theta, \varphi)$  can be obtained by

$$AID(\theta, \varphi) = \frac{\lambda^2}{A_{\text{txt}}} \cdot |\mathcal{F}\{e^{i\Delta\phi^{\text{T,R}}(x,y)}\}|^2, \quad (2.7)$$

whereas  $\mathcal{F}$  stands for the Fourier transform and  $A_{\text{txt}}$  for the area of the scattering surface. The spherical coordinates  $\theta$  and  $\varphi$  of the scattered light are related to the reciprocal lattice vectors  $k_x$  and  $k_y$  by

$$\sin \theta = \frac{\lambda}{2\pi} \sqrt{k_x^2 + k_y^2} \quad \text{and} \quad \tan \varphi = \frac{k_y}{k_x}. \quad (2.8)$$

For details on the calculations please refer to [11, 28, 45].

The  $AID$  is a measure for the diffraction pattern of the scattered light in the far field. For further calculations, the intensities of the light are binned in various groups:

- All light diffracted into angles larger or equal to the maximum scattering angle  $\theta_{\max} = 90^\circ$  is scattered into evanescent modes and is not regarded for the calculations.
- Light scattered into angles smaller than the maximum scattering angle  $\theta < \theta_{\max}$  is considered to be transmitted<sup>6</sup> and its intensity is cumulated in the total transmitted intensity

$$I_{\text{tot}} = \int_0^{360^\circ} \int_0^{90^\circ} AID(\theta, \varphi) d\varphi \sin \theta d\theta. \quad (2.9)$$

This total transmitted intensity is then divided into two parts:

- All light transmitted into angles in between a certain threshold angle  $\theta_0$  and the maximum angle  $\theta_0 < \theta < \theta_{\max}$  is considered to be transmitted diffusely and its intensity is denoted with

$$I_{\text{dif}} = \int_0^{360^\circ} \int_{\theta_0}^{90^\circ} AID(\theta, \varphi) d\varphi \sin \theta d\theta. \quad (2.10)$$

- The remaining intensities at angles  $\theta < \theta_0$  are considered to be transmitted specularly and are cumulated in  $I_{\text{spec}}$  (also see Fig. 2.6).

**Light Trapping Efficiency** Assuming total internal reflection of light at the a-Si:H–ZnO:Al interface at an angle  $\theta_0 = 24.5^\circ$ , all light which is diffracted diffusely ( $I_{\text{dif}}$ ) into angles larger than that critical angle  $\theta > \theta_0 = 24.5^\circ$  is considered to be trapped within the layer. To obtain a measure for the light trapping efficiency of a certain texture, the ratio of diffusely transmitted light and the total of all transmitted light is calculated for transmission as well as reflection. An arithmetic mean of these ratios for transmission and reflection is calculated for each wavelength. By spectral averaging over a given set of  $N$  wavelengths ( $\lambda_0, \dots, \lambda_N$ ), the monochromatic light trapping efficiency  $LTE$  can be calculated by

$$LTE = \frac{1}{N} \sum_{\lambda_0}^{\lambda_N} \left( 0.5 \cdot \frac{I_{\text{dif}}^{\text{T}}(\lambda)}{I_{\text{tot}}^{\text{T}}(\lambda)} + 0.5 \cdot \frac{I_{\text{dif}}^{\text{R}}(\lambda)}{I_{\text{tot}}^{\text{R}}(\lambda)} \right). \quad (2.11)$$

---

<sup>6</sup>transmitted or reflected depending if scattering by transmission through textured surface or scattering by reflection at textured surface is investigated.

Using wavelengths from  $\lambda_0 = 600 \text{ nm}$  to  $\lambda_N = 900 \text{ nm}$  in steps of  $\Delta\lambda = 10 \text{ nm}$ , the light trapping efficiency  $LTE$  has been shown to correlate with the external quantum efficiency of  $\mu\text{c-Si:H}$  solar cells [11].

## 2.2 Lasers

### 2.2.1 Properties of Laser Light and Beams

The following section is intended to give an overview of the most important properties of laser light and laser beams. First, inherent properties of laser light such as coherence and polarization are explained. Then the Gaussian beam optics with its characteristic fluence distribution and terminology are highlighted. After some geometrical considerations needed for beam propagation, the section concludes with the calculation of the laser intensity distribution within an interference volume of various coherent laser beams.

**Polarization** In contrast to many natural light sources, laser light has a well defined polarization. The polarization of a light wave describes the orientation of its electrical field vector and how it changes as the wave propagates through space. Due to the stimulated emission in the resonator of a laser system, a laser light wave traveling in z-direction has a constant phase difference  $\varphi_0$  between its electric field components in x and y direction. Depending on the value of this phase difference and the amplitudes in x and y-direction  $E_x^0$  and  $E_y^0$ , different types of polarizations are distinguished (see Fig. 2.7).

- If the phase difference is equal to zero ( $\varphi_0 = 0$ ), the wave is said to have linear polarization.
- For  $|\varphi_0| = \pi/2$  and  $E_x^0 = E_y^0$  it is said to have circular polarization. Circularly polarized waves can be left- or right-handed circularly polarized.
- For all other phase differences  $\varphi_0 = \text{const}$  the polarization is a mix of the types mentioned above and the wave is said to have elliptical polarization.

The naming of the types stems from the geometrical figure the tip of the electrical field vector describes during time when projected into the x,y-plane (see Fig. 2.7). Because averaged over time, linearly polarized laser light has a distinct orientation, the orientation of the polarization can be important for the laser-material interaction. In order to rotate the polarization, the electrical field along a given optical axis is retarded by half a wavelength. Practically, this can be achieved by introducing a half-wave plate into the beam path (see paragraph on rotating linear polarized light in Section 2.2.1). Furthermore, linearly polarized

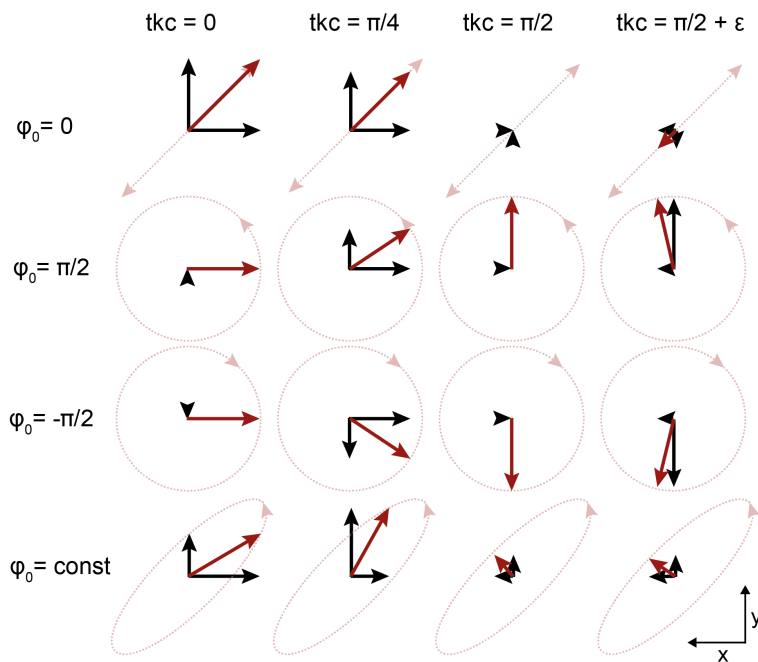


**Figure 2.7** Sketch of electrical field vectors for different types of polarizations at different times but constant  $z$ -position: With no phase difference in between  $x$ - and  $y$ -component of the electrical field ( $\varphi_0 = 0$ ), the wave is linearly polarized (top row). For  $|\varphi_0| = \pi/2$  the wave is circularly polarized, whereas the handedness depends on the sign of the phase difference. If the wave is traveling into the paper plane and is looked upon from the senders point of view, the second row ( $\varphi_0 = \pi/2$ ) is left-handed circularly polarized and the third row ( $\varphi_0 = -\pi/2$ ) is right-handed circularly polarized. For a constant but arbitrary phase difference of  $\varphi_0 = \text{const}$  the wave is polarized elliptically (bottom row). Here,  $k$  denotes the wavenumber,  $c$  the speed of light and  $t$  the time.  $\varepsilon$  is a small number ( $\varepsilon \ll \pi$ ).

light can be converted into circularly polarized light by retarding one electrical field component by a quarter of a wavelength and vice versa. Depending on the orientation of the quarter-wave plate introduced into a linearly polarized laser beam, the resulting beam can be left-handed, right-handed circularly or elliptically polarized.

**Coherence** An essential property of laser light is coherence. In general, two waves are considered coherent if they have a constant phase relation. Coherence and interference are strongly related. Although the superposition of any waves can be referred to as interference, the term interference is mainly associated with the superposition of coherent waves. Only the superposition of coherent waves can reveal a temporally constant but spatially varying intensity pattern like a standing wave. In laser optics and the characterization of laser beams, coherence is understood as a property of one single laser beam. If the laser beam is coherent with itself at another point in time or space it is considered temporally or spatial coherent respectively.

In more detail, spatial coherence is the cross-correlation of two spatial point within the same wave. Accordingly, if the waves at two points in the cross-section of a laser beam interfere, these two points lie within the area of spatial coherence of the beam. Spatial coherence is especially important for e.g. double-slit experiments, where two different parts of the laser beam profile are meant to interfere. Such Young interferometers can also be used to measure the spatial coherence of a laser beam [110].

Temporal coherence is the cross-correlation of the same wave at the same spatial point but different points in time. In a laser beam, it is the ability of the laser beam to interfere with itself at a different time. The maximum delay time that still produces interference is called the coherence time  $\Delta\tau_c$ . The distance the wave can propagate within that time is defined as the coherence length

$$\Delta l_c = \frac{c}{n} \cdot \Delta\tau_c. \quad (2.12)$$

Here,  $n$  denotes the refractive index of the medium the wave travels in.

For a more intuitive description, the coherence length can also be thought of as the distance within a wave packet with predictable phase (compare Fig. 2.8). Only perfect monochromatic waves can have infinite coherence length. However, every real wave packet consists of waves of different frequencies and has finite coherence length. The relation between coherence length and spectral width of the light source  $\Delta\lambda_L$  can be approximated by

$$\Delta l_c \approx \frac{\lambda_L^2}{n\Delta\lambda_L}, \quad (2.13)$$

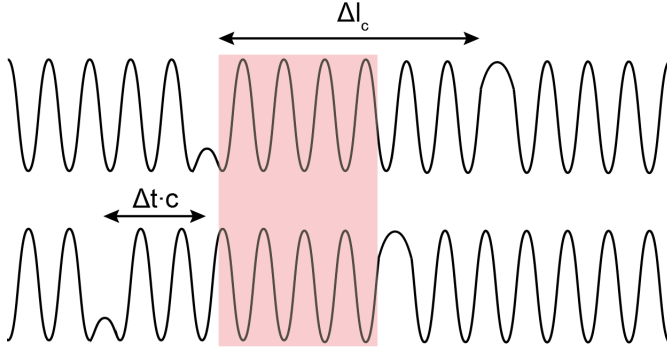


**Figure 2.8** Temporal coherence: The depicted wave has a coherence length of  $\Delta l_c$  (top) which corresponds to the distance within a wave that has a predictable phase. When delayed by  $\Delta t$  (bottom), the wave can only interfere with itself within the red shaded region. If  $\Delta t \cdot c$  is larger than the coherence length, the waves cannot interfere.

whereas  $\lambda_L$  denotes the central wavelength in the spectrum of the light source. The temporal coherence length can be measured by a Michelson interferometer [67].

**Beam Profile** In the cylindrical resonator of a laser system, a solution to the paraxial approximation of the radial component of the wave equation are the Laguerre-Gaussian modes. Of these modes, the fundamental Transverse Electro-Magnetic  $TEM_{00}$ <sup>7</sup> mode is the least divergent. Consequently, after the numerous reflections within the resonator cavity, the  $TEM_{00}$  is the most prevailing mode. The other modes have diverged and have been eventually blocked by the apertures of the resonator mirrors. Because of its Gaussian shaped intensity profile, the  $TEM_{00}$  mode is often called the Gauss-mode, and the beam a Gaussian beam. It is assumed that most laser system radiate in the Gauss-mode. Real laser beams always consist of a superposition of various modes, however, the assumption of the Gaussian beam profile often is an adequate approximation. For a more detailed introduction to Gaussian optics please refer to [79].

The intensity distribution  $I(x, y, z)$  of a Gaussian beam propagating in  $z$  is given by

$$I(x, y, z) = I_0(z) \exp\left(-2\frac{x^2 + y^2}{w(z)^2}\right), \quad (2.14)$$

<sup>7</sup>The fundamental Laguerre-Gaussian mode  $TEM_0^0$  is identical to the fundamental Hermite-Gaussian  $TEM_{00}$ . For reasons of simplicity the later nomenclature is used.

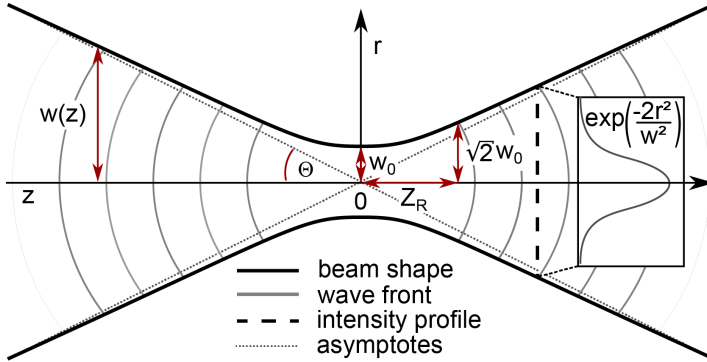


**Figure 2.9** Schematic drawing of beam waist in Gaussian beam.

with the beam radius  $w(z)$  and

$$I_0(z) = \frac{4P}{w(z)^2}, \quad (2.15)$$

whereas  $P$  denotes the total laser power.

At radius  $r = w$ , the intensity has dropped to  $I = 1/e^2 \cdot I_0$ . Every Gaussian beam has a divergence and a beam waist. By focusing optics these properties can be controlled. The shape of a Gaussian beam is depicted in Fig. 2.9<sup>8</sup>. The waist of the laser beam is often referred to as its focus and the radius of the beam in the focus is denoted with  $w_0$ . The angle of the asymptotic lines to the envelope of the beam is referred to as divergence of the beam and is denoted with  $\Theta$ . The divergence is related to the beam radius in the focus and the wavelength of the laser light  $\lambda_L$  by

$$\Theta = \arctan\left(\frac{\lambda_L}{\pi w_0}\right) \approx \frac{\lambda_L}{\pi w_0}. \quad (2.16)$$

Another parameter used to describe the focus of a laser beam is the Rayleigh length  $z_R$ . It is defined as the distance from the waist, along the propagation direction to the position where the area of the cross section of the beam has doubled (compare Fig. 2.9). It can be determined by

$$z_R = \frac{\pi w_0^2}{\lambda_L}. \quad (2.17)$$

**Fluence distribution on sample** The distribution of the energy deposited on the sample can be described in various ways. The describing quantities are often not

<sup>8</sup>Adapted from source Wikimedia.

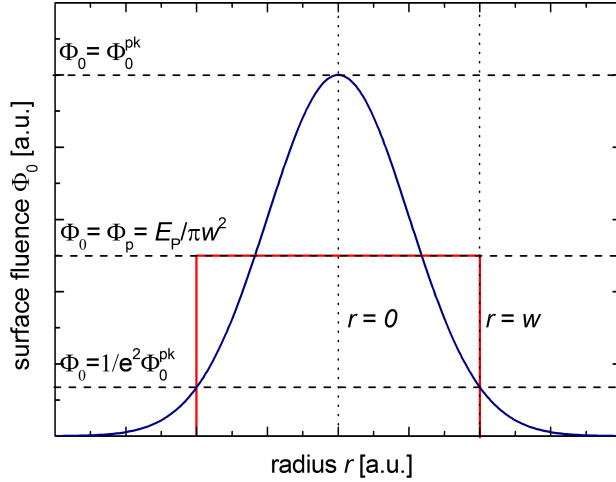


**Figure 2.10** Fluence distribution within the laser spot: The Gaussian distribution  $\Phi_0(\mathbf{r})$  is often approximated with a constant value  $\Phi_p = E_p/\pi w^2$  which assumes an equal distribution of the pulse energy  $E_p$ . The relation between peak fluence  $\Phi_0^{\text{pk}}$  and averaged fluence is given by the fact that both volumes under the curves (blue and red line) have to be equal to the pulse energy  $E_p$  and can be calculated to  $\Phi_0^{\text{pk}} = 2\Phi_p$

used consistently and their meaning varies throughout literature. To clarify their meaning in this manuscript, the most commonly used quantities are explained in the following paragraph.

The incident intensity on the sample surface is of radial symmetry and can be described by Eq. 2.14. Analogously, the deposited energy per area after one laser pulse can be described by

$$\Phi_0(\mathbf{r}) = \Phi_0^{\text{pk}} \exp\left(-\frac{2\mathbf{r}^2}{w^2}\right), \quad (2.18)$$

with  $\mathbf{r}^2 = x^2 + y^2$ . The quantity  $\Phi_0$  is referred to as fluence and has the dimensions  $[\Phi_0] = \text{J}/\text{m}^2$ . The subscript zero ( $\Phi_0(x, y)$ ) denotes the fluence as a surface fluence how it can be measured at the surface of the material before being absorbed. The fluence within the material is denoted as  $\Phi(x, y, z)$ . The highest (peak) fluence in the center of the beam is denoted with  $\Phi_0^{\text{pk}}$ .

Quite commonly, the Gaussian distribution of the fluence is neglected and a constant fluence  $\Phi_p$  within the laser pulse is assumed (see Fig. 2.10). This averaged pulse fluence  $\Phi_p$  is then calculated by

$$\Phi_p = \frac{E_p}{A_b} \quad \text{with} \quad A_b = \pi w^2. \quad (2.19)$$

Often this averaged pulse fluence  $\Phi_p$  is simply referred to as "the fluence". However, the exact fluence  $\Phi_0(\mathbf{r})$  depends on the position within the pulse area and only equals  $\Phi_p$  at

$$\Phi_0(|\mathbf{r}| = \sqrt{\ln 2/2} \cdot w) = \Phi_p. \quad (2.20)$$

Another way of describing the fluence is by its peak value  $\Phi_0^{\text{pk}}$  in the center of the pulse at  $\mathbf{r} = 0$ . Because the volume under the Gaussian fluence distribution has to be equal to the total pulse energy  $E_p$  the peak fluence can be calculated by integrating Eq. 2.18 and

$$\int_{\mathbb{R}^2} \Phi_0(\mathbf{r}) = E_p \quad (2.21)$$

which yields

$$\Phi_0^{\text{pk}} = \frac{2E_p}{\pi w^2} = 2\Phi_p. \quad (2.22)$$

Sometimes the radius of the fluence distribution is also given by the full width half maximum (FWHM) value where

$$\Phi_0(w_{50}) = \Phi_0^{\text{pk}}/2, \quad w_{50} = \sqrt{\ln 2/2} \cdot w. \quad (2.23)$$

The laser treated region on the sample is referred to as the laser spot. The radius of this region is referred to as the spot radius  $r_s$  and its area as the spot area  $A_s$ . The exact value of  $r_s$  can be difficult to determine. An approximation can be made by observing the sample in an optical microscope and estimating the visible spot radius  $r_s^{\text{vis}}$ . However, often  $r_s^{\text{vis}} < r_s$ . Furthermore, in general neither  $r_s$  nor  $r_s^{\text{vis}}$  coincide with the beam radius  $w$ .  $w$  is a beam property, but  $r_s$  and  $r_s^{\text{vis}}$  strongly depend on the treated material.

**Planar Treatments** In order to treat surfaces with pulsed laser systems, the laser spots on the sample can be stitched together to cover larger areas. Stitching here refers to subsequent treatment of the surface with overlapping treated areas. For a Gaussian beam and perpendicular incidence, circular laser spots on the sample are expected. When overlapping such circular spots, two different overlaps can be defined (compare Fig. 2.11). The line overlap in x-direction  $\xi_x$  denotes

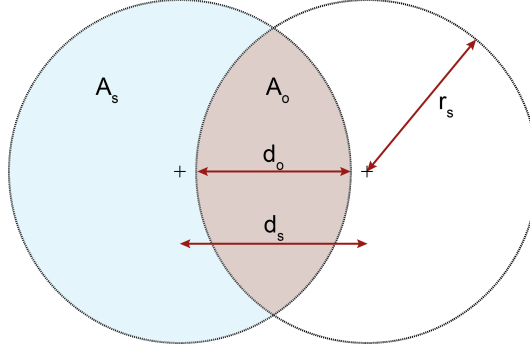


**Figure 2.11** Sketch of overlapping laser spots: The line overlap is defined as the ration of  $d_o$  and the spot diameter  $2r_s$ , whereas the area overlap is defined as the ratio of the overlapping area  $A_o$  (shaded red) and the spot area  $A_s$  (shaded blue).

the ratio of the overlapping distance  $d_o$  to the diameter of one laser spot  $2r_s$  and thus can be calculated by

$$\xi_x = \frac{d_o}{2r_s} = 1 - \frac{d_x}{2r_s}, \quad (2.24)$$

whereas  $d_s$  denotes the distance in between two adjacent laser spots (see Fig. 2.11). The area overlap in x-direction  $\Xi_x$  is defined as the ratio of the overlapping area  $A_o$  (red shaded area in Fig. 2.11) and the spot area  $A_s$ . By geometrical considerations it can be calculated to

$$\Xi_x = \frac{A_o}{A_s} = \frac{2r_s^2 \arccos\left(\frac{d_x}{2r_s}\right) - d_s \sqrt{r_s^2 - \left(\frac{d_x}{2}\right)^2}}{\pi r_s^2}. \quad (2.25)$$

**Rotation of Polarization by Half-Wave Plate** The polarization of a linear polarized laser beam can be expressed by the angle  $\gamma_i$  between a reference vector perpendicular to its wave vector and the vector of its electric field  $\hat{e}_i$ . If the electromagnetic wave perpendicularly hits a half-wave plate, the component of its electric field which is parallel to the optical axis of the plate is retarded by half a wavelength. Consequently, the polarization is rotated towards the optical axis by an amount of twice the angle in between polarization of laser beam and optical axis (Eq. 2.26). So for a laser beam with an initial polarization of  $\gamma_i^1$  and

an optical axis of the wave plate orientated at  $\alpha_{\text{opt}}$  the polarization of the laser beam after passing the plate is<sup>9</sup>

$$\gamma_i^f = 2(\alpha_{\text{opt}} - \gamma_i^i). \quad (2.26)$$

The rotation of a vector  $\mathbf{v}$  by an angle of  $\alpha$  in three-dimensional Cartesian coordinates can be expressed by

$$\mathbf{v}' = R \cdot \mathbf{v} \quad (2.27)$$

with

$$R = \begin{pmatrix} n_x^2(1 - c_\alpha) + c_\alpha & n_x n_y(1 - c_\alpha) - n_z s_\alpha & n_x n_z(1 - c_\alpha) + n_y s_\alpha \\ n_y n_x(1 - c_\alpha) + n_z s_\alpha & n_y^2(1 - c_\alpha) + c_\alpha & n_y n_z(1 - c_\alpha) - n_x s_\alpha \\ n_z n_x(1 - c_\alpha) - n_y s_\alpha & n_z n_y(1 - c_\alpha) + n_x s_\alpha & n_z^2(1 - c_\alpha) + c_\alpha \end{pmatrix} \quad (2.28)$$

and

$$c_\alpha = \cos \alpha, \quad s_\alpha = \sin \alpha, \quad \mathbf{n} = \begin{pmatrix} n_x \\ n_y \\ n_z \end{pmatrix}. \quad (2.29)$$

**Reflection of Laser Beam on Mirror** The geometrical reflection of a laser beam on a plane mirror can be calculated by reflecting its wave vector  $\mathbf{k}_i$  and its polarization vector  $\hat{\mathbf{e}}_i$  with respect to the normal  $\mathbf{n}$  of the mirror plane. The reflection of the vectors in Cartesian coordinates can be calculated by

$$\mathbf{v}' = (-1) \cdot T \cdot \mathbf{v} \quad (2.30)$$

with

$$T = \begin{pmatrix} 2n_x^2 - 1 & 2n_x n_y & 2n_x n_z \\ 2n_y n_x & 2n_y^2 - 1 & 2n_y n_z \\ 2n_z n_x & 2n_z n_y & 2n_z^2 - 1 \end{pmatrix} \quad \text{and} \quad \mathbf{n} = \begin{pmatrix} n_x \\ n_y \\ n_z \end{pmatrix}. \quad (2.31)$$

Here,  $\mathbf{v}$  denotes the original vector,  $\mathbf{v}'$  the reflected vector and  $\mathbf{n}$  the normal to the mirror surface.

---

<sup>9</sup>all angles are expressed with respect to the same reference vector

**Laser Interference** Laser beams can be considered perfectly monochromatic and coherent and ideally have a plane wave front. Consequently, a linearly polarized laser beam can be represented by a plane wave:<sup>10</sup>

$$\mathbf{E}_i(\mathbf{r}, t) = E_i e^{-j(\mathbf{k}_i \cdot \mathbf{r} - \phi_i)} e^{-j\omega t} \hat{\mathbf{e}}_i, \quad (2.32)$$

with the electric field amplitude  $E_i^0$ , wave vector  $\mathbf{k}_i$ , phase  $\phi_i$ , angular frequency  $\omega$  and the unit vector  $\hat{\mathbf{e}}_i$  pointing in the direction of its polarization. Whenever  $n$  laser beams overlap, the resulting electromagnetic field

$$\mathbf{E}_{\text{tot}}^{(n)}(\mathbf{r}, t) = \sum_{i=1}^n \mathbf{E}_i(\mathbf{r}, t) \quad (2.33)$$

can be calculated by the superposition of the  $n$  plane waves. To obtain a measure for the total laser intensity within the interference volume  $I_{\text{tot}}^{(n)}(\mathbf{r}, t)$  can be calculated by taking a time average of the squared total electric field:

$$\begin{aligned} I_{\text{tot}}^{(n)}(\mathbf{r}) &= \langle \mathbf{E}_{\text{tot}}^{(n)}(\mathbf{r}, t) \cdot \mathbf{E}_{\text{tot}}^{(n)}(\mathbf{r}, t) \rangle \\ &= \sum_{i=1}^n \left( \frac{1}{2} E_i^2 + \sum_{j>i}^n E_i E_j e_{ij} \cos((\mathbf{k}_j - \mathbf{k}_i) \cdot \mathbf{r} + \phi_i - \phi_j) \right) \end{aligned} \quad (2.34)$$

with

$$e_{ij} = \hat{\mathbf{e}}_i \cdot \hat{\mathbf{e}}_j. \quad (2.35)$$

Please note, that the relation of laser intensity and electric field amplitudes is assumed to be<sup>11</sup>

$$I = \frac{1}{2} E_0^2. \quad (2.36)$$

The phases of the individual beams  $\phi_i$  merely influence the spatial phase of the intensity pattern. Because the spatial phase is only of minor interest for the light trapping abilities of the texture, it is omitted in further calculations. The phases of the individual beams can then be set to zero ( $\phi_i = 0 \quad \forall i$ ) without losing information about the general shape of the intensity pattern. For three beams, Eq. 2.34 can then be simplified to

$$I_{\text{tot}}^{(3)}(\mathbf{r}) = I_0 [1 + V_{12} \cos(\mathbf{G}_{21} \cdot \mathbf{r}) + V_{13} \cos(\mathbf{G}_{31} \cdot \mathbf{r}) + V_{23} \cos(\mathbf{G}_{32} \cdot \mathbf{r})] \quad (2.37)$$

<sup>10</sup>Due to simplicity reasons, the nomenclature within this paragraph differs from the nomenclature in the rest of the thesis. Apart from this paragraph, however, the naming of variables is stringent throughout the thesis.

<sup>11</sup>This simplification can be used, because the same relation is also used to calculate the electric field amplitudes from measured laser intensity.

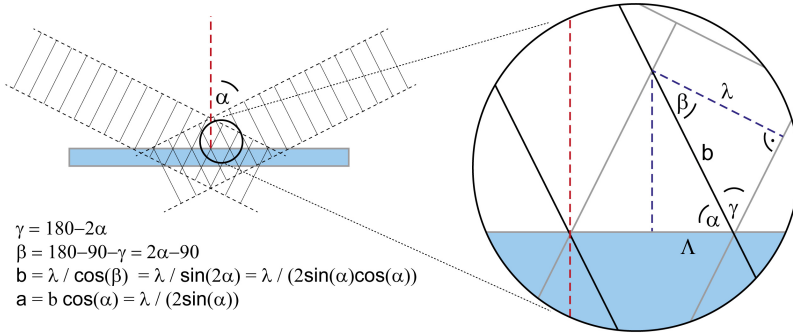


**Figure 2.12** Sketch of two-beam interference: For the special case of equiangular incidence of both beams, the spatial period of the intensity pattern can be calculated by simple geometric considerations.

with

$$I_0 = \frac{1}{2} \sum_{k=1}^3 E_k^2, \quad V_{ij} = \frac{E_i E_j e_{ij}}{I_0}, \quad e_{ij} = \hat{e}_i \cdot \hat{e}_j \quad \text{and} \quad \mathbf{G}_{ij} = \mathbf{k}_i - \mathbf{k}_j. \quad (2.38)$$

These intensity patterns can exhibit symmetries inherent in 5 of the 17 plane symmetry groups. For a more detailed description of the mathematical background and an analysis of the possible contrast and crystallography of such patterns please refer to [95]. Please note, that equation 2.37 is invariant for changes along the direction defined by the sum of the laser beams wave vectors:

$$I_{\text{tot}}^{(3)}(\mathbf{r}) = I_{\text{tot}}^{(3)}(\mathbf{r} + a \cdot (\mathbf{k}_1 + \mathbf{k}_2 + \mathbf{k}_3)) \quad \text{with} \quad a \in \mathbb{R}. \quad (2.39)$$

This can be particularly interesting for equiangular incidence of the beams, because then the intensity distribution is invariant in the direction of the surface normal.

For two beams, this equation can be further simplified yielding a one dimensional line like pattern with sinusoidal character:

$$I_{\text{tot}}^{(2)}(\mathbf{r}) = \frac{1}{2} E_1^2 + E_1 E_2 e_{12} \cos((\mathbf{k}_2 - \mathbf{k}_1) \cdot \mathbf{r}) + \frac{1}{2} E_2^2 \quad (2.40)$$

If the angle of both beams to the surface normal is equal (i.e. the sum of the two wave vectors  $\mathbf{k}_1$  and  $\mathbf{k}_2$  is perpendicular to the sample plane), the spatial period of the intensity pattern is given by

$$\Lambda = \frac{\lambda_1}{2 \sin \alpha}, \quad (2.41)$$

merely depending on the laser wavelength  $\lambda_1$  and the angle of the beams to the surface normal  $\alpha$ . This relation can also be visualized by geometric considerations as in Fig. 2.12. For an outlook on laser interference with more than three laser beams, please refer to [72].

## 2.2.2 Laser-Material Interaction

Laser material processing is based on the interaction of laser light and the material of the sample to be treated. The electromagnetic waves of the laser light first excite the electrons in the material. For laser pulse durations in the nanosecond regime, it can be assumed that the excited electrons have enough time to relax and transfer the energy into the lattice. The laser pulse duration  $\tau_p$  is significantly longer than the typical electron-lattice interaction time  $\tau_i$  and the electrons and lattice can be assumed to have the same "temperature" [24]. In this regime, the interaction of laser light and material can be reduced to a mere energy transfer from the laser into the material and a consequent heat distribution within the material. The following section delivers a rough mathematical description of the two basic physical principles needed for such a description: The absorption of incident laser light in the material and the diffusion of the resulting heat distribution within the material.

**Light Absorption in Material** When light travels through a material it is attenuated exponentially. For a given incident intensity  $I_0$  at the surface of the material, the remaining intensity  $I(z)$  at depth  $z$  can be expressed by Lambert-Beer's law

$$I(z) = I_0 e^{-\alpha z}, \quad (2.42)$$

where  $\alpha$  denotes the absorption coefficient of the material and  $z$  is the spatial coordinate perpendicular to the surface with positive values within the material. The absorption coefficient can be calculated from the extinction coefficient  $n''$  and the wavelength  $\lambda$  to

$$\alpha = \frac{4\pi n''}{\lambda}. \quad (2.43)$$

Consequently, the total absorbed intensity  $I_{\text{abs}}(z)$  in dependence of the depth  $z$  can be described by

$$I_{\text{abs}}(z) = I_0 - I(z) = I_0(1 - e^{-\alpha z}). \quad (2.44)$$

By derivation of Eq. 2.44 with respect to  $z$ , the absorbed power per volume  $\omega(z)$  can be calculated:

$$\frac{d}{dz}(I_0 - I(z)) = \omega(z) = I_0 \cdot \alpha \cdot e^{-\alpha z}. \quad (2.45)$$

**Heat Diffusion** The heat equation describes the distribution of heat in a given medium over time. For a medium with homogeneous and isotropic thermal diffusivity  $D$ , it can be expressed by the diffusion equation

$$\frac{\partial}{\partial t}\psi(\mathbf{r}, t) - D\Delta\psi(\mathbf{r}, t) = f(\mathbf{r}, t), \quad (2.46)$$

whereas  $\psi(\mathbf{r}, t)$  denotes the temperature at location  $\mathbf{r}$  and time  $t$ , and  $D$  is the thermal diffusivity of the medium,  $\Delta$  the Laplace operator and  $f(\mathbf{r}, t)$  the heat source.

The thermal diffusivity is a property of the medium and can be calculated from its heat conductivity  $\kappa$ , mass density  $\rho$  and isobaric mass heat capacity  $c_p$  by

$$D = \frac{\kappa}{\rho c_p}. \quad (2.47)$$

In three-dimensional Cartesian coordinates the Laplace Operator is given by

$$\Delta = \frac{\partial^2}{\partial x^2} + \frac{\partial^2}{\partial y^2} + \frac{\partial^2}{\partial z^2}. \quad (2.48)$$

If no additional heat is brought into the medium and merely the distribution of initially deposited heat is observed, the source term is set to zero and Eq. 2.46 becomes the homogeneous heat equation

$$\frac{\partial}{\partial t}\psi(\mathbf{r}, t) - D\Delta\psi(\mathbf{r}, t) = 0. \quad (2.49)$$

It describes how the initially introduced heat is distributed in the material over time. For the initial conditions of a punctual heat distribution at a given position  $\mathbf{r}$

$$\psi(\mathbf{r}, t = 0) = \delta(\mathbf{r}), \quad (2.50)$$

a solution to Eq. 2.49 is given by

$$H(\mathbf{r}, t) = \frac{1}{(4\pi Dt)^{3/2}} \exp\left(\frac{-|\mathbf{r}|^2}{4Dt}\right). \quad (2.51)$$

The coefficient was determined for normalization purposes so that

$$\int_{\mathbb{R}^2} H(\mathbf{r}, t) d\mathbf{r} = 1 \quad \forall t \in \mathbb{R} \quad (2.52)$$

The solution in Eq. 2.51 is a fundamental solution of the three-dimensional heat equation and can be used to solve specific problems for given boundary or initial conditions. It is often referred to as the "heat kernel".

The temperature distribution at a given time  $\psi(\mathbf{r}, t)$  can be calculated by convolving the heat kernel with the distribution of the initially deposited heat  $\psi_0(\mathbf{r})$ :

$$\psi(\mathbf{r}, t) = H(\mathbf{r}, t) * \psi_0(\mathbf{r}) \quad (2.53)$$

with the initial conditions

$$\psi(\mathbf{r}, t = 0) = \psi_0(\mathbf{r}) \quad (2.54)$$

and the convolution in three-dimensional space

$$(f * g)(\mathbf{r}) = \int_{\mathbb{R}^3} f(\mathbf{r}')g(\mathbf{r} - \mathbf{r}')d\mathbf{r}'. \quad (2.55)$$

For further reading please refer to textbooks on solving strategies for partial differential equations in general [30, 36, 37] the heat equation in particular [79] or books on mathematical methods [4].

The laser-material interaction with pulse durations  $\tau_p \ll 1$  ns is a much more complex process. For a first theoretical description the so called two-temperature model of different electron and lattice temperatures is used [2, 54]. The detailed mechanisms of the ablation, however, are still subject of current research [19, 100].

# 3 Devices and Methods

The following chapter focuses on the various devices and methods used throughout this thesis. In the first section devices and methods for characterization purposes are presented and explained. These are sub-categorized in devices for the characterization of lasers, textures and solar cells. The following section deals with devices used for the laser treatment. These are sub-categorized in laser sources and beam guiding devices. The last section gives a rough overview of the computational framework as well as the optimization algorithm used within this work.

## 3.1 Devices and Methods for Characterization

The first part of the following section deals with the characterization of laser sources. It is explained how characteristic properties like power, pulse energy, pulse duration, beam profile or coherence were measured. The following subsection deals with the characterization of textured ZnO:Al. The various methods used to obtain information about the topography as well as electro-optical properties are explained. In the last subsection the devices used for the characterization of solar cells are presented.

### 3.1.1 Laser Characterization

**Laser Power, Pulse Energy and Pulse Power** The temporal averaged laser power  $P_L$  was measured by pointing the laser beam on a laser power detector. The laser power detectors used were thermopile based, i.e. converting thermal energy into electrical energy. The electrical energy was then be read out by power monitors, which could be connected to computer systems for logging. Depending on the power range, different *Gentec* power detectors with convection or water cooling as well as *Gentec* monitors were used. If not stated otherwise, all power measurements were conducted at the sample. The repetition rate  $f_{\text{rep}}$  was assumed to be as nominally stated, so the energy of one pulse could be determined by

$$E_p = \frac{P_L}{f_{\text{rep}}}. \quad (3.1)$$

However, this assumes that all pulses carry the exact same energy. To get a measure for the average power of one single pulse  $P_p$ , a box-shaped pulse can be assumed. Accordingly the temporal averaged pulse power was calculated by

$$P_p = \frac{E_p}{\tau_p}. \quad (3.2)$$

To retrieve more information about the exact temporal pulse shape and the pulse-to-pulse stability, the duration and amplitude of single pulses can be evaluated by a photo diode and an oscilloscope.

**Pulse Duration, Shape and Stability** The laser beam was guided on a white screen and the reflections of the screen were detected by a commercially available *Thorlabs* photo diode. The generated current was analyzed with a *LeCroy LC 534 AM* oscilloscope. Each measurement was conducted over 1000 pulses. For each pulse the pulse duration  $\tau_p$  was recorded. Furthermore, the area under the current-time curve as well as the maximum current were recorded for each pulse. These values correspond to the pulse energy  $E_p$  and peak pulse power  $P_p^{\text{pk}}$  respectively. By evaluating the standard deviations of these values, a measure for the pulse-to-pulse stability could be obtained.

**Beam Profile** The beam profile of the unfocused or only slightly focused laser beam can be measured by pointing the beam on a special camera, a so called beam profiler. The light intensity distribution on the camera sensor is then evaluated by specific commercially available profiling software. The beam profiler used for most of the experiments was a *DataRay WinCamD-LCM4* beam profiling camera along with the corresponding *DataRay* software. In order to reduce the laser power on the camera chip, various neutral density (ND) filters can be mounted in front of the camera.

**Beam Radius** In a tightly focused laser beam, the laser intensity is too high for ND-filters, let alone a camera sensor. To overcome this, Liu et al. proposed a simple method for measuring the beam radius directly within the focus by controlled ablation of material [63]<sup>1</sup>. Within a Gaussian laser beam the surface fluence distribution in the focus is given by Eq. 2.18 and  $w = w_0$ . Inserting Eq. 2.22 and solving for  $r^2 = |\mathbf{r}|^2$  yields

$$r^2(\Phi_0) = \frac{w_0^2}{2} \left[ \ln(2E_p) - \ln(\pi w_0^2 \Phi_0) \right]. \quad (3.3)$$

---

<sup>1</sup>Please note, that this method can only be used for pulsed, Gaussian-shaped laser beams.

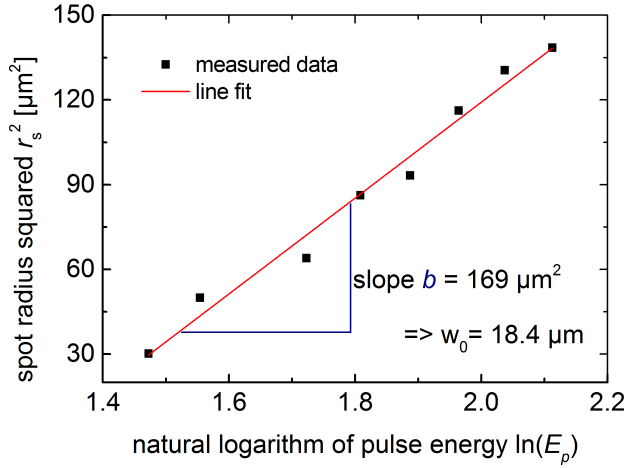


**Figure 3.1** Exemplary Liu plot: As proposed by Liu et al., the beam radius of pulsed Gaussian shaped laser beams can be determined by ablation experiments. Plotting the square of the spot radius  $r_s$  against the natural logarithm of the corresponding pulse energy  $E_p$  yields a straight line (compare Eq. 3.4). From the slope of the line, the beam radius can be determined.

If the local surface fluence reaches a certain threshold fluence  $\Phi_0 = \Phi_0^{\text{th}}$ , the material brought in the laser beam is ablated. Consequently, all material within the corresponding radius  $r^{\text{th}} = r(\Phi_0^{\text{th}})$  is ablated. This threshold radius  $r^{\text{th}}$  exactly resembles the spot radius  $r_s$  of the laser-treated area on the sample ( $r^{\text{th}} = r_s$ ) (for terminology please refer to Sec. 2.2.1). Accordingly, evaluating laser spots made with different pulse energies  $E_p$  and plotting the square of the spot radii  $r_s^2$  over the natural logarithm of the corresponding pulse energy  $\ln(E_p)$  yields a line plot, because

$$r_s^2(E_p) = \frac{w_0^2}{2} [\ln(2E_p) - \ln(\pi w_0^2 \Phi_0^{\text{th}})] = \frac{w_0^2}{2} \ln(E_p) + \text{const.} \quad (3.4)$$

By evaluating the slope  $b$  of a line fit to such data, it is possible to calculate the beam radius in the focus of the beam by

$$w_0 = \sqrt{2b}. \quad (3.5)$$

This method of measuring  $w_0$  is referred to as the Liu method and the corresponding plot as a Liu plot (see example<sup>2</sup> in Fig. 3.1).

<sup>2</sup>The example shown here is taken from measurements with *Rofin355*

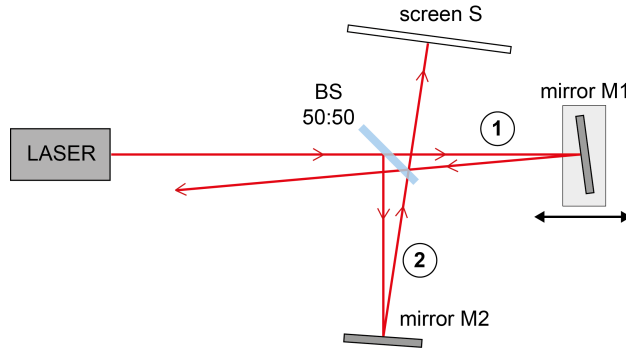


**Figure 3.2** Sketch of Michelson interferometer: The laser beam is split into two partial beams (1) and (2) by the 50:50 beam splitter BS. The partial beams are reunited at the screen S. If the coherence length of the laser is greater than the difference in beam path lengths of (1) and (2), an interference pattern can be observed on screen S. By moving mirror M1 the length of (1) can be changed and the coherence length  $\Delta l_c$  of the laser beam can be measured.

**Temporal Coherence** The temporal coherence (see Sec. 2.2.1) was measured by a Michelson interferometer. The Michelson interferometer consists of a 50:50 beam splitter, two mirrors and a screen (see sketch in Fig. 3.2). Due to the geometry of the setup, two partial beams are reunited at the sample. By moving one mirror, the propagation length of one partial beam can be altered. If the difference of the propagation lengths of both beams  $\Delta l_M$  is smaller than the length of the temporal coherence ( $\Delta l_M < \Delta l_c$ ) interference fringes can be observed on the screen. By moving the mirror in both direction until the interference fringes disappear, the length of the temporal coherence can be determined.

### 3.1.2 ZnO:Al Characterization

#### Topography

The topographies of the laser-treated and/or etched ZnO:Al layers were examined by various characterization tools. Whereas the Atomic Force Microscope (AFM) and Laser Scanning Confocal Microscope (LSCM) can be used to obtain quantitative information about the topography in x, y and z-direction, Scanning Electron Microscopy (SEM) and Optical Microscopy (OM) only offer quantitative information in the lateral x, y-directions. They can be used, however, to retrieve a qualitative image of the topography as well. LSCM and OM use visible light for

the measurement. Consequently, the resolution of these devices is more limited than SEM or AFM. For this thesis, all measurements that required a resolution of  $\Delta d \lesssim 5 \mu\text{m}$  or below, were conducted with AFM or SEM. Measurements of features larger than  $\Delta d \gtrsim 5 \mu\text{m}$  were conducted with the optical devices LSCM or OM.

**Atomic Force Microscope (AFM)** For almost all of the relevant topography measurements a *SIS Nanostation 300* AFM was used. In order to ensure a correct localization of the scan area, the AFM is combined with an optical microscope as well as a motorized sample holder. The whole system is mounted on a massive granite block so measurement accuracy of single nanometers is possible. All of the measurements were conducted in non-contact mode with *NanoWorld NCHR-50* tips. Scanning speeds were kept below  $v_{\text{scan}} < 30 \mu\text{m/s}$  in order to ensure accurate depth measurements. Due to the redeposited particles of melted ZnO:Al on the surface (especially after DLIP), AFM measurements of such textures proved very challenging. For these type of textures, only small parts of the scan field could be evaluated. However, the evaluation of partial areas often sufficed because of the periodic character of the DLIP textures.

**Laser Scanning Confocal Microscope (LSCM)** The *Keyence VK-X210* LSCM is a device which combines an optical microscope with a confocal laser scanning microscope. The largest objective lens of the microscope has a magnification of  $M = 150$  and a numerical aperture of  $\text{NA} = 0.95$ , respectively. The laser of the confocal microscope is a violet laser with a wavelength of  $\lambda = 408 \text{ nm}$ . The LSCM was mainly used for a first, quick evaluation of the samples after the laser treatment. Although the manufacturer states a height resolution of  $\Delta h_{\text{min}} = 12 \text{ nm}$  for the laser scanning, the LSCM was not used for critical texture measurements of feature sizes in the micrometer regime or below. For the evaluation of dimensions and depth profiles of whole laser spots, overlaps and area coverage, however, it delivered accurate measurements. Due to the partially transparent samples, all of the results of the laser scanning were interpreted with special caution.

**Scanning Electron Microscope (SEM)** For a qualitative and quick evaluation of textures in the sub-micrometer regime, a *ZEISS EVO MA10* SEM with a lanthanum hexaboride ( $\text{LaB}_6$ ) cathode was used. In order to obtain a picture of the topography, the accelerator voltage was kept below  $V_{\text{acc}} \leq 15 \text{ kV}$  for all measurements with the secondary electron (SE) detector. Apart from the SE topography measurements, some single measurements concerning contamination and phase changes were also conducted with the backscattered electrons (BSE) detector or a *Bruker Quantax 200* energy-dispersive x-ray spectroscopy (EDX) system built into the SEM.

**Optical Microscope (OM)** Optical microscopy was either carried out with the LSCM or a *Nikon Eclipse L200* optical microscope with a *Nikon Plan Fluor BD* objective lens, and *Zeiss* camera and measuring software. The objective lens had a magnification of  $M = 100$  and a numerical aperture of  $NA = 0.9$ .

## Electro-Optical Properties

The laser treated ZnO:Al layers were also characterized for their electro-optical properties. For the use in a solar cell, the layers have to show high transmission and light scattering abilities while retaining a low sheet resistance. The spectral transmission and scattering abilities were measured with a spectrometer, while the sheet resistance was measured by four-terminal-sensing.

**Spectrometer** For optical characterization a *PerkinElmer Lambda 950* spectrometer with an Ulbricht sphere was used. The measurements were conducted in the wavelength region from  $\lambda = 300$  nm to 1300 nm in steps of  $\Delta\lambda = 5$  nm. If not otherwise stated, the sample was mounted with the glass side facing the light source and the ZnO:Al layer facing the detector. All measurements were conducted at the ZnO:Al–air interface. The light transmitted through the sample (glass and layer) is detected in the Ulbricht sphere. The ratio of the detected light intensity to incoming light intensity is referred to as total transmittance  $TT$ . Furthermore, only the light transmitted in angles larger than  $\alpha > 5^\circ$  from the specular transmission direction can be detected. The fraction of this scattered light intensity to the incoming intensity is referred to as diffuse transmittance  $DT$ . By dividing the diffuse transmitted amount of light by the totally transmitted, one gets a measure for the scattering properties of the sample, the so called haze value

$$H = \frac{DT}{TT}. \quad (3.6)$$

Furthermore, the omni directional (total) reflectance  $TR$  of the sample can be measured. By

$$A = 1 - TT - TR \quad (3.7)$$

a measure for the absorbance of the sample can be obtained. However, light that is trapped within the sample and does not exit the sample within approx  $r \approx 1$  cm of the entry position is not accounted for in any of the measurements, and thus, will be considered as absorbed.

**Four-terminal-sensing** In order to allow precise measurements of the ZnO:Al layer's sheet resistance  $R_{\square}$ , a custom-made four-point probe measuring device was used. Multiple measurements were carried out at different areas of the treated

sample and the deviations of the results are presented with the results. In many cases, the relative deviations were smaller than  $u_R^{\text{rel}} < 1\%$ . If so, no deviation is stated with the measurement result.

### 3.1.3 Solar Cell Characterization

**J-V Characteristics** For the measurement of the J-V curves, the solar cells were illuminated by a sun simulator while the current-voltage characteristics were extracted by a *Keithley* source measuring unit. The class A sun simulator illuminated the cell with an AM1.5 solar spectrum with a radiation power density of  $p = 100 \text{ mW/cm}^2$ . During the measurements the cells were kept at a temperature of  $T = 25 \text{ }^\circ\text{C}$ .

**Quantum Efficiency** The measurements of the quantum efficiency of the solar cells was carried out by measuring the spectral response  $SR$  of the solar cell under monochromatic illumination. The spectral response  $SR$  is defined as the ration of generated electrical current density  $j_{\text{out}}$  and incident photon power  $P_{\text{ph}}$ :

$$SR(\lambda) = \frac{j_{\text{out}}(\lambda)}{P_{\text{ph}}(\lambda)}, \quad (3.8)$$

The external quantum efficiency (EQE) was then calculated by

$$EQE(\lambda) = SR(\lambda) \frac{hc}{e\lambda} \quad (3.9)$$

with the Planck constant  $h$ , speed of light  $c$  and elementary charge  $e$ . For the measuring of tandem solar cells, top and bottom cells were measured separately. During the measurements, the cell which was not measured was flooded by a powerful bias illumination of a wavelength which is not absorbed by the cell under investigation. Consequently, the total output current could be related to the current produced by the investigated cell and was not limited by the other cell.

## 3.2 Devices and Methods for Laser Treatment

The following section focuses on devices and methods used for the actual laser treatment. In the first subsection the various laser sources used throughout the thesis are laid out with their characteristic properties. The result of characterization measurements of the different sources are presented. The second part of the section focuses on beam guiding devices and experimental setups used throughout the thesis.

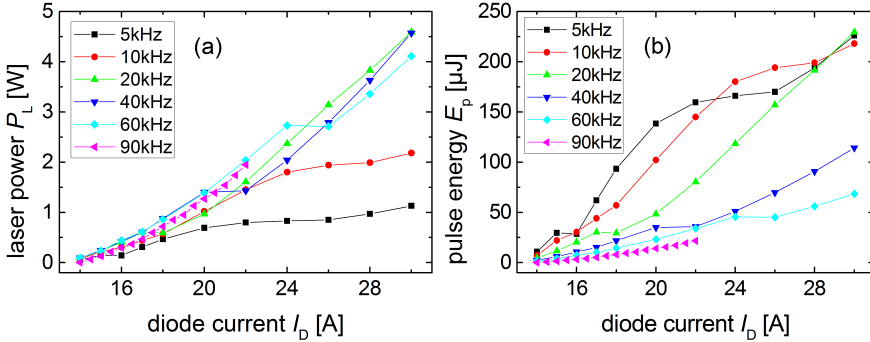


**Figure 3.3** *Rofin1064*: Laser power  $P_L$  and pulse energy  $E_p$  in dependence of input diode current  $I_D$  and repetition rate.

### 3.2.1 Laser Sources

For the experiments conducted in the framework of this thesis, various laser sources were used. Each laser source was characterized. The following section presents an overview of these laser sources and their characteristic properties. The findings are also summed up in Tab. 3.1 at the end of this section.

#### Rofin1064

One of the laser built into the structuring system is a *Rofin RSY10E* infrared (IR) nanosecond Nd:YVO<sub>4</sub> laser with a Gaussian shaped beam (TEM<sub>00</sub>) which is referred to as *Rofin1064*. The laser wavelength is  $\lambda_L = 1064$  nm and the pulse duration approximately  $\tau_p \approx 24$  ns. The laser was mainly used for the laser chemical etching (Sec. 4.2). The output laser power  $P_L$  as well as the pulse energy  $E_p$  can be adjusted by changing the electrical current for the pumping laser diode  $I_D$ . However, the adjustable repetition rate  $f_{\text{rep}}$  also has a strong influence on the resulting output power and pulse energy (see Fig. 3.3). The laser was mainly used with a repetition rate of  $f_{\text{rep}} = 10$  kHz due to the possible high pulse energies. An overview of the output laser power  $P_L$ , pulse energy  $E_p$  and repetition rate  $f_{\text{rep}}$  relations can be found in Fig. 3.3. For all experiments, the laser was focused with a  $f = 300$  mm lens, so the beam radius in the focus measured  $w_0 = 50$   $\mu$ m and pulse fluences up to  $\Phi_p = 3.1$  J/cm<sup>2</sup> could be realized. The laser on and off times were controlled by the structuring system's CNC system (see Sec. 3.2.2), while the repetition rate and the diode current was adjusted by an external device.

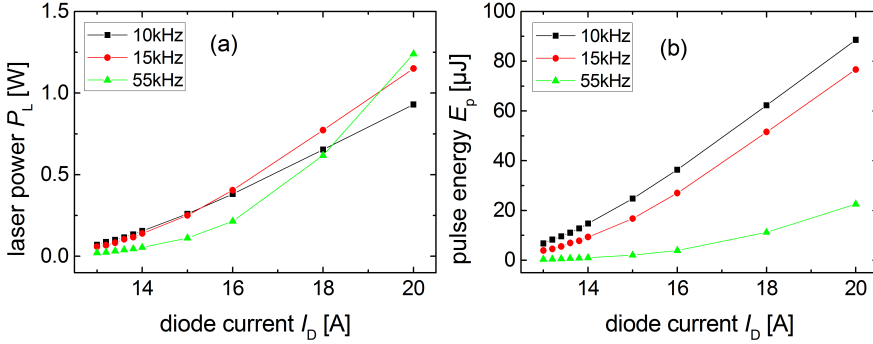


**Figure 3.4** *Rofin532*: Laser power  $P_L$  and pulse energy  $E_p$  in dependence of input diode current  $I_D$  and repetition rate  $f_{\text{rep}}$ .

## Rofin532

The *Rofin RSY20E SHG* is an internally frequency doubled nanosecond Nd:YVO<sub>4</sub> laser. It has a wavelength of  $\lambda_L = 532$  nm a Gaussian shaped beam and is referred to as *Rofin532*. The pulse durations range from  $\tau_p = 13$  ns to 30 ns. The main use of the laser in this thesis was for the texturing with a particle lens array (Sec. 4.3). Similar to the *Rofin1064*, the output power of the laser is adjusted by the diode current  $I_D$  (Fig. 3.4). For all experiments, the laser was used in combination with a  $f = 116$  mm focusing optic, resulting in a beam waist radius of  $w_0 = 20$   $\mu$ m. Pulse fluences up to  $\Phi_p = 7.1$  J/cm<sup>2</sup> could be realized. The control of the laser was equal to *Rofin1064*.

## Rofin355

The ultraviolet (UV) *Rofin RSYE20E THG* is the same type Nd:YVO<sub>4</sub> laser as the *Rofin532* but is frequency tripled to a resulting wavelength of  $\lambda_L = 355$  nm. Due to the frequency conversion, the power output of the laser is not stable at all powers and repetition rates [44]. Consequently, the laser is only operated at maximum power output (input diode current  $I_D = 29$  A) and a repetition rate of  $f_{\text{rep}} = 15$  kHz, because these parameters ensure a stable operation. The pulse duration with these standard operating parameters was determined to be  $\tau_p = 6$  ns. In order to be able to adjust the power on the sample, a half-wave plate along with a polarizer was brought into the beam path. By rotating the half-wave plate the amount of laser power transmitted through the polarizer and hence, the power on the sample could be adjusted (compare Fig. 3.5). The half-wave plate was mounted in a *Thorlabs* motorized rotational mount and could be adjusted via USB by a PC system. The laser was mainly used for the texturing with a particle

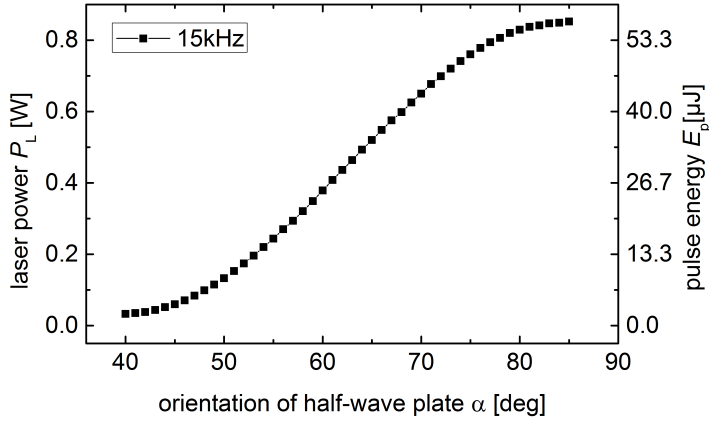


**Figure 3.5** *Rofin355*: Laser power  $P_L$  and pulse energy  $E_p$  in dependence of angle of half-wave plate: Due to stability reasons, the laser is only used with a repetition rate of  $f_{\text{rep}} = 15$  kHz and at maximum output laser power with a diode current of  $I_D = 29$  A. The laser power on the sample can be controlled by rotating a half-wave plate that is situated before a polarization dependent absorbing polarizer.

lens array (Sec. 4.3). However, the laser was also used for experiments to study the ablation mechanism of ZnO:Al in the ultraviolet regime. For all experiments, the laser was used with a  $f = 108$  mm focusing optic, resulting in a beam waist radius of  $w_0 = 19$   $\mu$ m. Consequently, pulse fluences up to  $\Phi_p = 4.8$  J/cm<sup>2</sup> could be realized with this setup.

## TruMicro5050

The *Trumpf TruMicro 5050* (E0851A0145) is an infrared, picosecond Yb:YAG laser with a wavelength of  $\lambda_L = 1030$  nm and Gaussian beam shape. The pulse duration could not be determined but is stated as  $\tau_p < 10$  ps by the producer of the system. The laser offers repetition rates up to  $f_{\text{rep}} = 400$  kHz and a laser power up to  $P_L = 50$  W. The output power can be adjusted by demanding a certain fraction of the total possible power in the laser's control interface. The laser source is then automatically adjusted and regulated to that power by an internal feedback control. In contrast to the Nd:YVO<sub>4</sub> lasers described above, the pulse energy of the *TruMicro5050* does not depend on the repetition rate. Only for very low repetition rates, a dependence could be observed. The internal feedback control allows a very controlled and linear adjustment of the laser power and/or pulse energy (compare Fig. 3.6). The laser was either controlled by an external

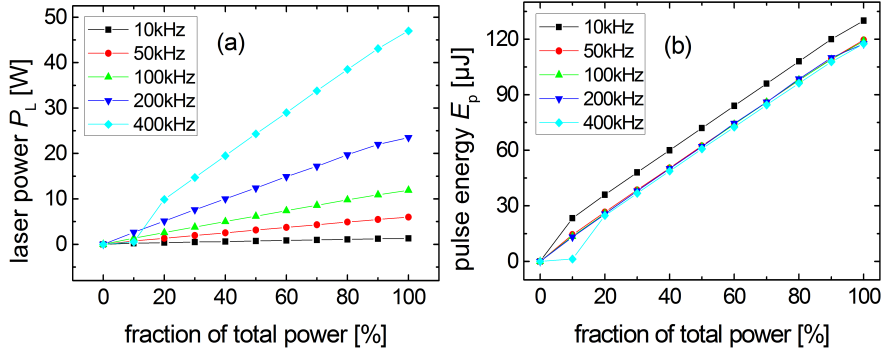


**Figure 3.6** *TruMicro5050*: Laser power  $P_L$  and pulse energy  $E_p$  in dependence of the input fraction of total power and repetition rate  $f_{\text{rep}}$ .

control interface or by connecting the laser to the *SAMLight* scanner software for an integrated scanner-laser control (Sec.3.2.2). For the beam guiding and focusing different scanner systems and lenses were used. In this thesis, the laser was mainly used for the generation of laser-induced periodical surface structures (LIPSS) (see Sec. 4.4).

## TruMicro5000

The *Tumpf TruMicro 5000* (E1151A0098) is a green, picosecond Yb:YAG laser with a wavelength of  $\lambda_L = 515$  nm and was also used for LIPSS creation. It is based on the *TruMicro5050* but has an internal frequency conversion. Average laser powers of up to  $P_L = 30$  W can be reached at the maximum repetition rate of  $f_{\text{rep}} = 800$  kHz. The nominal pulse duration is  $\tau_p < 10$  ps. Similar to the *TruMicro5050*, the power output is adjusted with a feedback control according to a given input fraction of the total power. Again, the internal power regulation allows a very exact adjustment of pulse energies independent of the repetition rate (Fig. 3.7). The control of the laser was equal to *TruMicro5050*.

## Powerlite8020

The *Continuum Powerlite8020* is a nanosecond flash-lamp pumped Nd:YAG laser source. Within this thesis it was used for the interference experiments. Since the interference experiments make up the main part of this thesis, the description of the *Powerlite8020* system is carried out in more detail. The fundamental wavelength of the laser is  $\lambda_L = 1064$  nm. However, for all of the experiments

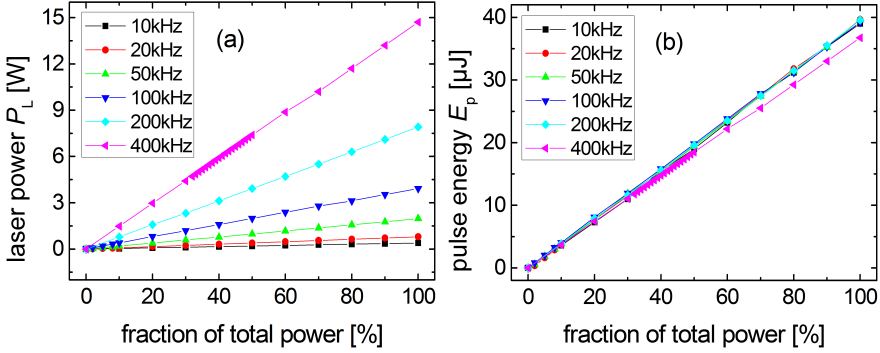


**Figure 3.7** *TruMicro5000*: Laser power  $P_L$  and pulse energy  $E_p$  in dependence of input fraction of total power and repetition rate  $f_{\text{rep}}$ .

in this thesis, it was frequency tripled by third harmonic generation (THG) in an external frequency converter also supplied by *Continuum*. The frequency converter box was mounted directly on the housing of the laser and the motorized mounts of the converter crystals as well as their heating could be controlled by the same interface as the laser itself. The crystal orientation was calibrated before each laser treatment to allow the maximum possible laser power output in UV ( $\lambda_L = 355$  nm). After this calibration, the laser could be used just as a nominal UV source.

**Laser Power Control** Within the laser head, the oscillator Nd:YAG crystal is pumped by one and the amplifier crystal by two flashlamps firing with a repetition rate of  $f_{\text{rep}} = 20$  Hz. Accordingly, the repetition rate of the whole laser system is limited to a maximum of  $f_{\text{rep}} = 20$  Hz. The output lasing power of the system can be adjusted by changing the Q-switch delay time  $\tau_Q$ . The Q-switch delay time is the time between the firing of the flashlamps and the opening of the resonator Q-switch. By adjusting this delay, the effectiveness of the stimulated emission in the resonator crystal can be influenced and hence, the output power. The dependence of Q-switch delay time and laser power as well as pulse energy can be observed in Fig. 3.8 (a). Due to larger instabilities in other regions, all of the experiments were conducted within the gray shaded area (also compare Fig. 3.9 (a)).

**Beam Profile** Due to the nonoperational seeder system (see below) and the inhomogeneous pumping of the asymmetric positioned flashlamps, the beam profile of the laser beam is a mixture of various different transversal resonator modes.

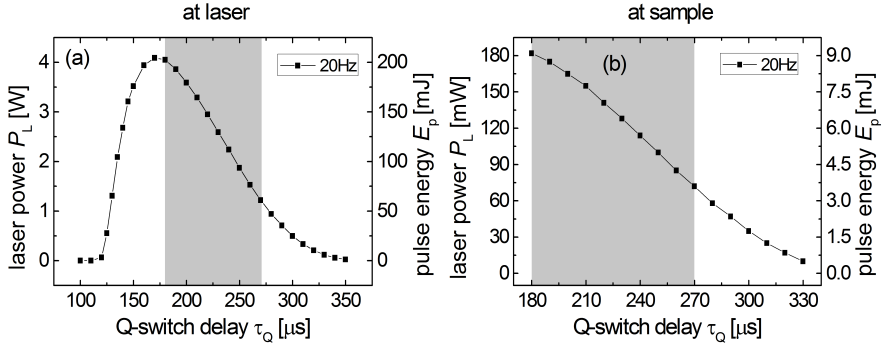


**Figure 3.8** *Powerlite8020*: Laser power  $P_L$  and pulse energy  $E_p$  at the laser (a) and at the sample in the three-beam-interference setup (b) in dependence of input Q-switch delay time. Due to power stability reasons and better adjustment, only the shaded region was used for the experiments. Because of the beam shaping and the numerous optics in the beam path (see Sec. 5.1.1), only about 5% of the output laser power reach the sample in the three-beam interference experiment.

Such inhomogeneous beam profile massively constrains the ability of quantitative statements about the intensity distribution within the beam and hence, about the energy intake in the material at a given position. To overcome this challenge, a beam shaping unit was designed and implemented for the three-beam interference setup (see Sec. 5.1.1). This unit allowed an almost perfect Gaussian shaped beam at the sample (see Fig. 5.2). However, only a small fraction of the laser output power can be transmitted. Nevertheless, due to the very high initial pulse energies, fluences at the sample barely sufficed for demonstrating laser texturing. The highest achievable pulse fluence at the sample was  $\Phi_p = 0.6 \text{ J/cm}^2$ . A power and pulse energy measurement conducted at the sample in the three-beam interference setup can be observed in Fig. 3.8 (b). The two-beam interference experiment was conducted with the unshaped, inhomogeneous beam profile and full power and pulse energies.

**Stability and Pulse Duration** In order to find the best operating range, a stability measurement of the pulse energies and pulse durations was conducted with a photo diode (see Sec. 3.1.1). Within the gray shaded range in Fig. 3.9, the laser reveals the most stable operation conditions while it is still possible to adjust the pulse energies. The standard deviation of peak pulse powers and pulse energies was determined to be less than 10% and 5% respectively. The pulse duration within the operating range was measured to be  $\tau_p \approx 5 \text{ ns}$ . Apart from

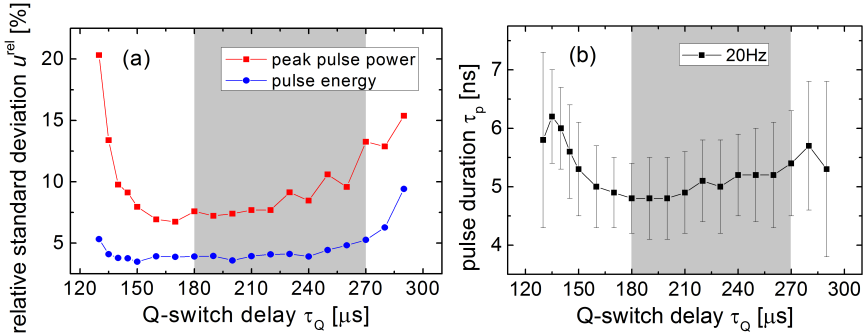


**Figure 3.9** *Powerlite8020*: Stability of pulse energy and peak pulse power (a) and pulse duration (b) in dependence of Q-switch delay time. In order to obtain stable operation, the operating range for the experiments was limited to the gray shaded area. Within this range the stability of the peak pulse powers and pulse energies is smaller than  $u_{\text{P}}^{\text{rel}} < 10\%$  and  $u_{\text{E}}^{\text{rel}} < 5\%$ , respectively. The pulse duration was measured to be  $\tau_{\text{p}} = 5$  ns. The y-values in (a) and the error bars in (b) are standard deviations based on 1000 measurements for each data point.

the pulse-to-pulse stability on sub-second time scales, a general mean laser power instability of  $u_{\text{P}}^{\text{rel}} \approx 5\%$  was measured on time-scales of several minutes. On even longer time scales of single days, slow power drifts of up to  $u_{\text{P}}^{\text{rel}} \approx 10\%$  could be observed.

**External Control** The laser as well as the frequency converter could be controlled by a remote box interface as well as externally by ASCII commands via RS232. The remote box allowed manual firing of single laser pulses with a given set of input parameters as well as automated operation with a given repetition rate  $f_{\text{rep}}$  and Q-switch delay time  $\tau_Q$ . Externally the laser system could be controlled either by Direct Access Triggering (DAT) of every single control signal needed for the operation of the laser, or by remote access of the controls on the remote box whereas the internal triggering of control signals is left to the laser system. For the external control of the laser within this thesis the later was used. The RS232 was converted to USB and controlled via *HTerm* Terminal or scripted with the *python pySerial* package. A complete listings of the commands and the command syntax can be found in the *Powerlite8020* manual.

	<i>Rofin1064</i>	<i>Rofin532</i>	<i>Rofin355</i>	<i>TruMicro5050</i>	<i>TruMicro5000</i>	<i>Powerlite8020</i>	<i>Powerlite8020</i> (beam shaped)
$\lambda_L$ [nm]	1064	532	355	1030	515	355	355
$\tau_p$ [ns]	24	13-30	6	<0.01 <sup>†</sup>	<0.01 <sup>†</sup>	5	5
profile	TEM <sub>00</sub>	TEM <sub>00</sub>	TEM <sub>00</sub>	TEM <sub>00</sub>	TEM <sub>00</sub>	inhom.	TEM <sub>00</sub>
$P_L$ [W]	4.5	1.25	0.8	48	15	4	0.18
$f_{\text{rep}}$ [kHz]	100	100	15	400	400	0.02	0.02
$E_p$ [ $\mu$ J]	230	90	55	130	40	200 000	9 000
$P_p$ [kW]	10	7	9	13 000	4 000	40 000	1 800
$\Phi_p$ [J/cm <sup>2</sup> ]	3.1	7.1	4.8	5	18	undef.	0.6

**Table 3.1** Overview of laser properties: Comparison of measured laser properties of laser sources used within this thesis (laser wavelength  $\lambda_L$ , pulse duration  $\tau_p$ , beam profile, max. laser output power  $P_L$ , max. pulse repetition rate  $f_{\text{rep}}$ , max. pulse energy  $E_p$ , max. laser pulse power  $P_p$ , max. surface pulse fluence  $\Phi_p$ ). The given maximum values are maximal values as used for the experiments within the thesis and are not necessarily maximum values of the device. The values marked with a dagger<sup>†</sup> are nominal values as stated by the manufacturer of the laser source and have not been verified experimentally.

**Seeder System Malfunction** The *Powerlite8020* laser can be operated with an optional *Lightwave 101-04* seeding laser. There are multiple advantages of a seeded operation:

- A more homogeneous beam profile because the resonator of the host laser merely amplifies the beam of the seeding laser.
- A longer coherence length on the order of the actual pulse length ( $\Delta l_c = 1.5$  m), because of single longitudinal mode operation of the resonator.
- Shorter pulses and higher pulse-to-pulse stability because of the controlled (seeded) initiation of the light emission within the resonator as compared to spontaneous broadband initiation.

All of these advantages would massively improve the performance of the laser and the outcome of the experiments. Unfortunately, albeit intensive efforts, it was not possible to accomplish the operation of the seeding laser. The defect was traced down to the laser diode within the seeding laser system, but due to a

lack of detailed information about its characteristic properties, it could not be replaced. Furthermore, the manufacturer does not offer any more information and/or service for the laser system and its components.

Consequently all experiments were conducted in unseeded operation. However, for an evaluation of the potential of the laser process, it has to be kept in mind that all the experiments within this thesis were conducted with a limited and not fully operational laser system.

### 3.2.2 Beam Guiding

Apart from the setups used for the interference experiments, mainly two other experimental setups were used. An integrated structuring system for the experiments on laser-induced chemical etching, particle lens arrays as well as general studies about laser-material interaction. And a setup consisting of a scanner and a lab jack for the experiments on Laser Induced Periodical Surface Structures. The following section presents the working principle of these two beam guiding systems. Details about the exact experimental procedure for each laser-treatment can be found in the corresponding sections in the following chapter (Chap. 4). A detailed description of the custom-made interference setups for the experiments on direct laser interference patterning can be found in Sec. 4.5 (two-beam interference) and Sec. 5.1 (three-beam interference).

## Structuring System

For the monolithic interconnection of the solar cell stripes in a solar module, at IEK-5 a laser structuring system is used [44]. This structuring system consists of various laser sources as well as flying optics and a movable stage all in one housing. The system is capable of fulfilling two tasks. On the one hand, it is designed to perform the standard scribing processes for the monolithic interconnection in thin-film silicon solar cells without the need of calibration or adjustment processes. On the other hand, it can be altered or expanded with additional components to be used as a laboratory system to investigate other techniques of laser processing. All processing, however, can be conducted inside the housing.

**Setup** The structuring system incorporates three laser sources with different wavelengths, the infrared *Rofin1064*, green *Rofin532* and ultraviolet *Rofin355* (see Sec. 3.2.1 for details about the laser sources). The laser beams of these laser sources are guided within the structuring system to a movable optical head above the stage. The stage is located in the horizontal  $x,y$ -plane and the laser beams are reflected from the optical head to have normal incidence on the stage. For

focusing of the laser beams, different lenses and lens systems can be mounted on the optical head. In order to control the focus of these lenses, they are mounted on a motorized stage that can be moved in z-direction. The optical head itself is motorized to be movable in x-direction, while the stage can be moved in y-direction, while the sample holder on the stage can be rotated around the vertical z-axis. The sample holder is capable of fastening samples of various sizes but can also be removed to mount additional equipment such as vacuum or reaction chambers onto the stage. All movable parts of the structuring system are mounted on a massive granite block to ensure high precision and position accuracy on the order of single micrometers. For the movement in x and y direction speeds of up to  $v_{x,y} = 1000$  mm/s can be reached. The movement in all three dimensions as well as the rotation can be controlled by a computer-based CNC system developed and implemented by *Schulz Systemtechnik*. The CNC system is also capable of controlling the laser sources' on and off times. Consequently, the scribing of straight or curved lines or hatching of areas can be entirely conducted from the computer system.

## Scanner Lab Jack Setup

For the experiments with ultra-short pulse lasers, the combination of a laser scanner, f-theta focusing optic and a motorized lab jack was used (Fig. 3.10). This experimental setup allows quick and very flexible processing of sample areas up to  $A = 100$  mm x 100 mm. It was used mainly for the creation of Laser Induced Periodical Surface Structures (see Sec. 4.4).

**Setup** The scanners used for the experiments in this thesis were *SCANLAB hurrySCAN II* which were mounted with f-theta lens systems in various focal lengths made by *Sill Optics*. The movement of the scanner mirrors, the on and off times of the laser as well as its output power was controlled by commercially available *SCAPS SAMLight* software. The software offers an integrated control and automation user interface but can also be controlled by the *Microsoft Component-Object-Model (COM)* standard. For the actual laser treatments the integrated *SAMLight* user interface was used, whereas for an automated focus search the scanner was controlled by *National Instrument LabVIEW* software via a *COM*-interface. For the positioning of the sample underneath the scanner, a sample holder was designed and constructed. Consequently, it could be removed and repositioned accurately, in order to characterize the sample in between the laser treatments. The sample holder was mounted on a *Thorlabs* motorized lab jack for z-positioning with an accuracy below 30  $\mu$ m. The lab jack could be controlled by external controls, an integrated user interface or *ActiveX*.

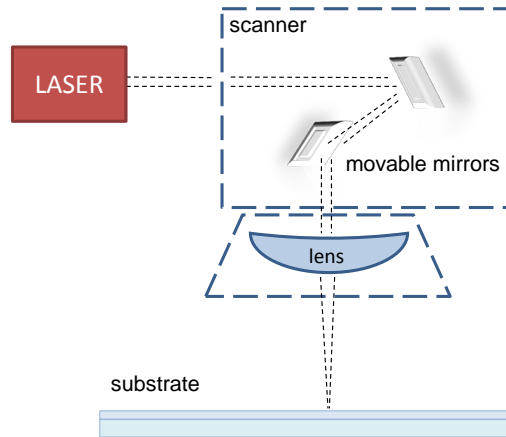


**Figure 3.10** Schematic drawing of scanner system: The laser beam enters the scanner and is reflected by two fast moving mirrors. The mirrors move in such way that an area underneath the scanner can be scanned by the laser beam. Because most laser processes require focusing of the laser light, the scanner systems can be equipped with a lens or lens system.

## Interference Setups

Apart from the two experimental setups mentioned above, a major part of the experiments was conducted with laser-interference setups. For the technology screening described in Chap. 4, a two-beam interference setup was designed and built (see Sec. 4.5.1). As a result of the screening, the interference process revealed a high potential for the laser-texturing of ZnO:Al. Consequently, later on, a highly flexible three-beam-interference setup was designed and built to further investigate the interference processing. Since the development of this setup is part of the results of this thesis, the detailed layout is not described here, but in the corresponding chapter about direct laser interference patterning (Sec. 5.1.1).

## 3.3 Computational Devices

Apart from the actual experiments, a large part of the work done for this thesis was of computational character. Starting from the automated actuating of the laser sources, the control of beam guiding devices and positioning systems over storing, managing and processing large amounts of measurement data in databases to optical calculations and simulations of heat diffusion, ablation mechanisms

and light trapping abilities. In order to simplify the interaction in between these different tasks, a single programming environment was used for almost all of these.

**Python Programing Environment** The *Python* programming language along with the *Spyder* integrated development environment presents a simple and powerful tool for all kinds of scientific computation. For data analysis and presentation, the packages *Scipy*, *Numpy* and *Matplotlib* were used. For building a web-served process database the *Django* framework was used. The actuating of machines was carried out with the *Serial* package. Evolutionary algorithms were implemented with the *DEAP* toolbox and parallelization was carried with the help of the *Multiprocessing* and *SCOOP* packages. Optimizations with evolutionary algorithms play an important part within the thesis. In order to be able to verify the results of the optimizations, the utilized algorithm is laid out in detail in the following paragraphs.

## Genetic Algorithm for Global Optimization

A schematic flow chart of the genetic algorithm used for various optimization tasks in this thesis is depicted in Fig. 3.11. The algorithm was implemented in the *Python* programming language with help of the *DEAP* toolbox [38, 82]. The general outline of the algorithm is explained in the following paragraphs.

The genetic algorithm mimics the evolution of individuals in a population over the course of many generations influenced by mating, mutation and selection of the fittest. Each individual  $I_i$  in a population  $P = I_1, I_2, \dots, I_n$  has a certain set of attributes  $x, y, z, \dots$ . According to these attributes, the individual can be evaluated and a fitness value  $f$  can be assigned to the individual by the optimality function  $f = f(I(x, y, z, \dots))$ . A population contains a certain number of individuals and evolves by mating of individuals within the population (two individuals somehow mix their attributes to create a new individual) or by mutation (random change) of certain attributes in certain individuals.

**Creation** The first population of  $n_{\text{pop}}$  individuals is created by randomly creating individuals. An individual is created by uniformly drawing a value (e.g.  $x_i$ ) for each of its attributes  $(x, y, z)$ <sup>3</sup> within the given boundaries for the attribute ( $[x_{\text{min}}, x_{\text{max}}]$ ). After the population has been created, it is first evaluated by assigning a fitness to each of its individuals by the optimality function. Thereafter the modification and re-selection of the population starts and is repeated for  $n_{\text{gen}}$  generations.

---

<sup>3</sup>For reasons of simplicity, from here on only three attributes are stated.

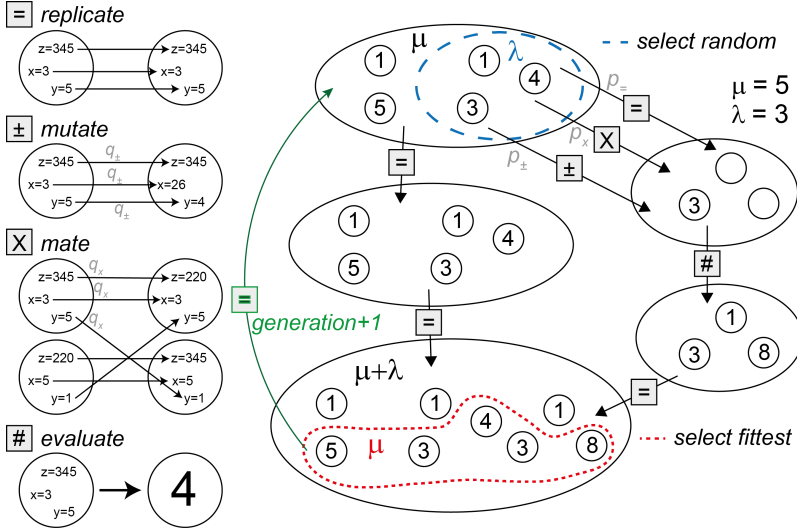


**Figure 3.11** Schematic flow chart of genetic algorithm used for global optimization.

**Modification** An amount of randomly selected  $\lambda$  individuals out of the population is modified in each generation. The modification can take place by *mating*, *mutation* or *replication*. The probabilities for each of the  $\lambda$  individuals to undergo one of the modifications are given by  $p_x$  for *mating*,  $p_{\pm}$  for *mutation* and  $p_{=}$  for *replication*. Whereas

$$p_x + p_{\pm} + p_{=} = 1 \quad (3.10)$$

has to be fulfilled.

The *replicate* algorithm leaves the individual and all of its attributes unchanged.

$$I_i(x_i, y_i, z_i) \longrightarrow I_f(x_i, y_i, z_i) \quad (3.11)$$

The *mutate* algorithm determines for each of the attributes of a given individual if it shall be mutated. The probability for mutation or not is  $q_{\pm}$  independent for every attribute. If a certain attribute is to be mutated, its value is replaced by a new value uniformly drawn within the boundaries for the given attribute.

$$I_i(x_i, y_i, z_i) \longrightarrow I_f(x_f, y_i, z_f) \quad (3.12)$$

with

$$x_f \in [x_{\min}, x_{\max}], z_f \in [z_{\min}, z_{\max}]. \quad (3.13)$$

The *mate* algorithm executes a uniform crossover of two individuals. For each attribute of the individuals it is determined if the two individuals exchange the value of the attribute or retain their original value according to a probability of  $q_x$ .

$$I_i(x_i, y_i, z_i) \longrightarrow I_f(x_j, y_j, z_i) \quad (3.14)$$

$$I_j(x_j, y_j, z_j) \longrightarrow I_g(x_i, y_i, z_j) \quad (3.15)$$

**Reproduction and Selection** After the modification, all new individuals are evaluated by the optimality function. The subpopulation of  $\lambda$  partially new individuals is then added to the original, unchanged population of  $\mu$  individuals (also see Fig. 3.11). In the final population of  $\mu + \lambda$  individuals, the fittest  $\mu$  individuals are selected according to their fitness value and placed in the next generation. This type of algorithm in which the next generation is selected from offspring *and* original population is also known as a  $(\mu + \lambda)$  algorithm.

**Evolution and Analytics** The process of modification, evaluation and selection is then carried out for each of the following generations until a given number of  $n_{\text{gen}}$  generations is reached. In each generation the population is analyzed and the minimum, maximum, mean and standard deviation of fitness values of its individuals are logged in a logbook (log). By analyzing these values, it can be investigated if the population is evolving in a certain direction and how the spread of attributes (the gen pool) within the population evolves. Furthermore, the all time best evaluated individuals are recorded in a hall of fame (hof).



## 4 Process Comparison

With the aim of developing a laser-based texturing process for ZnO:Al layers used as front contacts in thin-film silicon solar cells, a technology screening is conducted. Five different types of laser processes are evaluated and compared. The goal of the comparison is to pre-select industrial relevant processes concerning the criteria of size and adaptability of feature geometries, scalability to large areas and simplicity.

After laying out the criteria of the comparison in more detail, in each of the following sections one of the five techniques is explained and the experimental adaption for the texturing of ZnO:Al is described. ZnO:Al substrates textured with each of the different techniques are presented, characterized and discussed. In the end of the chapter each technique is assessed with respect to the criteria mentioned above, an overall conclusion is drawn and one technique is selected for further investigations.

Please note that an earlier stage of this technology screening has already been published [56]. Some phrases in the following subsections may be identical to the publication.

**Criteria for Comparison** The most important demand on the desired process is the capability of producing textures with small feature sizes. The feature sizes need to be on the order of the wavelength of the incident light. Only such small features can scatter the incoming light effectively (compare light trapping in Sec. 2.1.2). Furthermore, the feature sizes and geometries need to be adjustable and adaptable. Only a high flexibility of feature shapes and sizes yields an adaptable light management (see motivation of thesis in Chap. 1). To be applicable in an industrial environment, the process also needs to be scalable to large areas and retain a certain simplicity. Scalability here is not only understood as the capability to texture large areas, but also texture large areas in a reasonable amount of time ( $v_{\square} \gtrsim 1 \text{ m}^2/\text{min}$ ). To keep down the cost of machinery and ensure functionality in non-laboratory conditions, the process needs to be somewhat simple, stable and nonreactive to disturbances. The sum of these properties is referred to as “simplicity”.

## 4.1 Direct Writing

**Motivation** An obvious and at first sight also very simple technique of laser texturing is direct writing. The laser beam is focused directly on the sample. Given a sufficient laser fluence, the material within the perimeter of the focus spot is heated and ablated. The focus spot is then moved to a different area and the process is repeated. For slow movement velocities ( $v \lesssim 1$  m/s), the sample is moved relative to a fixed laser beam. To achieve higher writing velocities, scanner systems can be applied (see Sec. 3.2.2). With modern scanner, controller and computer systems, the numerous laser spots can be positioned with high accuracy and speed. Consequently, nominal ablation areas can be arranged in arbitrary shapes in the computer software and can then be "written" into the material with the laser beam. At first sight, this technique seems very promising for the application of producing light scattering textures.

**Feasibility Considerations** In order to produce the desired feature sizes, focusing of the laser beam to spot radii of about  $r_s = 500$  nm is necessary. This can only be achieved with very small working distances. Furthermore, according to Gaussian beam propagation small foci can only be obtained with a small Rayleigh length and thus very shallow depth of field (see Gaussian beam optics in Sec. 2.2.1). Assuming a laser wavelength of  $\lambda = 355$  nm, and a desired beam radius of  $w_0 = 500$  nm yields a Rayleigh length of  $z_R = 2$   $\mu$ m (compare Eq. 2.17). Accordingly, the variation of the distance in between the focusing optics and the sample surface needs to remain well within this limit of 2  $\mu$ m. Such high demands on accuracy and stiffness again ask for very costly machinery which is not feasible for industrial production. Furthermore, even if these high demands on optics and machinery can be met, the scalability to large areas is still limited. Assuming the use of a polygon scanner system with a velocity of  $v_{\text{scan}} = 100$  m/s, the processing of an area of  $A = 1$  m<sup>2</sup> would require

$$t_{\square} \approx \frac{1}{v_{\text{scan}} \sqrt{A_s}} \approx 188 \text{ min.} \quad (4.1)$$

Whereas the spot size  $A_s$  was assumed to be roughly equal to the beam area  $A_b = \pi w_0^2$ . In order for a laser to be able to handle such high scan speeds it would need a repetition rate of

$$f_{\text{rep}} = \frac{v_{\text{scan}}}{\sqrt{A_s}} \approx 110 \text{ MHz.} \quad (4.2)$$

While current mode-locked laser systems can reach such high repetition rates, the processing time of several hours per square meter is not feasible for industrial application.

## 4.2 Laser-Induced Chemical Etching

**Motivation** Laser-induced chemical etching offers a method to locally adapt the etching environment of the ZnO:Al. This is done by locally confined heating of the ZnO:Al and part of the surrounding etchant with laser light. The shape of the etch features as well as the speed of the etch process depend on the temperature [74]. By heating the etchant to higher temperatures than previously investigated, new feature shapes could possibly be obtained. Furthermore, a combination of etching with simultaneous laser illumination may allow a locally adaptable etch texture capable of a more adaptable light management within the cell.

### 4.2.1 Experimental Procedure

**Design of Reaction Chamber** For the experiments to laser-induced chemical etching, a reaction chamber was designed and built. The design of the chamber was laid out in a way that the sample can be processed from both sides. On the one hand, the sample can be submerged in the etchant and rests on a sample holder in the interior of the container. The container is sealed with a glass cover plate and filled. In this configuration the laser enters through the glass cover plate through part of the etchant and hits the sample from the film side. On the other hand, the sample holder can be left empty and the sample itself can be used as the cover plate of the chamber with the film facing the interior of the chamber. In this configuration, the laser beam does not have to penetrate the etchant first, but enters the sample directly from the glass side (compare Fig. 4.1). The chamber can be filled by a close able valve and a standing pipe guarantees proper filling. The chamber was carved out of polyether ether ketone (PEEK), a material capable of withstanding reactive substances and high temperatures. For the laser processing, the chamber can be mounted on the movable stage within the laser structuring system (see Sec. 3.2.2).

**Laser Treatment** For all experiments the configuration with the sample as lid of the reaction chamber was used, so the laser did not need to penetrate the etchant. After the mounting of the sample, the reaction chamber was filled with hydrochloric acid (HCl) and mounted in the laser system. The laser processing was carried out, the chamber was unmounted, the acid and the sample removed and cleaned with DI-water. Even without any laser processing, this procedure required approx.  $t_{\text{exp}} = 20$  min working time. For the experiments the nanosecond, infrared *Rofin1064* was used. Due to the rather low absorption of ZnO:Al at  $\lambda_L = 1064$  nm, the ZnO:Al layer was heated almost homogeneously in growth direction. The green (*Rofin532*) and ultraviolet lasers (*Rofin355*) were not expected to yield better results because of too low absorption in the liquid and too high absorption

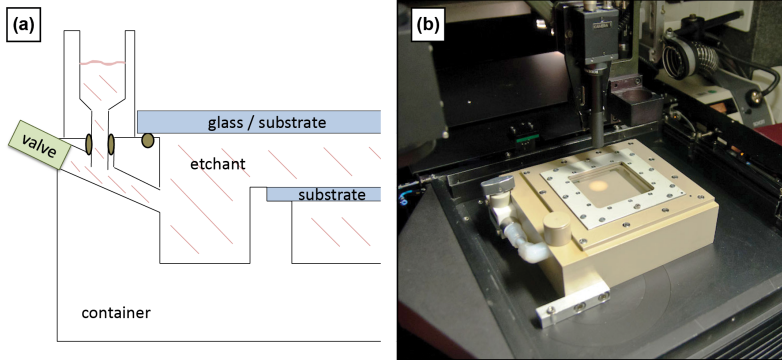


**Figure 4.1** Reaction chamber for laser-induced chemical etching: (a) The design of the chamber allows to mount the sample in two different ways, so processing of the film side through the etchant or through the glass side of the sample is possible. (b) Reaction chamber mounted in the structuring system.

at the glass–ZnO:Al interface respectively. The laser was used at a repetition rate of  $f_{\text{rep}} = 10 \text{ kHz}$  and the feed rate was varied down to  $v_{\text{feed}} = 0.1 \text{ mm/s}$ . With the beam radius measuring  $w_0 = 50 \mu\text{m}$  these parameters allowed a maximum dwell time of the laser beam of  $t_{\text{dwell}} = 1 \text{ s}$ .

Because of the required time for mounting and dismounting sample and chamber, the experiment was limited to the use of very weak concentrations of HCl. According to the experimental data published by Owen [73], for a volume concentration of  $\sigma_{\text{HCl}} = 0.031 \%$ , at room temperature of  $T_{\text{RT}} = 25 \text{ }^\circ\text{C}$  an etch rate of approx.  $k_{\text{HCl}} \cong 1 \text{ nm/s}$  is expected. Considering ZnO:Al films of  $h_{\text{ZnO:Al}} = 700 \text{ nm}$  thickness, the layer is destroyed after  $t_{\text{max}} = 11 \text{ min}$ . To overcome this problem, volume concentrations of  $\sigma_{\text{HCl}} = 0.01 \%$  have been used for the experiments. To further suppress parasitic etching without laser, the reaction chamber as well as the acid were cooled to  $T_{\text{HCl}} = 13 \text{ }^\circ\text{C}$  prior to the experiment.

## 4.2.2 Results and Discussion

**Experimental Findings** The treatment by laser-induced etching revealed similar textures as the mere etching without laser treatment. The surface texture as well as the etch rate were not significantly influenced by heat induction by the laser. The ablation threshold of the ZnO:Al film was determined to be at a fluence of  $\Phi_p = 0.81 \text{ J/cm}^2$ . Above this fluence, the film was removed completely. Closely underneath the ablation threshold at approximately  $\Phi_p = 0.77 \text{ J/cm}^2$  no significant differences in the texture could be measured. For comparison, two

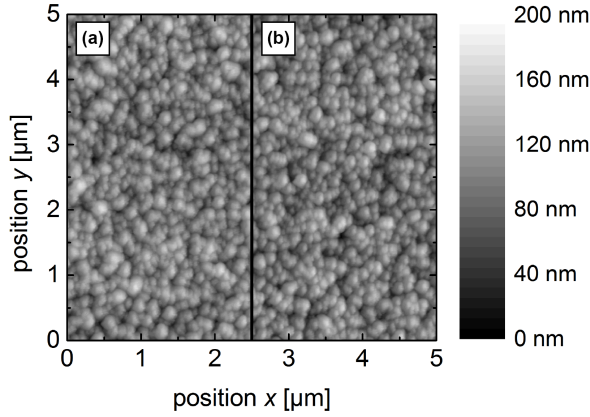


**Figure 4.2** Influence of laser heating on etching process (AFM images): (a) The sample was submerged in HCl with a volume concentration of  $\sigma_{\text{HCl}} = 0.01\%$  at  $T_{\text{exp}} = 13^\circ\text{C}$  for  $t_{\text{exp}} = 20$  min. (b) Additionally, a nanosecond infrared laser with a fluence of  $\Phi_p = 0.77\text{ J/cm}^2$  was scanned over the sample at  $v_{\text{feed}} = 0.1\text{ mm/s}$ . Due to the weak temperature dependence of the etch rates of highly diluted HCl, the measurements show no significant difference in the textures.

textures of a purely etched and an etched and simultaneously laser-treated area of the same sample are depicted in Fig. 4.2.

**Theoretical Considerations** To further investigate the findings of the low influence of the laser heating, an estimation of the temperature dependences of the etch rates was carried out. The total etch rate  $k_{\text{tot}}$  throughout the experiment can be calculated in dependence of the regular chemical etch rate at low temperature  $k_{\text{HCl}}$  and the laser heated etch rate at high temperature  $k_{\text{HCl+L}}$  by

$$k_{\text{tot}} = (t_{\text{exp}} - t_{\text{dwell}}) \cdot k_{\text{HCl}} + t_{\text{dwell}} \cdot k_{\text{HCl+L}}. \quad (4.3)$$

In order to be able to observe a difference in mere chemical etched and laser-heated etched material, a required increase of 10% of the total etch rate is assumed. The laser-heated etch rate then calculates to

$$k_{\text{HCl+L}} = \left( \frac{t_{\text{exp}}}{10 \cdot t_{\text{dwell}}} + 1 \right) \cdot k_{\text{HCl}}. \quad (4.4)$$

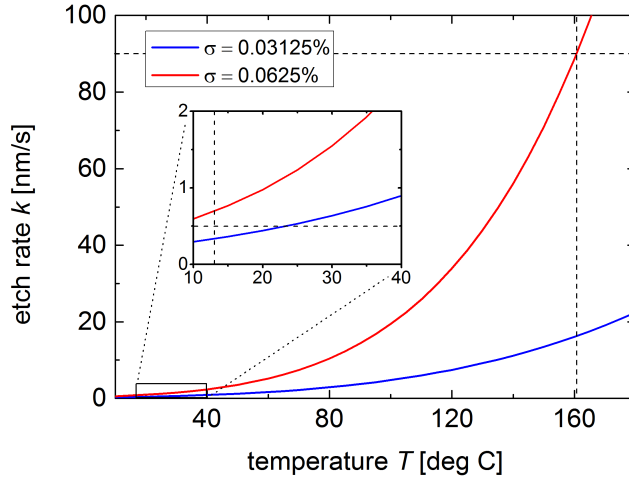


**Figure 4.3** Temperature dependence of the ZnO:Al etch rate of two concentrations of HCl (Data extracted from publication by Owen [73]). For the weak concentrations high temperatures are needed to achieve a significant speed-up of the etch reaction.

Assuming a minimum working time of  $t_{\text{exp}} = 30$  min, a laser dwell time of  $t_{\text{dwell}} = 1$  s and a maximum low temperature etch rate of  $k_{\text{HCl}} = 0.5$  nm/s, the etch rate has to be sped up by the laser heating to a rate of  $k_{\text{HCl+L}} \approx 90$  nm/s. Given the limitation for the etch rate  $k_{\text{HCl}} < 0.5$  nm/s at a temperature of  $T_{\text{exp}} = 13^\circ\text{C}$  (see preceding paragraphs) only concentrations of  $\sigma_{\text{HCl}} \lesssim 0.06\%$  were suitable for the experiment. The temperature dependence of the etch rate for the concentrations of  $\sigma_{\text{HCl}} = 0.031\%$  and  $\sigma_{\text{HCl}} = 0.062\%$  was extracted from Fig. 6.12 in the publication by Owen [73] and is depicted in Fig. 4.3. Given this data, it can be concluded that the required etch rate of  $k_{\text{HCl+L}} \approx 90$  nm/s can only be achieved for acid temperatures of above  $T_{\text{HCl}} > 160^\circ\text{C}$  (see Fig. 4.3).

Granted that the absorption coefficient of ZnO:Al is four orders of magnitude higher than the one for water, it is not possible to directly heat the acid to such high temperatures without ablation of the ZnO:Al layer. The acid has to be heated indirectly. A small volume of acid directly adjacent to the ZnO:Al surface is heated by heating the ZnO:Al layer with the laser. However, no significant change of the etch rate could be observed in the experiments. It is assumed that the dwell time of the laser is not long enough to heat a sufficiently large volume

of the acid so the etching process is sped up significantly. Higher laser powers again lead to the ablation of the ZnO:Al layer, while longer dwelling times than  $t_{\text{dwell}} = 1$  s inhibit industrial application. A setup with a laser beam parallel to the surface of the sample could be a possibility to overcome this challenge by directly heating the acid without risking an ablation of ZnO:Al. However, such a setup requires a more complex reaction chamber and was not further investigated since it does not seem feasible for industrial application due to the complex setup.

## 4.3 Particle Lens Array

**Motivation** Focusing the laser light to small spots for direct writing with the laser beam poses high demands on the machinery and optics (see Sec. 4.1). By bringing the focusing optics directly on the surface of the sample, these demands can be avoided. It has been shown that a particle lens array deposited on the surface of a material and irradiated by laser light leads to a local intensity enhancement underneath the spherical particle lenses (microspheres) [26, 27, 78]. This enhancement of the electromagnetic field can be used to texture the ZnO:Al with small crater-like features. Whereas this phenomenon is not a classical focusing phenomenon as in geometrical optics, the microspheres shall still be considered as "lenses" and are referred to as such.

### 4.3.1 Experimental Procedure

**Deposition of Microspheres** For the particle lens array, commercially available silica ( $\text{SiO}_2$ ) microspheres with a diameter of  $d = 450$  nm were used. The microspheres were purchased from *Corpuscular Inc.* They were dissolved in water and applied to the ZnO:Al film by drop coating. For the drop coating, volume concentrations ranging from  $\sigma_{\text{SiO}_2} = 0.01\%$  to  $5\%$  were used. In small, partial areas of the sample, a monolayer of touching spheres could be achieved for a concentration of  $\sigma_{\text{SiO}_2} = 0.5\%$  (see Fig. 4.4 (a)). However, it was not possible to cover larger areas with such monolayer. After drying, the substrate was mounted in the laser structuring system (see Sec. 3.2.2).

**Laser Treatment** The three nanosecond Nd:YVO<sub>4</sub> lasers *Rofin1064*, *Rofin532* and *Rofin355* were available for the treatments. Fluences measured in front of the particle lens array of up to  $\Phi_p = 3.1$  J/cm<sup>2</sup>,  $7.1$  J/cm<sup>2</sup> and  $4.8$  J/cm<sup>2</sup> could be realized respectively. Repetition rates were varied from  $f_{\text{rep}} = 10$  kHz to  $20$  kHz. Because almost all particles were removed by the laser irradiation, no cleaning step was needed after the laser treatment.

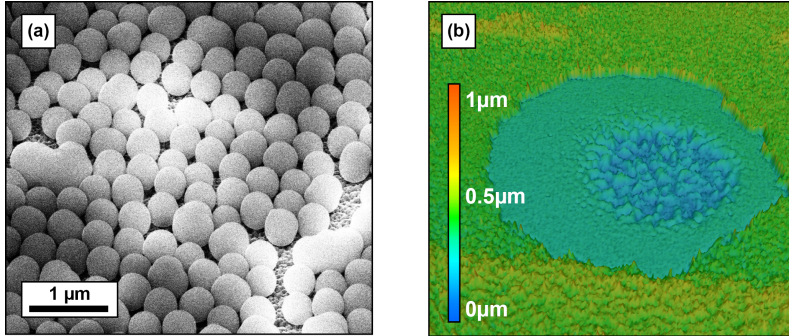


**Figure 4.4** Particle lens array – deposition and texture (SEM and LSCM pseudo 3D image): (a) The microspheres were deposited on the ZnO:Al by drop coating. In partial areas of the sample, the deposition of a monolayer of spheres could be achieved. (b) By laser ablation, a texture of unified craters is created in the center of the laser spot surrounded by single craters. Further on the outside, the energy of the laser does not suffice to texture the ZnO:Al but solely removes the spheres.

### 4.3.2 Results and Discussion

**Experimental Findings** By refocusing the laser beam with a particle lens array, crater-like structures could be obtained. Whereas the IR laser only damaged the surface of the ZnO:Al, the green laser revealed some single crater-like structures. However, these were only visible in some laser spots and the surface of the ZnO:Al around the craters appeared to be damaged. The UV laser showed the best results. Using fluences from  $\Phi_p = 0.19 \text{ J/cm}^2$  to  $0.23 \text{ J/cm}^2$ , a pattering of microscopic areas with single craters was possible with minimal uncontrolled surface damaging. Lower fluences merely removed the spheres from the surface without any pattering, whereas higher fluences led to a melting process and unification of more small craters to unwanted, larger features (referred to as unified craters). Above  $\Phi_p = 0.68 \text{ J/cm}^2$ , flake formation was observed and the ZnO:Al could be assumed to be damaged. The diameters of the single craters range from  $r_{\text{crater}} = 300 \text{ nm}$  to  $800 \text{ nm}$ . On average, the craters are approximately  $d_{\text{crater}} = 50 \text{ nm}$  deep, whereas there were strong deviations. Depths of up to  $d_{\text{crater}} = 200 \text{ nm}$  also occurred.

Due to the high sensitivity to fluences, covering larger areas was challenging. The flanks of the Gaussian beam spot did not carry enough energy to ablate the ZnO:Al and form craters. Nevertheless, the energy sufficed to remove the microspheres. This led to an untextured ring-shaped area around the beam spot where the microspheres were already removed (see Fig. 4.4 b). Accordingly, this

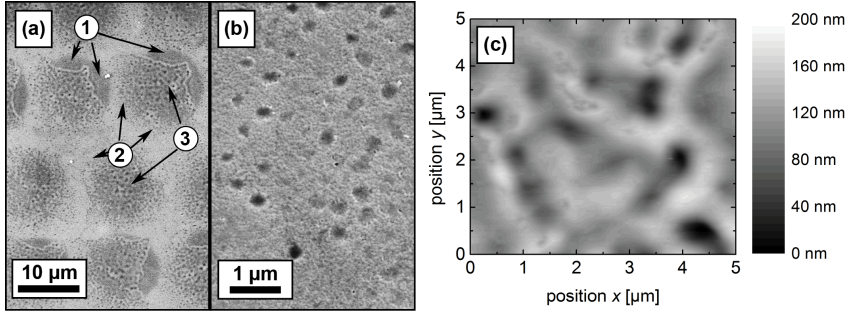


**Figure 4.5** Exemplary texture obtained by particle lens array created with  $\Phi_p = 0.22 \text{ J/cm}^2$  and  $\xi_x = \xi_y = 47\%$  (SEM images and AFM image): (a) Overview of patterned area containing three different processes: low fluences on the perimeter of the spots led to the removal of spheres and left untextured areas (1), medium fluences closer to the center of the spots led to a single crater texture (2), high fluences in the spot centers led to a fusion of craters to larger features (3). (b) Detail of single crater texture (as in (2)). (c) AFM measurement of spot center (as in (3)).

area could not be textured by the next adjacent pulse. Using the same overlap and higher fluences merely led to larger areas of unified craters in the center of the spots (3 in Fig. 4.4a)) without improving untextured area. Consequently, seamless stitching of Gaussian pulses and covering larger areas with the texture was not possible.

The partially textured substrates were characterized optically but do not significantly differ from the flat reference. Whereas the transmission remains on a high level, the haze value reveals only very little scattering abilities. The sheet resistance remained unchanged by the texturing. An exemplary texture created with  $0.22 \text{ J/cm}^2$  and a line overlap of the laser focal diameter of 47% is depicted in Fig. 4.5 (a) to (c). The UV Laser was used with a repetition rate of 15 kHz and a power of 38 mW. In this texture the three processes can be observed; single craters (Fig. 4.5 (b) and 2 in Fig. 4.5 (a)), larger features of melted unified craters (Fig. 4.5 (c) and 3 in Fig. 4.5 (a)) and untextured areas because of removal of the spheres (1 in Fig. 4.5 (a)).

Using the infrared laser, no crater-like texture could be obtained. For fluences up to  $0.4 \text{ J/cm}^2$  the ZnO:Al remained untouched, whereas for higher fluences cracks occurred. With the green laser, a similar texture as in Fig. 4.5 (a) to (c) could be obtained. However, the process window was even smaller compared to processing with the UV laser and higher fluences of  $3.5 \text{ J/cm}^2$  were needed.

## 4.4 Laser-Induced Periodical Surface Structures

**Motivation** Laser-Induced Periodical Surface Structures (LIPSS) also known as ripple structures are surface textures on the treated material. The size of the structures typically is on the order of the wavelength of the laser and below. They are mainly observed in multi-pulse processes of ultra-short-pulse lasers close to the ablation-threshold of the treated material. Because of the small feature sizes, LIPSS can possibly be used for texturing ZnO:Al layers for light in-coupling as well as light trapping (see Sec. 2.1.2).

**Theoretical Background** LIPSS have been first observed by Birnbaum [10] on various semiconductors in 1965. Thereafter, the formation of such ripple structures has been observed on various other materials as well [101]. Two different kinds of LIPSS can be observed. Low spatial frequency LIPSS (LSFL) have spatial periods  $\Lambda$  just below the wavelength of the incoming laser light ( $\Lambda \lesssim \lambda$ ). High spacial frequency LIPSS (HSFL) typically show much smaller periods down to approximately one fourth of the wavelength of the laser. Although LIPSS have been investigated for decades, their formation is still not fully understood [93], various theories exist [51, 64, 85, 102, 103] and experimental results still deviate from theoretical predictions [104]. The most promising, so-called "efficiency" theory was first developed by Sipe and Young [92, 109] in 1983. It assumes an interference of the incoming wave with a surface scattered wave to be the origin for the periodic energy deposition along the surface as first proposed by Emmony [34]. The theory was then further developed by Bonse [?, 16] and the research is still ongoing [46]. The exact underlying physcial processes that lead to the periodic energy deposition depend on the material [101]. For metals it is suggested that surface plasmon polaritons play an important role [17]. Taking into account the Drude theory and transient changes of the refractive index due to the generation of quasifree electrons during the laser-treatment [107], the spatial periods and orientations of LSFL and HSFL can be explained for single-crystalline ZnO [29]. There have also been various experimental studies of different LIPSS geometries on crystalline ZnO [41–43]. Furthermore the dependence of LIPSS formation on substrate material [111] and wavelength of incoming laser light [49] as well as two-beam treatment [50] was investigated.

### 4.4.1 Experimental Procedure

**LIPSS Setup** In order to obtain LIPSS with different spatial periods, the infrared *Tumpf TruMicro 5050* and green *Tumpf TruMicro 5000* picosecond Yb:YAG lasers were used (see Sec. 3.2.1). The polarization of the laser beam was controlled by quarter and/or half-wave plates to obtain circular polarized as well as linear

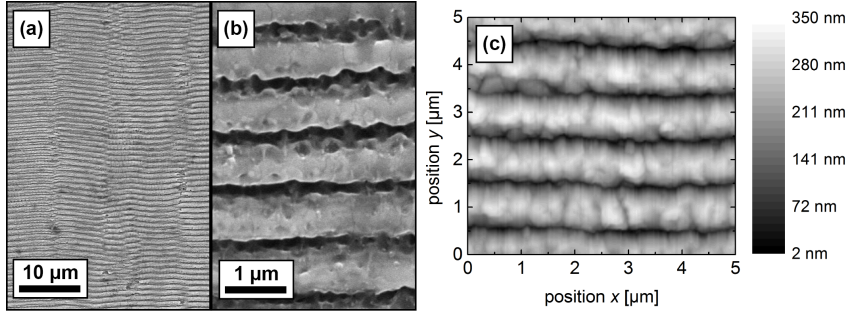


**Figure 4.6** Exemplary LSFL texture created with  $\Phi_p = 0.53 \text{ J/cm}^2$ ,  $\xi_x = \xi_y = 88\%$  and linearly polarized, infrared picosecond laser (SEM images and AFM image): (a) Overview with visible stitching effects. (b) Detailed image of feature geometry. (c) Measured Topography: The texture is of clear periodic character with a spatial period of  $\Lambda = 900 \text{ nm}$  and a groove depth of  $\Delta h = 300 \text{ nm}$ .

polarized light of any angle (Sec. 2.2.1). The beam was deflected by a galvo scanner system and focused by an f-theta lens system (see Sec. 3.2.2) on the film side of the substrate under normal incidence. Lenses of various focal lengths were used, yielding pulse fluences up to  $\Phi_p = 5 \text{ J/cm}^2$  and  $\Phi_p = 18 \text{ J/cm}^2$  for  $\lambda = 1030 \text{ nm}$  and  $515 \text{ nm}$  respectively.

## 4.4.2 Results and Discussion

### Low Spacial Frequency LIPSS (LSFL)

**Topography** Using the infrared laser with linear polarized light, LSFL could be created (see Fig. 4.6). The process windows ranged from  $\Phi_p = 0.53 \text{ J/cm}^2$  to  $0.61 \text{ J/cm}^2$  with a spatial pulse overlap of at least  $\xi_x = \xi_y = 80\%$ . Using lower fluences did not yield any effect on the ZnO:Al, whereas higher fluences led to flake formation and partial ablation of the ZnO:Al destroying the electrical properties of the film. Within the process window, the texture shows a clearly periodic ripple structure with a spatial period  $\Lambda$  of approximately  $\Lambda \approx 900 \text{ nm}$  and a groove depth  $\Delta h$  ranging from  $\Delta h = 200 \text{ nm}$  to  $300 \text{ nm}$ . It was possible to rotate the orientation of the grooves by changing the angle of the linear polarization (see Fig. 4.7). However, it was not possible to texture the same area twice with different LIPSS orientations as to obtain a cross hatched texture. Only the geometry of the second treatment remained. Furthermore, no creation of HSFL with spatial periods much smaller than the laser wavelength could be created.

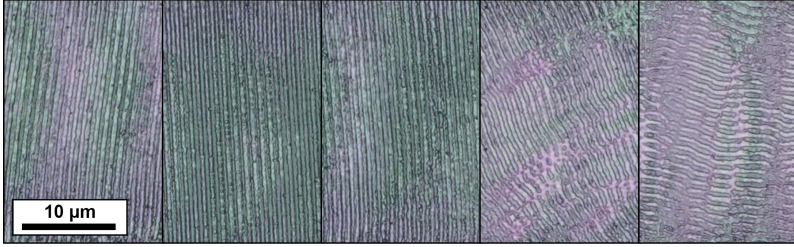


**Figure 4.7** Polarization dependence of LSFL (LSCM images): The orientation of the LSFL can be adjusted by changing the orientation of the linear polarized laser light. The ripples are orientated perpendicularly to the electrical field of the laser beam.

**Electro-optical Properties** Four point sheet resistance measurements revealed a slightly augmented sheet resistance of  $R_{\square} = 11 \Omega$ . The LSFL reveals better scattering properties than the untextured ZnO:Al. At the same time, the haze is not as large as the standard etched texture. Furthermore, the total transmission remains below the flat as well as standard etched texture (see Fig. 4.10) for short wavelengths, but surpasses the flat reference in the longer wavelength region (see Fig. 4.10).

An exemplary texture created with a fluence of  $\Phi_p = 0.53 \text{ J/cm}^2$  and an overlap of  $\xi_x = \xi_y = 88 \%$  is depicted in Fig. 4.6. Up scaling to larger areas  $A = 100 \text{ mm} \times 100 \text{ mm}$  was possible with only little stitching effects (see Fig. 4.6) (a)).

## High Spatial Frequency LIPSS (HSFL)

**Topography** Using the green laser with circular polarized light, a coral-like texture with features well below the wavelength of the incoming light could be created (see Fig. 4.8). For reasons of simplicity and due to the correlation with the LSFL process regarding polarization dependency and process parameters, this process is referred to as a HSFL process – albeit the periodicity not being very obvious. The fairly narrow process window ranged from  $\Phi_p = 0.68 \text{ J/cm}^2$  to  $0.75 \text{ J/cm}^2$  with line overlaps from 80 % to 85 %. For higher fluences or larger overlaps, there was a strong crack formation, whereas for lower fluences or smaller overlaps, no LIPSS formation could be observed and the ZnO:Al remained untextured. The feature sizes of the textures ranged from  $d = 200 \text{ nm}$  to  $350 \text{ nm}$ . Using linear polarized light, some of the features could be aligned according to the polarization. However, it was not possible to obtain a clearly periodic line-like texture (see Fig. 4.9). Furthermore it was not possible to produce a LSFL structure with spatial periods on the order or just below the wavelength of the incoming light.

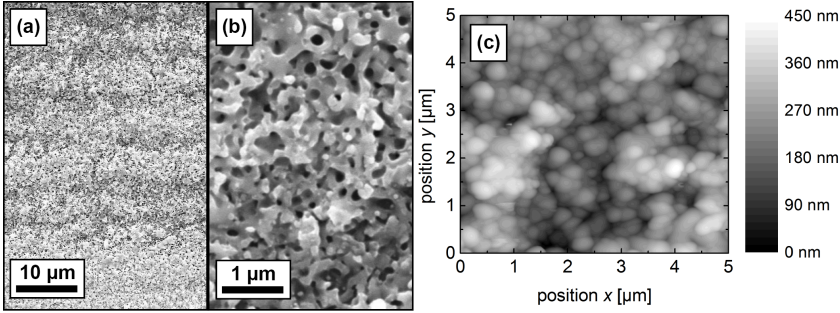


**Figure 4.8** Exemplary HSFL texture created with  $\Phi_p = 0.73 \text{ J/cm}^2$ ,  $\xi_x = \xi_y = 84\%$  and circularly polarized, green picosecond laser (SEM images and AFM image): (a) Overview of larger area. (b) Detailed image of feature geometry. (c) Measured Topography: The feature sizes of the texture range from  $d = 200 \text{ nm}$  to  $350 \text{ nm}$  with a rms roughness of  $R_{\text{rms}} \approx 100 \text{ nm}$ .

**Electro-optical Properties** The measured sheet resistance strongly varied over the substrate ranging from  $R_{\square} = 30 \Omega$  to  $100 \Omega$ . Measurements of the diffuse and total transmission revealed good scattering abilities of the HSFL texture at the ZnO:Al–air interface. Wavelengths below  $\lambda = 900 \text{ nm}$  are scattered significantly better than the flat reference but slightly worse than the etched reference. However, for longer wavelengths the HSFL texture shows higher scattering abilities than the standard etched reference. The total transmission shows a similar picture, while being less transparent than both references in the short wavelength regime, the HSFL textures is more transparent than both references above  $\lambda = 900 \text{ nm}$ .

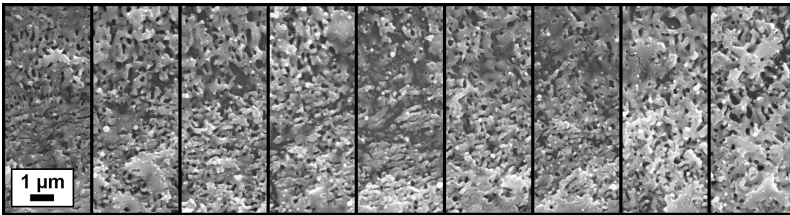


**Figure 4.9** Influence of polarization on HSFL texture (REM images): Using linear polarized green laser light, no line-like texture could be produced. Changing the orientation of the polarization only marginally influences the orientation of the HSFL features.

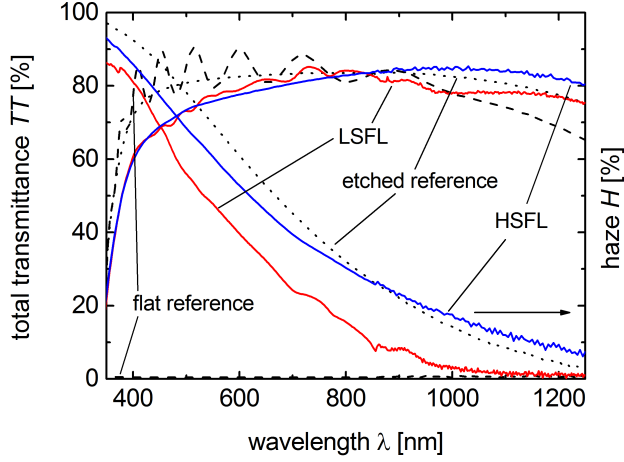


**Figure 4.10** Scattering properties of LIPSS (optical spectra): Both LSFL and HSFL textures show scattering properties at the ZnO:Al-air interface. LSFL and HSFL show higher haze values than the untextured reference. The total transmittance of LSFL and HSFL remains below both references in the shorter wavelength regime. In the longer wavelength regime the LSFL reveals a better transmittance than the flat reference, while the HSFL even surpasses the standard etched reference. The gain in transmittance is attributed to better in-coupling properties.

An exemplary texture is depicted in Fig. 4.8 (a) to (c). Circular polarized light, a fluence of  $\Phi_p = 0.73 \text{ J/cm}^2$  and a pulse overlap of  $\xi_x = \xi_y = 83 \%$  were used. A root mean square surface roughness  $R_{\text{rms}}$  of approximately  $R_{\text{rms}} \approx 100 \text{ nm}$  was calculated from AFM measurements (Fig. 4.8 (c)). Applying the texture to larger areas  $A = 100 \text{ mm} \times 100 \text{ mm}$  was possible with almost no stitching effects (compare Fig. 4.8 (a)).

#### 4.4.3 Speed Considerations

Assuming that a fluence of  $\Phi_p = 0.7 \text{ J/cm}^2$  and a line overlap of  $\xi_x = \xi_y = 80 \%$  (see definition of line overlap in Sec. 2.2.1) is needed, this would result in an effective fluence  $\Phi_{\text{eff}}$  of

$$\Phi_{\text{eff}} = \frac{\Phi_p}{(1 - \xi_x)(1 - \xi_y)} = 17.5 \text{ J/cm}^2. \quad (4.5)$$

The most recent commercially available picosecond laser systems for industrial application reach powers of up to  $P_L = 1 \text{ kW}$ <sup>1</sup>. Taking into account such average powers, the covering of an area of  $A = 1 \text{ m}^2$  would require  $t_{\square} = 175 \text{ s}$ .

## 4.5 Two-Beam Direct Laser Interference Patterning

**Motivation** Direct laser interference patterning (DLIP) is a technique which uses the intensity pattern of overlapping laser beams to directly induce topography pattern on a surface [6, 48, 59, 69]. Recently this techniques has also been applied in the field of photovoltaics [60, 71], for texturing of ZnO:Al layers [31, 32] and very recently even the production of functioning DLIP-patterned thin-film silicon solar cells was reported [86]. The technique promises potential areal processing speeds of  $v_{\square} = 1 \text{ m}^2/\text{min}$  [61] which makes it very suitable for industrial application.

**Theoretical Background** Whenever two laser beams overlap, the electromagnetic fields of the beams are superimposed to form a resulting intensity pattern within the overlapping volume (see Sec. 2.2.1). For two temporal coherent laser beams this intensity pattern is of spatial periodic character<sup>2</sup>. The electromagnetic waves of the laser beams interfere and produce a periodic intensity pattern in the overlapping volume which is often referred to as the interference volume. The spatial period of the interference pattern depends on the angle of incidence of the laser beams (compare Fig. 2.12). Bringing a sample within the interference volume results in a periodic laser intensity distribution along the surface of the sample. Consequently the sample is heated periodically. If the sample is heated sufficiently, a periodic ablation of material occurs and results in a periodically textured surface. For the use of ZnO:Al, a UV laser in nanosecond regime is suitable because it ablates the ZnO:Al nearly proportional to the intensity of the laser light [58]. Consequently, the intensity pattern of the interfering laser beams can be transferred to a topographical pattern on the surface of the ZnO:Al.

### 4.5.1 Experimental Procedure

**Two-Beam DLIP Setup** In Fig. 4.11 a schematic drawing of the two-beam interference setup is depicted. A frequency tripled Nd:YAG Laser with a wavelength of  $\lambda_L = 355 \text{ nm}$  and a pulse duration of  $\tau_p = 5 \text{ ns}$  was used. For the treatment

<sup>1</sup>e.g. AMPHOS 400

<sup>2</sup>Strictly speaking the intensity pattern is only periodic along any given axis that is not the axis represented by the sum of the wave vectors of the two interfering laser beams.

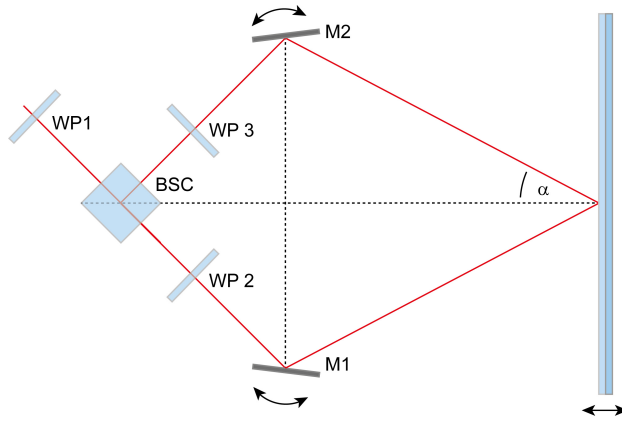


**Figure 4.11** Experimental setup for two-beam direct laser interference patterning (Sketch): A linear polarized UV nanosecond laser is split by a polarizing beam splitter cube (BSC). The polarizations of the partial beams are aligned by half-wave plates (WP2, WP3). The beams are reunited at the sample by two adjustable mirrors (M1, M2). The intensities of the partial beams can be adjusted by a half-wave plate (WP1) and the angle of incidence  $\alpha$  by a movement of the sample.

of the ZnO:Al only single pulses were used. The laser beam was split using a polarizing beam splitter cube and reunited at the substrate at an adjustable angle to the surface. The substrate was mounted vertically on a x, y, z manual positioning system. The intensities of the partial beams were equalized by a quarter-wave plate in front of the beam splitter cube and their polarization was aligned by two half-wave plates in each partial beam. Without focusing, pulse fluences of up to  $\Phi_p \approx 9 \text{ J/cm}^2$  could be reached.

## 4.5.2 Results and Discussion

**Experimental Findings** Using DLIP, it was possible to produce various, strictly periodic textures in ZnO:Al. With a single shot treatment, areas of approximately  $A_s = 2 \text{ mm}^2$  could be covered with a line-like texture. An exemplary line-like texture is shown in Fig. 4.12 (a) to (c). The texture was created with an angle of incidence ( $\alpha$  in Fig. 4.11) of  $\alpha = 6.8^\circ$  and a pulse energy  $E_p$  of approximately  $E_p \approx 30 \text{ mJ}$ . This yields an averaged<sup>3</sup> fluence of  $\Phi_p \approx 1.5 \text{ J/cm}^2$ . The texture is of clear periodic character, with a spatial period of  $\Lambda = 1.5 \mu\text{m}$  and a groove

<sup>3</sup>Spatially averaged over the estimated area where a texturing effect can be observed.

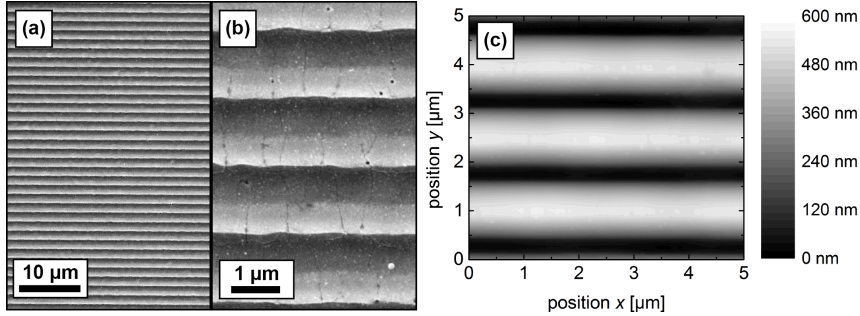


**Figure 4.12** Exemplary texture created by two-beam DLIP with  $\Phi_p \approx 1.5 \text{ J/cm}^2$  and angle of incidence  $\alpha = 6.8^\circ$  (SEM images and AFM image): (a) Overview of larger area. (b) Detailed image of feature geometry and some crack formation. (c) Measured Topography: The smooth texture is of strictly periodic character with a periodicity of  $\Lambda = 1.5 \mu\text{m}$  and a groove depth of  $\Delta h = 500 \text{ nm}$

depth of  $\Delta h = 500 \text{ nm}$  (Fig. 4.12 (c)). In areas of high energy intake, formation of small cracks can be observed (Fig. 4.12(b)).

The spatial periods of the textures could be continuously adjusted from  $\Lambda = 400 \text{ nm}$  to  $15000 \text{ nm}$ . However, for smaller spatial periods the depth of the grooves lessened to almost completely vanish at  $\Lambda = 400 \text{ nm}$ . The intensity distribution within the profile of the specific laser used for the experiments was very inhomogeneous. The laser power fluctuations of the system ranged up to  $u_p^{\text{rel}} \approx 20\%$ <sup>4</sup>. Consequently, the calculated fluences underlay strong variations and have to be treated with extreme caution. However, some general trends could be observed. For lower fluences the ZnO:Al was only ablated at the peak intensities of the interference pattern, while in between the grooves a flat, untreated area remained. With rising fluences, the groove depth rose until the ZnO:Al was ablated even in between the peak intensities, leading to a sine-like texture. In some areas of high energy deposition, formation of small cracks could also be observed. Due to the inhomogeneous, non-Gaussian beam profile of the specific laser used for the experiment (see Fig. 5.2 (a)) and the corresponding energy distribution within the laser spot, homogeneous covering of larger areas by stitching pulses was not possible. Consequently no sheet resistance measurements or extensive optical measurements could be performed. The illumination of the textures with a weak laser source, however, leads to a diffraction of the laser light. The diffraction pattern changes according to the

<sup>4</sup>By thorough characterization of the laser's instabilities and subsequent operation of the laser system only at the optimal operating point, this instability could be improved later on when using the same laser system for the three-beam interference setup.

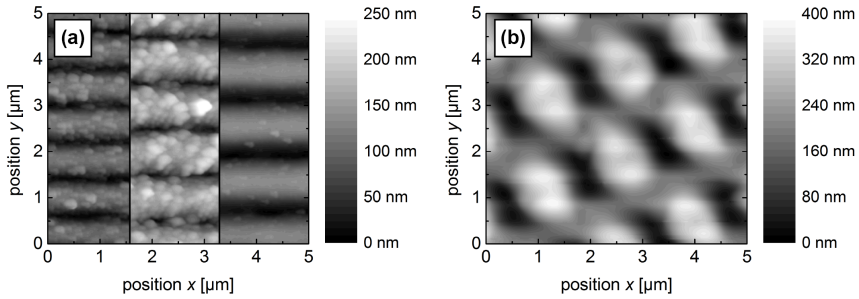


**Figure 4.13** Texture variety obtainable by two-beam DLIP (AFM measurements): (a) Three textures obtained with  $\Phi_p \approx 2 \text{ J/cm}^2$  and angles of incidence of  $\alpha = 8.5^\circ$  (left),  $10.2^\circ$  (middle) and  $12.8^\circ$  (right). The dent-like texture overlaying the periodic grooves is assumed to be ablated ZnO:Al resettling on the layer. (b) Texture obtained by superposing two line-like textures. The sample was textured with the same parameters as in Fig. 4.12, rotated for  $\beta = 45^\circ$  and processed again with the same parameters.

spatial period of the texture illuminated. These experiments indicate that the produced textures are capable of effective light scattering.

To demonstrate the flexibility of DLIP, examples of texture with spatial periods of  $\Lambda = 1200 \text{ nm}$ ,  $1000 \text{ nm}$  and  $800 \text{ nm}$  can be observed in Fig. 4.13 (a). The according angle of incidence was  $\alpha = 8.5^\circ$ ,  $10.2^\circ$  and  $12.8^\circ$  respectively. In order to obtain two-dimensional textures, two processes creating line-like textures could be superposed with a rotation of the substrate in between the treatments. An exemplary two-dimensional structure with a sample rotation of  $\phi = 45^\circ$  is shown in Fig. 4.13 (b). A detailed look at the height profile of the texture depicted in Fig. 4.12 (c) reveals a sine-like texture. An intensity profile of the two interfering laser beams can be calculated by superposition (see Sec. 2.2.1). Comparing the measured height profile of the surface with the inverse of the calculated intensity profile, there is a good match (Fig. 4.14). Please note that the calculated intensity profile is only of relative character and has been scaled in height to fit the measured data.

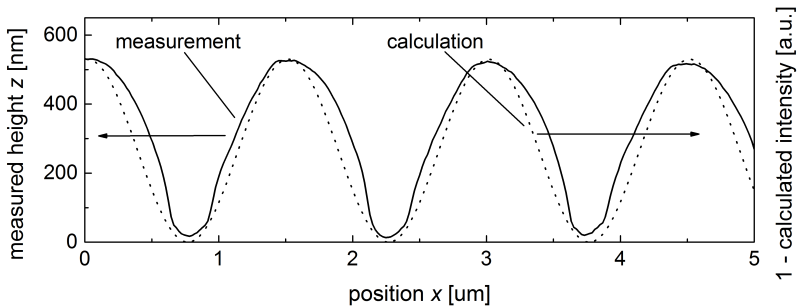


**Figure 4.14** Comparison of measured height profile and calculated intensity of two interfering laser beams: The measurement data is identical to the data presented in Fig. 4.12 (c). The intensity is scaled vertically to fit the measurement. The good match of measurement and calculation demonstrates the potential for an analytical description of possible textures.

## 4.6 Conclusion

The process for texturing the ZnO:Al has to meet many requirements. It needs to be capable of producing textures with feature sizes in the sub-micrometer range. Furthermore, the geometries and sizes of these features need to be adjustable so scattering properties can be controlled. In addition to these physical requirements on the outcome of the texturing process, the process itself needs to meet technological requirements for industrial applicability. It needs to be simple and scalable to large areas, in order to be compliant with the cost, material and energy effective manufacturing of thin-film silicon solar cells.

A simplified summary of the comparison in the preceding chapter with regard to these main demands is depicted in Tab. 4.1.

**Direct Writing** The approach of direct writing could be capable of producing feature sizes on the right order of magnitude and with a very high flexibility of potential feature shapes. However, the very high demands on the machinery ask for a complicated and costly setup and the possible production rates inhibit industrial application.

**Laser-Chemical Etching** The technique of laser-induced etching did not reveal promising results. Whereas the experimental setup was somewhat complex, it could be scalable to larger areas in an industrial environment. However, the

	<i>Feature Sizes</i>	<i>Flexibility</i>	<i>Scalability</i>	<i>Simplicity</i>
Direct Writing	+	+	-	-
Laser-Induced Chemical Etching	-	-	0	0
Particle Lens Array	0	0	-	-
Laser-Induced Periodical Surface Structures	+	0	0	+
Direct Laser Interference Patterning	+	+	+	0

**Table 4.1** Summary of process comparison: Direct laser interference patterning shows the highest potential of the processes under investigation. It is capable of producing flexible textures with feature sizes on the order of the wavelength of visible light and can be scaled to industrial application while maintaining a comparably simple setup.

possible gain in feature shapes and/or sizes did not justify further investment in the experimental expertise required to further investigate the technique.

**Particle Lens Array** Refocusing the laser with a particle lens array was capable of producing crater-like textures. Whereas the diameters of the craters were of the right order of magnitude, the average depth is too shallow for effective light scattering. The distances between the craters are determined by the position of the microspheres and could be adjusted by using differently sized microspheres. Furthermore, seamless stitching of Gaussian pulses to large areas was not possible due to the high fluence sensitivity of the process. Moreover, the deposition of a homogeneous monolayer of microspheres on larger areas by simple deposition methods was challenging. Although it has been demonstrated that perfect monolayers of microspheres can be deposited [20, 21, 62], the deposition of such by simple and cost effective methods like drop coating could not be achieved. More complex deposition methods like spin coating, however, are not applicable to larger scales in a production environment. In conclusion, the process was not capable of producing the right feature sizes, the flexibility of the setup was limited and a possible industrial application is very challenging due to the difficult scalability and high complexity of the experimental procedure.

**LIPSS** On the one hand, the formation of LIPSS with ultra short pulse lasers is a very simple process capable of producing usable textures. The experimental setup merely consisted of a device to scan the focused laser over the substrate. The

covering of large areas was possible with only little stitching effects. The feature sizes of the two textures created are well suited for light trapping ( $d = 900$  nm) and light in-coupling ( $d = 200$  nm to 350 nm). On the other hand, there are three restrictive disadvantages. Firstly, the process is limited considering achievable feature sizes and shapes. Only two distinct types of textures could be produced. Whereas the orientation of the LIPSS could be controlled by polarization, there was no simple method to control the size of the features. There have been studies indicating that the spatial period can be controlled by changing the wavelength of the incoming laser light [49] and/or the angle of the incident beam [29]. The experimental setups for such adjustments, however, are much more complex so the process loses its main advantage of simplicity. Secondly, the deposition of solar cells on the HSFL texture can be difficult due to the challenging growth of silicon on the very porous texture [81]. Finally, the long processing times, the small process window and the high costs of high power, ultra-short pulse laser systems strongly limit industrial feasibility.

**DLIP** The processing by DLIP showed a very high degree of flexibility and adaptability of small feature sizes and shapes. The created feature sizes were of the order of the wavelength of visible light and below. Feature sizes could be adjusted arbitrarily by the angles of incidence of the interfering beams. Whereas two-beam DLIP only produces line-like textures, these textures could be superposed by consecutive treatments. Consequently, various two-dimensional textures could be realized with a simple setup by rotating the sample in between the treatments. By expanding the setup to three-beam-interference, even more complex two dimensional textures can be created with a single shot treatment. Furthermore, the produced textures are very similar to calculated laser intensity patterns, promising a predictable and calculable geometric shape of the textures. Consequently, optical modeling software can be used to adapt the texture to the need of a certain solar cell. Concerning scalability, the experimental setup is slightly more complex than the one for the LIPSS creation. However, it is simple enough to be scaled to industrial application. Likewise, the required fluences and the absence of spatial overlaps combined with the comparably low cost of nanosecond laser systems allow an application in an industrial environment.

The main draw-back concerning scalability were stitching issues due to the beam profile of the laser. The inhomogeneous beam profile prevented a homogeneous patterning of macroscopic areas. Consequently the process could not be scaled to larger areas and no electro-optical properties of the ZnO:Al could be determined. However, the difficulties in macroscopic patterning mainly were an experimental issue due to the laser system used in this specific experimental setup and not of the technique itself. A rectangular, homogeneous top-hat profile for example could overcome these challenges.

Given the requirements of an industrially feasible process that is able to produce adaptable textures with feature-sizes in the sub-micrometer range, the DLIP process shows the highest potential. Especially because of the predictability and adaptability of the textures and the possible application in an industrial environment DLIP was chosen to be investigated further.

# 5 Three-Beam Direct Laser Interference Patterning (DLIP)

The two-beam DLIP setup described in the previous chapter showed promising results for the texturing of ZnO:Al. In order to broaden the variety of possible textures, a three-beam interference setup is designed and implemented. Three-beam DLIP is able to produce a large variety of hexagonal, two-dimensional textures. However, line-like textures can also be produced by merely using two beams. Apart from the experiment itself, a theoretical description of the experiment is derived and implemented. This theoretical description is aimed to model the actual experiment starting from the beam propagation through the experimental setup over the actual beam interference to the ablation of ZnO:Al on the sample and the resulting textures. The goal of this model for virtual laser interference patterning (named *VLIP*) is to be able to predict the producible texture for a given setup of the experiment.

In the following sections, first the experimental setup along with its adjustment and controls as well as the conduct of the experiment is described. In the next sections, exemplary interference patterns are presented and the influence of various setup parameters on the patterns is discussed. The subsequent section investigates the surface textures which can be produced by DLIP. Exemplary textures are presented, the deliberate control of texture properties is discussed and assumptions about the ablation process are made. In the last section of this chapter, the *VLIP* model is developed. A simple theoretical model for the energy intake in the material, heat diffusion and consequent ablation is derived. It is adapted to the use with ZnO:Al by determining characteristic material properties and its predictive power is discussed.

## 5.1 Experimental Setup

**Demands** The variety of laser intensity patterns producible with three laser beams is described by Eq. 2.37. The independent parameters are the electric field amplitudes  $E_i$  (i.e. the intensities), the directions of polarization  $\hat{e}_i$  and the wavevectors  $\vec{k}_i$  (i.e. directions) of the partial beams. With these 15 parameters the

laser intensity pattern and the resulting texture on the sample can be influenced and adjusted. A major requirement and precondition for the selection of a suitable texturing process was a high degree of flexibility (see Chap. 4). In order to retain this high flexibility, the experimental setup needs to be designed in such way that as many of these 15 parameters as possible can be adjusted independently. Apart from the major demand for flexibility of the textures itself, the setup needs to be designed so macroscopic areas can be textured in reasonable amounts of time. This is necessary to be able to conduct optical and electrical measurements on the textured samples as well as to be able to build solar cells on the obtained textures. Accordingly, an automated and synchronized scanning of the laser beam over the sample needs to be implemented.

**Challenges** Due to the ablation behavior of ZnO:Al in the UV nanosecond regime [58] and the required high pulse energies, the *Powerlite8020* ( $\lambda_L = 355$  nm,  $\tau_p = 5$  ns) laser system was used for the experiments. However, due to the malfunctioning of the seeder system, the laser only provided a very inhomogeneous beam profile and a short coherence length (for details see Sec. 3.2.1). In order to be able to quantify the actual laser intensity on the material, the beam profile of the laser needed to be improved. The same is true to allow a somewhat homogeneous covering of macroscopic areas by stitching of laser pulses. Because of the limited temporal coherence, the three partial beam paths had to be of almost exact equal length. Consequently, two possibilities for independent adjustment of the beam path lengths had to be incorporated in the individual partial beam paths.

Apart from these specific challenges caused by the laser system, the general design of a three-beam DLIP setup was somewhat more complex than the design of a two-beam setup. The simpler mirror symmetry of the setup had to be substituted by a rotational symmetry with respect to one axis. Such rotational symmetry required a higher amount of complexity concerning the support as well as the adjustment of the optics used for the experiment. Furthermore, to insure the maximal possible interference effect, the beam profile of each partial beam on the sample had to be identical to the other ones. The partial beam profiles must not be orientated or mirrored in some sort. This posed further restrictions on the amount of mirrors in each partial beam path as well as their orientations. Last but not least, to minimize polarizing effects of the mirrors, shallow angles of incidence needed to be avoided on all mirrors.

All of these demands were considered for the design of the setup and were fulfilled in the final layout of the experiment.

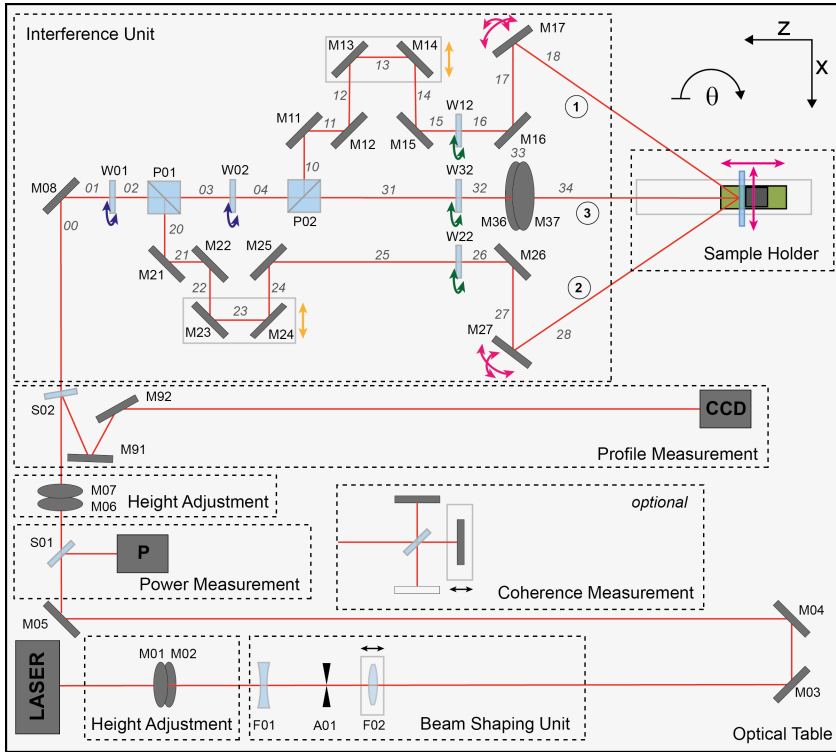


**Figure 5.1** Layout of three-beam interference setup – top view, logical units and optical components.

### 5.1.1 Layout of Experimental Setup

An overview of the final layout of the experimental setup for three-beam DLIP is depicted in Fig. 5.1, 5.3 and 5.4. All of the components of the experiment were mounted on one optical table. However, the experiment was divided into logical units, which will be explained in the following paragraphs starting from the laser source and ending at the sample.

**Height Adjustment** Mirrors M01 and M02 are used for a height adjustment of the laser beam. For a simpler handling and more stable constructions, the beam is lowered from the exit of the harmonic generator to a height of  $h = 130$  mm above the optical table.

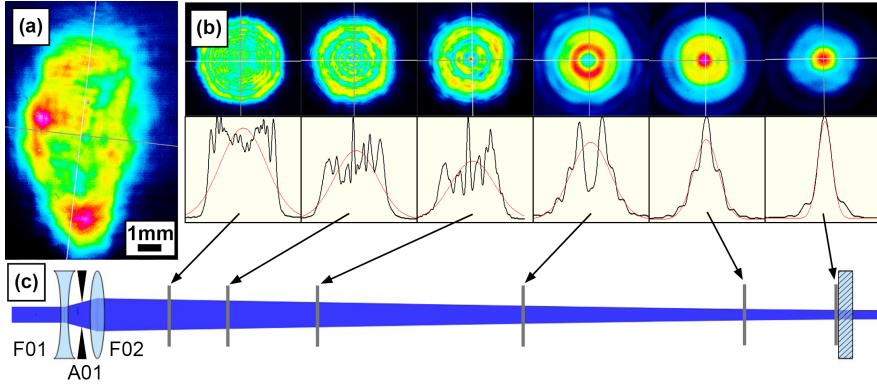


**Figure 5.2** Beam shaping unit ((a,b) measured beam profiles and (c) calculated beam caustic): (a) Before the beam shaping unit, the beam exhibits an inhomogeneous profile. (b) Directly behind the beam shaping unit, ring-like airy pattern can be observed because of diffraction on the hard aperture edge (left in (b)). After  $l \approx 6$  m propagation, the airy pattern have diverged out of the beam profile leaving a Gaussian shaped beam profile at the sample plane (right in (b)). (c) By adjusting the beam shaping lens system (left in (c)), the beam divergence can be controlled to slightly focus the beam at the sample plane (right in (c)).

**Beam Shaping Unit** In order to improve the beam profile of the laser beam, a beam shaping unit was implemented (see. Fig. 5.2). The unit consists of a plano-concave lens F01 with a focal length of  $f_{F01} = -216$  mm, an iris aperture A01 with a diameter of  $d_{A01} = 2.5$  mm and a plano-convex lens F02 with a focal length of  $f_{F02} = 432$  mm. The unit fulfills two tasks. Firstly, the two lenses function as a Galileo-type telescope, expanding the laser beam in diameter. The expanded beam has a lower intensity so the laser can be used at full power without destroying the delicate optics used in the interference unit (see Sec. 5.1.1). In addition to this, the beam divergence and consequently the position and diameter of the beam waist can be adjusted by slightly moving the lens F02. This slight focusing of the laser beam is crucial in order to obtain sufficiently high fluence on the sample, while keeping the fluence low on the optical components. Secondly, the aperture together with a long beam path thereafter can be used to clean up the beam profile. Most of the inhomogeneous beam profile (compare Fig. 5.2 (a)) is blocked and absorbed in the aperture. Only a small part of the profile is transmitted. The aperture is positioned so the part of the highest intensity of the profile is transmitted. However, roughly 80% of the laser power is lost in the aperture. Due to refraction on the hard aperture edges, ring like structures (so

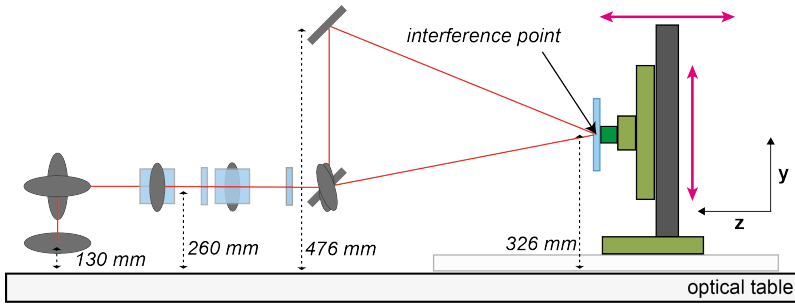


**Figure 5.3** Layout of three-beam interference setup – side view and beam heights.

called airy pattern) appear in the intensity profile of the laser beam. In order to get rid of these, the laser beam was slightly focused (by changing the divergence, see above) and guided across the optical table and back to elongate the propagation path. Because the Gaussian beam mode is the least divergent of all beam modes (see Sec. 2.2.1) it can be focused better than the airy pattern. As a result, along the beam path, the airy pattern diverge out of the center of the beam profile (see Fig. 5.2) until they are finally blocked out by the inherent aperture of a mirror. Consequently, the resulting beam profile after a long enough propagation is of Gaussian shape. Since the sample plane is approx  $l \approx 6$  m behind the aperture, the sample can be treated with a Gaussian shaped beam profile. For more details on the adjustment of the beam shaping unit, please refer to Sec. 5.1.2.

**Power and Coherence Measurement Branch** The beam sampler S01 reflects approximately 1% of the laser power into the power meter while transmitting the rest unchanged. The proportion of the reflected light depends on the polarization of the laser beam and the exact angle of reflection. Once set up, however, it remains constant. Accordingly, a fixed percentage of the total laser power can be measured and in-situ power measurements can be conducted during the laser treatments. Alternatively, this beam path can be used to measure the temporal coherence of the laser beam with a Michelson interferometer [67]. Details of the measurement are described in Sec. 5.1.2

**Height Adjustment** Mirrors M06 and M07 are used as a height adjustment to lift the laser beam from  $h = 130$  mm to  $h = 260$  mm (Fig. 5.3). This height is less stable for vibrations and poses a higher demand on the supporting structures of the optics, but is needed for the following interference setup and sample mounting.

**Profile Measurement Branch** Beam sampler S02 has the same properties as S01. It was used to open another beam path to be able to measure the beam profile in-situ. The mirrors M91 and M92 are needed to retain a small angle of reflectance on the beam sampler. The beam sampler reflects differently polarized light in slightly different angles. For smaller angles of reflection this effect vanishes, so the whole beam profile can be measured with the beam profiler. The beam profiler was positioned so the length of the total beam path from the laser exit was the same to the profiler and to the sample.

**Interference Unit** The actual interference unit begins at the half-wave plate W01 (top view in Fig. 5.1, side view in Fig. 5.3). The linear polarization of the laser beam can be rotated by rotating the waveplate. The beam is then split according to its polarization at the polarizing beam splitter cube P01. Light polarized perpendicular to the table is reflected into partial beam 2 (section 20 in Fig. 5.1), while horizontally polarized light is transmitted into section 03. The transmitted beam then again passes a half-wave plate (W02), the polarization can be adjusted anew and is split again at polarizing beam splitter cube P02. The reflected part opens partial beam 1 (section 10), the transmitted part is from thereon referred to as partial beam 3 (section 31). Beams 1 and 2 undergo an adjustment of the beam path length by the set of mirrors M22, M23, M24, M25 and M12, M13, M14, M15 respectively. The mirrors M23, M24 as well as M13 and M14 are mounted on linear precision stages and can be moved in the directions of the arrows either shortening or elongating the beam path. The position accuracy of these manual stages is on the order of tens of micrometers. After section 15, 25 and 31 each partial beam again passes through half-wave plates W12, W22 and W32 respectively. The wave plates again allow an adjustment of the polarization of each individual beam. The mirrors M16, M26 and M36 are used to reflect the beams to the final set of mirrors (M17, M27, M37). Mirror M16 and M26 are needed in order to prevent shallow angles of incidences on the final set of mirrors and resulting polarization effects. Furthermore, the partial beam paths all have to undergo either an even or an odd amount of reflections in order to maintain the same beam profile at the sample<sup>1</sup>. The final set of mirrors (M17, M27, M37) are positioned in the vertices of an equilateral triangle with a side length of  $a = 250 \text{ mm}$ . The plane of the triangle is perpendicular to the laser beam before the interference setup ( $z$ -direction) and parallel to the sample surface ( $x$ - $y$  plane in Fig. 5.1, 5.3 and 5.4). The mirrors are mounted on gimbal mirror mounts which allow an independent adjustment of two rotation angles each over the full  $360^\circ$ . With the help of these mirrors, the laser beams are reunited on the sample at the interference point X at  $(x_{\text{int}}, y_{\text{int}}, z_{\text{int}})$ .

---

<sup>1</sup>Please note the reflections within the beam splitter cubes which also mirror the beam profile.

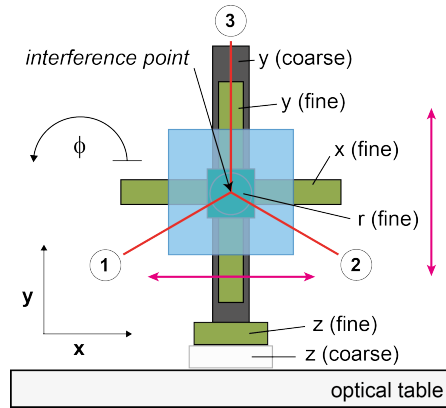


**Figure 5.4** Layout of three-beam interference setup – sample holder and possible sample movements.

**Sample Holder** The sample is mounted in the center of a manual turntable allowing for rotations around the  $z$ -direction. The turntable is mounted on a commercially available motorized *Movtec*  $x, y$  stage. The maximum travel of each of the axes is  $l_{\max} = 200$  mm. According to the data sheets a maximum speed of  $v = 90$  mm/s and a repetition accuracy of  $\Delta d < 20$   $\mu\text{m}$  is possible. However, practically these values could not be confirmed. The  $x, y$  stage is again mounted on manual sliders on a vertical profile allowing for coarse adjustments in the  $y$ -direction. The profile sits on a manual precision stage that allows micrometer exact positioning in  $z$ -direction. For coarse changes in  $z$ -direction, this precision stage is mounted on a slider on a horizontal rail. The  $z$ -rail is  $l = 2$  m long and is mounted on the optical table. This setup of the sample holder allows for motorized movements in  $x$  (fine) and  $y$  (fine) direction as well as manual movements in  $\phi$  (fine),  $y$  (coarse) and  $z$  (fine and coarse) (compare Fig. 5.4). The motorized stage was controlled via RS232 by a *Python* programming environment allowing for synchronization with laser controls which were also controlled via RS232.

### 5.1.2 Adjustment and Calibration of Laser Beam Properties

The following section offers an overview on how various laser beam properties were measured and adjusted within this specific experimental setup. For a general understanding of basic laser beam properties, please refer to Sec. 2.2.1.

**Power** Due to the beam shaping and the numerous optics to pass, the laser power at the sample ( $P_L^{\text{smp}}$ ) only made up 4.5% of the laser power at the exit of

the harmonic generator  $P_L^{\text{laser}}$ . The laser power could be adjusted by changing the Q-switch delay  $\tau_Q$  in between the triggering of the flash lamps and the Q-switch opening. Before each treatment, a reference power measurement was conducted at the sample for various Q-switch delay times. This reference measurement was then used to calculate the laser power at the sample  $P_L^{\text{smpl}}$  during the treatment. The laser power was further monitored by the in-situ power measurement. However, due to the very low laser powers in the in-situ power branch, these measurements were afflicted with high measurement uncertainties. The powers on the partial beams in dependence of the W01 and W02 wave plate orientations were calculated by the *Propagation* module (see Sec. 5.2.1). To account for the different absorptions on the partial beam paths, a reference measurement was conducted for each partial beam and the *Propagation* module was calibrated accordingly. All power measurements were averaged over  $t = 10$  s and were conducted with a repetition rate of  $f_{\text{rep}} = 20$  Hz.

**Temporal Coherence** The temporal coherence length of the laser was measured with a Michelson interferometer (see Sec. 3.1.1) and was determined to be  $\Delta l_c \approx 3$  mm. The temporal coherence is an inherent property of the laser resonator and cannot be changed. Consequently, in order to be able to obtain laser interference pattern, the pairwise differences in propagation lengths of the partial beams in the interference unit  $\Delta l_{123}$  have to be smaller than  $\Delta l_{123} < 3$  mm. By moving the stages under the mirrors M13, M14 and M23, M24, the propagation lengths of beams 1 and 2 were adjusted to match the length of beam 3.

**Beam Profile** Due to the airy pattern caused by the beam shaping (see Sec. 5.1.1), even in the sample plane, the beam profile was not purely Gaussian shaped. On the outside of the profile some small shoulders remained (see Fig. 5.2). These shoulders did not affect the actual laser treatment because even at full power only the energy in the tip of the Gaussian shape was used for the ablation. However, for the automated fitting routine within the software of the beam profiler, they can be misleading. To overcome this misinterpretation, the beam diameter for full width half maximum  $2w_{50}$  was read out and converted to the  $1/e$  value  $w$  (see Sec. 2.2.1). The diameter of the beam at the sample could be changed by moving F02. It was adjusted to the smallest value which was possible without damaging the optical components. Furthermore, the beam profile could be changed by the opening of the aperture in A01. However, for larger openings, the airy pattern disturbed the Gaussian beam profile in the sample area. It was adjusted to the largest possible opening without destroying the Gaussian beam shape at the sample.

**Beam Alignment** Apart from the beam optics, a USB camera could be mounted on the z-rail in front of the sample. With the help of a macro lens system, extension tubes and neutral density filters the camera could be used to monitor the laser beams on the sample during the processing. Even more importantly, the camera could be used to align the three beams on a dummy substrate of thoroughly scratched glass. This dummy substrate was then replaced by the sample to be treated. Likewise, the *WinCamD-LCM4* beam profile camera could be mounted vertically on the z-rail. Consequently, the beam profile camera could also be used to align the beams directly on the camera chip. However, the offset between the camera sensor, and the actual position of the sample has to be taken into account when changing the beam profile camera for the sample to be treated. With the back of the camera housing touching the sample surface, the offset was determined to be  $d_{\text{off}} = 13.8$  mm.

### 5.1.3 Setup Parameters

Once the experiment was calibrated, nine independent setup parameters could be adjusted in order to change the intensity distribution in the interference volume, and hence the resulting texture:

- The intensities  $I^{(1)}, I^{(2)}, I^{(3)}$  and consequently, the electric field amplitudes  $E_0^{(1)}, E_0^{(2)}, E_0^{(3)}$  of each partial beam could be adjusted by the Q-switch delay  $\tau_Q$  and the orientations of the half-wave plates W01 and W02.
- The polarizations angles  $\gamma^{(1)}, \gamma^{(2)}, \gamma^{(3)}$  and thus, the polarization vectors  $\hat{e}^{(1)}, \hat{e}^{(2)}, \hat{e}^{(3)}$  of the partial beams could be adjusted by the orientation of the half-wave plates W12, W22 and W32 respectively. For a desired polarization at the sample, the corresponding wave plate orientation was calculated using the *Propagation* module of the simulation software (see Sec. 5.2.1).
- The angles of incidence and thus, the wave vectors  $\mathbf{k}^{(1)}, \mathbf{k}^{(2)}, \mathbf{k}^{(3)}$  could be controlled by the rotational orientations of the mirrors M17, M27, M37 as well as the x, y, z positioning of the sample. However, these 12 parameters are constrained by the fixed positions of the mirrors M17, M27, M37, the fact that all three beams have to unite at the interference point and a common wave vector magnitude of  $k = 2\pi/\lambda_L$ . These conditions only leave three independent parameters, which can be described by the x, y and z position of the point of interference  $x_{\text{int}}, y_{\text{int}}$  and  $z_{\text{int}}$ .

These nine independent parameters (W01, W02,  $\tau_Q$ , W12, W22, W32,  $x_{\text{int}}, y_{\text{int}}, z_{\text{int}}$ ) were used to alter and adjust the laser intensity pattern in the interference volume. Throughout the thesis, they are referred to as *setup parameters*.

## 5.2 Interference Pattern

The following section focuses on the different laser intensity distributions that can be produced in the interference volume by the experimental setup. All of these intensity distributions are of periodic character and thus, are often referred to as intensity or interference pattern. In the first subsection, a way of calculating such interference patterns in dependence of the setup parameters is introduced. In the second subsection, exemplary pattern are presented and the influence of the various setup parameters on the pattern is described.

### 5.2.1 Simulate Interference Model (SINT)

In order to determine the influence of the setup parameters on the intensity pattern in the interference volume, the *SINT* model was developed and implemented. *SINT* is a numerical model implemented in the *Python* programming language. Its input are the setup parameters as described in Sec. 5.1.3. A schematic drawing of the model is depicted in Fig. 5.5. It consists of the two independent modules *Propagate* and *Interfere*. The module *Trace* is the inverse of the *Propagate* module. Each of the modules is briefly described in the following paragraphs.

**Module Propagate** The *Propagate* module translates from the setup parameters to the beam parameters. The setup parameters were directly accessible in the experimental setup (see Sec. 5.1.3). The beam parameters are the actual physical properties of each of the partial laser beams at the sample. These are the wave vectors  $\vec{k}_i$ , polarization vectors  $\hat{e}_i$  and electric field amplitudes  $E_i^0$ . The *Propagate* module mainly consists of geometrical considerations combined with calibration measurements as described in Sec. 5.1.2. It contains the exact orientations of all optical components of the interference unit and virtually propagates the laser beam by subsequent reflection and/or rotation of its propagation direction and/or polarization. Rotations and reflections of polarization and propagation vectors are carried out according to Eq. 2.27 and 2.30 respectively.

The output of the *Propagate* module is a set of beam parameters consisting of

- The electric field amplitudes  $E_0^{(1)}, E_0^{(2)}, E_0^{(3)}$  of the partial beams at the sample.
- The polarizations angles<sup>2</sup>  $\gamma^{(1)}, \gamma^{(2)}, \gamma^{(3)}$  of the partial beams at the sample.

---

<sup>2</sup>The angle  $\gamma^{(j)}$  is defined as the left-handed angle between the polarization direction  $\hat{e}^{(j)}$  of the partial laser beam  $j$  and the vector perpendicular to the propagation direction that has the smallest angle to the positive  $y$ -axis in the laboratory system.

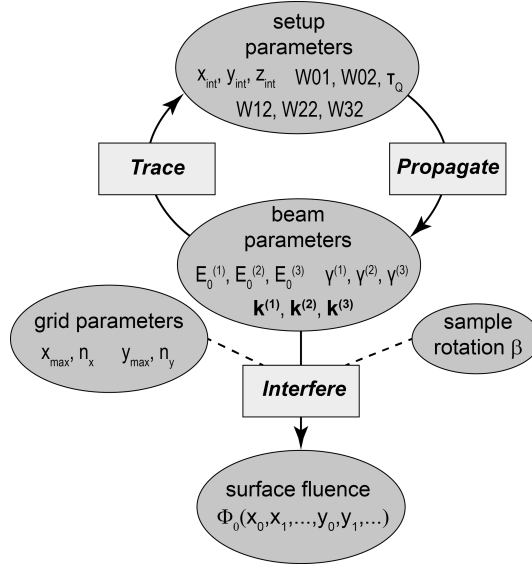


**Figure 5.5** Schematic flowchart of *SINT* model: The *SINT* model consists of the three independent modules *Propagate*, *Trace* and *Interfere*. The model can be used as a whole to calculate the expected interference pattern in the interference volume for a given set of setup parameters. Furthermore, the individual modules can be used independently e.g. to set up the experiment according to given set of beam parameters.

- The wave vectors  $\mathbf{k}^{(1)}$ ,  $\mathbf{k}^{(2)}$ ,  $\mathbf{k}^{(3)}$  of the partial beams at the sample.

The *Propagate* module can also be inversed and can be used for finding the appropriate setup parameters for any set of given beam parameters. The inverse is referred to as the *Trace* Module.

**Module Interfere** The *Interfere* module calculates the spatially resolved laser fluence distribution ( $\Phi_0(\vec{r})$ ) on the surface of the sample. Input are a set of beam parameters, the rotational orientation of the sample  $\beta$  and a set of grid parameters. Grid parameters define the spatial extension and resolution of the grid for which the fluence is calculated. The intensity distribution at the surface of the sample  $I_0(x, y, z = 0)$  is then calculated according to Eq. 2.37 and converted to a fluence distribution under the consideration of the pulse duration  $\tau_p$  so that

$$\Phi_0(x, y) = I_0(x, y)\tau_p. \quad (5.1)$$

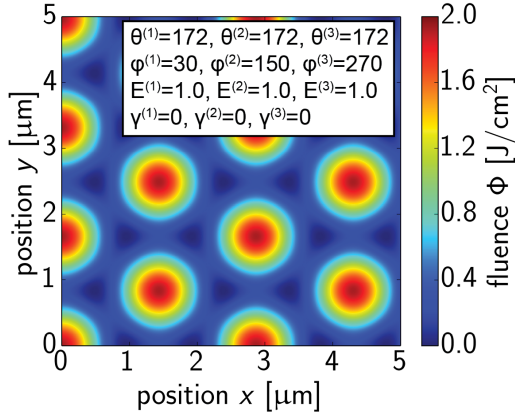


**Figure 5.6** Exemplary interference pattern: This pattern can be created by three laser beams with equal intensity  $E_0^{(j)} = 1$  for  $j = 1, 2, 3$ , aligned polarization  $\gamma^{(j)} = 0^\circ$  for  $j = 1, 2, 3$ , equal polar angle of incidence  $\theta^{(j)} = 172^\circ$  for  $j = 1, 2, 3$  and equiangular distance in between the azimuth angles of incidence  $\varphi^{(1)} = 30^\circ$ ,  $\varphi^{(2)} = 150^\circ$ ,  $\varphi^{(3)} = 270^\circ$ . The fluence distribution is of clear periodic character with periodicities of  $\Lambda_A = \Lambda_B = 1.64 \mu\text{m}$  along the main axes of the hexagonal lattice. This pattern is used as a reference for the subsequent investigation of beam property influences.

As an alternative to input grid parameters, a set of grid parameters can also be determined automatically to form a unit cell of the grid. The fluence distribution is analyzed for its periodicity ( $\Lambda_x$ ) and the spatial extensions ( $x_{\text{max}}$ ) of the grid is set to equal  $x_{\text{max}} = n \cdot \Lambda_x$  for each dimension<sup>3</sup>. The resulting fluence distribution on such a grid has periodic boundary conditions. This type of grid parameters is referred to as *unit grid*. The spatial resolution in the unit grid is then calculated according to a given minimal resolution and the constraint of  $2^n n \in \mathbb{N}$  pixels along each axis to allow further processing with Fast Fourier Transform (FFT) algorithms.

## 5.2.2 Exemplary Pattern

In the following section, exemplary fluence distributions are presented. Due to their periodic character, the fluence distributions are also referred to as interference pattern. Starting from an arbitrarily chosen reference pattern (depicted in Fig.

<sup>3</sup> $n \in \mathbb{N}$  can be determined by the user.

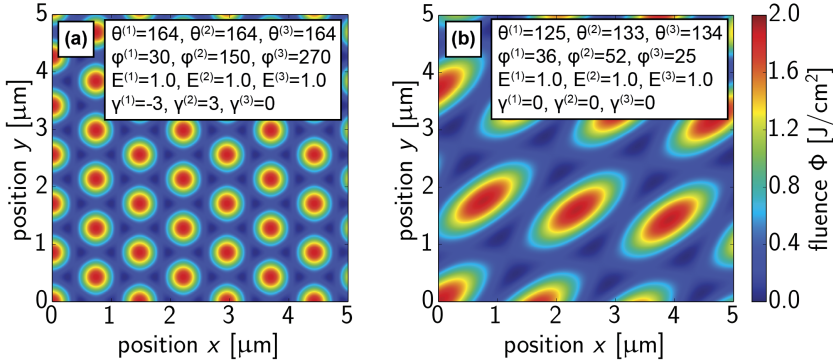


**Figure 5.7** Variation of angles of incidence (calculated interference patterns): By changing the polar  $\theta^{(i)}$  and azimuth angles  $\varphi^{(i)}$  of the interfering beams, the periodicity of the interference pattern as well as the orientation of the main axes of symmetry can be altered. (a) A smaller mutual polar angle  $\theta_{\text{int}} = 164^\circ$  but unchanged azimuth angles leads to an interference pattern which resembles the pattern in Fig. 5.6 but has a smaller periodicity  $\Lambda_{A,B} < 1.64 \mu\text{m}$  along both main lattice axes. (b) By individually changing the polar and azimuth angles, the orientation of the lattice axes as well as the periodicities along these axes can be changed individually ( $\Lambda_A \neq \Lambda_B$ ). The resulting interference pattern appears to be stretched compared to the reference texture in Fig. 5.6.

5.6), in each of the following paragraphs one beam property is changed while leaving the other beam properties unchanged. The according changes in the interference patterns are demonstrated and discussed.

**Angles of Incidence** The angles of incidence of the three partial beams on the surface of the sample are reflected in the wave vectors of the partial beams  $\mathbf{k}^{(i)}$  and can be adjusted in the experimental setup by changing the position of the interference point  $X$  at  $(x_{\text{int}}, y_{\text{int}}, z_{\text{int}})$ . If  $x_{\text{int}} = y_{\text{int}} = 0$ , the wave vectors of all three partial beams share a common polar angle  $\theta^{(j)} = \theta_{\text{int}}$ ,  $j = 1, 2, 3$  (compare Fig. 5.1, 5.3 and 5.4 for coordinate system). This is due to the triangular positioning of the final set of mirrors. The size of  $\theta_{\text{int}}$  can be altered mutually by changing the  $z$ -position of the interference point. For smaller values of  $z_{\text{int}}$  (towards the final set of mirrors)  $\theta_{\text{int}}$  lessens (more shallow incidence), whereas for larger values of  $z_{\text{int}}$ ,  $\theta_{\text{int}}$  augments (steeper incidence). The angle  $\theta_{\text{int}}$  influences the angle in between each pair of partial laser beams and hence, the properties of the interference pattern. Varying  $\theta_{\text{int}}$  changes the periodicity of the interference

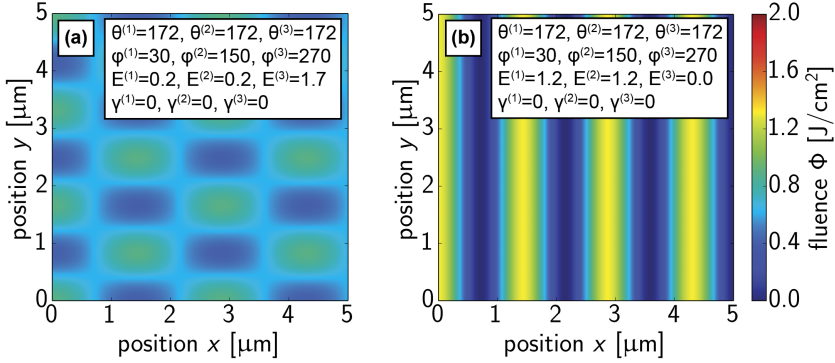


**Figure 5.8** Variation of electrical field amplitudes (calculated interference patterns): By individually varying the electrical field amplitudes, the general morphology of the interference pattern can be changed. (a) Augmenting the electrical field in one partial beam by an order of magnitude ( $E_0^{(3)} = 10 \cdot E_0^{(j)}$ ,  $j = 1, 2$ ) while leaving the overall power unchanged, leads to a check-board like pattern. (b) If the same total power is distributed to only two partial beams ( $E_0^{(3)} = 0$ ), the resulting interference pattern is of line-like character.

pattern. Smaller values of  $\theta_{\text{int}}$  lead to smaller periodicities  $\Lambda$ , whereas larger  $\theta_{\text{int}}$  lead to larger  $\Lambda$ . The overall shape of the pattern remains the same (compare Fig. 5.6 and 5.7 (a)).

By changing  $x_{\text{int}}$  and  $y_{\text{int}}$  to nonzero values, the polar angles of incidence of the individual beams  $\theta^{(i)}$  are altered individually. Furthermore, also the individual azimuth angles  $\varphi^{(j)}$  are influenced. For the interference pattern this translated to a stretching of the pattern. The main axes of symmetry change orientation and the spatial periodicities along these axes also differs. An exemplary interference pattern is demonstrated in Fig. 5.7 (b).

**Power** The total power of the laser beams is reflected in the sum of the squared electric field amplitudes ( $P_L \propto \sum_i E_0^2$ ) and can be controlled by adjusting the q-switch delay time  $\tau_Q$ . The total laser power is distributed to the partial beams according to the orientation of the wave plates W01 and W02 (see Fig. 5.1). Augmenting the total laser power results in a total increase of the fluence in the interference pattern. However, the morphology of the fluence distribution remains unchanged. By independently changing the individual electric field

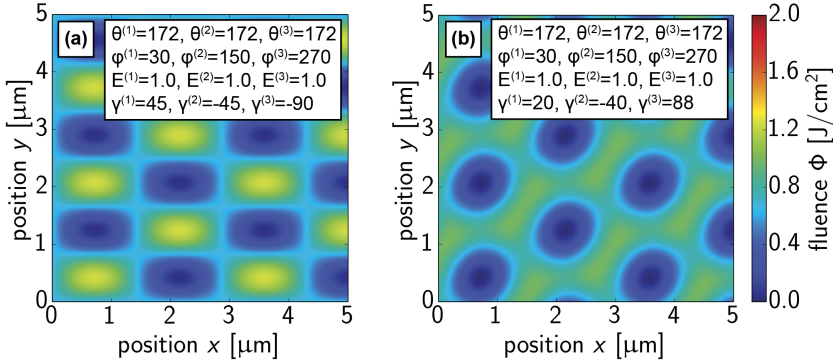


**Figure 5.9** Variation of polarization (calculated interference patterns): By changing the polarization of the individual beams, the pairwise possibility to interfere can be controlled. Only beams with partially aligned polarization can interfere. (a) By omitting the interference of beam 1 and 2 by adjusting perpendicular polarization ( $\gamma^{(1)} \perp \gamma^{(2)}$ ), a check-board like pattern with higher contrast than in Fig. 5.8 (a) can be created. (b) Example of another pattern produced by partially aligned polarizations of individual beams.

amplitudes  $E_0^{(j)}$  a variety of interference pattern can be produced<sup>4</sup>. Two exemplary interference pattern obtained by disparate laser intensities are presented in Fig. 5.8. Augmenting the laser intensity of one partial beam leads to a check board-like interference pattern. A vanishing intensity in one partial beam leads to a line-like pattern as observed with the two-beam interference setup.

**Polarizations** The polarization orientation of the linear polarized partial beams are reflected in the polarization angles  $\gamma^{(j)}$  and can be controlled by the orientation of the half-wave plates W12, W22 and W32. Two laser beams only interfere if a component of their polarization is aligned. Perpendicular polarizations lead to a flat fluence distribution without any interference pattern. Consequently, it can be controlled which of the partial beams interfere and to what extend by adjusting the individual polarizations. However, due to the geometry of the setup, the pairwise alignment can not be adjusted independently. An example of partially aligned polarization in beam 1 and 3 as well as 2 and 3, and perpendicular polarization in beam 1 and 2 can be observed in Fig. 5.9 (a). The perpendicular polarization of beam 1 and 2 omits interference in between the two beams. The resulting pattern

<sup>4</sup>For reasons of simplicity, the electric field amplitudes have been normalized. However, to maintain comparability, all quantified electric field amplitudes are normalized by the same factor.

is a check-board like pattern which is similar in appearance to the pattern in Fig. 5.8 (b) which was also produced with a suppressed interference of beam 1 and 2 due to the higher power in beam 3. It can be further observed that the contrast of the polarization controlled pattern is higher than the one in the pattern induced by disparate partial intensities.

However, by changing the individual polarizations, many more interference patterns can be created. Another example can be observed in Fig. 5.9 (b).

**Other Adjustments** Apart from the beam parameters mentioned above, the interference pattern can also be altered by other adjustments of the experimental setup.

- The sample can be tilted to produce different fluence distributions on the sample surface. However, this has not been investigated in this thesis.
- The sample can be rotated. Nevertheless, the induced pattern changes by rotation do not matter for the application as light trapping device.
- The fluence distribution on the sample can be changed by varying the length of the individual beam paths. Such changes, however, only diminish the effective coherence length and lead to less contrast in the fluence distribution. Small contrast is generally not of interest for producing textures with high aspect ratios. Consequently, the length of the beam paths were adjusted to produce the highest possible contrast and were not used for further influencing the interference pattern.

**Variety of Interference Pattern** Each of the pattern presented in this section is a mere example for one specific change of one single beam property. However, each beam parameter can be adjusted continuously and a change can be arbitrarily combined with a change of any of the other eight independent parameters. Accordingly, the variety of producible intensity pattern is very large.

**Conclusion** The experimental setup is capable of producing a large variety of interference pattern. By variation of the nine independent setup parameters, the fluence distribution within the interference volume can be deliberately controlled and shaped. The influence of each of the parameters can be modeled by the *SINT* model and the fluence distribution for a given set of parameters can be calculated. Due to the large number of independent parameters, there is a large variety of possible fluence distributions.

## 5.3 Surfaces Textures

As demonstrated in the previous section, a large variety of intensity patterns can be created in the interference volume. However, it remains to be examined if the large variety of intensity patterns can also be translated into a variety of possible surface textures. The following section focuses on the producible textures and their correlation with the intensity pattern. In the first subsection, a typical DLIP-processed sample is analyzed, the second subsection deals with the correlation of fluences and textures and the control of texture properties, whereas the third subsection examines the ablation mechanism and the underlying physical processes.

**Single Pulse Processing from Film Side** Due to the microscopic scales of the texture periodicities and the complexity of the setup, multi-pulse processing was avoided. Sub-micrometer scale movements of the optical components along with a slight beam pointing instability of the laser system prohibited a phase constant reproduction of the interference patterns. The fluence distribution of a second laser pulse was uncontrollably shifted in  $x$  and/or  $y$ , so multi-pulse processing lead to unpredictable double textures. Furthermore, the processing through the glass side of the sample did not reveal promising results. Low powers lead to no texturing effects, whereas for higher powers, the whole ZnO:Al film in the laser treated area detached. Consequently, all laser treatments were carried out with single laser pulses incident from the film side of the ZnO:Al substrates.

### 5.3.1 General Features of DLIP Textures

After the calibration and adjustment of the experimental setup (see Sec. 5.1.2), it can be used for the treatment of ZnO:Al. Bringing a ZnO:Al sample into the interference volume and treating it with a single laser pulse results in a small treated area on the sample surface which is referred to as the laser spot.

**Optical Appearance** The radius of the laser spot depends on the setup parameters, but is on the order of  $r_s \approx 0.5$  mm. To the eye, the laser spot shimmers in various colors depending on the angle of the surface to the light (Fig. 5.10 (a)). This is due to the periodic texture within the spot which diffracts light into different angles depending on its wavelength. In the optical microscope at low magnification ( $M = 5$ ), a circular brownish spot can be observed (Fig. 5.10 (b)). The darker color within the spot suggests that the illumination light of the microscope is scattered, and compared to smooth surfaces, less light is reflected

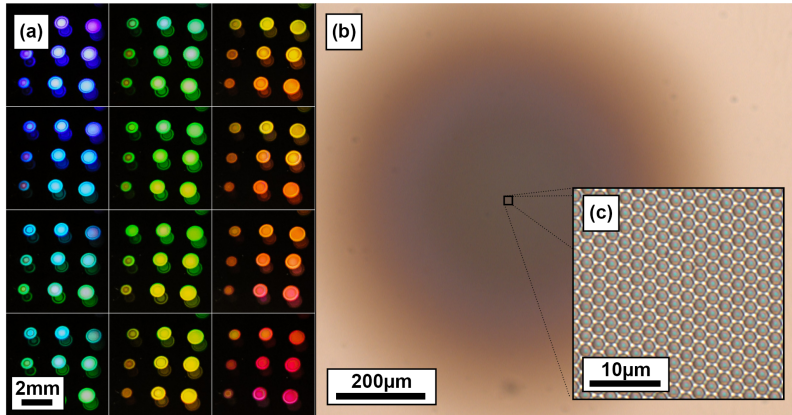


**Figure 5.10** Optical appearance of DLIP processed sample: (a) Photographs of laser spots. Due to the wavelength-dependent diffraction at the periodic texture, the laser spots shimmer in different colors depending on the angle of illumination. (b) Image of optical microscope at low magnification  $M = 5$ . Due to the scattering of the microscope's illuminating light, the laser spot appears darker than the surrounding areas. (c) Image of optical microscope at high magnification  $M = 100$ . Only at high magnifications the hexagonal periodic texture itself can be detected with the optical microscope.

back into the objective lens. Only for high magnifications ( $M = 100$ ), the actual periodic texture becomes apparent (Fig. 5.10 (c)).

**Homogeneity** The texture is strictly periodic and extends homogeneously over a large amount of periods. However, due to the Gaussian beam shape (compare Sec. 2.2.1), the fluence is not distributed evenly in the entire spot. From the center to the borders of the spot, the fluence and hence, the depth of texture lessens. Nevertheless, the periodicity of the texture remains constant within the whole area of the laser spot. The investigations in this section only focus on texture measurements at the center of the laser spot for the following reasons: On the one hand, the spatial variation in a Gaussian fluence distribution is minimal at the center. On the other hand, the center of the laser spot is easy to detect when characterizing the samples. Consequently, by focusing on textures in the center of the laser spot, the experimental error in correlating texture and fluence is minimized. The challenge of achieving homogeneous textures over larger distances is dealt with in the following chapter (Sec. 6.1.1).

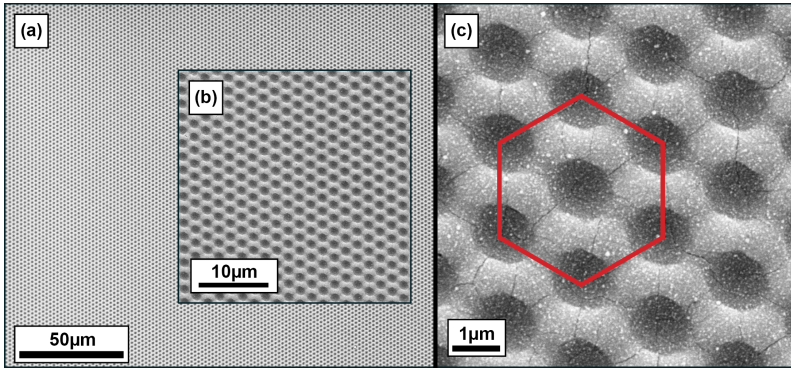


**Figure 5.11** Homogeneity and hexagonal periodic character of DLIP texture (SEM images): (a) Up to single hundreds of micrometers, the surface texture of DLIP treated ZnO:Al samples (b) is very homogeneous. (c) By high magnification, the hexagonal character of the texture becomes apparent.

**Detail** To further investigate the details of the produced texture, SEM imaging was used. An image of the center of the laser spot underlines the strict periodic character and the homogeneity of the texture over microscopic large areas on the order of single hundreds of micrometers (Fig. 5.11 (a)). Please keep in mind, that the features are not individual laser spots, but much smaller features within one single laser spot. With an approximate spot size of  $A_s = 0.8 \text{ mm}^2$  and a feature size of  $A_{\text{feat}} = 2.5 \text{ } \mu\text{m}^2$  more than 300 000 features can be created with one single laser pulse. With higher magnifications, the hexagonal lattice of the texture becomes even more obvious (Fig. 5.11 (b)). The darker and lighter areas correspond to concave dips and convex bulges respectively. Apart from the texture itself, small cracks in the ZnO:Al as well as some redeposited debris can be observed.

**Conclusion** With single-shot laser treatments from the film side, very homogeneous periodic surface textures can be created. By one single laser pulse, the area of  $A_s \approx 0.8 \text{ mm}^2$  can be covered with more than 300 000 features. Within that area the texture depth differs, but the lattice and its spatial periodicity are constant. The textured areas appear to shimmer so the feature sizes of the textures are small and deep enough to diffract visible light. Consequently, the textured surfaces show the potential to be used for light trapping.

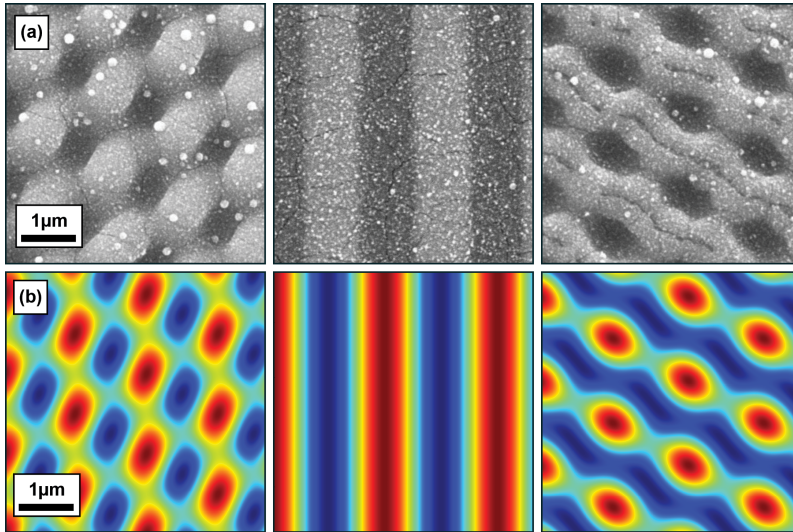


**Figure 5.12** Comparison of fluence and texture for exemplary interference patterns ((a) SEM images of DLIP-textured surfaces and (b) corresponding calculated fluence distributions): The general shape of the fluence distributions is reflected in the DLIP-textured surface topographies.

### 5.3.2 Control of Texture

In order to adapt the DLIP textures to the application in solar cells, the topography of the laser-treated samples has to be control and adjustable. In the following section, exemplary fluence distributions and their corresponding surface topographies are compared and correlated. It is then investigated if the fundamental texture properties of depth and spatial periodicity can be controlled and adjusted deliberately.

**Correlation of Texture and Fluence** By varying the setup parameters, the fluence distributions within the interference volume can be changed and controlled. To investigate how these changes translate into a resulting texture, a comparison of SEM images of DLIP textures with their corresponding texture calculated fluence distribution is presented in Fig. 5.12. It can be observed that the general geometry of the texture shows a good correlation with the calculated fluence. The spatial periodicities of the measured textures match the periodicities in the fluence distribution. Furthermore, the symmetry of the lattice unit cell of the different pattern is the same for fluence and topography.

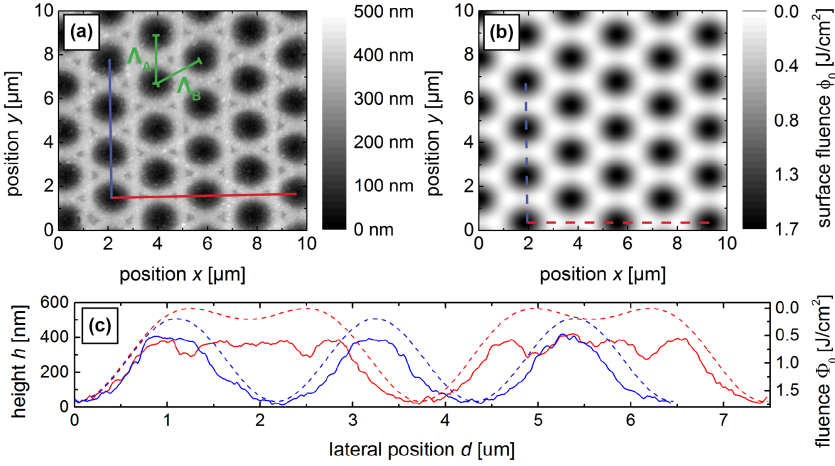


**Figure 5.13** Comparison of fluence and texture – profiles: (a) AFM measurement of DLIP-textured surface, (b) inverse of corresponding fluence distribution and (c) profile measurements along the marked lines. While the general shape of topography and fluence distribution is very similar, the detailed texture within a lattice unit cell differs from the fluence distribution.

In order to quantify the topography of the DLIP textures, AFM scans were conducted on selected samples. The obtained topography of an exemplary texture can be observed in Fig. 5.13 (a). Referenced to the highest parts of the texture, the dips are approx.  $h \approx 380$  nm deep. The periodicity along the two main axes of the hexagonal lattice are  $\Lambda_A = \Lambda_B = 2.14 \mu\text{m}$ . Fig. 5.13 (b) shows the corresponding fluence distribution obtained by *SINT*. The lateral periodicities of the pattern are perfectly reproduced. Furthermore, the general shape of the topography of the lattice unit cell is also reproduced. However, the fine topography within the unit cell does not match the inverse of the fluence distribution. This becomes especially apparent when comparing a height profile of the measurement with a calculated fluence profile (Fig. 5.13 (c)). The differences in between fluence distribution and texture are due to the fact that the process of laser ablation is a complex process which is influenced by various factors. In Sec. 5.3.3 the process is investigated in more detail whereas in Sec. 5.4.1 a simple ablation model is derived which accounts for the main driving forces of the ablation process. However, in the following paragraphs the deliberate control of texture properties is examined first.

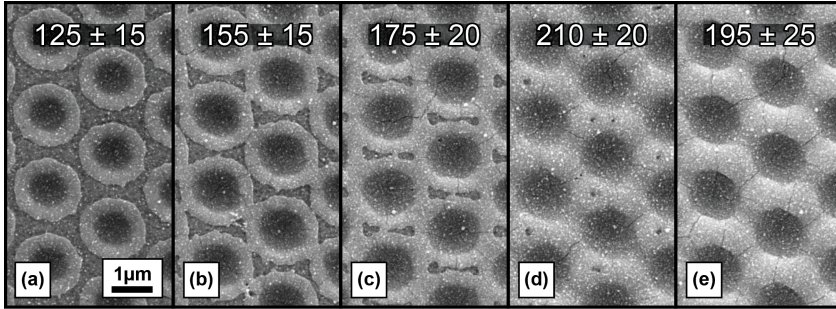


**Figure 5.14** Control of texture depth (SEM images): Textures created with equal setup parameters but varying total laser power  $P_L$ . The depicted numbers are the depth of the texture in nanometers. Applied powers: (a)  $P_L = 93$  mW, (b)  $P_L = 107$  mW, (c)  $P_L = 126$  mW, (d)  $P_L = 150$  mW, (e)  $P_L = 171$  mW. Low laser powers leave untextured areas in between the dipo. With augmenting laser power, the untextured areas vanish and the texture depth rises.

**Control of Texture Depth** In order to investigate the dependence of total laser power and texture depth, a series of textures with different laser powers was produced. The textures were characterized by AFM and their texture depth  $h$  was determined<sup>5</sup>. As can be observed in Fig. 5.14, the depth of the texture can be controlled by changing the overall incident laser power. With augmenting laser power, the depth of the texture augments. However, the dependence of texture depth to incident laser power is not linear and for high powers there seems to be a saturation effect. Furthermore, it can be observed that at low powers the surface area in between the hexagonally located dipo remains untreated (Fig. 5.14 (a) and (b)). In these areas the laser fluence does not suffice for melting or ablation of the ZnO:Al. With augmenting power, the untreated area lessens until it completely disappears (here at approx.  $P_L = 150$  mW in Fig. 5.14 (d)). Moreover, it can be observed that for even higher incident laser powers, more micro-cracks appear in the treated areas.

**Control of Texture Periodicity** As described in Sec. 5.2.2, the periodicity of the fluence pattern can be controlled by changing the angles of incidence of the

<sup>5</sup>The depth of a texture is defined as the difference in height in between the highest parts of the texture and the lowest. Particles or other redeposited debris are not taken into account. Due to measurements artifacts as well as debris, the measurements have to be treated with caution. The stated errors were determined by estimating an uncertainty according to the general quality of the given measurement as well as multiple measurements of the same texture. Potential systematical errors are not included in the measurement uncertainties.

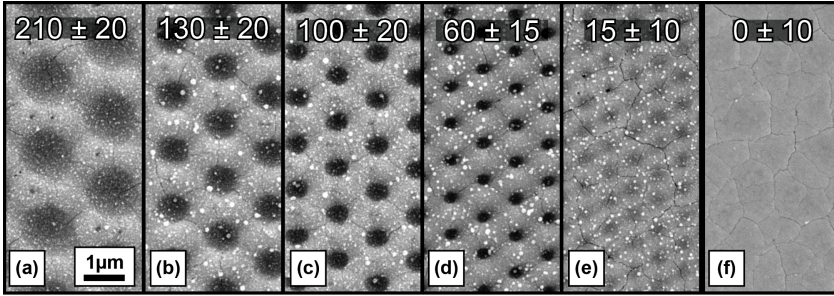


**Figure 5.15** Control of texture periodicity (SEM images): Textures created with equal setup parameters but different mutual polar angle of incidence  $\theta_{\text{int}}$ . The depicted numbers are the depth of the texture in nanometers. The nominal periodicities of the calculated corresponding fluence distributions were: (a)  $\Lambda_{A,B} = 2 \mu\text{m}$ , (b)  $\Lambda_{A,B} = 1.5 \mu\text{m}$ , (c)  $\Lambda_{A,B} = 1.25 \mu\text{m}$ , (d)  $\Lambda_{A,B} = 1 \mu\text{m}$ , (e)  $\Lambda_{A,B} = 0.75 \mu\text{m}$  and (f)  $\Lambda_{A,B} = 0.5 \mu\text{m}$ . The nominal periodicities are perfectly reproduced in the textured surfaces. However, towards smaller periodicities the depth of the texture lessens and particles and micro-cracks augment.

interfering beams. In Fig. 5.15 a series of SEM images of textured ZnO:Al surfaces is depicted. These textures result from patterning with a series of fluence distributions with varying spatial periodicities of the hexagonal lattice  $\Lambda_{A,B}$ . It can be observed that the nominal periodicities of the fluence distributions is perfectly reproduced in the textures. However, it can be further observed that for smaller periodicity the depth of the textures decreases. At a periodicity of  $\Lambda \approx 500 \text{ nm}$  (Fig. 5.15 (f)) the texture completely vanishes. Furthermore, small spherical particles on top of the textured surface were detected in some of the textures. Apart from the texture with the smallest periodicity, the amount of particles augments towards textures with smaller periodicities. Similarly, the amount of micro-crack-formation in the ZnO:Al layer rises for smaller periodicities.

**Conclusion** Judging from the observations in the preceding paragraphs, the producible texture can be influenced by changing the setup parameters and hence, the fluence distribution within the interference volume. To a certain extend, it is possible to deliberately control texture properties like depth or periodicity. However, the calculable fluence distribution is not perfectly proportional to the resulting texture and cannot be used directly to predict the resulting topography. Effects like untextured areas, the vanishing of the texture for smaller periods or a nonlinear increase of texture depth with rising laser power are not reflected by

the simple assumption of a fluence proportional topography. In order to be able to understand and also to possibly predict such effects, an investigation of the ablation process is required.

### 5.3.3 Ablation Process

The following section tries to draw a picture of a possible ablation process. Based on the observations made in the previous section, assumptions about the physical principles and processes underlying the ablation process are made. These assumptions are then used in the following section to develop a model for the ablation process.

**Untreated Areas** The untreated areas in between the dents of the textures were mainly observed at low laser power (e.g. Fig. 5.14 (a)). It can be assumed that a minimum threshold fluence is needed to start the ablation process. At low laser power the fluence in between the dents is insufficient to trigger the ablation so the surface remains untreated.

**Non-linear Depth-Power Dependence** The non-linear dependence of texture depth and laser power as observed in Fig. 5.14 can be explained by the non-linear absorption behavior of laser light in matter (see Sec. 2.2.2). As the laser light intensity decays exponentially, also the deposited energy follows an exponential decay along the z-direction into the material. This, as well as heat diffusion in z-direction are assumed to be the cause for the non-linear power-depth dependence.

**Vanishing Small Periodicities** The diminishing of texture depth towards smaller periodicities (see Fig. 5.15) can possibly be explained by heat diffusion in x, y and z-direction. Fig. 5.16 (a) illustrates the assumed heat diffusion and resulting ablation processes. The dashed red line represents the laser fluence distribution which initially heats the material in the red shaded areas. However, the heat diffuses into the material in all directions. The characteristic length  $l_0$  describes the order of magnitude of the heat diffusion. Due to the heat transfer, more material than the red shaded area is heated sufficiently to be ablated. The solid black line represents the surface topography after the ablation. It is assumed that  $l_0$  only depends on the material and laser properties. Consequently, for smaller periodicities (see Fig. 5.16 (b)), the diffusion suffices to heat more material in between the dents above the critical ablation temperature. As a result, the texture depth  $h$  lessens.

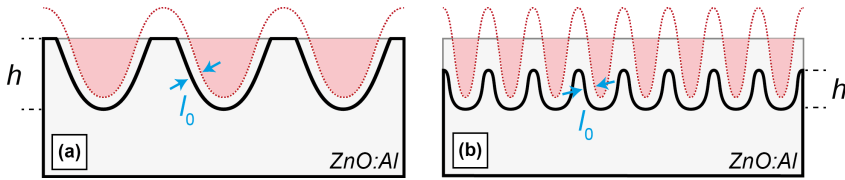


**Figure 5.16** Heat diffusion within material and lessening of texture depths for small spatial periodicities (illustration): The dashed red line represents the laser fluence, which heats the red shaded areas. The heat diffuses a typical length  $l_0$  into the material. The resulting topography after the ablation is represented by the solid black line. For constant  $l_0$  and equal laser power, the resulting texture depth  $h$  is less for (b) smaller periodicities than for (a) larger periodicities.

**Bulges** In some of the textures circular bulges around the dents of the texture were observed (e.g. Fig. 5.14 (a) and (b)). It is assumed that these bulges are molten and resolidificated ZnO:Al. During the laser process, some material is heated above the melting temperature<sup>6</sup> (light red shaded area in Fig. 5.17 (a)) and some material is heated above the boiling temperature (dark red shaded area in Fig. 5.17 (a)). In the next step, two effects can be the reason for the bulging. On the one hand the sudden evaporation of the material in the center of the dent leads to high pressures, and thus, the surrounding liquid material is pushed towards the outside (small black arrows in Fig. 5.17 (a)). On the other hand, even without evaporation there is a force pulling the liquid ZnO:Al to the outside. Due to the heat gradient from inside to outside, there is also gradient in surface tension. This gradient in surface tension leads to a convective flux (blue arrows in Fig. 5.17 (b)) which is also known as Marangoni convection [5, 80] and has been observed for many materials during laser processing [7, 22, 99]. After the liquid ZnO:Al is pulled and/or pushed towards the outside of the dent, it is cooled down, resolidificates and creates bulges (Fig. 5.17 (c)).

In order to find out if a layer of molten and resolidificated ZnO:Al exists, one of the samples was cut by a Focused Ion Beam (FIB) and then investigated by SEM imaging. It can be observed that the micro-crystalline structure of the ZnO:Al is disturbed in a small layer right underneath the surface (see Fig. 5.18). It is assumed that this approx 65 nm thick layer consists of resolidificated ZnO:Al which rapidly congealed in an almost amorphous structure.

<sup>6</sup>At room temperature and atmospheric pressure crystalline ZnO is known to sublimate [3]. However, the observations by SEM strongly suggest that there is a melting process involved at the very high temperatures and pressures during the laser treatment [40, 96].

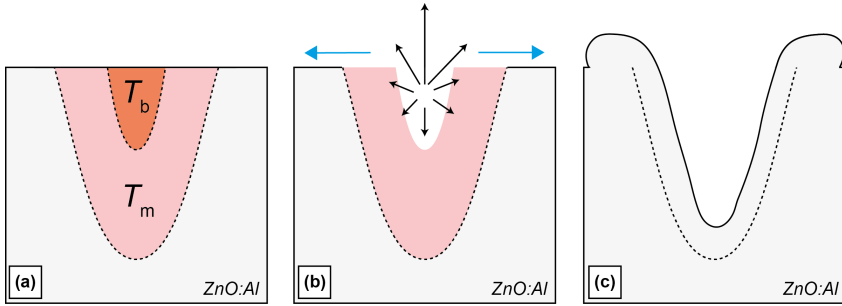


**Figure 5.17** Bulging of ZnO:Al (illustration of possible ablation process): (a) The light red shaded area is heated above the melting temperature  $T_m$ , the dark red area is heated above the boiling temperature  $T_b$ . (b) The sudden evaporation leads to high pressures on the molten ZnO:Al (black arrows). A gradient in surface tension due to the temperature gradient also leads to convection of molten ZnO:Al along the surface to the outside (blue arrows). These two forces lead to (c) the bulging of ZnO:Al in the perimeter of the dents.

**Micro Cracks** The micro cracks can mainly be observed for medium to high laser powers (Fig. 5.14 (d) and (e)) in areas of previously molten ZnO:Al. It is assumed that during the cooling of the liquid ZnO:Al and its resolidification, stress is built up within the previously melted layer. If the stress is too high, micro cracks occur to relieve the stress.

**Particles** Particles on the sample surface were mainly observed for high laser powers and wherever the whole sample was covered by a melt layer and no untreated areas within the dents remained. These particles are believed to be molten ZnO:Al that was propelled away from the surface due to the sudden evaporation and the resulting high pressures (see Fig. 5.17 (b)). In the air, the material then resolidifies to spherical particles and drops back onto the surface. The higher the laser power, the more material is melted and evaporated and thus more particles are created. The effect is assumed to be especially pronounced, if the laser power is high enough so the bulges of two adjacent dents unify. Then larger amounts of molten ZnO:Al are propelled into the air and more particles are formed. X-ray Diffraction (XRD) measurements were conducted on particle covered surfaces and revealed the particles to be micro-crystalline ZnO:Al with arbitrary orientation, which underlines the assumption.

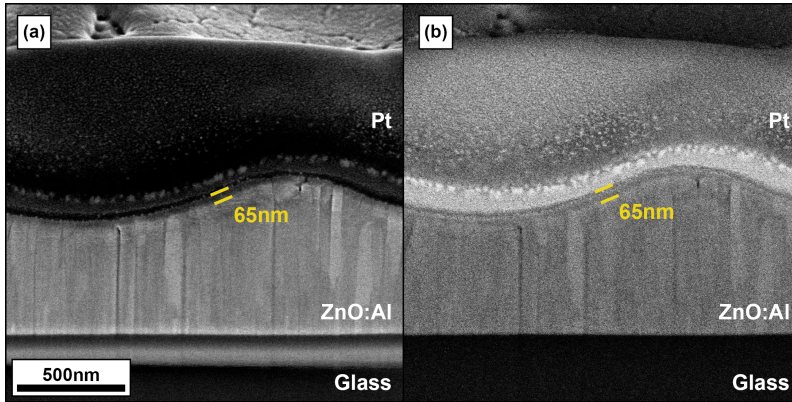


**Figure 5.18** Layer of molten and resolidificated ZnO:Al (SEM image after FIB cut, (a) secondary electron detector, (b) back scattering electron detector): In a thin layer right underneath the surface, the micro-crystalline structure of the ZnO:Al is disturbed. It is assumed that this is due to rapid congealing of the ZnO:Al to an almost amorphous phase. As a preparation for the FIB treatment the samples were covered with a platinum layer (black and light gray in (a) and (b) respectively).

**Conclusion** It is assumed that by the laser treatment, an intensity dependent heat distribution is induced into the material. The heat spreads within the material so the temperature distribution changes. Insufficiently heated areas remain untreated, whereas ZnO:Al in areas of higher temperature is melted or vaporized. Some of the molten ZnO:Al is propelled away from the surface to form particles which then redeposit on the surface. The remaining molten ZnO:Al eventually forms a thin layer of resolidificated material with bulges and micro-cracks.

It is presumed that in order to limit particle formation, excess energy deposition must be avoided. It is further assumed that the lateral heat diffusion is the cause for the vanishing of small periodicities. To further quantify this effect, a more detailed model for the energy deposition, heat diffusion and consequent ablation is developed in the next section.

## 5.4 Modeling Ablation

In the previous section it was observed that the produced texture correlates with the calculable fluence distribution. However, it is not possible to predict the resulting texture from a given fluence distribution. This section focuses on deriving a model for the ablation process which allows the computation of an expected surface topography for a given fluence distribution. To adapt the model for the use with ZnO:Al, characteristic material properties needed for the simulation are determined by a comparison with experimental data. After the determination of the material properties, the model for the ablation is combined with the *SINT* model (see Sec. 5.2.1) to form a complete model for Virtual Laser Interference Patterning (VLIP). This *VLIP* model is then used to predict the expected surface topography for a given set of setup parameters. Finally, the virtual textures computed by *VLIP* are compared to real textures created by DLIP.

### 5.4.1 Ablation Model

The model for the laser ablation aims to predict the expected topography  $h(\vec{r})$  of the sample after the laser treatment by modeling the ablation process. It is based on a highly simplified model of the laser-material interaction during the ablation process. Input to the model is the spatially resolved fluence distribution on the sample surface ( $\Phi_0(x, y)$ ) and an optional input topography to allow modeling of texture superpositions by multiple laser treatments.

For reasons of better understanding, first, the basic idea of the model is described by deriving a simplified model which does not take into account heat diffusion within the material. In the following section, the complete model including heat diffusion is derived and described.

### Ablation without Heat Diffusion

**Theory** In Sec. 4.5 a first and very simple model for the ablation was presented. The topography was assumed to be proportional to the inverse of the laser fluence:

$$z(x, y) = -a \cdot \Phi_0(x, y). \quad (5.2)$$

With  $a$  being a fit parameter.

To refine and improve the model, the exponential attenuation of the incoming laser light and the existence of a threshold fluence needs to be taken into account. To incorporate these effects, it is assumed that all material heated above a certain threshold temperature  $T_{\text{th}}$  is removed while material below that temperature

remains unchanged. Furthermore, it is assumed that the energy of one laser pulse  $E_p$  is deposited instantly.

The consequent change in volumetric energy density  $\Delta\varepsilon$  in the material before and after the laser pulse can then be expressed by

$$\Delta\varepsilon = \omega\tau_p \quad (5.3)$$

with the absorbed volumetric power density  $\omega$  and the pulse duration  $\tau_p$ . The change in power density within the material is related to the incident laser intensity as derived in Sec. 2.2.2. Applying Eq. 5.1 and Eq. 5.3 on Eq. 2.45<sup>7</sup> and introducing the fluence distribution within the material

$$\Phi(x, y, z) = \Phi_0(x, y)e^{\alpha z} \quad (5.4)$$

yields

$$\Delta\varepsilon(x, y, z) = \tau_p\alpha I_0(x, y)e^{\alpha z} = \alpha\Phi_0(x, y)e^{\alpha z} = \alpha\Phi(x, y, z). \quad (5.5)$$

Assuming a temperature independent isobaric mass heat capacity  $c_p$  and mass density  $\rho$ , the temperature change in the volume of the material can be expressed by

$$\Delta T(x, y, z) = \frac{\alpha}{\rho c_p}\Phi_0(x, y)e^{\alpha z}. \quad (5.6)$$

It is now assumed that all material heated above the critical temperature difference  $\Delta T_{th}$  is removed, while cooler material remains untouched. Consequently, the surface of the sample after the laser treatment is identical to an isothermal surface of the temperature distribution within the material. Even without explicit knowledge of  $\Delta T_{th}$  its isothermal surface can be expressed by rearranging Eq. 5.6 to

$$z(x, y, \Delta T_{th}) = \frac{1}{\alpha} \ln \left( \frac{\rho c_p}{\alpha} \frac{\Delta T_{th}}{\Phi_0(x, y)} \right). \quad (5.7)$$

The critical temperature change  $\Delta T_{th}$  can also be expressed by a critical change in volumetric energy density  $\Delta\varepsilon_{th}$  or the corresponding critical threshold fluence  $\Phi_{th}$  within the material (Eq. 5.5):

$$\Delta T_{th} = \frac{\Delta\varepsilon_{th}}{\rho c_p} = \frac{\alpha}{\rho c_p}\Phi_{th}. \quad (5.8)$$

---

<sup>7</sup>Please note that the spatial coordinate  $z$  is negative within the sample and zero at the surface. Also compare the coordinates in Fig. 5.1 for orientation.

Consequently, by inserting Eq. 5.8 into Eq. 5.7 the resulting topography  $h(x, y)$  can be described in dependence of the laser fluence at the surface of the sample  $\Phi_0(x, y)$  :

$$h(x, y) = -\frac{1}{\alpha} \cdot \ln \left( \frac{\Phi_0(x, y)}{\Phi_{\text{th}}} \right) \quad \forall \Phi_0(x, y) \geq \Phi_{\text{th}} \quad (5.9)$$

$$h(x, y) = 0 \quad \forall \Phi_0(x, y) < \Phi_{\text{th}}. \quad (5.10)$$

For insufficient surface fluence  $\Phi_0(x, y) < \Phi_{\text{th}}$ , no ablation takes place.

## Ablation with Heat Diffusion

**Theory** To extend the model and take into account heat diffusion effect within the sample, the homogeneous heat equation (see Sec. 2.2.2) is used. It describes the heat distribution within a material after the heat was initially deposited at  $t = 0$ . It is assumed that all of the energy of one laser pulse  $E_p$  is deposited instantly. The temperature distribution  $\Delta T$  directly after the deposition can be described by Eq. 5.6. To calculate the diffused temperature distribution  $\Delta T'$  at a given time  $\tau_0$  after the deposition, the initial temperature distribution  $\Delta T$  is convolved with the three dimensional heat kernel  $H$  (see Eq. 2.53 in Sec. 2.2.2):

$$\Delta T'(x, y, z, \tau_0) = H(x, y, z, \tau_0) * \Delta T(x, y, z). \quad (5.11)$$

The three dimensional convolution integral on the right side of Eq. 5.11 can be analytically simplified to a two dimensional convolution in  $x$  and  $y$ <sup>8</sup>:

$$\Delta T'(x, y, z, \tau_0) = \frac{\alpha}{\rho c_p} e^{D\tau_0\alpha^2} e^{\alpha z} \cdot H^{(2)}(x, y, \tau_0) * \Phi_0(x, y). \quad (5.12)$$

Here,  $H^{(2)}$  represents the two-dimensional heat kernel

$$H^{(2)}(x, y, \tau_0) = \frac{1}{4\pi D\tau_0} \exp \left[ -\frac{x^2 + y^2}{4D\tau_0} \right]. \quad (5.13)$$

Similar to Eq. 5.7, the isothermal surface for the temperature change  $\Delta T_{\text{th}}$  can be determined by rearranging Eq. 5.12:

$$z(x, y, \Delta T_{\text{th}}) = \frac{1}{\alpha} \ln \left( \frac{\rho c_p}{\alpha} \frac{\Delta T_{\text{th}}}{H^{(2)}(x, y, \tau_0) * \Phi_0(x, y)} \right) - D\tau_0\alpha. \quad (5.14)$$

<sup>8</sup>For details on the simplification calculations please refer to the Appendix A.

To obtain a more intuitive picture, the optical penetration depth

$$l_\alpha = \frac{1}{\alpha} \quad (5.15)$$

is introduced. It is a characteristic quantity for light transmittance of a given material. Similarly, the heat diffusion length

$$l_T = 2\sqrt{D\tau_0} \quad (5.16)$$

describes the width of the Gaussian heat kernel (compare Eq. 2.51) and thus, is a measure for the characteristic scale of heat diffusion within a material. By inserting Eq. 5.16, Eq. 5.15 and Eq. 5.8 in Eq. 5.14, the isothermal surface of  $\Delta T_{\text{th}}$  can be described in dependence of the material characteristic properties  $l_\alpha$ ,  $l_T$  and  $\Phi_{\text{th}}$ :

$$z(x, y, \Delta T_{\text{th}}) = l_\alpha \cdot \ln \left( \frac{\Phi_{\text{th}}}{H^{(2)}(x, y, l_T) * \Phi_0(x, y)} \right) - \frac{l_T^2}{4l_\alpha}. \quad (5.17)$$

Similar to the ablation model without heat diffusion, the model with heat diffusion assumes that all material heated above the critical temperature is ablated while cooler material remains unchanged.

Consequently, the resulting sample topography can be described by

$$h(x, y) = -l_\alpha \cdot \ln \left( \frac{\Phi_0^{\text{eff}}(x, y, l_T)}{\Phi_{\text{th}}} \right) - \frac{l_T^2}{4l_\alpha} \quad \forall \Phi_0^{\text{eff}} > \Phi_{\text{th}} \exp \left[ -\frac{l_T^2}{4l_\alpha^2} \right] \quad (5.18)$$

$$h(x, y) = 0 \quad \forall \Phi_0^{\text{eff}} \leq \Phi_{\text{th}} \exp \left[ -\frac{l_T^2}{4l_\alpha^2} \right] \quad (5.19)$$

with an effective fluence

$$\Phi_0^{\text{eff}}(x, y, l_T) = \Phi_0(x, y) * H^{(2)}(x, y, l_T) \quad (5.20)$$

and the two-dimensional heat kernel

$$H^{(2)}(x, y, l_T) = \frac{1}{\pi l_T^2} \exp \left[ -\frac{x^2 + y^2}{l_T^2} \right]. \quad (5.21)$$

No ablation takes place if the diffused temperature at the surface of the sample is smaller than the critical temperature:

$$\Delta T'(x, y, z = 0, l_T) < \Delta T_{\text{th}}. \quad (5.22)$$

Inserting Eq. 5.12, Eq. 5.20 and Eq. 5.8 in Eq. 5.22 yields the condition

$$\Phi_0^{\text{eff}}(x, y, l_T) < \Phi_{\text{th}}^{\text{eff}}(l_T, l_\alpha) \quad (5.23)$$

with the effective threshold fluence

$$\Phi_{\text{th}}^{\text{eff}}(l_T, l_\alpha) = \Phi_{\text{th}} \exp \left[ -\frac{l_T^2}{4l_\alpha^2} \right]. \quad (5.24)$$

At  $\Phi_{\text{th}}^{\text{eff}}$  the actual ablation under consideration of heat diffusion in z-direction starts to occur. This condition is equivalent to allowing only negative values for  $h$  in Eq. 5.18.

**Interpretation** To obtain a more intuitive picture of the convolution in Eq. 5.18, this convolution with a Gaussian shaped function can be looked upon in different ways. In the language of signal processing such convolution can be interpreted as low-pass filtering of spatial periods with a Gaussian shaped filter. In digital image processing a similar process is known as "Gaussian Blurring" of an image. In optics, the Gaussian  $H$  can be interpreted as a point spread function which resembles the blurring of a punctual light source by an optical element. However, all of these concepts are base on the broader principle of impulse responses or Green functions.

**Implementation and Challenges** The theoretical description of the ablation process was implemented as a numerical model in *Python* and is referred to as the *Ablate* module. Input to the module is a fluence distribution  $\Phi_0(x, y)$  on a given grid. The convolution of  $\Phi_0(x, y)$  with the heat kernel was calculated numerically by discrete Fourier transformations and multiplication according to the convolution theorem

$$\mathcal{F}\{f * g\} = c \cdot \mathcal{F}\{f\} \cdot \mathcal{F}\{g\}. \quad (5.25)$$

Here,  $\mathcal{F}$  stands for the Fourier transformation. If possible, the Fourier transformations were carried out with the Fast Fourier Transform (FFT) algorithm. Whenever non-unit grids were used, the non-periodic boundary conditions at the spatial limits of the input fluence distribution  $\Phi_0(x, y)$  led to artifacts in the transformed distribution  $\Phi_0^{\text{eff}}(x, y)$ . These artifacts only appear on the edges of the transformed distribution due to the convolution of the step-functions at the borders. The artifacts were cut off by cropping  $\Phi_0^{\text{eff}}(x, y)$  by the equivalent of  $2l_T$  on each side. All further calculations were based on the cropped distribution.

To avoid such artifacts from the beginning and speed up processing time, unit grid parameters were used (see description in Sec. 5.2.1 ). However, with unit

cells different challenges arise. In order to perform a representative convolution, the spatial extension of the grid  $x_{\max}, y_{\max}$  has to be large enough to fully support the Gaussian heat kernel (standard deviation  $\sigma = l_T/\sqrt{2}$ ). For smaller spatial extensions of the grid, only the center part of the Gaussian in the heat kernel is supported by the grid. A large part of the flanks of the Gaussian is cut off and the convolution becomes increasingly inaccurate. As minimum grid size a criterion of  $x_{\max}, y_{\max} > 4l_T$  was chosen and the grid parameters were selected to fulfill this criterion.

For large grids and small heat diffusion lengths another challenge arose. If the standard deviation of the Gaussian is smaller than half of the grid's sampling interval, quantization artifacts become very pronounced. The majority of the Gaussian is only represented by one single data point which can lead to normalization errors. An additional normalization of the Gaussian was introduced to prevent these errors.

### 5.4.2 Determination of Material Properties

For an application of the theoretical model to the ablation of ZnO:Al, the characteristic material properties heat diffusion length  $l_T$ , optical penetration depth  $l_\alpha$  and threshold fluence  $\Phi_{\text{th}}$  have to be determined. For this task, a genetic algorithm is used. It compares measured and simulated textures and optimizes  $l_T$ ,  $l_\alpha$  and  $\Phi_{\text{th}}$  for the best match. Details about the optimization procedure, a discussion on the reliability of the results and a comparison of virtual and real textures are presented in the following subsections.

## Optimization

**Procedure** In order to obtain data for a comparison, a variety of line-like<sup>9</sup> DLIP-textures was created with the DLIP setup. Altogether  $N = 30$  textures were created with varying laser power and texture periodicity. The textures were characterized by AFM and the depth of the real textures  $h^{(r)}$  was determined by multiple profile measurements in the AFM data. For each measurement  $i$  a measurement uncertainty  $u_i$  was estimated according to the general quality of the measurement. With the same setup parameters as used in the experiment, fluence distributions were calculated by the *SINT* model. These fluences were taken as input in the *Ablate* module to calculate virtual textures and their texture depths  $h^{(v)}$  were extracted. As the spatial periodicity of the texture is already very well reproduced in the interference pattern (see Sec. 5.3.2) and is not influenced by

---

<sup>9</sup>The line-like textures were chosen, because they revealed the smallest potential measurement error due to debris particles.

the characteristic properties of the material, the optimization merely focuses on the texture depths. In the next step, a genetic optimization algorithm was applied to minimize the difference of modeled and measured texture depth by variation of the characteristic properties  $l_T$ ,  $l_\alpha$  and  $\Phi_{th}$ .

**Genetic Optimization** For the optimization, the genetic algorithm described in Sec. 3.3 was used. The individuals  $I$  were assigned three attributes  $l_T$ ,  $l_\alpha$  and  $\Phi_{th}$ . The boundary conditions for the attributes were:

$$\begin{aligned} l_T &\in [1, 10^6] \text{ nm} && \text{type} = \text{log} \\ l_\alpha &\in [1, 10^6] \text{ nm} && \text{type} = \text{log} \\ \Phi_{th} &\in [0, 1] \text{ J/cm}^2 && \text{type} = \text{lin.} \end{aligned}$$

The type value states, if new attributes are drawn uniformly on a linear or logarithmic scale. The surface threshold fluence was limited to a maximum of  $\Phi_0^{\text{eff}} = 1 \text{ J/cm}^2$ , because in experiments, ablation could already be observed well below that value. The starting population contained  $n_{\text{pop}} = 10^4$  individuals. For each individual, virtual textures depths  $h_i^{(v)}$  for each set of setup parameters were calculated using *SINT* and the *Ablate* module. The evaluation of the fitness of the individuals was based on the difference in depth of measured and modeled textures. The fitness was calculated by averaging over all  $N = 30$  measured textures weighted by the inverse of the individual measurement uncertainties:

$$f = \sqrt{\sum_i^N \left( \frac{h_i^{(r)} - h_i^{(v)}}{u_i} \right)^2}. \quad (5.26)$$

The selection of the fittest individual was then carried out by selecting the  $\mu = 2000$  individuals with the smallest fitness value. In each generation  $\lambda = 1000$  individuals were selected for modification. Modification was carried out according to the probabilities  $p_x = p_\pm = 0.5$  and  $q_x = q_\pm = 0.5$ . A total of  $n_{\text{gen}} = 100$  generations were evaluated. Please refer to Sec. 3.3 for a detailed description of the algorithm and its parameters.

**Result of Optimization** The developing of the average fitness as well as the minimum (which in this case is the best) fitness within the population is depicted in Fig. 5.19. After approximately 60 generations the population has settled on individuals with attributes resulting in a fitness of  $f \approx 11.6$ . Although thereafter the individuals were still mutated with a mutation probability of  $p_\pm = 0.5$ , neither the minimum fitness nor the average fitness changed within in the course of the

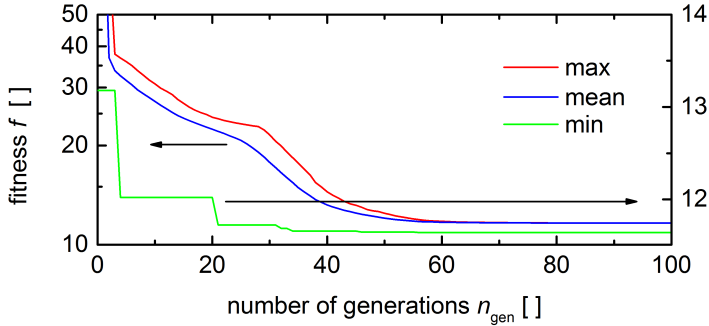


**Figure 5.19** Evolution of population in genetic optimization algorithm: Throughout the course of generations, the minimal (here: best) fitness detected within the population lessens. The mean fitness of the population also evolves towards a minimum. Albeit a high mutation probability of  $p_{\pm} = 0.5$  no further fitness improvement in any of the individuals in the population was detected after 60 generations.

following 50 generations. This suggests that the individuals of the final population scatter close to the global minimum. Furthermore, multiple runs of the same evolution have shown similar results.

The all-time best evaluated individual throughout the course of the evolution had the following attributes:

- heat diffusion length  $l_T = 305$  nm
- optical penetration depth  $l_{\alpha} = 181$  nm
- threshold fluence  $\Phi_{th} = 0.683$  J/cm<sup>2</sup>

## Reliability of Optimization Results

**Heat Diffusion Length** In laser processing literature [5, 79] a common estimation for the magnitude of the heat diffusion length is made by introducing the laser pulse duration  $\tau_p$  as characteristic diffusion time (see Eq. 5.16). Consequently, the expected heat diffusion length can be estimated by laser and material properties:

$$l_T = 2\sqrt{D\tau_p} = 2\sqrt{\frac{\kappa\tau_p}{\rho c_p}}. \quad (5.27)$$

Using this approximation and literature values for undoped, crystalline ZnO at room temperature [33], a heat diffusion length of  $l_T = 612$  nm can be estimated.

The result of the optimization ( $l_T = 305$  nm) is on the same order of magnitude but suggests less heat diffusion. However, considering the high temperatures during the laser process, a decreased heat diffusion is also expected. It can be assumed that with the rising temperature, also the phonon density in the material rises. Consequently, phonon-phonon interaction becomes more prominent. Similarly, the amount of free charge carriers rises and leads to an increase of electron-phonon interactions. Both of these scattering mechanisms diminish the thermal diffusivity of the ZnO:Al and thus lead to a reduction of the heat diffusion length for higher temperatures. Considering the high temperatures during the laser process as well as the use of doped, non-crystalline ZnO:Al, a smaller heat diffusion length than the theoretical estimation has to be expected. Consequently, the result of the optimization is in good agreement with these expectations.

**Optical Penetration Depth** Similarly, the optical penetration depth can be estimated by measuring the absorption coefficient and Eq. 5.15. Using data measured at IEK-5 by photothermal deflection spectroscopy (PDS) measurements at a typical front contact ZnO:Al layer, at room temperature the optical penetration depth calculates to  $l_\alpha = 950$  nm. However, due to the transient creation of large numbers of free charge carriers during the laser illumination, it is expected that the ZnO:Al becomes less transparent during the laser process. A rigorous theoretical calculation of the transient change of the dielectric function of ZnO taking into account Drude model and Kerr effect was carried out by Dufft et al. [29]. Summarizing, the transient augmentation of the free charge carrier density leads to a greater extinction coefficient  $n''$  and hence, a greater absorption coefficient  $\alpha$ . It is assumed that because of the much greater free charge carrier densities, this effect overcompensates the opposed band filling effect known as Burstein-Moss shift [88]. Consequently, the optical penetration depth is expected to be shorter during the laser process than when measured in standard laboratory conditions.

**Threshold Fluence** To obtain an estimation for the expected threshold fluence, measurements according to the Liu-method (see Sec. 3.1.1) can be used. Extrapolating the linear fit of the acquired data to the x-intercept, the pulse energy  $E_p$  at which visible ablation starts to occur can be extracted. From this pulse energy a peak fluence  $\Phi_0^{\text{pk}}$  in the center of the beam can be calculated according to Eq. 2.22. A corresponding measurement with a single beam (no interference effects) of the laser used for the experiments, yielded a fluence of  $\Phi_0^{\text{pk}} = 0.37$  J/cm<sup>2</sup> at which visible ablation in the center of the spot starts to occur. For the comparably large laser spots on the order of some hundred micrometers ( $r_s \gg l_T$ ), lateral heat diffusion can be neglected ( $\Phi_0^{\text{eff}}(x, y, l_T) = \Phi_0(x, y)$ ). Calculating the effective threshold fluence  $\Phi_{\text{th}}^{\text{eff}}$  by inserting the determined material properties  $l_T$ ,  $l_\alpha$  and

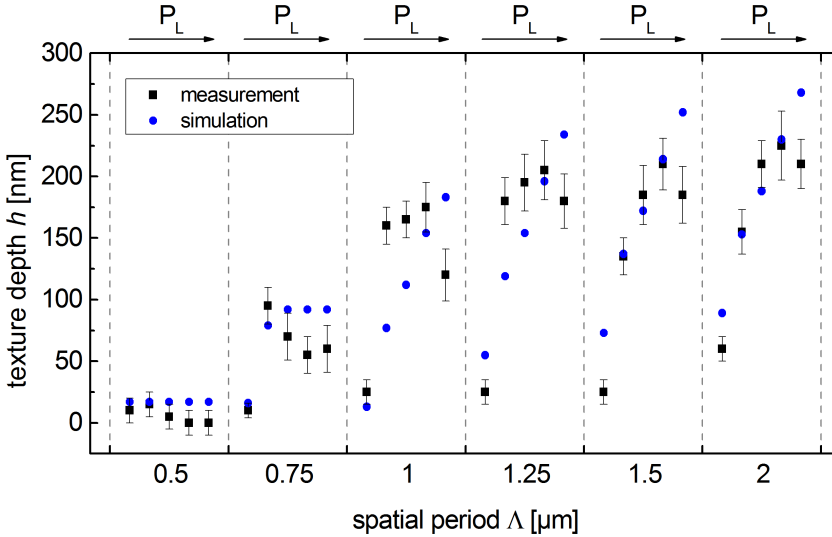


**Figure 5.20** Validation of optimization results (Texture depths for various spatial periodicities and laser powers): After the optimization of the characteristic material properties  $l_T$ ,  $l_\alpha$  and  $\Phi_{th}$ , the diminishing of texture depths for small periodicities is reproduced by the model. Furthermore, the trend of deeper textures with higher laser powers within one spatial periodicity is reproduced. The smaller texture depths at the highest powers in the experiment are assumed to be due to measurement errors.

$\Phi_{th}$  in Eq. 5.24, yields an expected threshold fluence of  $\Phi_{th}^{eff} = 0.34 \text{ J/cm}^2$ . Considering that only slightly ablated surfaces cannot be detected with the optical microscope and hence the empirical fluence ( $\Phi_0^{pk} = 0.37 \text{ J/cm}^2$ ) is expected to be slightly higher than the modeled fluence ( $\Phi_{th}^{eff} = 0.34 \text{ J/cm}^2$ ), the model and experiment are in good agreement.

## Comparison of Model and Experiment

To validate the results of the optimization, the calculated and measured texture depths are compared (see Fig. 5.20). The calculated depths were obtained by the *Ablation* module with the optimized values for  $l_T$ ,  $l_\alpha$  and  $\Phi_{th}$ . It can be observed that while the calculation does not perfectly match the measurements in all data points, the general trend is replicated. For smaller spatial periodicities the texture depth lessens and vanishes. This trend can be observed in measurement and

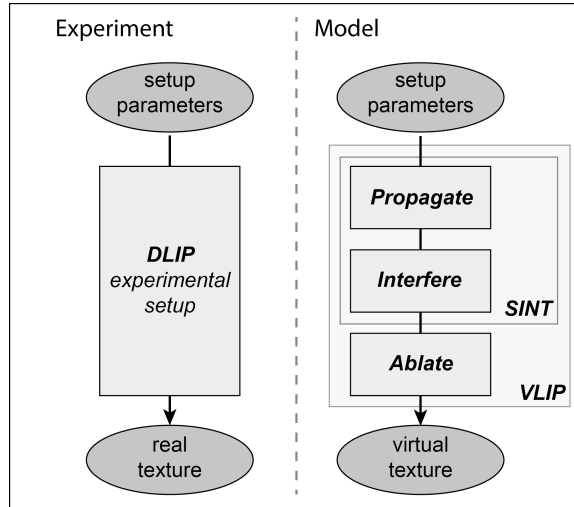


**Figure 5.21** Direct and virtual laser interference patterning (illustration): Schematic outline of VLIP model and components.

simulation. Furthermore, it can be observed that within a set of textures of the same periodicity, the texture depth generally augments for higher laser powers. However, in the measured data this is not true for the highest power value in most of the periodicities. This deviation is assumed to be due to measurement artifacts.

In high-power treatments large amounts of particles were detected on the sample surface (see Sec. 5.3.3). These particles can lead to systematical errors in the AFM measurements. On the one hand, the sample is covered with a layer of particles so the actual underlying surface topography is difficult to detect. On the other hand, the particles can be picked up by the AFM tip and adhere to the tip during the measurement. This can cause a change in the tip vibrational resonance characteristics which again can cause a measurement error. Consequently, AFM measurements on particle covered surfaces have to be treated with caution. Moreover, it was not possible to remove the particles by a cleaning step without altering the underlying topography.

Summarizing it can be stated, however, that apart from these effects the general trends are well reproduced and there is a good match in between measurement and simulation.

### 5.4.3 Virtual Laser Interference Patterning (VLIP)

After the determination of the relevant characteristic properties of ZnO:Al in the given setup, the *Ablate* module can be used to model the ablation process in the DLIP setup. It is combined with the *SINT* model to form a complete model of Virtual Laser Interference Patterning (VLIP). Starting with the setup parameters of the experimental setup, a fluence distribution on the sample can be calculated by the *SINT* model. This fluence distribution is then used as input in the *Ablate* module to simulate a surface topography of the sample after the laser process (also see Fig. 5.21). In the following section *VLIP* is used to calculate a variety of textures. The geometry and texture depth of these virtual textures was then compared to real textures obtained from experimental DLIP. Hence, the *VLIP* model can be validated and its predictive power can be judged.

**Texture Geometry** A variety of dent-like textures were created with the DLIP setup and characterized by AFM and SEM. With the same sets of setup parameters, virtual textures were calculated using *VLIP*. A visual comparison of the virtual and real textures is depicted in Fig. 5.22. As already observed for the fluence distributions, the spatial periodicities are very well reproduced in the virtual textures and are in very good agreement with the periodicities of the real textures. Furthermore, it can be observed that both, the virtual and real textures similarly diminish towards smaller periodicities. The critical periodicity for an almost complete vanishing is also well reproduced by *VLIP*. The comparison of a height profile of an exemplary texture as depicted in Fig. 5.22 (c) reveals the differences in between virtual and real textures. Whereas the general shape and periodicity of the profiles matches, the detailed fine structure differs. The bulging of molten and resolidificated material on the rim of the dent and in between adjacent dents cannot be reproduced by the model. Furthermore, the general surface roughness and inhomogeneities of the material as well as resettled debris and particles cannot be predicted by *VLIP*. The shape and steepness of the dent flanks, however, can be reproduced.

**Texture Depths** A comparison of calculated and measured texture depths of the dent-like textures is depicted in Fig. 5.23. Given the restrictions of the somewhat difficult and potentially inexact AFM measurements (see above), the predicted texture depths are in good agreement with the measured ones. The critical periodicity for vanishing texture depths is represented by the model. For larger periodicities, it can be observed that real and virtual texture depths depend on the laser power. Although this trend can already be observed for textures with a periodicity of  $\Lambda \geq 1 \mu\text{m}$  in the measured data, it is only reproduced for textures with a periodicity of  $\Lambda \geq 1.25 \mu\text{m}$  by the model. However, this could be due to

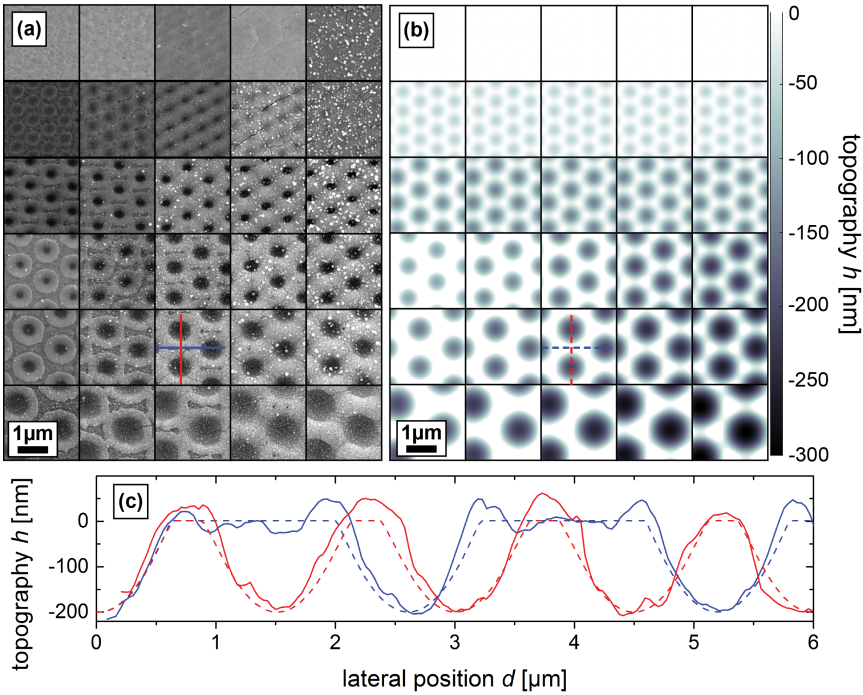


**Figure 5.22** Comparison of model and experiment - general geometry and exemplary height profile: (a) SEM images of variety of dent-like DLIP-textures. (b) Corresponding textures simulated by VLIP. (c) Exemplary height profile extracted from simulation and AFM measurement. The general topography of the DLIP textures is reproduced by the model.

systematical errors in the measurement. In general, the texture depths are well reproduced by the VLIP model.

**Conclusion** The VLIP model is capable of reproducing the main topographical properties of the DLIP textures. The main geometry, lattice type, spatial periodicities, texture depth and coarse height profile are well reproduced. However, topographical features due to melting effects like bulges or particle formation cannot be reproduced by the model. Consequently, the detailed fine structure of measurement and simulation differs. Nevertheless, VLIP provides a good estimation of the expected surface topography.

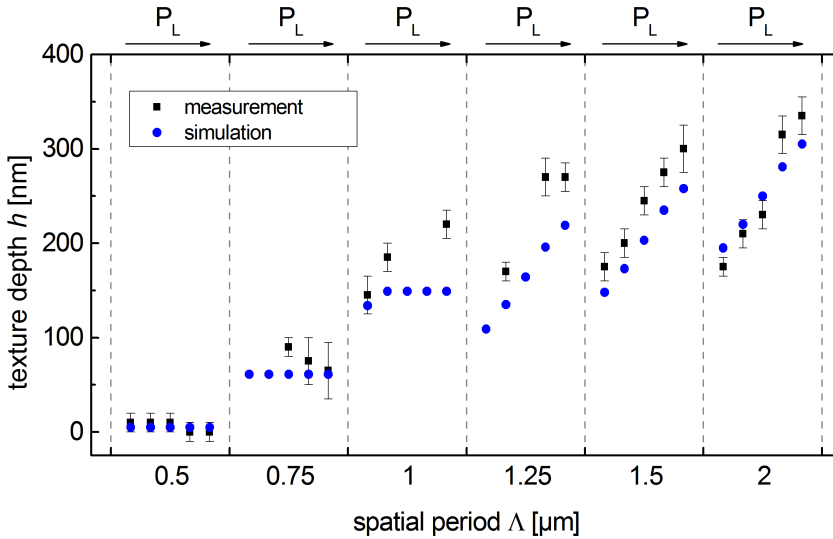


**Figure 5.23** Comparison of model and experiment - texture depths: Similar to the line-like textures used for the determination of material properties (Fig. 5.20), the texture depths of the dent-like textures are well reproduced by the model. Due to debris and particle resettlement on the surface, the resulting data is prone to a high measurement uncertainty and some textures could not be characterized at all.

## 5.5 Summary

**Experiment** On the experimental side, a highly flexible setup for three-beam direct laser interference patterning was designed and constructed. By a total of nine independent setup parameters, the beam properties of each of the partial beams can individually be adjusted. Each of these beam properties such as electrical field amplitude or orientation of polarization influences the intensity distribution in the interference volume. Consequently, a large variety of adjustable fluence distributions can be created on the sample's surface by according variation of the setup parameters. By means of direct laser ablation, these fluence distributions can then be transferred to adjustable surface textures on the ZnO:Al sample. With a single laser pulse, an area of  $A_s \approx 0.8 \text{ mm}^2$  can be textured with micrometer-sized features. All of the producible textures are strictly periodic with a continuously adjustable periodicity and visibly diffract incident light.

**Model** On the modeling side, a comprehensive model for "virtual laser interference patterning" (*VLIP*) was developed. Starting from the adjustable parameters of the experimental setup, the model mimics the experiment by virtually propagating the laser beams and changing their properties according to the setup parameters. The intensity distribution in the interference volume is calculated by superposition of the electrical fields of the partial beams. The energy intake in the material is calculated under consideration of the optical properties and an initial temperature distribution within the material is calculated. The subsequent three-dimensional heat diffusion is modeled by convolution of the initial temperature distribution with the heat kernel. Finally, the resulting topography of the sample's surface is estimated from the temperature distribution after the heat diffusion.

The experiment and the model are found in good agreement. Consequently, the *VLIP* model can be used to predict the expected surface topography for a given set of setup parameters.

# 6 Application in Solar Cells

To demonstrate the applicability of DLIP in the manufacturing of solar cells, thin-film silicon a-Si:H/ $\mu$ c-Si:H tandem solar cells are built on selected DLIP-textured ZnO:Al layers. In order to be able to use the textured layers in the manufacturing of solar cells, the texture has to be applied to areas larger than single laser spots. The covering of such macroscopic areas is done by applying multiple laser spots adjacent to each other – the so called "stitching" of laser spots.

In the first section of this chapter, the texture distribution within a single laser spot as well as the macroscopic texturing by stitching of laser spots along with its inherent limitations of homogeneity is described. The macroscopically textured samples are then characterized for their optical and electrical properties. In the second section the deposition of thin-film silicon a-Si:H/ $\mu$ c-Si:H tandem solar cells on the textured layers is described. Finally, these solar cells are characterized and their characteristic properties such as quantum efficiency and J-V curves are discussed.

## 6.1 Macroscopic Texturing

**Experimental Procedure** Three series of DLIP-textured substrates were produced. Each series contained five different textures. Furthermore, untextured as well as texture-etched ZnO:Al substrates were used as references. The applied texture on all DLIP-textured substrates was the hexagonal dent-like texture of the same general shape as depicted in Fig. 5.11. Within each series, the spatial periodicity of the hexagonal lattice  $\Lambda_{A,B} = \Lambda$  was varied<sup>1</sup>. The produced spatial periodicities were  $\Lambda = 2 \mu\text{m}, 1.75 \mu\text{m}, 1.5 \mu\text{m}, 1.25 \mu\text{m}$  and  $1 \mu\text{m}$ . In two of the series, the laser was used at maximum power output (approx.  $P_L \approx 140 \text{ mW}$  at sample). In the other series less laser power was used ( $P_L \approx 110 \text{ mW}$ ). Because of the redeposited particles and debris, one of the series produced with maximum power was cleaned in 0.5% HCl for  $t = 1 \text{ s}$ . The other two series were not cleaned after the laser treatment. Unfortunately, the cleaning with HCl led to an undesired crack formation due to the changed etch behavior of the previously laser-treated areas.

---

<sup>1</sup>For reasons of simplicity the index "A,B" is omitted hereafter.

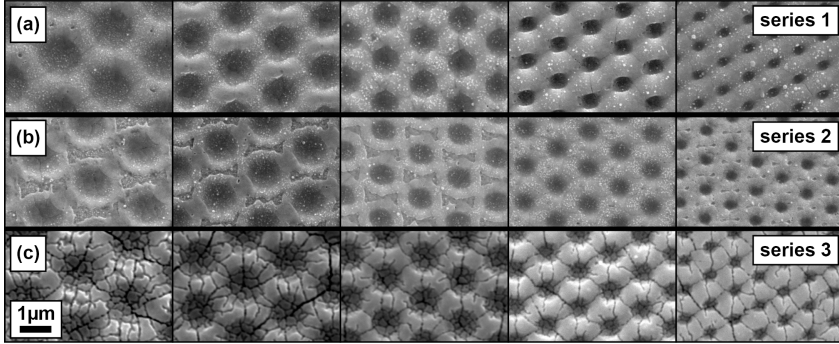


**Figure 6.1** Overview of DLIP textures incorporated in solar cells (SEM images): (a) Debris and particles can be observed on the surfaces of the high-power textures of series 1. (b) Series 2 shows less particles and debris due to less excess laser power (see Sec. 5.3.3). (c) To remove the debris, the substrates were cleaned in 0.5% HCl for  $t = 1$  s which led to an undesired crack formation in areas of previously laser-treated ZnO:Al. All presented textures were measured in the center of the laser spots.

In brief, the series were:

- Series 1: High Power, no cleaning
- Series 2: Low Power, no cleaning
- Series 3: High Power, 1 s HCl cleaning

SEM images of the textures are depicted in Fig. 6.1.

### 6.1.1 Stitching of Laser Spots

The preceding chapters have focused on microscopically textured areas within one laser spot ( $A_s \approx 0.8 \text{ mm}^2$ ). However, in order to properly characterize the textured ZnO:Al for electrical and optical properties and for its application in the construction of solar cells, larger areas of at least  $A_{sc} \approx 1 \text{ cm}^2$  need to be textured. For a potential industrial application in the production of solar modules, even areas of  $A_{sm} \approx 1 \text{ m}^2$  are required. Since the maximum pulse energy is limited by the laser system and only single pulse process can be used, the laser spot cannot be enlarged arbitrarily. Consequently, macroscopic texturing needs to be done by stitching numerous small laser spots to large areas.

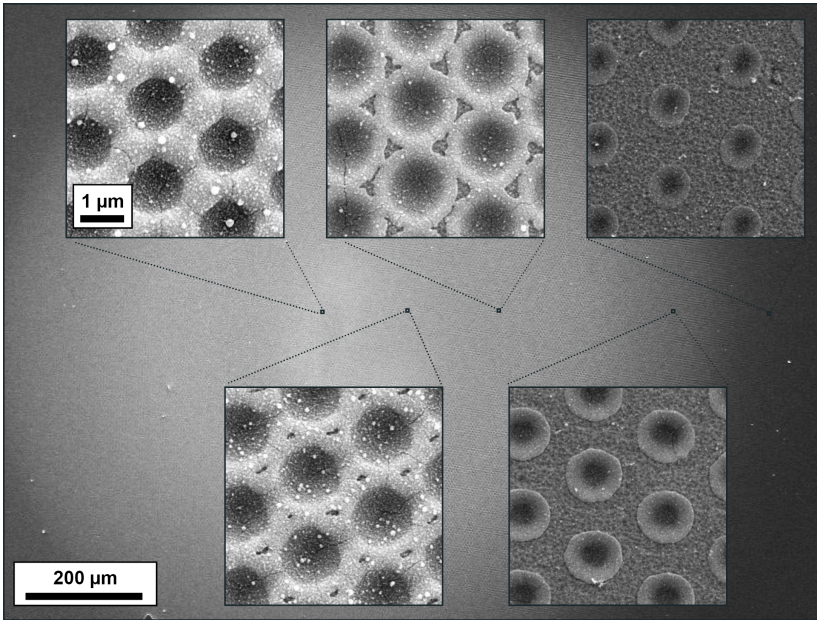


**Figure 6.2** Variation of surface topography within one laser spot (SEM images): Due to the Gaussian-shaped intensity distribution of the laser beam, the energy intake in the material varies within the laser spot. Consequently, also the produced texture varies along the cross section of the laser spot. The spatial periodicities, however, remain constant throughout the whole spot.

**Texture Variations within Laser Spot** Apart from concentrating on the microscopic textured area within one laser spot, all preceding investigations even only focused on the texture within the very center of the laser spot. This was reasonable, because the very center of the laser spot can be easily determined, so comparative measurements of different textures in various laser spots could be conducted. Furthermore, due to the Gaussian-shaped fluence distribution within the laser beam (see Sec. 2.2.1), the lateral fluence variation is minimal at the center of the pulse allowing more accurate measurements. However, the texture within the pulse varies.

So far, it was assumed that the spatial average of the microscopic periodic surface fluence distribution (due to the interference)  $\Phi_0^{\text{mean}}$  is equal to the peak surface fluence within the macroscopic, Gaussian-shaped fluence distribution (due to the

laser beam properties)<sup>2</sup>  $\Phi_0^{\text{mean}} = \Phi_0^{\text{pk}}$ . However, moving away from the center, the spatially averaged surface fluence  $\Phi_0^{\text{mean}}$  lessens. At a distance of the beam radius  $w$  from the center, it has dropped to  $\Phi_0^{\text{mean}} = 1/e^2 \Phi_0^{\text{pk}}$ . Outside the area defined as the beam area  $A_b = \pi w^2$  (see Sec. 2.2.1) it is even smaller, but remains nonzero.

Consequently, the texture within the observable laser spot also varies. In Fig. 6.2 various textures observed along the radius of a laser spot are depicted. The texture depth as well as the fine structure of the textures varies just as would be expected for textures created with different laser powers (compare Fig. 5.14). Even on the outside rim of the visible laser spot where  $r = r_s^{\text{vis}}$ , a minor texture remains. Only further out at  $r_s$ , where even the maximum fluence of the interference pattern falls beneath the threshold fluence  $\Phi_0^{\text{max}}(r > r_s) < \Phi_{\text{th}}^{\text{eff}}$ , the surface remains untreated<sup>3</sup>.

**Macroscopic Texture Variations** For the texturing of macroscopic areas by stitching laser spots this means that there will always be variations in the texture. It is not possible to perfectly homogeneously texture large areas by stitching. By positioning the centers of the laser spots in a hexagonal lattice, the largest area of the surface can be covered by laser spots (compare closest packing of circles [23, 98]). The distance in between the centers of neighboring laser spots  $d_s$  defines the spatial overlap of the adjacent spots and thus, the area of untextured as well as double textured regions. For close stitching ( $d_s < 2r_s$ ) the amount of untextured area lessen, but the area covered with unpredictable double textures augments. Since the exact geometry of double textures of the same periodicity cannot be predicted due to setup instability, a double texturing was avoided.

For  $d_s \geq 2r_s$  no double texture exists but areas in between the laser spots remain untextured. Even for perfect stitching with  $d_s = 2r_s$  approximately 9% of the total surface area remains untextured (compare Fig. 6.3 (a)). The other 91% are covered with a range of textures ranging from the very shallow texture induced by the threshold fluence  $\Phi_0^{\text{th}}$  to the deepest texture induced by the peak fluence  $\Phi_0^{\text{pk}}$ . The distribution and the frequency of the different types of textures can be calculated according to the Gaussian fluence distribution. However, it has to be kept in mind that the frequency of occurrence of shallow textures which are located towards the outside of the beam spot is much higher than the frequency of the deep textures in the center of the spot.

<sup>2</sup>To avoid confusion, the maxima and minima of the microscopic, periodic fluence distribution are referred to as  $\Phi_0^{\text{max}}$  and  $\Phi_0^{\text{min}}$ .  $\Phi_0^{\text{pk}}$  always refers to the peak value of the Gaussian-shaped distribution.

<sup>3</sup>Please note that  $\Phi_0^{\text{max}}$  and  $\Phi_0^{\text{pk}}$  denote different quantities.

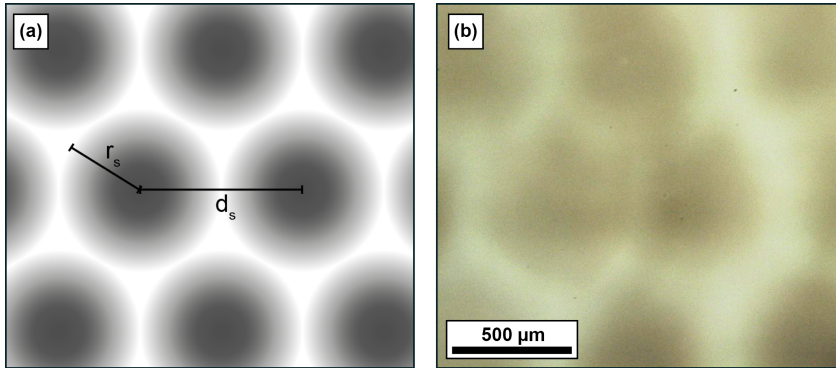


**Figure 6.3** Stitching of laser spots: (a) Illustration of fluence distribution on sample surface using a perfect hexagonal lattice with Gaussian laser spots at a distance of  $d_s = 2r_s$ . (b) OM image of spot stitching pattern as used for the construction of solar cells. Due to the beam pointing and pulse-to-pulse instabilities of the laser, the size and shape of the spots as well as their positioning strongly varies.

**Experimental Issues** For the manufacturing of the samples used for characterization and the deposition of solar cells, the laser spots were stitched in a hexagonal lattice with a spot distance of  $d_s = 2r_s^{\text{vis}}$ . The visible spot radius  $r_s^{\text{vis}}$  was determined by examination under the optical microscope and estimating the visible radius of the laser spot<sup>4</sup>. The visible spot radius  $r_s^{\text{vis}}$  was determined independently for each set of setup parameters, and thus, type of texture.

The pointing instability of the laser beam leads to strong irregularities in the positioning of the laser spots in the nominal hexagonal pattern. Furthermore, the pulse-to-pulse instability of the laser system leads to varying spot sizes. Both effects can be observed in Fig. 6.3(b). For these reasons as well as the general variation of the macroscopic texture as described in the preceding paragraphs, the manufactured macroscopically DLIP-textured ZnO:Al samples do not represent the best textures achievable by DLIP patterning. They are merely used as a proof of concept for the DLIP-patterning process in the production of thin-film silicon solar cells.

<sup>4</sup>In general  $r_s^{\text{vis}} \neq r_s$

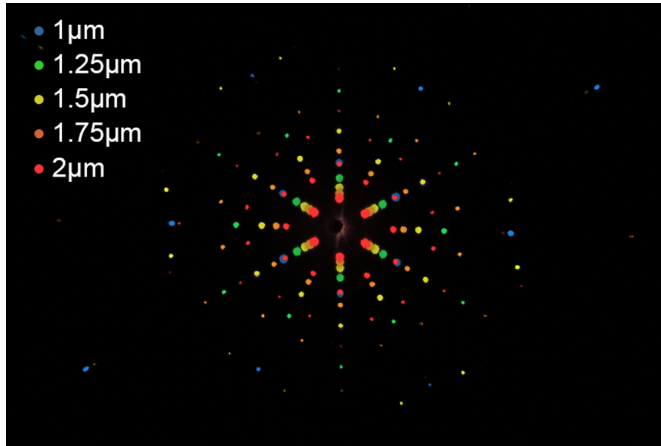


**Figure 6.4** Light diffraction of DLIP textures (superposed, colored photographs of diffraction pattern of series 1): The strictly periodic textures refract the light of a monochromatic light source ( $\lambda_L = 405 \text{ nm}$ ) into discrete angles. For smaller spatial periods of the texture (see legend), the light is diffracted into larger angles.

### 6.1.2 Electro-Optical Characterization

In order to be able to thoroughly characterize the macroscopically textured substrates without taking the risk of a contamination of the substrates, each texture was created on two substrates. One substrate was used directly for the construction of solar cells whereas the other substrate was used for the characterization. The textured areas on the characterization substrate were  $A = 20 \text{ mm} \times 20 \text{ mm}$  and each texture was created directly after the corresponding texture for the solar cell was created without a change of the experimental setup. After the characterization of the textures on the characterization substrate, the substrate was cleaned similarly to the substrates used for the solar cells (0.5% HCl for  $t = 1 \text{ s}$ ). After the cleaning, each texture was characterized again. Fig. 6.1 shows SEM images of the reference textures of series 1, 2 and 3.

**Diffraction** The periodic textures diffract monochromatic laser light into discrete directions. To visualize the diffraction pattern, the diffracted light of the textures of series 1 was photographed at a ground glass screen behind the sample. The photographs were artificially colored and superposed to be able to compare the diffraction abilities of different textures (see Fig. 6.4). The discrete diffraction pattern underlines the strict periodic nature of the texture even on macroscopic

areas of single millimeters. Further, it can be observed that the textures with smaller periods diffract into larger angles.

**Spectral Transmittance** To spectrally quantify the amount of transmitted light, the substrates were characterized in a spectrometer. Since the amount of diffusely transmitted light (haze value) does not necessarily correlate with the light trapping abilities of a texture [53, 89], the haze value is not evaluated. Also reflectance measurements in air only have very limited significance, because texture-driven light in-coupling effects are less pronounced at the ZnO:Al–air interface than at the ZnO:Al–a-Si:H interface in a solar cell. Furthermore, the ZnO:Al layer is used as the front contact of the solar cell so it is of minor relevance if the non-transmitted light is absorbed or reflected.

Consequently, all further investigations solely concentrate on the total transmittance of the ZnO:Al layer. However, even these measurements have to be treated with caution since the less reflective ZnO:Al–air interface in the measurement can lead to a higher measured transmittance as would be expected in the compound of a solar cell (see Sec. 2.1.2). Nevertheless, the spectral transmittance can be used to obtain a general idea of the transparency of the ZnO:Al layers. The measured total transmittances of the textures used for the solar cell manufacturing are depicted in Fig. 6.5. A spectrally averaged transmittance  $TT_{\text{avg}}$  was calculated for the short ( $\lambda = 350 \text{ nm}$  to  $600 \text{ nm}$ ) as well as the long wavelength region ( $\lambda = 600 \text{ nm}$  to  $1100 \text{ nm}$ ) and is presented in Tab. 6.1.

As a first observation it can be stated that within each single series, the textures with different spatial periods all show similar transmittance. Compared with the etched reference, it can be observed that the total transmittance of the series 1 textures is generally lower than the etched reference. The broadband reduction is assumed to be due to debris resettling on the sample surface during the laser treatment with high powers (as can be observed in Fig. 6.1 (a)). This is underlined by the fact that series 2 (Fig. 6.5(b)) textures in general reveal a higher transmittance than series 1. Due to the lower powers used in series 2, there is a lower excess energy intake and less debris and particles (also compare Fig. 6.1 (a) and (b)). A comparison of the uncleaned textures of series 1 with the same but cleaned textures of series 3 reveals a broadband gain in transmittance after the cleaning (see Fig. 6.5). This further underlines the assumption that debris is the cause for the loss in transmittance. After the cleaning it can be observed that in the wavelength region from  $\lambda = 500 \text{ nm}$  to  $900 \text{ nm}$ , some DLIP-textures of series 3 reveal an even higher transmittance than the standard etched texture. In the longer wavelength region ( $\lambda > 900 \text{ nm}$ ) both clean and unclean textures show a reduced transmittance when compared to the standard etched reference. This is assumed to be due to the larger effective layer thickness in the DLIP-textured ZnO:Al layers.

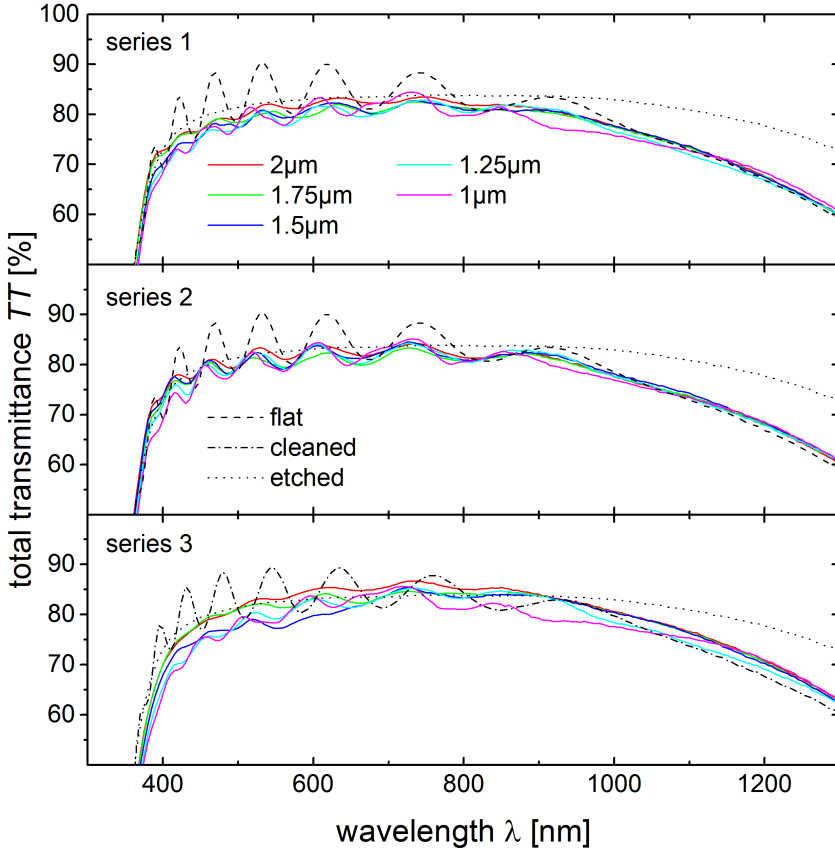


**Figure 6.5** Total transmittance of DLIP textured ZnO:Al layers used in solar cells: The broadband reduction of transmittance of series 1 compared to the etched reference is assumed to be due to debris and redeposited particles. Due to less debris series 2 reveals better transmittance than series 1. After cleaning the samples and removing the debris (series 3), the transmittance is improved for all wavelengths. The lower transmittance of all DLIP textures in the long wavelength region is attributed to the higher effective layer thickness of the DLIP-textured ZnO:Al layer compared to the etched reference.

Series	$\Lambda$ [um]	$TT_{\text{avg}}^{\text{top}}$ [%]	$TT_{\text{avg}}^{\text{bot}}$ [%]	$TT_{\text{avg}}^{\text{tot}}$ [%]
etched		75.87	83.24	80.75
cleaned		77.34	82.24	80.58
flat		77.21	82.00	80.35
1	2	74.78	80.48	78.54
1	1.75	73.92	79.66	77.72
1	1.5	72.96	79.84	77.51
1	1.25	72.14	79.52	77.02
1	1	72.40	79.01	76.75
2	2	76.05	80.61	79.05
2	1.75	78.88	82.24	81.05
2	1.5	75.21	80.67	78.80
2	1.25	74.47	80.50	78.44
2	1	73.45	80.09	77.82
3	2	74.58	83.39	80.40
3	1.75	74.04	82.43	79.59
3	1.5	71.15	82.01	78.36
3	1.25	71.06	81.70	78.09
3	1	70.52	80.48	77.10

**Table 6.1** Spectrally averaged total transmittances extracted from measurements as depicted in Fig. 6.5. The averaged transmittance for the top cell  $TT_{\text{avg}}^{\text{top}}$  was averaged over the wavelength region from  $\lambda = 350$  nm to 600 nm,  $TT_{\text{avg}}^{\text{bot}}$  over  $\lambda = 600$  nm to 1100 nm and  $TT_{\text{avg}}^{\text{tot}}$  over  $\lambda = 350$  nm to 1100 nm.

**Sheet Resistance** After the texturing, the sheet resistance  $R_{\square}$  of the ZnO:Al layers was slightly augmented. Typically, it changed from  $R_{\square} = 3.5 \Omega$  in the untextured layer to  $R_{\square} \approx 4.5 \Omega$  in the DLIP-textured layer. After the cleaning step in HCl it again augmented by  $\Delta R_{\square} \approx 0.5 \Omega$  to typically  $R_{\square} \approx 5 \Omega$ . The slight increase in resistance is attributed to the decrease in effective layer thickness of the ZnO:Al layer after the DLIP process as well as after the cleaning process.

## 6.2 Solar Cells

On the macroscopic DLIP-textured substrates, thin-film silicon a-Si:H/ $\mu$ c-Si:H tandem solar cells were deposited by a standard deposition process. After the deposition, the solar cells were characterized to investigate quantum efficiency

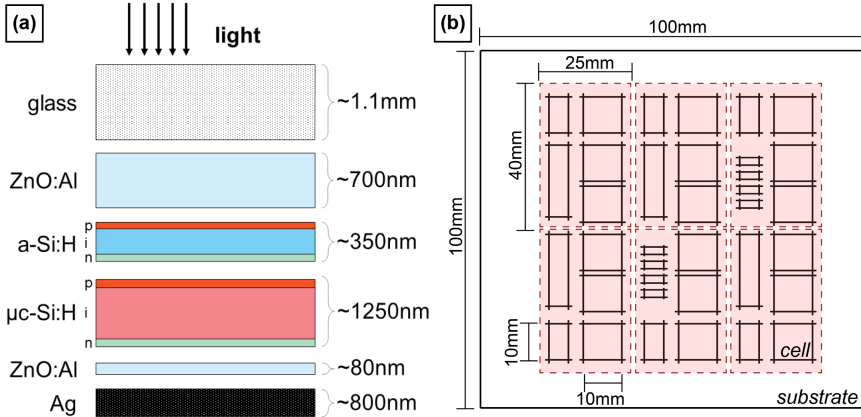


**Figure 6.6** Schematic sketch of deposited thin-film silicon a-Si:H/ $\mu$ c-Si:H tandem solar cell (illustrations): (a) Layer stack and estimated layer thicknesses (proportions are not in scale). The p- and n-layers have an approximate thickness of  $d = 40$  nm each. (b) Layout of textured areas and solar cells on substrate: Each of the red dashed rectangles of size  $A_{DLIP} = 40$  mm x 25 mm was patterned with a different DLIP texture. For each texture, three  $A_{SC} = 10$  mm x 10 mm cells were evaluated.

and J-V characteristics of the cells. In the following section, the deposition of the layer stack and the results of the characterization are presented and discussed.

### 6.2.1 Deposition of Tandem Solar Cells

All cells were deposited in a large area deposition tool at IEK-5 in the same deposition. The layer stack was deposited according to a slightly altered recipe for standard a-Si:H/ $\mu$ c-Si:H tandem solar cells. The layer thicknesses were slightly reduced in order to be able to better investigate light trapping effects. The deposited layer stack with the approximate layer thicknesses is depicted in Fig. 6.6 (a). After the deposition of the a-Si:H and  $\mu$ c-Si:H layers, a thin layer of ZnO:Al was sputtered on the substrate to enhance reflection and finally, a silver back contact was deposited thermally. Prior to the silver deposition, the substrates were masked and a standard IEK-5 cell design was applied. After the deposition, each DLIP-textured areas was incorporated in 3 solar cells with an area of  $A_{SC} = 1$  cm<sup>2</sup> each (see substrate layout in Fig. 6.6 (b)). To be able to access the front contact, the substrates were scratched at an additionally deposited silver strip in between the cells, so this strip was in electrical contact with the front ZnO:Al layer.

## 6.2.2 Characterization of Solar Cells

For all but one of the DLIP textures at least one fully functional solar cell could be determined. In order to minimize measurement errors due to detection of photo current which was generated in an area larger than the actual solar cell, the best solar cells for each texture were electrically isolated. This was done by removing the absorber layer in the circumference of the deposited back contact by laser ablation. Afterwards these solar cells were characterized by spectral response measurements, sun simulator and spectrometer to obtain spectral quantum efficiencies, J-V curves and solar cell reflectance (see Sec. 2.1.1).

**External Quantum Efficiency (EQE)** In order to investigate the spectral light trapping properties of the solar cells, the external quantum efficiency (EQE) of the cells was determined. The EQEs of the cells within series 1, 2 and 3 are depicted in Fig. 6.7. The short-circuit current densities calculated from the EQE measurements as well as the maximal texture depths of the various DLIP textures are presented in Tab. 6.2.

Similar to the transmittances, it can be observed that the EQEs of textures within a single series are somewhat similar. Nevertheless a slight trend with a maximum at approx  $\Lambda \approx 1.5 \mu\text{m}$  or  $\Lambda \approx 1.75 \mu\text{m}$  can be observed in all series. However, this trend can also be due to experimental variations and is not considered pronounced enough to be stress-able.

Focusing on the top cell and the short wavelength region ( $\lambda = 350 \text{ nm}$  to  $600 \text{ nm}$ ), light trapping effects of the textures are negligible. Almost all of the light that passes through the top cell without being absorbed is absorbed in the thicker bottom cell, so light trapping is of very little importance. In this region, it can be observed that the cells of series 1 show lower EQEs and  $J_{\text{sc}}^{\text{top}}$  than series 2, which is assumed to be due to the lower transmittance of series 1 (see Sec. 6.1.2). Furthermore, both series 1 and 2 reveal lower EQEs than the standard etched reference. This loss is attributed to better light in-coupling of the etched reference due to the smaller feature sizes of the etch texture. Series 3 shows the best EQEs and  $J_{\text{sc}}^{\text{top}}$  of all DLIP textures. Due to the short etching step in the cleaning of the substrates for series 3, the DLIP texture is superposed with a texture of small cracks (also see Fig. 6.1 (c)). The small feature sizes of the cracks (better in-coupling) along with the better transmittance due to the removal of debris are assumed to be the reason for the gain in the top cell quantum efficiency (also see next paragraph about solar cell reflectance).

In the bottom cell and long wavelength region ( $\lambda = 600 \text{ nm}$  to  $1100 \text{ nm}$ ), light trapping plays a more significant role. Here, series 1 cells have a similar if not slightly better EQE than the cells of series 2. It is assumed that the deeper

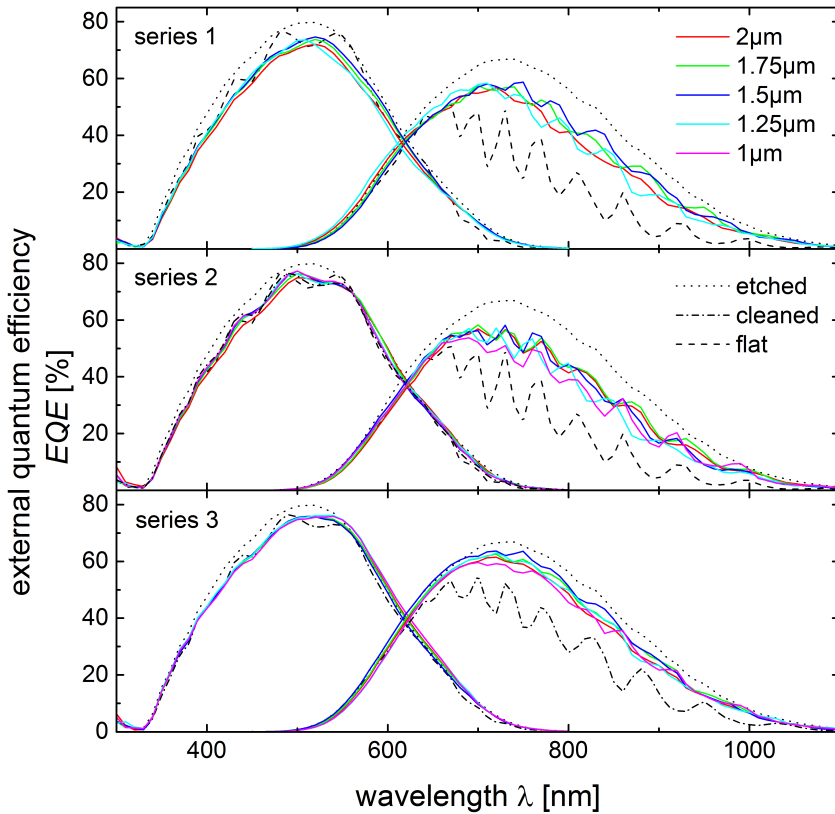


**Figure 6.7** External quantum efficiency of solar cells: Comparing series 1 and 2, the cells of series 2 show a higher EQE in the top cell and similar or slightly lower EQE in the bottom cell (also compare short-circuit current densities in Tab. 6.2). Series 3 shows the highest EQE compared to the other DLIP cells, but does not reach the level of the standard etched reference. Within each series, a slight trend favoring the  $\Lambda \approx 1.5 \mu\text{m}$  and  $\Lambda \approx 1.75 \mu\text{m}$  periodicities can be observed.

Series	$\Lambda$ [ $\mu\text{m}$ ]	$h_{\text{max}}$ [nm]	$J_{\text{sc}}^{\text{top}}$ [mA/cm <sup>2</sup> ]	$J_{\text{sc}}^{\text{bot}}$ [mA/cm <sup>2</sup> ]	$J_{\text{sc}}^{\text{sum}}$ [mA/cm <sup>2</sup> ]
etched			10.80	12.56	23.36
cleaned			10.05	8.76	18.81
flat			9.92	7.17	17.09
1	2	295	9.42	10.10	19.52
1	1.75	285	9.71	10.48	20.19
1	1.5	275	9.87	10.66	20.53
1	1.25	250	9.46	10.35	19.81
1	1	170	–	–	–
2	2	175	10.13	10.20	20.33
2	1.75	230	10.21	10.46	20.67
2	1.5	220	10.11	10.30	20.41
2	1.25	175	10.16	9.82	19.98
2	1	130	10.13	9.66	19.79
3	2	295	10.40	11.16	21.56
3	1.75	285	10.37	11.52	21.89
3	1.5	275	10.25	11.86	22.11
3	1.25	250	10.59	11.20	21.79
3	1	170	10.49	10.97	21.46

**Table 6.2** Overview of short-circuit current densities of solar cells: The texture’s spatial periodicity  $\Lambda$  obtained by SEM measurements, the approximate maximum texture depth  $h_{\text{max}}$  obtained by AFM measurements, the short-circuit current density of top and bottom cell calculated from EQE measurements ( $J_{\text{sc}}^{\text{top}}$  and  $J_{\text{sc}}^{\text{bot}}$  respectively) as well as their sum  $J_{\text{sc}}^{\text{sum}} = J_{\text{sc}}^{\text{top}} + J_{\text{sc}}^{\text{bot}}$  are specified.

textures of series 1 lead to better light trapping which is reflected in a greater EQE of the bottom cell and thus, a greater  $J_{\text{sc}}^{\text{bot}}$ . The gain due to the improved light trapping partially even overcompensates the generally lower transmittance of series 1 (see Sec. 6.1.2). Series 3 shows the possible potential of the DLIP textures. Assuming that the change of texture due to the cleaning does not have a large effect on the light trapping (the size of the cracks is comparably small to the wavelength of the light), the gain of EQE and  $J_{\text{sc}}^{\text{bot}}$  in series 3 is mainly attributed to the better transmittance of the cleaned substrate. However, the DLIP textures of series 3 still show lower EQEs than the etched reference.

Nevertheless, it has to be kept in mind, that the covering of the substrate with the texture is very inhomogeneous (see Sec. 6.1.1). Parts of the substrate

remain untextured and in others only a very shallow texture exist. An optimized experimental setup and laser process can lead to a higher homogeneity of the texture on the substrate as well as to less debris on the samples surface.

**Reflectance** Fig. 6.8 shows the spectra of total reflectance of cells in series 1 to 3. The measurements of the reflectance of the solar cells help to better understand the optical properties of the textured layers. Losses in quantum efficiency can be further investigated and parasitic absorption or reflection due to insufficient light in-coupling can be distinguished. Furthermore, the reflectance in the long wavelength region can be used to obtain a measure for the light trapping efficiency of a solar cell. All reflectance measurements of the DLIP-textured cells show interference effects throughout the whole spectrum. However, since the exact position of the maxima and minima is a result of many overlaying interference and modal effects, they are not further employed for interpretation.

In the short wavelength region, the solar cells of series 1 and 2 both show higher reflectance than the etched reference. This underlines the assumption that insufficient light in-coupling of the DLIP textures is the reason for the loss of EQE in the short wavelength region when compared to the etched reference. The reduction of reflectance when compared to the flat reference, however, indicate an improved light in-coupling due to the laser texturing. The cells of series 3 in the short wavelength region reveal a reflectance similar to the etched reference. It can be assumed that the crack formation due to the cleaning step leads to better in-coupling abilities. The persisting loss of EQE in the very short wavelength region (when compared to the etched reference) is attributed to a higher parasitic absorption in the ZnO:Al layer of the DLIP-textured substrate. This loss of transmission is also reflected in the transmission measurements of the ZnO:Al layers (see Fig. 6.5 and Tab. 6.1).

In the long wavelength region, the reflectance of all DLIP cells is significantly lower than the flat reference, which suggests improved light trapping properties due to the laser texturing. However, the etched reference reveals an even lower reflectance which is also reflected in the higher EQE in the bottom cell (see Fig. 6.7).

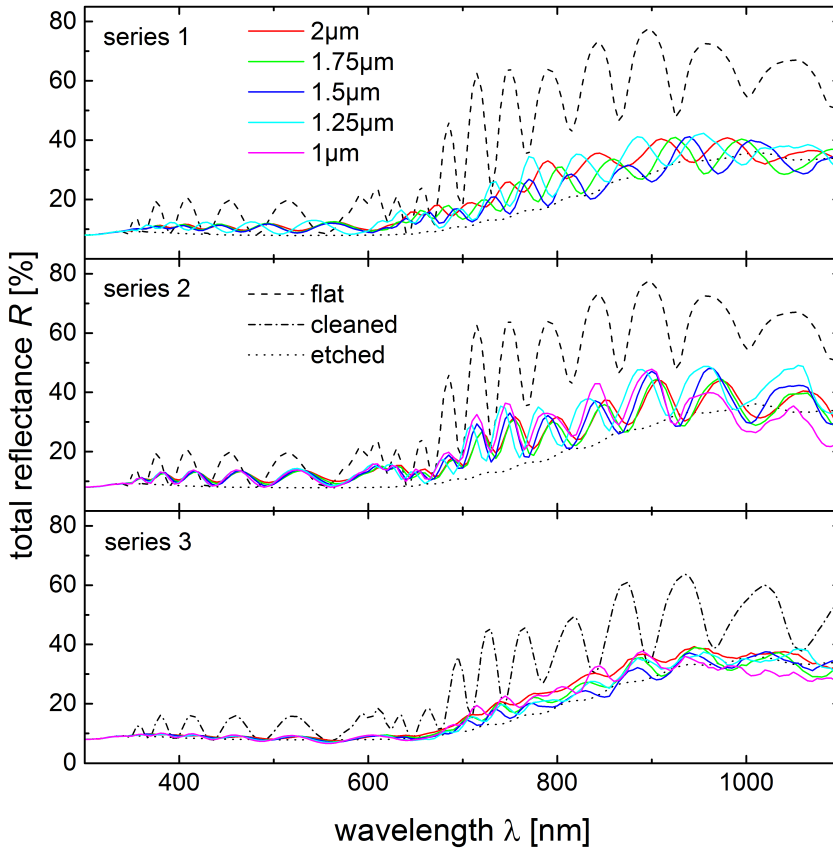


**Figure 6.8** Reflectance of solar cells: All DLIP textures show lower reflectance than the flat reference. Compared to the etched reference, series 1 and 2 show higher reflectance in the whole wavelength region. The reflectance of series 3 is generally lower than the ones of series 1 and 2. In the short wavelength region it is similar to the etched reference.

**J-V Characteristics** In order to proof the functionality of the created solar cells, the J-V characteristics of the layer stack under standard illumination with the solar spectrum (AM1.5) was determined (See Sec. 2.1.1). The J-V curves for series 1, 2 and 3 are depicted in Fig. 6.9. The determined cell parameters are presented in Tab. 6.3. It can be observed that while the short-circuit current density  $J_{sc}$  is similar for the cells in series 1 and 2, the open-circuit voltage  $V_{oc}$  is slightly higher in series 2. This could be attributed to a better layer growth on the slightly less textured low-power series 2. Series 3 on the other hand has a strongly deteriorated  $V_{oc}$ . Some cells show a  $V_{oc}$  more than  $\Delta U = 100$  mV worse than that of the flat as well as cleaned reference cells. Again, no significant trend within the cells of a series could be determined.

Series	$\Lambda$ [nm]	$V_{oc}$ [mV]	$J_{sc}$ [mA/cm <sup>2</sup> ]	FF %	$\eta$ %
etched		1390	11.74	70.23	11.46
cleaned		1390	9.65	77.41	10.39
flat		1416	7.65	81.63	8.84
1	2	1386	10.30	68.29	9.75
1	1.75	1387	10.52	69.34	10.12
1	1.5	1378	10.69	68.87	10.15
1	1.25	1390	10.46	68.48	9.96
1	1	–	–	–	–
2	2	362	10.64	62.25	2.40
2	1.75	1392	10.97	68.96	10.54
2	1.5	1401	10.72	69.84	10.49
2	1.25	1392	10.47	70.85	10.33
2	1	1402	10.17	71.94	10.26
3	2	1242	11.40	59.80	8.66
3	1.75	1293	11.39	60.26	8.88
3	1.5	1308	11.14	61.55	8.97
3	1.25	1242	11.50	59.80	8.55
3	1	1256	11.34	60.33	8.59

**Table 6.3** Overview of cell parameters: Open-circuit voltage  $V_{oc}$ , short-circuit current density  $J_{sc}$ , fill factor FF and solar cell efficiency  $\eta$  measured with sun simulator. Due to the mismatching of some of the cells, the values of fill factor and solar cell efficiency only have limited significance.

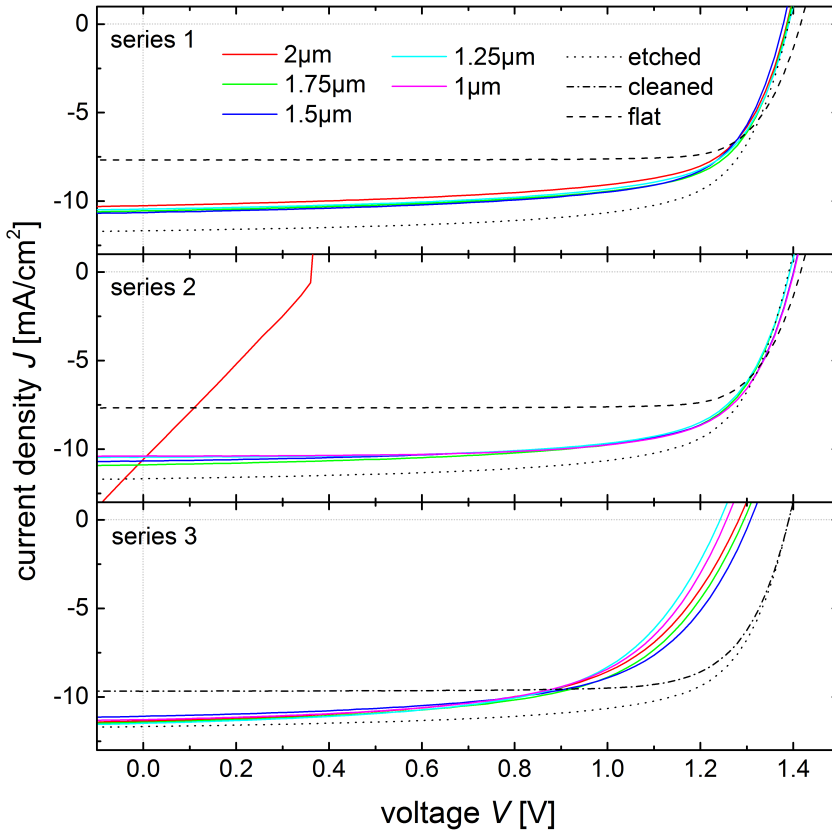


**Figure 6.9** J-V characteristics of solar cells under illumination with AM1.5: While the short-circuit current  $J_{sc}$  density is similar for cells of series 1 and 2, the open-circuit voltage  $V_{oc}$  is slightly higher in cells of series 2. Series 3 shows the highest  $J_{sc}$  but a deteriorated  $V_{oc}$ . An overview of the measured cell parameters can be found in Tab. 6.3.

## 6.3 Conclusion

Fully functional solar cells can be deposited on DLIP-textured substrates without growth or adhesion problems. In general, the cells show better light trapping abilities than the flat reference cells but worse light trapping abilities than the standard etched reference cells. However, neither the texturing process nor the layer stack of the solar cell were optimized for efficiency. Consequently, the results must not be taken as a benchmark for the potential of the process but merely demonstrate the applicability of DLIP textures in thin-film silicon solar cells.

**Effects of Periodicity** Taking the short-circuit current densities of the bottom cell as a measure for the light trapping abilities of the cells, within each of the three series, a slight trend with a maximum in the region of  $\Lambda = 1.5 \mu\text{m}$  and  $\Lambda = 1.75 \mu\text{m}$  is observed. An explanation for such a trend could be that, on the one hand, smaller texture periodicities lead to diffraction of the incoming light in larger angles and hence, improve light trapping. On the other hand, due to the heat diffusion within the ZnO:Al during the laser process, the DLIP texture is less pronounced for smaller periodicities (see Sec. 5.3.2). This again leads to lower light intensity in the diffracted beam paths. Accepting the measurement data, the best trade-off in between these two effects is in the region of  $\Lambda = 1.5 \mu\text{m}$  to  $1.75 \mu\text{m}$ . However, these trends are very marginal and can also be purely due to experimental variations during the stitching of the laser spots (see Sec. 6.1.1).

**Effects of Depth** Investigating the impact of the texture depth, it is assumed that the deeper textures of series 1 lead to better light trapping abilities than the ones of series 2. In the long wavelength region, the better light trapping even slightly overcompensates the loss of EQE due to the generally lower transmittance of series 1. However, due to the more difficult growth of silicon on the deeper textures, also the  $V_{oc}$  slightly lessens.

**Effects of Cleaning** In order to further explore the potential of the light trapping abilities of the deeper textures, the substrates of series 3 were cleaned to regain transmittance. The cleaning of the substrates (0.5% HCl for  $t = 1 \text{ s}$ ) revealed undesired effects on the topography of the ZnO:Al layer. In areas of previously melted and resolidificated ZnO:Al, strong crack formation occurred during the cleaning process. These cracks are assumed to negatively affect the growth of the a-Si:H p-layer which is the first layer deposited onto the ZnO:Al (see Fig. 6.6 (a)). The potentially malfunctioning a-Si:H p-layer then impedes the formation of a sufficiently large electric field in the top cell. As a consequence, the  $V_{oc}$  of the whole device decreases. Nevertheless, the cleaning of the substrates led to the

desired regain of transmittance of the ZnO:Al layer (Fig. 6.5) and thus, to an increased solar cell EQE (Fig. 6.7).

**Potential of DLIP process** Assuming that the crack formation only marginally influences the light trapping abilities, the cells of series 3 can be used to obtain an estimation for the potential of the DLIP process. The measured EQEs are higher than any of the ones of the uncleaned DLIP textures. However, even the highest short-circuit current densities within all DLIP textures do not fully reach the level of the ones of standard etched cells. It has to be kept in mind, however, that due to the experimental restraints the substrates were covered very inhomogeneously (see Sec. 6.1.1). A more sophisticated experimental setup with a tailored laser process could produce a more homogeneous coverage of textures and reduce debris formation at the same time. Both of these effect could further improve the quantum efficiency of deposited solar cells.

Finally, it has to be emphasized that the cells constructed in the framework of this thesis were deposited according to standard recipes for cells optimized for the standard etch texture. No optimization of the layer thicknesses or the general deposition process for cells on DLIP textures was carried out. Furthermore, with the given experimental DLIP setup and the Gaussian shaped laser beam, the substrates could only be covered inconsistently and inhomogeneously. Consequently, the cells cannot be interpreted as a benchmark for the DLIP process. They merely serve as a proof of concept that DLIP patterning can be introduced in the manufacturing process of thin-film silicon solar cells and fully functional solar cells can be created.



# 7 DLIP Potential

The preceding chapter demonstrated that DLIP-textured ZnO:Al layers can be used for the production of thin-film silicon solar cells. However, it remains unclear how the different textures influence the performance of the solar cell, which of the numerous textures promises the best performance, and what is the potential of the DLIP process when loosening the constraints of the current experimental setup.

The following section introduces the light trapping efficiency *LTE* as a measure for the light trapping ability of a given texture when implemented in a solar cell. To validate the light trapping efficiency, the results of the solar cell characterization are compared with the calculated *LTE* of the textures used for construction of the cells. By means of the light trapping efficiency, it is then investigated how the different setup parameters, and thus texture geometries, influence the light trapping ability of the texture. In the third section, a global optimization is used to determine the set of setup parameters which is capable of producing the texture with the best light trapping abilities within the limits of the existing experimental setup. Finally, an outlook of the potential of the process is provided by also taking into account multi-pulse processes and short laser pulses durations.

## 7.1 Light Trapping Efficiency

**Motivation** To judge the effectiveness of a given texture when used for light trapping, different methods can be applied. A simple method is to compare the measured amount of diffusely scattered light to the amount of totally transmitted. However, this so called haze value (see Sec. 3.1.2) has revealed to only have very limited predictive power for the efficiency of a solar cell built upon the texture [53, 89]. Another approach is the rigorous solving of the Maxwell equations for the given geometry by finite-difference time-domain (FDTD) methods. However, such simulations pose a very high demand on computing power and, at the time being, cannot be used to predict the scattering abilities of the numerous possible textures. The phase model and the derived light trapping efficiency (Sec. 2.1.3), on the other hand, offer a good compromise in between required computing power and reliability of results. It can be determined without measurements,

only requires limited computing power and has shown to correlate with solar cell efficiency [12].

### 7.1.1 Calculation of $LTE$ and $LTE_{\text{eff}}$ (PyLTE)

**PyLTE** The light trapping efficiency  $LTE$  was determined according to the phase model (see Sec. 2.1.3). In the wavelength range from  $\lambda_0 = 600$  nm to  $\lambda_N = 900$  nm and steps of  $\Delta\lambda = 10$  nm the  $LTE$  was calculated according to Eq. 2.11. The calculations were carried out numerically and were implemented in a module named *PyLTE*. *PyLTE* can be integrated in the existing simulation framework to allow an integrated calculation of the  $LTE$  value starting from the setup parameters (compare Fig. 1.1 in Introduction). The processing times<sup>1</sup> to calculate a light trapping efficiency for a given set of setup parameters were on the order of  $t_{\text{calc}}^u \approx 0.6$  s for unit grids and  $t_{\text{calc}}^{nu} \approx 25$  s for non-unit grids, depending on the grid size and resolution. If not otherwise stated, all calculations were carried out on unit grids.

**Effective Light Trapping Efficiency** By the phase model, a  $LTE$  value can be assigned to a given texture. However, when using DLIP, the texture on the substrates varies due to the stitching of the laser spots as well as the inherently inhomogeneous fluence distribution within a Gaussian laser beam (see Sec. 6.1.1). Consequently, no strictly defined  $LTE$  can be determined for the macroscopic texture distribution which is used for the building of a solar cell. To adapt the light trapping efficiency for the use with DLIP, the concept of an effective light trapping efficiency  $LTE_{\text{eff}}$  was derived. The  $LTE_{\text{eff}}$  aims to represent the distribution of different textures in a distribution of different corresponding  $LTE$  and calculates a weighted average of these  $LTE$  according to their areal fraction on the substrate (also see Fig. 7.1). The total fluence range from the maximum  $\Phi_0^{\text{pk}}$  to a given minimum  $\Phi_0^{(N)}$  is divided into  $N$  equidistant parts  $\Phi_0^{(i)}$ . All of these values with odd indices  $2i + 1$  are weighted with the area of a ring  $A_{2i+1}$  resulting from the difference of the circular areas corresponding to the radii  $r_{2i}$  and  $r_{2i+2}$  of the adjacent even  $\Phi_0^{(2i)}$  and  $\Phi_0^{(2i+2)}$ .

In detail, the effective light trapping efficiency  $LTE_{\text{eff}}$  is calculated by

$$LTE_{\text{eff}}(\Phi_0^{(N)}, N) = 0.91 \cdot \frac{1}{\pi r_N^2} \cdot \sum_{i=1}^N LTE(\Phi_0^{(2i+1)}) \cdot A_{2i+1} \quad (7.1)$$

with

$$A_j = \pi r_{j+1}^2 - \pi r_{j-1}^2. \quad (7.2)$$

<sup>1</sup>on a standard laptop PC (Intel i5-2520M CPU, Win7 64bit OS)

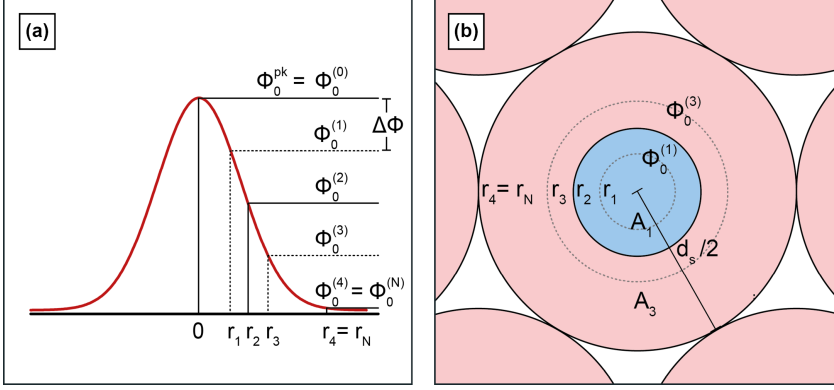


**Figure 7.1** Effective light trapping efficiency (illustrations): The effective light trapping efficiency  $LTE_{\text{eff}}$  takes into account the texture distribution within a Gaussian laser spot (a) and the stitching of laser pulses. By weighting the textures according to their areal fraction  $A_i$  (b), an averaged light trapping efficiency is calculated for macroscopic areas in dependence of the laser spot distance  $d_s$  in a hexagonal lattice.

The factor 0.91 accounts for the approximate 9% of the total area that remains untextured in a perfect hexagonal stitching (see Sec. 6.1.1).

The sampling radii  $r_i$  are defined by

$$\Phi_0(r_i) = \Phi_0^{(i)}, \quad (7.3)$$

whereas the sampling points  $\Phi_0^{(i)}$  are defined by

$$\Phi_0^{(0)} = \Phi_0^{\text{pk}} \quad \text{and} \quad \Phi_0^{(i+1)} - \Phi_0^{(i)} = \Delta\Phi = \text{const} \quad \forall i, \quad (7.4)$$

as well as the total amount of sampling points  $N$  and the outer limit  $\Phi_0^{(N)}$ .

The local light trapping efficiency  $LTE(\Phi_0^{(i)})$  is calculated from the given setup parameters and an adapted total laser power  $P_L$ , so that the local fluence spatially averaged within the interference pattern results in  $\Phi_0^{\text{mean}} = \Phi_0^{(i)}$ .

### 7.1.2 Comparison with Solar Cells

In order to investigate the predictive power of  $LTE_{\text{eff}}$ , it was compared to the results of the solar cell characterization. The short-circuit current density of the bottom cell  $j_{\text{sc}}^{\text{bot}}$  can be used as a measure for the light trapping abilities of a

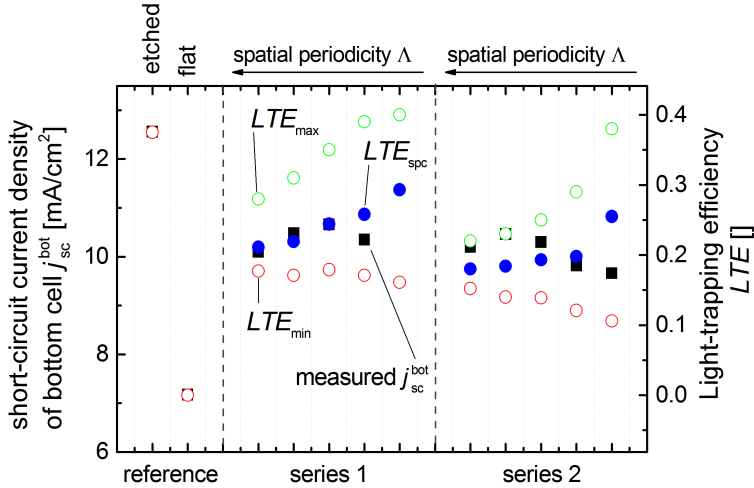


**Figure 7.2** Comparison of measured solar cell performance and calculated light trapping efficiency: The specific light trapping efficiency  $LTE_{spc}$  is in good agreement with the corresponding short-circuit current densities of the bottom cells  $j_{sc}^{bot}$ . The values of  $LTE_{max}$  and  $LTE_{min}$  show the potential influence of the stitching procedure. The scale for the light trapping efficiencies was calibrated according to reference measurements with flat and etched textures. Within each series, the spatial periodicities from left to right are  $\Lambda = 2 \mu\text{m}$ ,  $1.75 \mu\text{m}$ ,  $1.5 \mu\text{m}$ ,  $1.25 \mu\text{m}$  and  $1 \mu\text{m}$ .

solar cell and also directly correlates with the solar cell efficiency  $\eta$  [12] (see Sec. 2.1.3).

**Maximal, Minimal and Specific Light Trapping Efficiency** Fig. 7.2 shows a comparison of  $j_{sc}^{bot}$  and different types of light trapping efficiencies which take into account different types of laser pulse stitching. The light trapping efficiencies were calculated from a set of setup parameters by means of *VLIP* and *PyLTE*. The scale for the light trapping efficiencies was calibrated by calculating the  $LTE$  of a standard etched as well as a flat reference texture and setting these values equal to the corresponding experimental results (reference-section in Fig. 7.2). For the DLIP-textures three types of light trapping efficiencies values were calculated:

- The maximal light trapping efficiency  $LTE_{\max}$  is the light trapping efficiency calculated for the texture at the center of the laser spot where  $\Phi_0 = \Phi_0^{\text{pk}}$ :

$$LTE_{\max} = LTE(\Phi_0^{\text{pk}}). \quad (7.5)$$

- The minimal light trapping efficiency  $LTE_{\min}$  is the effective light trapping efficiency calculated for a hexagonal stitching with a spot distance  $d_s = r_s^{\text{th}}$  whereas  $r_s^{\text{th}}$  is the spot radius at the position where the fluence  $\Phi_0$  has dropped to the threshold level for ablation  $\Phi_{\text{th}}^{\text{eff}}$ :

$$LTE_{\min} = LTE_{\text{eff}}(\Phi_0^{(N)} = \Phi_{\text{th}}^{\text{eff}}, N = 100). \quad (7.6)$$

- The specific light trapping efficiency  $LTE_{\text{spc}}$  is calculated for the very specific experimental setup and stitching like it was used for the production of the solar cells<sup>2</sup>. It is the effective light trapping efficiency calculated for a hexagonal stitching with a spot distance  $d_s = r_s^{\text{vis}}$ , whereas  $r_s^{\text{vis}}$  is the visible spot radius as determined with the optical microscope during the manufacturing of the solar cells (see Sec. 6.1.1). Consequently, the stitching is different for each texture due to the individual  $r_s^{\text{vis}}$ . The specific light trapping efficiency is calculated by

$$LTE_{\text{spc}} = LTE_{\text{eff}}(\Phi_0^{(N)} = \Phi_0(r_s^{\text{vis}}), N = 100). \quad (7.7)$$

### 7.1.3 Discussion

**Specific light trapping efficiency** The specific light trapping efficiency  $LTE_{\text{spc}}$  in general shows good agreement with the measured  $j_{\text{sc}}^{\text{bot}}$ . For all of the cells of series 1 (high power), measurement and simulation are very well matched. The slight deviation of the cell with the smallest spatial periodicity is assumed to be due to the large amount of debris and particles at these periodicities and high powers (see Sec. 5.3.3). The cells of series 2 (low power) are underestimated for large spatial periodicities and overestimated for small periodicities. The underestimation is assumed to be due to the bulges and other detailed topography which is not reproduced by the ablation model (also see corresponding textures in Fig. 6.1 (b)). These small features also have an influence on the light scattering and could improve the light trapping abilities of the real texture. These features are not represented in the virtual textures used for the calculation of  $LTE_{\text{spc}}$  and thus, the measured  $j_{\text{sc}}^{\text{bot}}$  is higher than expected. The overestimation at smaller periodicities, on the other hand, is assumed to be due to the vanishing of the small features and the increase of debris during the laser process. However, the

<sup>2</sup>Experimental instabilities and variations were not taken into account for the calculations.

calculation of  $LTE_{\text{spc}}$  strongly depends on the assumed stitching process. Due to the high instabilities of the experimental setup and the inhomogeneous stitching (also see Fig. 6.3) the deviations of simulation and experiment could also purely be due to experimental issues.

**Minimal and Maximal light trapping efficiency** To further highlight the strong influence of the stitching process, the quantities  $LTE_{\text{max}}$  and  $LTE_{\text{min}}$  are plotted in Fig. 7.2. Both quantities are calculated from the same set of setup parameters and merely show the influence of the stitching process. Although they do not strictly represent maxima and minima values, they can be interpreted as such.

The quantity  $LTE_{\text{min}}$  is calculated by assuming that the laser spots are positioned at a distance so no double texture exists. The spot distance is chosen to be  $d_s = 2r(\Phi_{\text{th}}^{\text{eff}})$ , so the texture of one laser spot is completely vanished ( $\Phi_0 = \Phi_{\text{th}}^{\text{eff}}$ ) until the texture induced by the adjacent spot begins. However, practically a large area towards the outside of the laser spot does not actively contribute to the light scattering – albeit showing a shallow texture. So, while such a stitching has a well defined spot distance  $d_s$ , it is not very suited for practical use. Nevertheless, it can be used to define a minimum for the effective LTE.

The quantity  $LTE_{\text{max}}$ , on the other hand, represents the light trapping efficiency in the very center of the laser spot. Covering of macroscopic areas with that texture is not possible without double textures. However, by using a different experimental setup with a smaller spot radius steeper flanks in the Gaussian beam profile can be achieved. A tighter stitching would then improve the areal fraction of the deeper textures (like the ones in the center of the Gaussian). Summarizing, it can be stated that although the homogeneous covering of large areas with the single texture corresponding to  $LTE_{\text{max}}$  cannot be achieved,  $LTE_{\text{max}}$  can be used to obtain a picture for the potential of a given texture. Consequently,  $LTE_{\text{max}}$  is used as a measure for the light trapping abilities of a given texture in the following sections.

### 7.1.4 Conclusion

To adapt the concept of the light trapping efficiency  $LTE$  to laser textured surfaces, the quantities  $LTE_{\text{eff}}$ ,  $LTE_{\text{spc}}$  and  $LTE_{\text{max}}$  were developed. However, all of these are mere applications of the underlying, generic light trapping efficiency  $LTE$ .

The effective light trapping efficiency  $LTE_{\text{eff}}$  takes into account the inhomogeneous fluence distribution in a Gaussian laser beam as well as stitching effects induced

by macroscopic texturing. Consequently,  $LTE_{\text{eff}}$  strongly depends on the assumed beam profile and stitching parameters.

The specific light trapping efficiency  $LTE_{\text{spc}}$  is a special case of an effective light trapping efficiency. It is the  $LTE_{\text{eff}}$  calculated according to the exact beam profile and stitching parameters used for the manufacturing of the solar cells and thus, represents the actually expected light trapping efficiency for this specific experimental setup. Accordingly, it can be used for an experimental verification of the predictions of *PyLTE*. Calculated  $LTE_{\text{spc}}$  and experimental data from the characterization of the DLIP solar cells (Chap. 6) are in good agreement. Consequently, it can be assumed that the concept of the light trapping efficiency can also be applied on DLIP textures and the estimations by *PyLTE* offer a reliable measure for the light trapping potential.

The  $LTE_{\text{max}}$  represents the light trapping efficiency of a given texture without taking into account the macroscopic texture variations induced by a specific beam profile and pulse stitching. Consequently, to obtain a picture of the potential of a given texture, the  $LTE_{\text{max}}$  can be used as a scale.

However, it has to be kept in mind that the light trapping efficiency is based on a very rough model of the light trapping within a solar cell and cannot perfectly reflect the potential of a given texture. Accordingly, the  $LTE$  values stated in the following sections should not be overrated. Nevertheless, the light trapping efficiency offers a good measure for an estimation of the light trapping potential.

## 7.2 Influence of Setup Parameters on Light Trapping Efficiency

In the following section, the influence of the various setup parameters and their corresponding texture properties on the light trapping behavior of the textured layer are investigated. To obtain a feeling for the influence of certain parameters, parameter scans are evaluated. Different pairs of setup parameters are varied while leaving the other parameters unchanged. For each set of parameters, the light trapping efficiency  $LTE_{\text{max}}$  is used as a measure for the potential light trapping abilities. The trends of altering light trapping efficiency due to a change in setup parameters are evaluated and discussed. All light trapping efficiency values stated in this chapter are  $LTE_{\text{max}}$  values, however due to their functionality as indicator for light trapping abilities as well as reasons of simplicity, they are simply referred to as  $LTE$ .

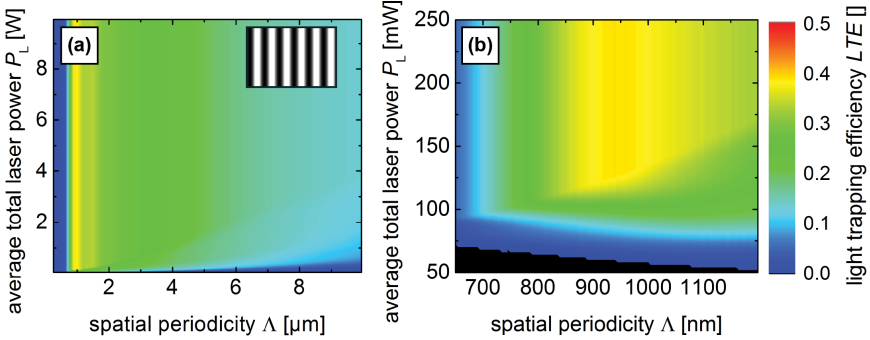


**Figure 7.3** Light trapping efficiency  $LTE$  in dependence of laser power  $P_L$  and spatial periodicity  $\Lambda$  for line-like textures ((a) Overview, (b) Detail): From the maximum at around  $\Lambda_{\text{opt}}^1 \approx 950$  nm, the light trapping efficiency decreases towards smaller periodicities due to the decreasing texture depth. Larger  $\Lambda$  lead to smaller diffraction angles and also decrease the  $LTE$ . Up to a periodicity dependent threshold power  $P_{\text{th}}(\Lambda)$ , more power leads to higher  $LTE$ . Beyond  $P_{\text{th}}$ , the  $LTE$  is not further increased by augmenting laser power. Highest  $LTE$  were achieved around  $\Lambda_{\text{opt}}^1 \approx 950$  nm and  $P_{\text{opt}}^1 \approx 130$  mW. The inset shows an exemplary texture for quick comparison.

## 7.2.1 Periodicity and Total Power

The variation of the z-position of the beam interference point  $z_{\text{int}}$  and the Q-switch delay time  $\tau_Q$  results in a variation of the spatial periodicity  $\Lambda$  of the texture and the total laser power  $P_L$ . Both of which have an influence on the texture depth  $h$ . For the two typical textures of line-like and hexagonal dent-like pattern, parameter scans of  $P_L$  and  $\Lambda$  were conducted.

The total laser power of the experimental setup used for the experiments within this thesis is limited to  $P_L^{\text{max}} = 150$  mW. However, this is a fairly soft limitation which could be loosened by simple alterations of the setup. By a redesign of the beam shaping unit, the use of fewer mirrors or stronger focusing of the laser beam, the setup would loose flexibility but gain the capability to produce higher fluences. To investigate if such alterations can be advantageous, the laser power is not limited to  $P_L^{\text{max}} = 150$  mW in the following parameter scans. The assumed maximum of  $P_L^{\text{max}} = 10$  W corresponds to a fluence of  $\Phi_0^{\text{mean}} \approx 40$  J/cm<sup>2</sup> which is not industrial feasible but can be achieved by current laser systems and corresponding focusing.

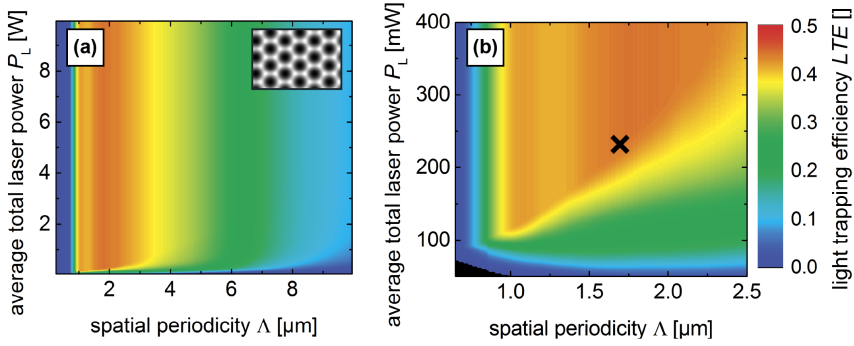


**Figure 7.4** Light trapping efficiency  $LTE$  in dependence of laser power  $P_L$  and spatial periodicity  $\Lambda$  for dent-like textures ((a) Overview, (b) Detail): Similar to Fig. 7.3, a threshold laser power  $P_{th}(\Lambda)$  can be observed and the light trapping efficiency decreases towards small and large values of  $\Lambda$ . However, generally  $LTE$  values are higher and the maximum is shifted to larger  $\Lambda$  and  $P_L$ . Highest  $LTE$  were achieved around  $\Lambda_{opt}^d \approx 1700$  nm and  $P_{opt}^d \approx 230$  mW. The cross marks the parameter set used as a reference for the following parameter scans. The inset shows an exemplary texture for quick comparison.

The spatial periodicity of the line-like textures is limited to a minimum of  $\Lambda_{min}^1 = 178$  nm due to the geometry of the interfering beams in a two-beam setup (see Eq. 2.41). For the dent-like texture, the periodicity is limited to  $\Lambda_{min}^d = 205$  nm for similar reasons. The parameter scans were limited accordingly. The results for scans over great and small parameter ranges are depicted in Fig. 7.3 and 7.4.

**Spatial Periodicity** Concerning the spatial periodicity  $\Lambda$ , two contrary trends can be observed for both of the textures. On the one hand, in the region of large periodicities, the light trapping efficiency lessens with increasing periodicity. On the other hand, for small periodicities, the light trapping efficiency lessens with decreasing periodicity. The first trend is assumed to be due to the less efficient light scattering of feature sizes  $d_{feat} > \lambda$ . However, this trend is suppressed in the region of small periodicities. Here, the texture depth strongly diminishes with decreasing  $\Lambda$  due to heat diffusion. Consequently, also the scattering abilities of the texture decrease and the light trapping efficiency lessens. Accepting the data, the best trade-off in between the two trends is at  $\Lambda_{opt}^1 \approx 950$  nm for line-like textures and  $\Lambda_{opt}^d \approx 1700$  nm for dent-like textures.

**Total Power** Concerning the total applied laser power, it can be observed that for small powers the light trapping efficiency increases with increasing laser power. This is assumed to be due to the increase of laser fluence in the maxima of the interference pattern and the resulting deepening of the texture. However, for powers larger than a periodicity dependent threshold value  $P_{\text{th}}(\Lambda)$ , the light trapping efficiency ceases to increase and remains constant. This somewhat non-intuitive trend can be explained by the observation that also the texture depths remain constant for powers  $P_{\text{L}} > P_{\text{th}}(\Lambda)$ . Here, also the minima in the fluence distributions carry enough energy to ablate material. As the ratio of maximal and minimal fluence in a given interference pattern is constant and does not depend on the total laser power, also the texture depth remains constant (see Eq. 2.37 and Eq. 5.18). The texture depth can only be increased by increasing powers as long as the fluence in the minima of the given interference pattern remains below the ablation threshold. If the laser power is increased further, there is a constant, homogeneous energy intake in all of the material. Such energy intake is not desired, since it mainly leads to greater debris and particle generation (see Sec. 5.3.3). For the optimal spatial periodicities within the scan range  $\Lambda_{\text{opt}}$ , threshold powers of  $P_{\text{opt}}^{\text{l}} = P_{\text{th}}^{\text{l}}(\Lambda_{\text{opt}}^{\text{l}}) = 130 \text{ mW}$  and  $P_{\text{opt}}^{\text{d}} = P_{\text{th}}^{\text{d}}(\Lambda_{\text{opt}}^{\text{d}}) = 230 \text{ mW}$  were determined.

To investigate the influence of the other setup parameters, a reference set of setup parameters was chosen (see cross mark in Fig. 7.4). Starting from this set, other pairs of parameters are varied while leaving the other seven parameters constant.

## 7.2.2 Partial Beam Power

By changing the orientation of the half-wave plates W01 and W02, the partial beam powers  $P_{\text{L}}^{(j)}$  in the three beam paths can be adjusted. W01 controls the ratio of powers  $P_{\text{L}}^{(2)}$  and  $P_{\text{L}}^{(13)} = P_{\text{L}}^{(1)} + P_{\text{L}}^{(3)}$ , whereas W02 controls the ratio of  $P_{\text{L}}^{(1)}$  and  $P_{\text{L}}^{(3)}$ . The variation of the partial beam powers is especially interesting, because it induces a strong variation of interference pattern. The extreme cases of no interference and two-beam interference also lay within the scan range. The result of the parameter scan is depicted in Fig. 7.5. A large texture variety and diverse corresponding light trapping efficiencies can be observed. In the black areas all of the laser power is concentrated in one single partial beam only and no interference takes place at all. In the surrounding blue areas of very low *LTE*, the other beams begin to carry some energy and slight interference effects can be observed (top inset). If two partial beams carry a similar amount of laser power and the power of the third beam can be neglected, the resulting texture is of line-like character (middle inset). These type of textures lead to light trapping efficiencies on the order of  $LTE \approx 0.35$ . The highest light trapping efficiency

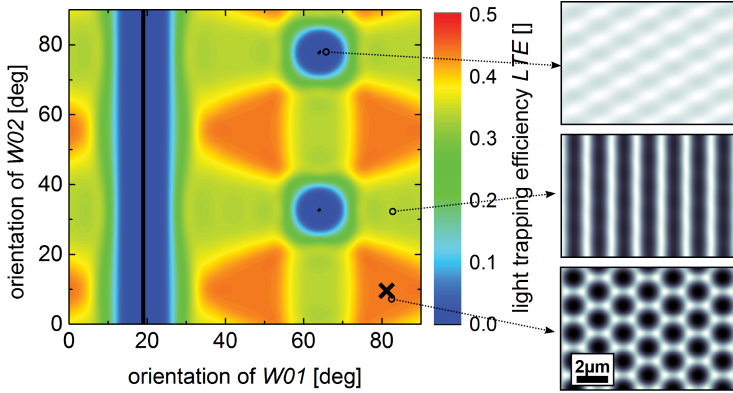


**Figure 7.5** Light trapping efficiency  $LTE$  in dependence of partial beam powers (parameter scan and virtual textures): Depending on the orientation of the wave plates  $W01$  and  $W02$ , the total beam power is distributed to the partial beams. Constellations leading to similar powers in all three beams result in dent-like textures (top inset). A distribution in mainly two beams only leads to line-like textures with lower  $LTE$  (middle inset). If only one partial beam carries most of the total power, the interference effects vanish resulting in a flat texture and very low  $LTE$  (bottom inset). The reference parameter set is marked with a cross.

within the parameter range ( $LTE = 0.44$ ) was obtained by the dent like textures of three equally strong partial beams, similar to the reference parameter set (cross mark in Fig. 7.5 and bottom inset).

### 7.2.3 Partial Beam Polarizations

By changing the orientation of the half-wave plates  $W12$ ,  $W22$  and  $W32$ , the orientation of the linear polarization of the partial beams is controlled. By individually adjusting the polarizations of the partial beams, the pairwise interference of the corresponding beams can be controlled (see Sec. 5.2.2). Polarization adjustments can be used to obtain fairly high contrast checkerboard-like pattern (see Fig. 5.9). In Fig. 7.6 a variation of the polarizations of beam 1 and 2 can be observed. The polarization of beam 3 is fixed at  $W32 = 45^\circ$  without further limiting the variety of possible textures. The changes of light trapping efficiency that can be induced by the polarization variation are not as drastic as with the partial beam powers. Again, the dent-like texture with equally aligned polarization of all three partial beams reveals the highest light trapping efficiencies of  $LTE \approx 0.44$  (see top inset).

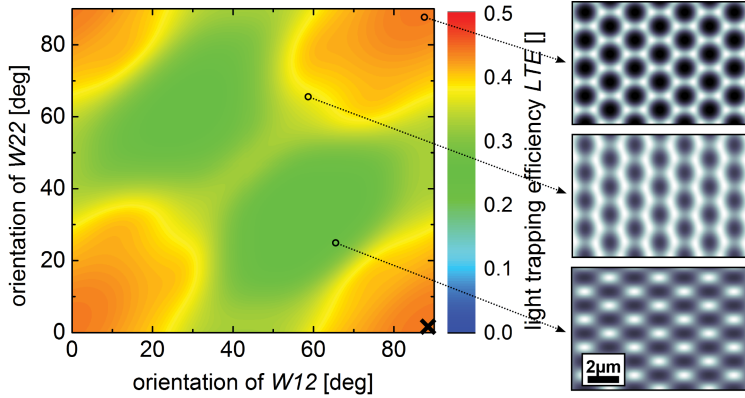


**Figure 7.6** Light trapping efficiency  $LTE$  in dependence of partial beam polarizations (parameter scan and virtual textures): The orientation of the half-wave plates  $W12$  and  $W22$  control the polarization of partial beam 1 and 2. By individually adjusting the polarizations, the pairwise interference can be controlled and various textures can be created (middle and bottom inset). However, the dent-like texture (top inset) achieves the highest  $LTE$  values. The reference parameter set is marked with a cross.

The checkerboard-like pattern (bottom inset) do not reach such high levels. By slightly favoring the interference of a pair of beams (here : beam 1 and 2), the light trapping efficiency also diminishes (see middle inset) when compared to the equally aligned polarizations.

### 7.2.4 Angle of Incidence

Fig. 7.7 depicts a parameter scan in which the position of the interference point was altered. By changing the x and y-position of the interference point  $x_{int}$ ,  $y_{int}$ , the texture can be stretched so it loses its hexagonal character. However, the changes that can be induced by the comparably small maximum offset of  $|x_{int}^{max}| = |y_{int}^{max}| = 100 \text{ nm}$  are very small (compare insets). Consequently, also the light trapping efficiency is almost equal for all of the textures within the parameter range. Due to the non-rectangular unit cells of the textures, the calculations of the light trapping efficiency needed to be carried out on non-unit grids. Accordingly, the presented data is affected by artifacts originating from the non-periodic boundary conditions in the Fourier transformation needed for the calculation of the  $LTE$ . The variation of the  $LTE$  within the ranges of the parameter scan

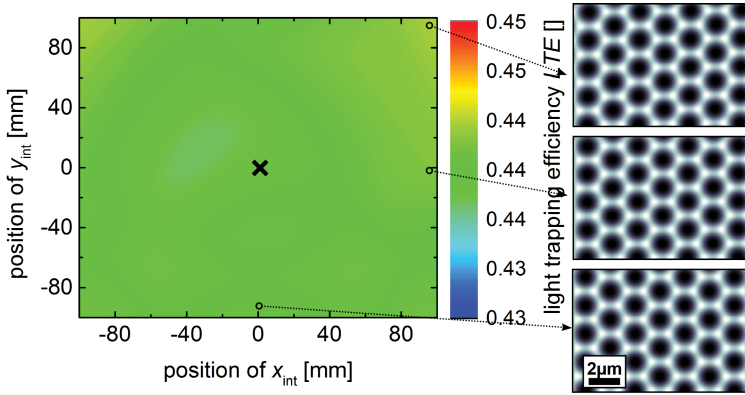


**Figure 7.7** Light trapping efficiency  $LTE$  in dependence of interference point shift (parameter scan and virtual textures): By changing the  $x$ - and  $y$ -coordinates of the interference point  $x_{\text{int}}$  and  $y_{\text{int}}$ , the angles of incidence of the partial beams are varied. The slight variations achievable within the limits of the experimental setup only translated to small changes in the textures (see insets). The variation of the resulting light trapping efficiency is marginal (note the different color bar). The reference parameter set is marked with a cross.

is on the order of the assumed error produced by these artifacts, so no definite statement on the significance of the variations can be made. Nevertheless, it can be concluded that within the scan range, the influence of  $x_{\text{int}}$ ,  $y_{\text{int}}$  on the light trapping efficiency is marginal.

### 7.2.5 Conclusion

In parameter scans of laser power and periodicity, a periodicity dependent maximum beneficial laser power  $P_{\text{th}}(\Lambda)$  can be observed. Laser powers above  $P_{\text{th}}(\Lambda)$  do not further contribute to a gain in  $LTE$ . The highest  $LTE$  values for line- and dent-like texture could be determined at spatial periodicities of  $\Lambda_{\text{opt}}^1 \approx 950$  nm and  $\Lambda_{\text{opt}}^d \approx 1700$  nm respectively. In all of the parameter scans, dent-like texture types revealed to be favorable to other types of texture, such as line-like or checkerboard-like textures. While they can be produced with different sets of setup parameters, they all correspond to equal partial beam powers, equally aligned polarizations, equally spaced azimuth, and equal polar angle of incidence. The resulting textures show similar values of  $LTE$  which are the highest within the scan ranges ( $LTE = 0.44$ ).

### 7.3 Global Optimization of Setup Parameters

In the preceding section, the influence of single pairs of setup parameters on the light trapping efficiency was investigated. This section aims to find a global optimum of all setup parameters for a given experimental setup. Three different experimental setups were investigated:

- (a) The exact experimental setup used in the framework of this thesis.
- (b) The same experimental setup as (a) but with a maximum laser power of  $P_L^{\max} = 1 \text{ W}$  which could be achieved by a redesign of the setup.
- (c) A notional simplified setup with perfect rotational symmetry as could be used for industrial application.

The higher maximum laser power  $P_L^{\max}$  in (b) was used, because it is assumed that by an improved redesign of the experimental setup<sup>3</sup> higher laser powers could be achieved at the sample. Experimental setup (c) assumes a setup with perfect rotational symmetry, equal beam powers in all three partial beams and maximal aligned polarizations of the beams at the sample. Such a setup yields perfect hexagonal dent-like textures and could be implemented in a more simple experimental setup for the use in industry. To simulate such a setup, the setup parameters were restricted accordingly.

**Optimization Procedure** The genetic optimization algorithm as introduced in Sec. 3.3 was applied to maximize the light trapping efficiency  $LTE$  by variation of all of the nine setup parameters. Each individual contained all nine setup parameters as attributes.

The fitness of each individual was evaluated by calculating the light trapping efficiency according to its setup parameters using *VLIP* and *PyLTE*. The grid used for the calculations was non-unit with dimensions  $x_{\max} = y_{\max} = 10 \mu\text{m}$  and  $256 \times 256$  pixels. The starting population consisted of  $n_{\text{pop}} = 5000$  individuals, whereas the first selection of the fittest individual was carried out by selecting the  $\mu = 2000$  individuals with the highest fitness value. In each generation  $\lambda = 1000$  individuals were selected for modification. Modification was carried out according to the probabilities  $p_x = p_{\pm} = 0.5$  and  $q_x = q_{\pm} = 0.5$ . A total of  $n_{\text{gen}} = 200$  generations were evaluated. Please refer to Sec. 3.3 for a detailed description of the algorithm and its parameters.

---

<sup>3</sup>Due to the inhomogeneous beam profile and the introduced beam shaping unit only about 5% of the output laser power reach the sample (see Sec. 5.1.2). By a redesign of the setup this could possibly be improved (also compare Sec. 7.2.1).

The boundary conditions of the attributes were chosen to resemble the limits of the given experimental setup<sup>4</sup>:

$x_{\text{int}} \in [-100, 100]$ mm	type = lin
$y_{\text{int}} \in [-100, 100]$ mm	type = lin
$z_{\text{int}} \in [50, 2500]$ mm	type = lin
$W12 \in [0, 90]^\circ$	type = lin
$W22 \in [0, 90]^\circ$	type = lin
$W32 \in [0, 90]^\circ$	type = lin
$W01 \in [0, 90]^\circ$	type = lin
$W02 \in [0, 90]^\circ$	type = lin
$P_L \in [0, 150/1000]$ mW	type = lin

**Results of Optimization** The resulting sets of setup parameter for each of the experimental setups under investigation are displayed in Tab. 7.1, the corresponding textures and their light trapping efficiencies are depicted in Fig. 7.8<sup>5</sup>. For each of the optimization results also the experimentally optimal laser power was determined. Since all total laser powers above the threshold power  $P_L > P_{\text{th}}$  lead to the exact same light trapping efficiency (see Sec. 7.2.1 or Fig. 7.9), the optimization algorithm converges in any value  $P_L > P_{\text{th}}$ . However, experimentally, the best laser power is around  $P_L = P_{\text{th}}$  for each given set of setup parameters. Higher powers do not lead to a further deepening of the texture but merely deposit excess energy into the material leading to debris and particles (see Sec. 5.3.3). To determine  $P_{\text{th}}$  for the resulting sets of setup parameters, parameter scans of  $P_L$  were conducted leaving the other setup parameters constant. The result of the scans is depicted in Fig. 7.9.

For the existing setup and a maximal laser power at the sample of  $P_L^{\text{max}} = 150$  mW (experimental setup (a)), the texture corresponding to the resulting setup parameters is depicted in Fig. 7.8 (a). It has a spatial periodicity of  $\Lambda^{(a)} = 1.20$   $\mu\text{m}$  and a texture depth of  $h = 208$  nm. In appearance it is very close to a dent-like texture, but shows a small break in symmetry and a preferred direction. The light trapping efficiency of the texture calculates to  $LTE = 0.426$ .

<sup>4</sup>For experimental setup (a), the total laser power was limited to  $P_L^{\text{max}} = 150$  mW, for (b) and (c) to  $P_L^{\text{max}} = 1000$  mW. For setup (c), the setup parameters were further restricted to only produce the assumed beam properties.

<sup>5</sup>The evolution of the average and maximum fitness within the population for each generation draws a similar picture as depicted in Fig. 5.19 and is not displayed for reasons of brevity.

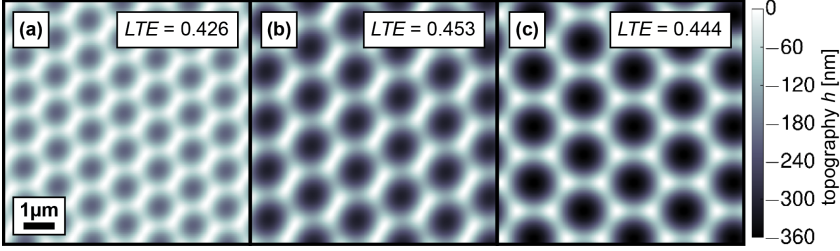


**Figure 7.8** Textures corresponding to optimized sets of setup parameters and their values of  $LTE$  (simulations): (a) For the existing setup, the lowest light trapping efficiency is scored. (b) By allowing higher laser power, a slightly higher light trapping efficiency is achieved. (c) By limiting the experimental setup to a strongly simplified version, only slightly worse light trapping efficiencies can be achieved.

Loosening the constraints of the experimental setup and assuming  $P_L^{\max} = 1$  W (experimental setup (b)), a different set of setup parameters is favored by the algorithm. The corresponding texture has a spatial periodicity of  $\Lambda^{(b)} = 1.59 \mu\text{m}$  and a texture depth of  $h = 309$  nm (Fig. 7.8 (b)). Apart from the different periodicity and texture depth, in appearance it is very close to the resulting texture for setup (a). The light trapping efficiency of the texture calculates to  $LTE = 0.453$

For a potential industrial application, the simplicity of the experimental setup is relevant. In order to determine the best achievable textures for a setup with rotational symmetry ( $x_{\text{int}} = y_{\text{int}} = 0$ ), equal laser powers in the partial beams ( $P_L^{(1)} = P_L^{(2)} = P_L^{(3)}$ ) and maximal aligned polarization of the beams at the sample ( $\gamma^{(1)} = \gamma^{(2)} = \gamma^{(3)}$ ), the setup parameter were constraint accordingly. The resulting texture of the optimization is depicted in Fig. 7.8(c). It has a spatial periodicity of  $\Lambda^{(c)} = 1.81 \mu\text{m}$  and a depth of  $h = 360$  nm. Its light trapping efficiency calculates to  $LTE = 0.444$ .

setup	$x_{\text{int}}$	$y_{\text{int}}$	$z_{\text{int}}$	W12	W22	W32	W01	W02	$P_L$	$P_{\text{th}}$	$LTE$
(a)	-85	26	710	62	69	22	41	10	146	146	0.426
(b)	-91	76	948	71	75	24	88	55	539	214	0.453
(c)	0	0	1092	88	2	45	81	10	623	260	0.444

**Table 7.1** Optimized sets of setup parameters for experimental setups (a), (b) and (c). The threshold laser power  $P_{\text{th}}$  did not direct result from the optimization but was determined by a parameter scan of  $P_L$  (see Fig.7.9).

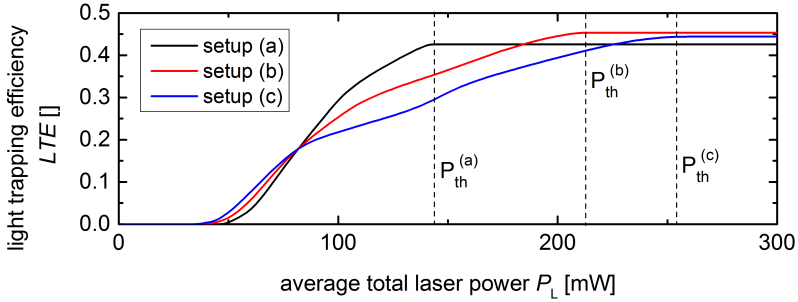


**Figure 7.9** Determination of experimentally favored threshold laser power  $P_{th}$ . Laser powers  $P_L > P_{th}$  do not further increase  $LTE$ , but lead to particle formation. The threshold laser powers for each optimized set of setup parameters are determined by a parameter scan of  $P_L$ .

**Conclusion** Accepting the results of the optimization algorithm, the best achievable textures for the given experimental setup are slightly altered dent-like textures. Depending on the available maximum laser power, the best achievable textures have spatial periodicities of  $\Lambda^{(a)} = 1.20 \mu\text{m}$  and  $\Lambda^{(b)} = 1.59 \mu\text{m}$  for  $P_L^{\text{max}} = 150 \text{ mW}$  and  $P_L^{\text{max}} = 1 \text{ W}$  respectively. The expected light trapping efficiencies calculate to  $LTE^{(a)} = 0.426$  and  $LTE^{(b)} = 0.453$ , showing only a small gain for higher powers. In comparison to the light trapping efficiency of a standard wet chemical etched texture of  $LTE_{\text{ref}} = 0.37$ , this promises an improvement of solar cell efficiencies by incorporation of optimized DLIP textures. However, a direct comparison with a non-laser processes has to be treated with caution, since stitching effects are not accounted for in the calculations.

It has further been observed that restricting the experimental setup to rotational symmetry as well as equal powers and polarizations in the partial beams, does not strongly limit the maximal achievable light trapping efficiency ( $LTE^{(c)} = 0.444$ ). Consequently, a much more simple setup with a lower degree of flexibility could be designed for industrial application without heavily sacrificing functionality.

## 7.4 Outlook

After determining the theoretically best achievable light trapping efficiency with the existing experimental setup and single pulse processing, this section provides an outlook on further potential of the DLIP process by means of parameter scans of selected parameters.

By removing the constraints of the existing experimental setup, the amount of texture defining parameters drastically increases – especially when taking into account multi-pulse processing. On the one hand *VLIP* and *PyLTE* offer a possibility to determine the influence of each of these parameters on light trapping efficiency and could be used for a global optimization taking into account all of them. On the other hand, a global optimization would require very high computational power and eventually only suggest one perfect solution. It does not offer much insight about the reasons leading to the result or about other alternatives. For these reasons, the following section only focuses on two additional parameter variations and investigates how the light trapping efficiency is affected.

In the first subsection, multi-pulse processing by two consecutive treatments with rotated line-like textures are presented. As the line-like textures only require a much simpler two-beam interference setup, they yield the potential of simple industrial applicability. Hence, it is investigated if the achievable light trapping efficiencies of such a setup can be improved by multi-pulse processing. The second subsection investigated how a laser system with a shorter pulse duration could affect the textures and the achievable light trapping efficiency. It is assumed that by shortening the pulse duration, much deeper textures with smaller periodicities can be created and the light trapping efficiencies can be enhanced significantly.

### 7.4.1 Two Pulse Processing

Due to the mechanical instability of the experimental setup and beam pointing instability of the laser system, no multi-pulse processes were further investigated experimentally in the framework of this thesis. However, assuming independent ablation behavior of the multiple processes, the resulting topography can be estimated by simple superposition of the resulting topographies of the single processes. Consequently, an overall resulting topography can be estimated by the *VLIP* model and can be investigated for its light trapping abilities. An experimental proof of concept of such a texture can be observed in Fig. 4.13. However, it remains unclear if the simple superposition of virtual textures is a valid assumption.

**Parameter Scans** To investigate the potential of such multi-pulse processes, the *LTE* was calculated for a variety of topographies resulting from two-pulse processes with crossed line-textures. In the first process, a virtual line-like texture (like depicted in Fig. 5.12 (a) middle) was created. It was assumed that after the first treatment the sample was rotated by an angle  $\beta$  around the  $z$ -axis. The second line-like texture was then superposed with the first texture to obtain the final topography. The final topographies were then evaluated with *PyLTE*.

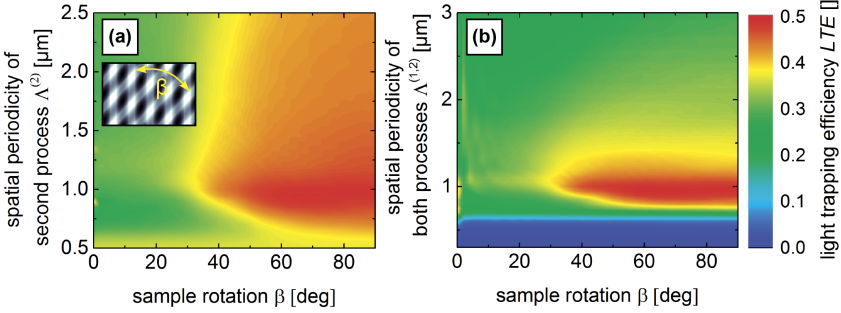


**Figure 7.10** Light trapping efficiency  $LTE$  of two crossed line-like textures in dependence of rotation  $\beta$  and spatial periodicities  $\Lambda^{(1,2)}$ : (a) With the periodicity of first process constant at  $\Lambda = 950$  nm the highest  $LTE$  was achieved for angles  $\beta > 45^\circ$ . (b) Varying  $\Lambda^{(1)} = \Lambda^{(2)}$  in the same amount reveals similar results with the highest  $LTE$  at  $\Lambda^{(1)} = \Lambda^{(2)} = 950$  nm for  $\beta > 40^\circ$ . The achieved  $LTE$  values exceeded the highest values obtained for single-pulse processing. The inset shows an exemplary texture for quick comparison.

Fig. 7.10 shows the result of a variation of rotation angles  $\beta$  and spatial periodicities  $\Lambda^{(1)}$  and  $\Lambda^{(2)}$  of the first and second line-like texture respectively. In the beginning of Sec. 7.2.1 it was shown that a line-like texture with a spatial periodicity of  $\Lambda_{\text{opt}}^1 \approx 950$  nm and a laser power of  $P_{\text{opt}}^1 = 130$  nm shows promising results (Fig. 7.3). Consequently, for the first parameter scan, the setup parameters for the first process were set constant at  $\Lambda^{(1)} = \Lambda_{\text{opt}}^1$  and  $P_L^{(1)} = P_{\text{opt}}^1$ . The laser power of the second process was equally constant ( $P_L^{(1)} = P_{\text{opt}}^1$ )<sup>6</sup>. The spatial periodicity of the second process  $\Lambda^{(2)}$  as well as the sample rotation in between the processes  $\beta$  were varied (Fig. 7.10 (a)). It can be observed that sample rotations of  $\beta > 35^\circ$  are required to possibly obtain a higher light trapping efficiency as could be obtained by single pulse treatments (compare Fig. 7.3). However, for angles  $\beta > 60^\circ$  and spatial periodicities  $\Lambda^{(2)} > 800$  nm, all double textures show a higher potential than the single texture. The highest values ( $LTE = 0.49$ ) are reached for spatial periodicities  $\Lambda^{(2)} \approx \Lambda_{\text{opt}}^1 = 950$  nm and  $\beta > 60^\circ$ .

In the second parameter scan (Fig. 7.10 (b)), the power of both processes was held constant at  $P_L^{(1)} = P_L^{(2)} = P_{\text{opt}}^1$ . As one parameter, the rotation angle  $\beta$  was varied and as the other parameter the spatial periodicities of both processes  $\Lambda^{(1)} = \Lambda^{(2)}$  were varied equally. Again, the most promising textures ( $LTE = 0.49$ ) have

<sup>6</sup>All other setup parameters were equally held constant.

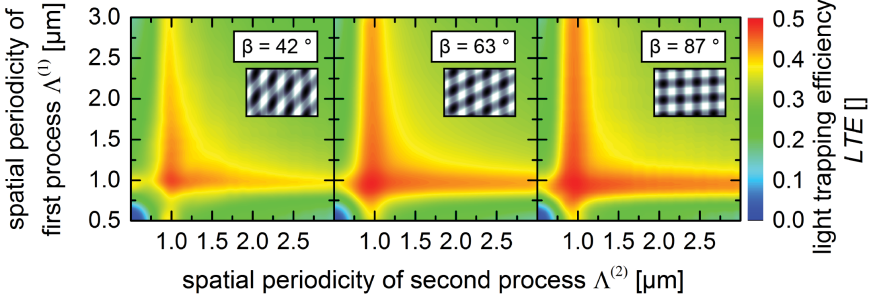


**Figure 7.11** Light trapping efficiency  $LTE$  of two crossed line-like textures in dependence of spatial periodicities  $\Lambda^{(1)}$  and  $\Lambda^{(2)}$ : The independent variation of the spatial periodicities does not lead to higher light trapping efficiencies. The highest  $LTE$  values were achieved for  $\Lambda^{(1)} = \Lambda^{(2)}$ . The inset shows an exemplary texture for quick comparison.

spatial periodicities  $\Lambda^{(1)} \approx \Lambda^{(2)} \approx \Lambda_{\text{opt}}^1 = 950 \text{ nm}$  and a rotation angle  $\beta > 45^\circ$  and hardly show any variations within that range.

To analyze the influence of an independent variation of  $\Lambda^{(1)}$  and  $\Lambda^{(2)}$ , the spatial periodicities were varied independently for selected angles of rotation. An exemplary result of this parameter scan for  $\beta = 42^\circ$ ,  $63^\circ$  and  $87^\circ$  is depicted in Fig. 7.11. Again, it can be observed that by double-texturing higher light trapping efficiencies could be reached than with single textures, as long as one of the textures in the double texture has a spatial periodicity around  $\Lambda_{\text{opt}}^1$ . If both textures have that optimal periodicity, the highest light trapping efficiencies of  $LTE = 0.49$  were reached. For sufficiently large rotation angles  $\beta > 45^\circ$ , no strong influence of the same could be detected.

## 7.4.2 Short Laser Pulse Durations

By employing laser systems with shorter pulse durations  $\tau_p$ , the heat diffusion length  $l_T$  can be reduced (see Eq. 5.27). With a shorter heat diffusion length, it is assumed that smaller feature sizes can be created because the energy deposition is better confined locally. To investigate the potential of the use of a laser system with shorter pulse durations, similar parameter scans as in Sec. 7.2.1 were conducted, but shorter pulse durations were assumed and  $l_T$  was adapted accordingly.

For the parameter scans of total laser power  $P_L$  and spatial periodicity  $\Lambda$ , dent-like textures were used because they reveal the highest potential of the single-process textures. The results for an assumed pulse duration of  $\tau_p = 500 \text{ ps}$  are depicted in

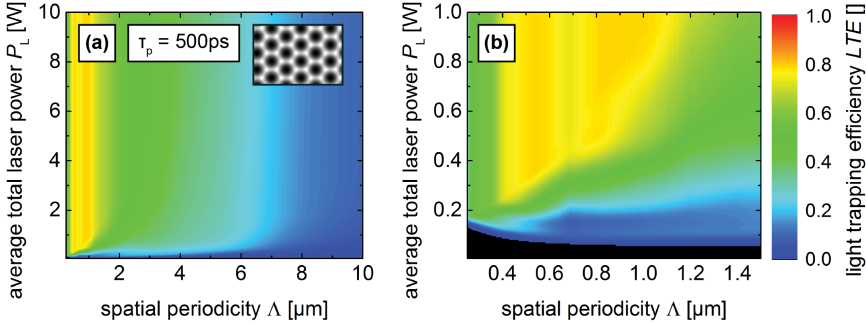


**Figure 7.12** Light trapping efficiency  $LTE$  in dependence of laser power  $P_L$  and spatial periodicity  $\Lambda$  for dent-like textures at an assumed pulse duration of  $\tau_p = 500$  ps (a) Overview, (b) Detail): By reducing the pulse duration, the heat diffusion length is reduced and deeper textures can be created also at smaller spatial periodicities. For periodicities  $\Lambda \gtrsim 3 \mu\text{m}$  the  $LTE$  is similar to the corresponding  $\tau_p = 5$  ns values in Fig. 7.4. For smaller periodicities much higher light trapping efficiencies up to  $LTE \approx 0.8$  can be reached. The inset shows an exemplary texture for quick comparison.

Fig. 7.12. Concerning the laser power, similar trends as for longer pulse duration can be observed. From a periodicity-dependent threshold power  $P_{th}^d(\Lambda)$  to higher powers, the light trapping efficiency does not improve. Also, similar to longer pulse durations, there are two maxima along the periodicity axis once exceeding the threshold power. The first is at  $\Lambda \approx 540$  nm, the second at  $\Lambda \approx 810$  nm. However, they are shifted to smaller periodicities. Due to the shorter heat diffusion length, textures with these spatial periodicities are deeper than the corresponding textures achieved with longer pulse durations (see Fig. 7.4). The texture depths are  $h = 280$  nm and  $h = 370$  nm at  $\Lambda = 540$  nm and  $\Lambda = 810$  nm respectively. The deeper textures lead to better light scattering and higher light trapping efficiency. For periodicities  $\Lambda \gtrsim 3 \mu\text{m}$  the  $LTE$  values are about equal to the ones obtained by longer pulse durations<sup>7</sup>. For smaller periodicities, the light trapping efficiency strongly improves and values up to  $LTE = 0.77$  are reached in the mentioned maxima.

For even shorter pulse durations of  $\tau_p = 10$  ps, this trend continues (Fig. 7.13). Periodicities  $\Lambda \gtrsim 1 \mu\text{m}$  lead to similar light trapping efficiencies as with  $\tau_p = 500$  ps, but shorter periodicities reach even higher levels. The highest light trapping efficiencies ( $LTE = 0.93$ ) are reached around  $\Lambda \approx 360$  nm with a corresponding

<sup>7</sup>Please note the different color scales in Fig. 7.12 and Fig. 7.4

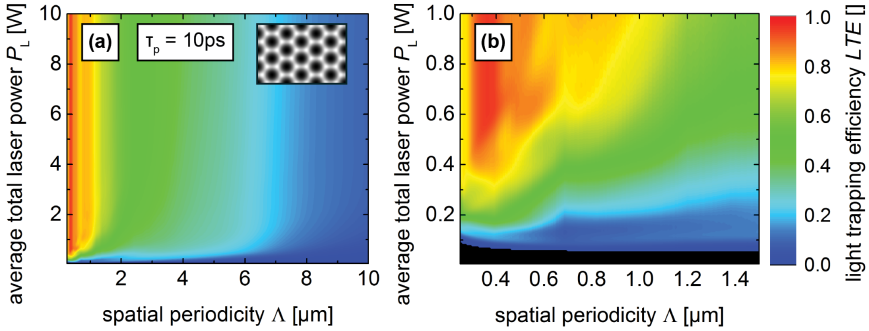


**Figure 7.13** Light trapping efficiency  $LTE$  in dependence of laser power  $P_L$  and spatial periodicity  $\Lambda$  for dent-like textures at an assumed pulse duration of  $\tau_p = 10$  ps ((a) Overview, (b) Detail): Further reducing the pulse duration to  $\tau_p = 10$  ps leads to even higher achievable light trapping efficiencies for  $\Lambda \lesssim 1 \mu\text{m}$ . The inset shows an exemplary texture for quick comparison.

texture depth of  $h = 390$  nm. However, it has to be kept in mind, that these estimations are based on a simple ablation model only validated for pulse durations in the nanosecond regime. It remains to be determined, if the model can also be applied for laser pulse durations as short as  $\tau_p = 10$  ps (see Sec. 2.2.2).

### 7.4.3 Conclusion

It can be concluded that using the same laser, higher light trapping efficiencies can be obtained by using multi-pulse processing instead of single shots. Furthermore, the presumed line-like textures can be created with a much simpler experimental setup which further underlines the potential of industrial applicability. By exchanging the laser system with a system with shorter pulse durations, the simulations show that very high light trapping efficiencies up to  $LTE = 0.93$  can be obtained. Nevertheless, the stated values are maximal values and it is not assured that the VLIP model produces reliable texture estimations for double textures and shorter laser pulses. Furthermore, it remains to be determined if solar cells can be grown on the potentially steep textures ( $h_{\max} \approx 400$  nm,  $\Lambda_{\min} \approx 350$  nm).

## 7.5 Summary

The light trapping efficiency calculated by the phase model is a reliable measure to estimate the light trapping abilities of a given texture. To also take into account the Gaussian beam profile as well as stitching effects of the macroscopic patterning, the concept of an effective light trapping efficiency  $LTE_{\text{eff}}$  was developed. A comparison of experimental data with calculated values of  $LTE_{\text{eff}}$  reveal good agreement in between model and experiment (Fig. 7.2). The maximal achievable light trapping efficiency – independent of the exact experimental setup and the stitching process – is represented by  $LTE_{\text{max}}$ . Consequently,  $LTE_{\text{max}}$  can be used to obtain an estimation for the light trapping potential of a given DLIP texture.

Selected parameter scans in regions of assumed high  $LTE$  were conducted. Total laser powers exceeding a certain  $P_{\text{th}}$  do not further improve the light trapping efficiency of the texture. It is assumed that to avoid particle generation, the experimental optimum is at  $P_{\text{L}} = P_{\text{th}}$ . In all of the parameter scans, the dent-like texture type revealed to be the most promising textures. The highest values were reached in a region of spatial periodicities around  $\Lambda \approx 1.7 \mu\text{m}$  and texture depths of  $h \approx 340 \text{ nm}$  corresponding to average total laser powers of  $P_{\text{L}} \approx 230 \text{ mW}$ . Highest  $LTE$  for line-like textures were determined to be at  $\Lambda \approx 950 \text{ nm}$  and  $h \approx 130 \text{ nm}$  corresponding to  $P_{\text{L}} \approx 130 \text{ mW}$ .

To discover the best achievable texture within the restrictions of the given experimental setup, a global optimization was computed for all of the nine setup parameters. The results show a favoring of slightly altered dent-like texture types (Fig. 7.8) with  $\Lambda \approx 1.2 \mu\text{m}$  and  $h \approx 208 \text{ nm}$ . Allowing higher maximum laser powers leads to a slight increase of light trapping efficiency. An assumed restriction of the experimental setup to a more simple layout, leads to only slightly decreased light trapping efficiency. Consequently, a more simple layout of the experiment could be used for an industrial application.

In order to explore the potential of other experimental setups, two-pulse processing and shorter pulse durations were investigated. By crossing two line-like textures by subsequent processing, higher values of  $LTE$  can be achieved than with single pulse processing. This underlines the industrial applicability of DLIP with a simple two-beam setup. Assuming a shorter pulse duration of the laser system, the heat diffusion length is also reduced and steeper features can be created. Depending on the assumed pulse duration, very high values of  $LTE$  can be achieved. However, it is not assured that the  $VLIP$  model delivers reliable results for pulse duration in the picosecond regime and if solar cells can be grown on such steep textures.



# 8 Summary and Outlook

## Summary

In order to find a flexible, more controllable alternative to the wet chemical etching of the ZnO:Al front contact, five groups of laser-based processes were evaluated. Apart from the demand to be able to produce textures with feature sizes in the right order of magnitude, the main focus was on flexibility and industrial applicability. While laser-induced chemical etching did not reveal promising results, direct writing by scanner systems as well as refocusing the laser light by particle lens arrays are of very limited industrial relevance. Creating laser-induced periodical surface structures by ultra-short laser pulses, however, proved to be a simple method to produce small feature sizes. Nevertheless, it lacks flexibility. Only direct laser interference patterning (DLIP) offers a high degree of flexibility concerning the variety of textures while being applicable in an industrial environment.

To further investigate DLIP, a highly flexible experimental setup for three-beam interference was designed and implemented. With a single laser pulse, hundreds of thousands, strictly periodic, micrometer-scale features could be created. By adjusting any of nine independent setup parameters, the size and shape of these features could be adjusted. Accordingly, a large variety of textures could be produced. Various textures were realized in layers of ZnO:Al. The characterization of these layers revealed a slight decrease in transmittance whereas the electrical properties of the layers remained nearly unchanged.

Parallel to the experiment, a model was developed which mimics the propagation of the laser beams through the setup, takes into account the modifications by the setup parameters, and calculates the resulting laser intensity distribution on the sample. By a further modeling of the energy intake, heat diffusion and ablation process, an expected topography of the sample's surface could be predicted from a given intensity distribution. A comparison of such estimated virtual textures with experimentally realized textures revealed good agreement. Consequently, the model offers a quick and easy way to estimate the expected ZnO:Al texture for a given set of setup parameters.

The applicability of DLIP processing in the manufacturing of solar cells was proven by incorporating selected DLIP-textured ZnO:Al layers in solar cells. The

layers were textured macroscopically by stitching of laser pulses and thin-film silicon tandem solar cells were deposited on the DLIP textures. The solar cells were fully functional and showed an improved light trapping when compared to flat reference cells. Nevertheless, the reference cells built on wet chemical etched ZnO:Al layers showed better light trapping abilities than the DLIP cells. However, neither the layout of the solar cell, the process parameters, choice of DLIP texture, nor the stitching of the laser spots were optimized for high efficiency solar cells. Consequently, the results may not be interpreted as a benchmark for the potential of the process, but merely prove the applicability of DLIP in the production of thin-film silicon solar cells.

An estimation of the potential of DLIP processing was conducted by utilizing the concept of a theoretical light trapping efficiency *LTE*. This scalar *LTE* is a measure of the light trapping abilities of a given texture when incorporated in a solar cell and correlates with experimentally measured solar cell efficiencies. The concept of the light trapping efficiency was expanded to incorporate effects resulting from the stitching of laser pulses and the inherent texture distribution within a Gaussian laser spot. The prediction of the light trapping abilities was verified by a comparison of measured cell characteristics of DLIP solar cells and corresponding *LTE* calculations.

By means of the light trapping efficiency *LTE*, the influence of the various texture properties on the light trapping abilities was investigated. A "best achievable" texture within the limits of the given experimental setup was determined by an optimization algorithm. Furthermore, it was revealed that hexagonal dent-like textures offer very good light trapping abilities close to the best achievable values of *LTE* resulting from the optimization. Such dent-like textures are created by equal angle of incidence, equal power and aligned polarization which can be realized with a much more simple experimental setup. According to the simulations, even higher light trapping efficiencies can be reached by two-pulse processing and crossing of two line-like textures. Last but not least, DLIP texturing by laser systems with shorter laser pulses is assumed to be able to produce much smaller feature sizes with higher aspect ratios yielding very high light trapping efficiencies.

## Outlook

Utilizing the existing setup, the experimental realization of double line-like textures needs to be further investigated and the created textures need to be compared to modeled predictions. If *VLIP* and *PyLTE* are found to make valid predictions for these types of textures, a simple two-beam interference setup will suffice to reach better light trapping efficiencies than achievable by wet chemical etching.

---

The redesign of the setup could further improve the achievable textures and hence, solar cell efficiencies. By simplifying the setup and limiting the variety of producible textures to line- and dent-like textures, the scattering performance of the resulting front contacts is not strongly limited. However, the gained stability could allow phase constant multi-pulse processing to further deepen the textures. Furthermore, such a simplified setup can easily be incorporated in an industrial environment.

In order to achieve even better light scattering abilities of ZnO:Al front contacts, DLIP processing with shorter pulses durations needs to be investigated. High power subnanosecond laser systems are currently available for industrial application and could significantly improve light trapping efficiencies far beyond the ones of current state-of-the-art textures.

In addition to this, to fully exploit the potential of DLIP texturing, the layer stack of the solar cell has to be adapted to incorporate the DLIP textures more efficiently. DLIP offers the possibility to texture other TCO materials which can also be utilized as front contacts but cannot be textured by wet chemical etching. Moreover, due to the capability to directly texture different kinds of materials without the need of extra resist layers or exerting strong influence on adjacent layers, DLIP can also be used to texture back contacts, intermediate reflectors, etc. By independently adjusting the textures of different layers, completely new light trapping schemes could be developed.

For a further validation of the ablation model, experimental studies on materials with different thermal and optical characteristics (e.g. metals, plastics or c-Si) need to be conducted. If such validations are performed successfully, the whole toolbox of texturing by DLIP, prediction by *VLIP* and optimization by *PyLTE* can be used to also improve light trapping in other types of solar cells. Flexible cells on PET carriers or liquid phase crystallized thin-film silicon solar cells, for example, currently still lack a good light trapping scheme. DLIP, *VLIP* and *PyLTE* now offer the possibility to develop such a light trapping scheme and hence, to further improve the energy conversion efficiencies of such cells.

Finally, the texturing by DLIP is not limited to the application in solar cells. Due to its capability to rapidly texture large areas with adjustable feature sizes and shapes, it can be used for many kinds of surface functionalization. Possible applications range from light out-coupling in light emitting devices, over changing the tribological or hydrophobic properties of surfaces, to decorative enhancements due to the shimmering of textured areas and the creation of counterfeit-proof security features. In addition, the potentially simple setup, the scalability to large areas and the capability to texture non-planar surfaces make DLIP texturing very suitable for industrial application.



# Bibliography

- [1] W. G. Adams and R. E. Day. The action of light on selenium. *Proceedings of the Royal Society of London*, 25:113–117, 1876.
- [2] S. Anisimov, B. Kapeliovich, and T. Perelman. Electron emission from metal surfaces exposed to ultrashort laser pulses. *Journal of Experimental and Theoretical Physics*, 66(776):375–377, 1974.
- [3] D. F. Anthrop and A. W. Searcy. Sublimation and thermodynamic properties of zinc oxide. *The Journal of Physical Chemistry*, 68(8):2335–2342, 1964.
- [4] G. B. Arfken and H. J. Weber. *Mathematical Methods For Physicists*. Academic press, 6. edition, 2005.
- [5] D. Bäuerle. *Laser processing and chemistry*, volume 3. Springer, 2000.
- [6] S. Beckemper. Generation of Periodic Micro- and Nano-structures by Parameter-Controlled Three-beam Laser Interference Technique. *Journal of Laser Micro/Nanoengineering*, 6(1):49–53, Mar. 2011.
- [7] T. Bennett, D. Krajnovich, C. Grigoropoulos, P. Baumgart, and A. Tam. Marangoni mechanism in pulsed laser texturing of magnetic disk substrates. *Journal of heat transfer*, 119(3):589–596, 1997.
- [8] M. Berginski. *Lichtstreuende Oberflächen, Schichten und Schichtsysteme zur Verbesserung der Lichteinkopplung in Silizium-Dünnschichtsolarzellen*. Phd thesis, RWTH Aachen University, Forschungszentrum Jülich, 2008.
- [9] M. Berginski, J. Hüpkes, M. Schulte, G. Schöpe, H. Stiebig, B. Rech, and M. Wuttig. The effect of front ZnO:Al surface texture and optical transparency on efficient light trapping in silicon thin-film solar cells. *Journal of applied physics*, 101(7), 2007.
- [10] M. Birnbaum. Semiconductor Surface Damage Produced by Ruby Lasers. *Journal of Applied Physics*, 36(11), 1965.
- [11] K. Bittkau, W. Böttler, M. Ermes, V. Smirnov, and F. Finger. Light scattering at textured back contacts for n-i-p thin-film silicon solar cells. *Journal of Applied Physics*, 111(8):–, 2012.

- [12] K. Bittkau, A. Hoffmann, and R. Carius. Improvement of light trapping in thin-film silicon solar cells by combining periodic and random interfaces. *Canadian Journal of Physics*, 92(7/8):888–891, 2014.
- [13] K. Bittkau, M. Schulte, M. Klein, T. Beckers, and R. Carius. Modeling of light scattering properties from surface profile in thin-film solar cells by Fourier transform techniques. *Thin Solid Films*, 519(19):6538–6543, 2011.
- [14] M. Boccard, C. Battaglia, S. Hänni, K. Söderström, J. Escarré, S. Nicolay, F. Meillaud, M. Despeisse, and C. Ballif. Multiscale transparent electrode architecture for efficient light management and carrier collection in solar cells. *Nano Letters*, 12(3):1344–1348, 2012.
- [15] M. Boccard, T. Söderström, P. Cuony, C. Battaglia, S. Hänni, S. Nicolay, L. Ding, M. Benkhaira, G. Bugnon, A. Billet, M. Charrière, F. Meillaud, M. Despeisse, and C. Ballif. Optimization of ZnO Front Electrodes for High-Efficiency Micromorph Thin-Film Si Solar Cells. *IEEE Journal of Photovoltaics*, 2(3):229–235, 2012.
- [16] J. Bonse, M. Munz, and H. Sturm. Structure formation on the surface of indium phosphide irradiated by femtosecond laser pulses. *Journal of Applied Physics*, 97(1), 2005.
- [17] J. Bonse, A. Rosenfeld, and J. Krüger. On the role of surface plasmon polaritons in the formation of laser-induced periodic surface structures upon irradiation of silicon by femtosecond-laser pulses. *Journal of Applied Physics*, 106(10), 2009.
- [18] W. Böttler, V. Smirnov, J. Hüpkens, and F. Finger. Texture-etched ZnO as a versatile base for optical back reflectors with well-designed surface morphologies for application in thin film solar cells. *physica status solidi (a)*, 209(6):1144–1149, 2012.
- [19] N. Brouwer and B. Rethfeld. Excitation and relaxation dynamics in dielectrics irradiated by an intense ultrashort laser pulse. *JOSA B*, 31(11):C28–C35, 2014.
- [20] F. Burmeister, W. Badowsky, T. Braun, S. Wieprich, J. Boneberg, and P. Leiderer. Colloid monolayer lithography-A flexible approach for nanostructuring of surfaces. *Applied Surface Science*, 144-145:461–466, 1999.
- [21] F. Burmeister, C. Schäfle, T. Matthes, M. Böhmisch, J. Boneberg, and P. Leiderer. Colloid monolayers as versatile lithographic masks. *Langmuir*, 13(11):2983–2987, 1997.
- [22] C. Chan, J. Mazumder, and M. Chen. Three-dimensional axisymmetric model for convection in laser-melted pools. *Materials Science and Technology*, 3(4):306–311, 1987.

- [23] H.-C. Chang and L.-C. Wang. A Simple Proof of Thue ' s Theorem on Circle Packing. *arXiv.org*, 2010.
- [24] B. N. Chichkov, C. Momma, S. Nolte, F. Alvensleben, and A. Tünnermann. Femtosecond, picosecond and nanosecond laser ablation of solids. *Applied Physics A*, 63(2):109–115, 1996.
- [25] H. W. Deckman, C. R. Wronski, H. Witzke, and E. Yablonovitch. Optically enhanced amorphous silicon solar cells. *Applied Physics Letters*, 42(11):968–970, 1983.
- [26] R. Denk, K. Piglmayer, and D. Bäuerle. Laser-induced nanopatterning of PET using a-SiO<sub>2</sub> microspheres. *Applied Physics A*, 74:825–826, 2002.
- [27] R. Denk, K. Piglmayer, and D. Bäuerle. Laser-induced nano-patterning by means of interference subpatterns generated by microspheres. *Applied Physics A*, 76(1):1–3, 1 2003.
- [28] D. Dominé, F.-J. Haug, C. Battaglia, and C. Ballif. Modeling of light scattering from micro- and nanotextured surfaces. *Journal of Applied Physics*, 107(4), 2010.
- [29] D. Dufft, A. Rosenfeld, S. K. Das, R. Grunwald, and J. Bonse. Femtosecond laser-induced periodic surface structures revisited: A comparative study on ZnO. *Journal of Applied Physics*, 105(3), 2009.
- [30] G. Dziuk. *Theorie und Numerik Partieller Differentialgleichungen*. Walter de Gruyter, 2010.
- [31] S. Eckhardt, T. Roch, C. Sachse, and A. F. Lasagni. Light management of aluminum doped zinc oxide thin films by fabricating periodic surface textures using direct laser interference patterning. *Advanced Engineering Materials*, 15(10):941–947, 2013.
- [32] S. Eckhardt, C. Sachse, and A. F. Lasagni. Light management in transparent conducting oxides by direct fabrication of periodic surface arrays. *Physics Procedia*, 41:552–557, 2013.
- [33] K. Ellmer, A. Klein, and B. Rech. *Transparent conductive zinc oxide: basics and applications in thin film solar cells*. Springer Science & Business Media, 2007.
- [34] D. C. Emmony. Laser mirror damage in germanium at 10.6  $\mu\text{m}$ . *Applied Physics Letters*, 23(11):598, 1973.
- [35] M. Ermes, K. Bittkau, and R. Carius. Comparison of light scattering in solar cells modeled by rigorous and scalar approach. *Journal of Applied Physics*, 113(7), 2013.

- [36] L. C. Evans. *Partial Differential Equations*. American Mathematical Society, 1998.
- [37] S. J. Farlow. *Partial differential equations for scientists and engineers*. Courier Corporation, 2012.
- [38] C. Gagn. DEAP : Evolutionary Algorithms Made Easy. *Journal of Machine Learning Research*, 13:2171–2175, 2012.
- [39] J. Gjessing, A. S. Sudbø, and E. S. Marstein. Comparison of periodic light-trapping structures in thin crystalline silicon solar cells. *Journal of Applied Physics*, 110(3), 2011.
- [40] G. G. Gladush and I. Smurov. *Physics of Laser Material Processing*. Springer, 2011.
- [41] X. Guo, R. Li, Y. Hang, Z. Xu, B. Yu, Y. Dai, B. Lu, and X. Sun. Coherent linking of periodic nano-ripples on a zno crystal surface induced by femtosecond laser pulses. *Applied Physics A*, 94(2):423–426, 2009.
- [42] X. Guo, R. Li, Y. Hang, Z. Xu, B. Yu, H. Ma, B. Lu, and X. Sun. Femtosecond laser-induced periodic surface structure on ZnO. *Materials Letters*, 62:1769–1771, 2008.
- [43] X. Guo, R. Li, Y. Hang, Z. Xu, B. Yu, H. Ma, and X. Sun. Raman spectroscopy and luminescent properties of ZnO nanostructures fabricated by femtosecond laser pulses. *Materials Letters*, 61:4583–4586, 2007.
- [44] S. Haas. *Untersuchung und Optimierung der Serienverschaltung von Silizium-Dünnschicht-Solarmodulen*. Phd thesis, RWTH Aachen University, Forschungszentrum Jülich, 2010.
- [45] J. E. Harvey, C. L. Vernold, A. Krywonos, and P. L. Thompson. Diffracted radiance: a fundamental quantity in nonparaxial scalar diffraction theory. *Applied Optics*, 38(31):6469–6481, 1999.
- [46] S. Höhm, A. Rosenfeld, J. Krüger, and J. Bonse. Femtosecond diffraction dynamics of laser-induced periodic surface structures on fused silica. *Applied Physics Letters*, 102(5), 2013.
- [47] J. Hüpkens, J. I. Owen, S. E. Pust, and E. Bunte. Chemical Etching of Zinc Oxide for Thin-Film Silicon Solar Cells. *ChemPhys*, 13:66–73, 2012.
- [48] J. Huang, S. Beckemper, A. Gillner, and K. Wang. Tunable surface texturing by polarization-controlled three-beam interference. *Journal of Micromechanics and Microengineering*, 20(9), 2010.

- [49] M. Huang, F. Zhao, Y. Cheng, N. Xu, and Z. Xu. Large area uniform nanostructures fabricated by direct femtosecond laser ablation. *Optics Express*, 16(23):19354–65, 2008.
- [50] M. Huang, F. L. Zhao, T. Q. Jia, Y. Cheng, N. S. Xu, and Z. Z. Xu. A uniform 290 nm periodic square structure on ZnO fabricated by two-beam femtosecond laser ablation. *Nanotechnology*, 18(50), 2007.
- [51] N. R. Isenor. CO<sub>2</sub> laser-produced ripple patterns on Ni<sub>x</sub>P<sub>1-x</sub> surfaces. *Applied Physics Letters*, 31(3):148, 1977.
- [52] K. Jäger, M. Fischer, R. A. C. M. M. Van Swaaij, and M. Zeman. A scattering model for nano-textured interfaces and its application in optoelectrical simulations of thin-film silicon solar cells. *Journal of Applied Physics*, 111(8), 2012.
- [53] G. Jost, T. Merdzhanova, T. Zimmermann, and J. Hüpkes. Process monitoring of texture-etched high-rate ZnO:Al front contacts for silicon thin-film solar cells. *Thin Solid Films*, 532(0):66 – 72, 2013.
- [54] M. Kaganov, I. Lifshitz, and L. Tanatarov. Relaxation between Electrons and Crystalline Lattice. *Soviet Physics*, 4(173):89–102, 1957.
- [55] O. Kluth, G. Schöpe, J. Hüpkes, C. Agashe, J. Müller, and B. Rech. Modified Thornton model for magnetron sputtered zinc oxide: film structure and etching behaviour. *Thin Solid Films*, 442(1-2):80 – 85, 2003.
- [56] T. Knüttel, S. Bergfeld, and S. Haas. Laser Texturing of Surfaces in Thin-Film Silicon Photovoltaics - A Comparison of Potential Processes. *Journal of Laser Micro/Nanoengineering*, 8(3):222–229, 2013.
- [57] M. Kroll, S. Fahr, C. Helgert, C. Rockstuhl, F. Lederer, and T. Pertsch. Employing dielectric diffractive structures in solar cells – a numerical study. *physica status solidi (a)*, 205(12):2777–2795, 2008.
- [58] S. Ku, S. Haas, G. Schoepe, B. E. Pieters, Q. Ye, and U. Rau. Direct ablation of ZnO with UV and IR laser for thin film solar modules. *Journal of Optoelectronics and Advanced Materials*, 12(3):616–620, 2010.
- [59] A. Lasagni, C. Holzapfel, and F. Mücklich. Periodic pattern formation of intermetallic phases with long range order by laser interference metallurgy. *Advanced Engineering Materials*, 7(6):487–492, 2005.
- [60] A. Lasagni, F. Mücklich, M. Nejati, and R. Clasen. Periodical Surface Structuring of Metals by Laser Interference Metallurgy as a New Fabrication Method of Textured Solar Selective Absorbers. *Advanced Engineering Materials*, 8(6):580–584, June 2006.

- [61] A. Lasagni, T. Roch, M. Bieda, D. Benke, and E. Beyer. High speed surface functionalization using direct laser interference patterning, towards  $1\text{ m}^2/\text{min}$  fabrication speed with sub- $\mu\text{m}$  resolution. In *SPIE Photonics West 2014*, 2014.
- [62] L. Li, W. Guo, Z. B. Wang, Z. Liu, D. Whitehead, and B. Luk'yanchuk. Large-area laser nano-texturing with user-defined patterns. *Journal of Micromechanics and Microengineering*, 19(5), 2009.
- [63] J. M. Liu. Simple technique for measurements of pulsed gaussian-beam spot sizes. *Optics letters*, 7(5):196–198, 1982.
- [64] G. N. Maracas, G. L. Harris, C. A. Lee, and R. A. McFarlane. On the origin of periodic surface structure of laser-annealed semiconductors. *Applied Physics Letters*, 33(5), 1978.
- [65] E. Marins, M. Warzecha, S. Michard, J. Hotovy, W. Böttler, P. Alpuim, and F. Finger. Flexible nip thin film silicon solar cells on polyimide foils with textured ZnO:Ga back reflector. *Thin solid films*, 571:9–12, 2014.
- [66] J. Metzdorf. Calibration of solar cells. 1: The differential spectral responsivity method. *Applied Optics*, 26(9):1701–1708, 1987.
- [67] A. A. Michelson and E. W. Morley. On the relative motion of the earth and the luminiferous ether. *American journal of science*, 203(1):333–345, 1887.
- [68] J. Müller, B. Rech, J. Springer, and M. Vanecek. TCO and light trapping in silicon thin-film solar cells. *Solar Energy*, 77(6):917 – 930, 2004.
- [69] F. Mücklich, A. Lasagni, and C. Daniel. Laser interference metallurgy - periodic surface patterning and formation of intermetallics. *Intermetallics*, 13(3-4):437–442, Mar. 2005.
- [70] J. Müller, G. Schöpe, B. Rech, H. Schade, P. Lechner, R. Geyer, H. Stiebig, and W. Reetz. Role of the glass/tco substrate in thin film silicon solar cells. In *Photovoltaic Energy Conversion, 2003. Proceedings of 3rd World Conference on*, volume 2, pages 1839–1842 Vol.2, May 2003.
- [71] L. Müller-Meskamp, Y. H. Kim, T. Roch, S. Hofmann, R. Scholz, S. Eckardt, K. Leo, and A. F. Lasagni. Efficiency Enhancement of Organic Solar Cells by Fabricating Periodic Surface Textures using Direct Laser Interference Patterning. *Advanced Materials*, 24(7):906–910, 2012.
- [72] Y. Nakata, K. Murakawa, K. Sonoda, K. Momoo, and N. Miyanaga. Design of interference using coherent beams configured as a six-sided pyramid. *Applied optics*, 51(21):5004–10, 2012.

- [73] J. I. Owen. *Growth, Etching, and Stability of Sputtered ZnO: AI for Thin-film Silicon Solar Cells*. Phd thesis, RWTH Aachen University, Forschungszentrum Jülich, 2011.
- [74] J. I. Owen, S. E. Pust, E. Bunte, and J. Hüpkes. ZnO Etch-Feature Control via Concentration and Temperature of Various Acids service ZnO Etch-Feature Control via Concentration and Temperature. *ECS Journal of Solid State Science and Technology*, 1(1):10–17, 2012.
- [75] Ü. Özgür, Y. I. Alivov, C. Liu, A. Teke, M. A. Reshchikov, S. Doğan, V. Avrutin, S.-J. Cho, and H. Morkoç. A comprehensive review of ZnO materials and devices. *Journal of Applied Physics*, 98(4), 2005.
- [76] U. W. Paetzold, E. Moulin, D. Michaelis, W. Böttler, C. Wächter, V. Hagemann, M. Meier, R. Carius, and U. Rau. Plasmonic reflection grating back contacts for microcrystalline silicon solar cells. *Applied Physics Letters*, 99(18), 2011.
- [77] B. Petroleum. Bp statistical review of world energy, 2011.
- [78] K. Piglmayer, R. Denk, and D. Bäuerle. Laser-induced surface patterning by means of microspheres. *Applied Physics Letters*, 80(25), 2002.
- [79] R. Poprawe. *Lasertechnik*. Lehrstuhl für Lasertechnik LLT, 1998.
- [80] R. Poprawe. *Lasertechnik für die Fertigung*. Springer, 2005.
- [81] M. Python, E. Vallat-Sauvain, J. Bailat, D. Dominé, L. Fesquet, A. Shah, and C. Ballif. Relation between substrate surface morphology and microcrystalline silicon solar cell performance. *Journal of Non-Crystalline Solids*, 354:2258–2262, 2008.
- [82] D. Rainville, F.-A. Fortin, M.-A. Gardner, M. Parizeau, C. Gagné, et al. Deap: A python framework for evolutionary algorithms. In *Proceedings of the 14th annual conference companion on Genetic and evolutionary computation*, pages 85–92. ACM, 2012.
- [83] U. Rau, D. Abou-Ras, and T. Kirchartz. *Advanced characterization techniques for thin film solar cells*. John Wiley & Sons, 2011.
- [84] B. Rech and H. Wagner. Potential of amorphous silicon for solar cells. *Applied Physics A*, 69(2):155–167, 1999.
- [85] J. Reif, O. Varlamova, S. Varlamov, and M. Bestehorn. The role of asymmetric excitation in self-organized nanostructure formation upon femtosecond laser ablation. *Applied Physics A*, 104(3):969–973, 2011.

- [86] S. Ring, S. Neubert, C. Schultz, S. S. Schmidt, F. Ruske, B. Stannowski, F. Fink, and R. Schlatmann. Light trapping for a-Si:H/ $\mu$ c-Si:H tandem solar cells using direct pulsed laser interference texturing. *physica status solidi (RRL) - Rapid Research Letters*, 2014.
- [87] H. Sai, H. Jia, and M. Kondo. Impact of front and rear texture of thin-film microcrystalline silicon solar cells on their light trapping properties. *Journal of Applied Physics*, 108(4):044505, 2010.
- [88] A. Sarkar, S. Ghosh, S. Chaudhuri, and A. Pal. Studies on electron transport properties and the burstein-moss shift in indium-doped zno films. *Thin Solid Films*, 204(2):255 – 264, 1991.
- [89] H. Schade, P. Lechner, R. Geyer, H. Stiebig, B. Rech, and O. Kluth. Texture properties of TCO uniquely determining light trapping in thin-film silicon solar cells. In *Conference Record of the IEEE Photovoltaic Specialists Conference*, pages 1436–1439, 2005.
- [90] M. Schulte, K. Bittkau, K. Jäger, M. Ermes, M. Zeman, and B. E. Pieters. Angular resolved scattering by a nano-textured ZnO/silicon interface. *Applied Physics Letters*, 99(11):15–18, 2011.
- [91] W. Shockley and H. J. Queisser. Detailed Balance Limit of Efficiency of p-n Junction Solar Cells. *Journal of Applied Physics*, 32(3):510–519, 1961.
- [92] J. E. Sipe, J. F. Young, and J. S. Preston. Laser-induced periodic surface structure. I. Theory. *Physical Review B*, 27(2):1141–1154, 1983.
- [93] J. Z. P. Skolski. Modeling of Laser Induced Periodic Surface Structures. *Journal of Laser Micro/Nanoengineering*, 5(3):263–268, 2010.
- [94] D. L. Staebler and C. R. Wronski. Reversible conductivity changes in discharge-produced amorphous Si. *Applied Physics Letters*, 31(4):292–294, 1977.
- [95] J. L. Stay and T. K. Gaylord. Three-beam-interference lithography: contrast and crystallography. *Applied optics*, 47(18):3221–30, June 2008.
- [96] W. Steen, K. G. Watkins, and J. Mazumder. *Laser material processing*. Springer Science & Business Media, 2010.
- [97] H. Stiebig, N. Senoussaoui, C. Zahren, C. Haase, and J. Müller. Silicon thin-film solar cells with rectangular-shaped grating couplers. *Progress in Photovoltaics: Research and Applications*, 14(1):13–24, 2006.
- [98] A. Thue. Über die dichteste Zusammenstellung von kongruenten Kreisen in einer Ebene. *Christiania : Dybwad in Komm.*, 1(1-9), 1910.

- [99] G. Tsotridis, H. Rother, and E. Hondros. Marangoni flow and the shapes of laser-melted pools. *Naturwissenschaften*, 76(5):216–218, 1989.
- [100] A. K. Upadhyay, N. A. Inogamov, B. Rethfeld, and H. M. Urbassek. Ablation by ultrashort laser pulses: Atomistic and thermodynamic analysis of the processes at the ablation threshold. *Physical Review B*, 78(4):045437, 2008.
- [101] H. van Driel, J. Sipe, and J. Young. Laser-Induced Periodic Surface Structure on Solids: A Universal Phenomenon. *Physical Review Letters*, 49(26):1955–1958, 1982.
- [102] O. Varlamova and J. Reif. Evolution of Femtosecond Laser Induced Surface Structures at Low Number of Pulses near the Ablation Threshold. In *Proceedings of LAMP 2013*, 2013.
- [103] O. Varlamova, J. Reif, S. Varlamov, and M. Bestehorn. The laser polarization as control parameter in the formation of laser-induced periodic surface structures: Comparison of numerical and experimental results. *Applied Surface Science*, 257(12):5465–5469, 2011.
- [104] R. Wagner, J. Gottmann, A. Horn, and E. W. Kreutz. Subwavelength ripple formation induced by tightly focused femtosecond laser radiation. *Applied Surface Science*, 252(24):8576–8579, 2006.
- [105] K. Wilken, V. Smirnov, O. Astakhov, and F. Finger. Thin-film silicon solar cells fabricated at low temperature: A versatile technology for application on transparent flexible plastic substrates and in integrated photoelectrochemical water splitting modules. In *Photovoltaic Specialist Conference (PVSC), 2014 IEEE 40th*, 2014.
- [106] P. Würfel. *Physics of solar cells: from basic principles to advanced concepts*. John Wiley & Sons, 2009.
- [107] Q. Wu, Y. Ma, R. Fang, Y. Liao, Q. Yu, X. Chen, and K. Wang. Femtosecond laser-induced periodic surface structure on diamond film. *Applied Physics Letters*, 82(11):1703, 2003.
- [108] E. Yablonovitch. Statistical ray optics. *Journal of the Optical Society of America*, 72(7):899–907, 1982.
- [109] J. F. Young, J. S. Preston, H. M. V. Driel, and J. E. Sipe. Laser-induced periodic surface structure. II. Experiments on Ge, Si, Al, and brass. *Physical Review B*, 27(2):1155–1172, 1983.
- [110] T. Young. The Bakerian Lecture: On the Theory of Light and Colours. *Philosophical Transactions of the Royal Society of London*, 92:12–48, 1802.

- [111] M. Zamfirescu, A. Dinescu, M. Danila, G. Socol, and C. Radu. The role of the substrate material type in formation of laser induced periodical surface structures on ZnO thin films. *Applied Surface Science*, 258(23):9385–9388, 2012.
- [112] M. Zeman. Thin-Film Silicon PV Technology. *Journal of Electrical Engineering*, 61(5):271–276, 2010.

# List of Tables

3.1	Overview of laser system properties . . . . .	43
4.1	Summary of process comparison . . . . .	70
6.1	Transmittances of DLIP textured ZnO:Al layers . . . . .	123
6.2	Short-circuit current densities of DLIP solar cells . . . . .	127
6.3	Cell parameters of DLIP solar cells . . . . .	130
7.1	Result of optimization . . . . .	150



# List of Figures

1.1	Outline of Thesis . . . . .	3
2.1	Illustration of single-junction solar cell . . . . .	6
2.2	Exemplary J-V characteristics of solar cell . . . . .	7
2.3	Optical spectra of ZnO:Al . . . . .	8
2.4	Light management and texture-etched ZnO:Al . . . . .	10
2.5	Illustration of phase model . . . . .	12
2.6	Exemplary angular intensity distribution . . . . .	13
2.7	Illustration of different types of polarization . . . . .	16
2.8	Illustration of temporal coherence . . . . .	18
2.9	Schematic drawing of beam waist in Gaussian beam . . . . .	19
2.10	Illustration of fluence distribution within laser spot . . . . .	20
2.11	Sketch of overlapping laser spots . . . . .	22
2.12	Sketch of two-beam interference . . . . .	25
3.1	Exemplary plot for Liu method . . . . .	31
3.2	Sketch of Michelson interferometer . . . . .	32
3.3	Power and pulse energy of <i>Rofin1064</i> . . . . .	36
3.4	Power and pulse energy of <i>Rofin532</i> . . . . .	37
3.5	Power and pulse energy of <i>Rofin355</i> . . . . .	38
3.6	Power and pulse energy of <i>TruMicro5050</i> . . . . .	39
3.7	Power and pulse energy of <i>TruMicro5000</i> . . . . .	40
3.8	Power and pulse energy of <i>Powerlite8020</i> . . . . .	41
3.9	Stability of <i>Powerlite8020</i> . . . . .	42
3.10	Schematic drawing of scanner system . . . . .	46
3.11	Schematic flow chart of genetic algorithm . . . . .	48
4.1	Reaction chamber for laser-induced chemical etching . . . . .	54
4.2	Influence of laser heating on etching process . . . . .	55
4.3	Temperature dependence of ZnO:Al etch rate . . . . .	56
4.4	Particle lens array – deposition and laser ablation . . . . .	58
4.5	Exemplary texture obtained by particle lens array . . . . .	59
4.6	Exemplary LSFL texture . . . . .	61
4.7	Polarization dependence of LSFL . . . . .	62
4.8	Exemplary HSFL texture . . . . .	63

4.9	Influence of polarization on HSFL texture . . . . .	63
4.10	Scattering properties of LIPSS . . . . .	64
4.11	Experimental setup for two-beam DLIP . . . . .	66
4.12	Exemplary line-like texture obtained by two-beam DLIP . . . . .	67
4.13	Texture variety obtainable by two-beam DLIP . . . . .	68
4.14	Comparison of height and intensity in two-beam DLIP . . . . .	69
5.1	Top view of three-beam interference setup . . . . .	75
5.2	Beam shaping unit of three-beam interference setup . . . . .	76
5.3	Side view of three-beam interference setup . . . . .	77
5.4	Sample holder of three-beam interference setup . . . . .	79
5.5	Schematic flowchart of <i>SINT</i> model . . . . .	83
5.6	Exemplary interference pattern . . . . .	84
5.7	Fluence distributions, variation of angles of incidence . . . . .	85
5.8	Fluence distributions, variation of electrical field amplitudes . . . . .	86
5.9	Fluence distributions, variation of polarization . . . . .	87
5.10	Optical appearance of DLIP processed sample . . . . .	90
5.11	Homogeneity and periodic character of DLIP texture . . . . .	91
5.12	Comparison of fluence distribution and texture – geometry . . . . .	92
5.13	Comparison of fluence distribution and texture – profiles . . . . .	93
5.14	Control of texture depth . . . . .	94
5.15	Control of texture periodicity . . . . .	95
5.16	Illustration of heat diffusion within material . . . . .	97
5.17	Illustration of bulging of ZnO:Al . . . . .	98
5.18	Layer of molten and resolidificated ZnO:Al . . . . .	99
5.19	Evolution of population in optimization . . . . .	107
5.20	Validation of optimization results . . . . .	109
5.21	Flow Chart DLIP – <i>VLIP</i> . . . . .	110
5.22	Comparison of model and experiment – geometry . . . . .	112
5.23	Comparison of model and experiment – texture depths . . . . .	113
6.1	DLIP textures incorporated in solar cells . . . . .	116
6.2	Variation of surface topography within laser spot . . . . .	117
6.3	Stitching of laser spots . . . . .	119
6.4	Light diffraction of DLIP textured ZnO:Al layers . . . . .	120
6.5	Total transmittance of DLIP textured ZnO:Al layers . . . . .	122
6.6	Sketch of deposited tandem solar cell . . . . .	124
6.7	External quantum efficiency of solar cells . . . . .	126
6.8	Reflectance of solar cells . . . . .	129
6.9	J-V characteristics of solar cells . . . . .	131
7.1	Illustration to effective light trapping efficiency . . . . .	137
7.2	Solar cell characteristics and light trapping efficiency . . . . .	138

---

7.3	<i>LTE</i> – variation of power and periodicity – line-like . . . . .	142
7.4	<i>LTE</i> – variation of power and periodicity – dent-like . . . . .	143
7.5	<i>LTE</i> – variation of partial powers . . . . .	145
7.6	<i>LTE</i> – variation of partial polarizations . . . . .	146
7.7	<i>LTE</i> – variation of interference point position . . . . .	147
7.8	Textures corresponding to results of optimization . . . . .	150
7.9	Determination of threshold laser power . . . . .	151
7.10	<i>LTE</i> – variation of angle – crossed line-like . . . . .	153
7.11	<i>LTE</i> – variation of periodicity – crossed line-like . . . . .	154
7.12	<i>LTE</i> – 500 ps – variation of power and periodicity – dent-like . . .	155
7.13	<i>LTE</i> – 10 ps – variation of power and periodicity – dent-like . . .	156



# A Appendix

## Simplifying 3D Convolution Integral

The three dimensional convolution of the heat kernel  $H$  and the temperature distribution  $\Delta T$  is expressed by

$$\Delta T'(x, y, z, t) = H(x, y, z, t) * \Delta T(x, y, z) \quad (\text{A.1})$$

$$= \iiint_{-\infty}^{\infty} H(x - x', y - y', z - z', t) \Delta T(x', y', z') dx' dy' dz' \quad (\text{A.2})$$

with

$$H(x, y, z, t) = \frac{1}{(4\pi Dt)^{3/2}} e^{-\frac{|r|^2}{4Dt}} \quad (\text{A.3})$$

$$\Delta T(x, y, z) = \frac{\alpha}{\rho c_p} \Phi_0(x, y) e^{\alpha z}. \quad (\text{A.4})$$

Inserting yields

$$\Delta T'(x, y, z, t) = \frac{\alpha}{\rho c_p (4\pi Dt)^{3/2}} \iiint_{-\infty}^{\infty} e^{-\frac{|r|^2}{4Dt}} \Phi_0(x, y) e^{\alpha z'} dx' dy' dz' \quad (\text{A.5})$$

$$= \frac{\alpha}{\rho c_p (4\pi Dt)^{3/2}} \int_{-\infty}^{\infty} e^{-\frac{(z-z')^2}{4Dt}} e^{\alpha z'} dz' \iint_{-\infty}^{\infty} \Phi_0(x, y) e^{-\frac{(x-x')^2 + (y-y')^2}{4Dt}} dx' dy'. \quad (\text{A.6})$$

The integrals on the right of Equation A.6 can be expressed by the convolution of the two dimensional heat kernel  $H^{(2)}(x, y, t)$  and  $\Phi_0(x, y)$ :

$$H^{(2)}(x, y, t) * \Phi_0(x, y) = \frac{1}{4\pi Dt} \iint_{-\infty}^{\infty} e^{-\frac{(x-x')^2 + (y-y')^2}{4Dt}} \Phi_0(x', y') dx' dy' \quad (\text{A.7})$$

Furthermore the first integral in Equation A.6 can be solved by solving the expression

$$\int_{-\infty}^{\infty} \exp(a_1 x) \exp\left(\frac{-(a_2 - x)^2}{a_3}\right) dx = \quad (\text{A.8})$$

Substituting  $y = a_2 - x$  yields

$$- \int_{\infty}^{-\infty} \exp(a_1(a_2 - y)) \exp\left(\frac{y^2}{a_3}\right) dy. \quad (\text{A.9})$$

expanding yields

$$\int_{-\infty}^{\infty} \exp\left(\frac{-\frac{1}{4}a_1^2a_3^2 - a_1a_3y - y^2 + \frac{1}{4}a_1^2a_3^2 + a_1a_2a_3}{a_3}\right) dy \quad (\text{A.10})$$

$$= \exp\left(\frac{a_1^2a_3}{4} + a_1a_2\right) \int_{-\infty}^{\infty} \exp\left(-\frac{(\frac{a_1a_2}{2} + y)^2}{a_3}\right) dy \quad (\text{A.11})$$

With the substitution  $z = \frac{a_1a_2}{2} + y$  the integral in Equation A.10 can be evaluated. So finally

$$\int_{-\infty}^{\infty} \exp(a_1x) \exp\left(\frac{-(a_2 - x)^2}{a_3}\right) dx = \exp\left(\frac{a_1^2a_3}{4} + a_1a_2\right) \cdot \sqrt{\pi a_3} \quad (\text{A.12})$$

Inserting Equation A.12 with the substitutions

$$x = z', \quad a_1 = \alpha, \quad a_2 = z, \quad a_3 = 4Dt \quad (\text{A.13})$$

and Equation A.7 into Equation A.6 yields

$$\Delta T'(x, y, z, t) = \frac{\alpha}{\rho c_p} e^{Dt\alpha^2} e^{\alpha z} \cdot H^{(2)}(x, y, t) * \Phi_0(x, y). \quad (\text{A.14})$$

Consequently, the convolution of the three dimensional heat kernel  $H(x, y, z, t)$  and the temperature distribution within the material  $\Delta T(x, y, z)$  can be simplified to a convolution of the two dimensional heat kernel  $H^{(2)}(x, y, t)$  and the fluence on the surface of the sample  $\Phi_0(x, y)$ .

# Danke

Zuerst möchte ich meinem Doktorvater Herrn Prof. Dr. Uwe Rau für die fachliche Unterstützung, die immer freundlichen und konstruktiven Gespräche, aber auch für seine wohlwollende und humorvolle Art danken.

Des Weiteren danke ich Prof. Dr. Andrés Fabián Lasagni für sein ausgesprochenes Interesse an der Arbeit sowie sein freiwilliges Angebot, als Zweitgutachter zu fungieren. Vielen Dank für die Hilfestellungen und dass Du mich in die Gruppe der DLIPer aufgenommen hast.

Meinem direkten Betreuer Dr. Stefan Haas danke ich von ganzem Herzen. Ohne ihn wäre die Arbeit definitiv so nicht möglich gewesen. Stefan, vielen Dank für die viele ausgiebigen Diskussionen, gemeinsamen Erörterungen sowie für Deine Geduld mir elektrotechnische Hintergründe und die Welt der Photovoltaik beizubringen. Vielen Dank auch dafür, dass Du mir viel Freiraum gegeben hast mich zu entfalten, Deine Tür aber wirklich immer offen war, wenn ich Diskussionsbedarf hatte. Vor Allem aber danke ich Dir für deine stets freundliche und kameradschaftliche Art.

Ich danke Prof. Dr. Stefan Bergfeld für die Betreuung meiner Arbeit seitens der 4JET GmbH. Vielen Dank, dass Du mich mitgenommen hast und mir nicht nur in die technischen, sondern vor Allem auch wirtschaftlichen Fragestellungen eines jungen Unternehmens nahegelegt hast. Von Dir habe ich viel strategisches Denken gelernt.

Ich danke Jörg Jetter, dass ich bei 4JET promovieren durfte. Ich danke Dir für Deine unkomplizierte Art, für Dein Bemühen den familiären Zusammenhalt bei 4JET weiter zu stärken und für den hundefreundlichen Betrieb. Vor Allem aber danke ich Dir dafür, dass Du mir den Rücken frei gehalten hast, so dass ich mich voll auf meine Promotion konzentrieren konnte.

Ich danke Dr. Uwe Stute für ausgiebige physikalische und nichtphysikalische Diskussionen sowie für seinen Rauschebart.

Ich bedanke mich bei Dr. Karsten Bittkau und Dr. André Hoffmann für die vielen fruchtbaren Optik Diskussionen. Vielen Dank auch für die sonstigen Hilfestellungen im Bereich der Simulation und Programmierung und gesonderten Dank an Karsten fürs Korrekturlesen.

Der Mann für alles: Gunnar Schöpe. Danke für deine immer positive und aufmunternde Art und die ständige Hilfsbereitschaft, wenn mal wieder irgendwo was klemmte. Für den Kicker! Für die Laserbox, die Werkstatt, den Honig, das Autoradio. Fürs gunnareske Kickern samt Lustlauten — aber vor Allem auch dafür die gute Seele am Institut zu sein. Du hast mir den Arbeitsalltag sehr erheitert und erleichtert. Wenn ich mal groß bin, möchte ich auch Gunnar werden.

Dr. Bugra Turan: Mein erster Ansprechpartner für sämtliche dumme Fragen bezüglich Lasern im Allgemeinen und Besonderen, elektrotechnischen Anfängerübungen, politischen Grundsatzdiskussionen, geschichtlichem Hintergrundwissen, sämtlicher sonstiger Trivia, dem Universum und dem ganzen Rest. Unglaublich, was sich für ein nicht endendes Wissen in diesem Menschen verbirgt! Vielen Dank, dass ich dieses Wissen immer wieder anzapfen durfte. Vielen Dank aber vor Allem auch für Deinen figurativen und komikescenen Humor, die sinnbildliche Seifenblasenpfeife beim Integrallösen und das sonntägliche Enten in den Teich schubsen.

Mr. ZnO, nun Dr. Sommer: Vielen Dank an Dr. Nicolas Sommer für die vielen klärenden Gespräche über physikalische Themen, die vielen verklärenden Gespräche über alles andere und dein Gefuddel auf der E-Gitarre. Du hast mir als physikalischer Sparringpartner bei vielen vertrackten Fragen wirklich sehr geholfen. Danke.

Ich danke Martin Vieten für die Arbeit bei der Implementierung von PyLTE sowie für Einblicke in die Welt der genetischen Algorithmen. Ich danke Andreas Bauer für das mühselige mikrometeregenaue Ausschneiden meiner hochheiligen Solarzellen, fürs Übernehmen diverser Bestellanfragen und für den kleinen Mann im großen Auto. Ich danke Pascal Foucart für die AFM Messungen und sein verschmitztes Grinsen.

Vielen Dank an Dr. Ulrich Paetzold und Michael Smeets für die Einführungen in die Welt der Plasmonik und Michael für die Hilfestellungen am DSR. Ich danke Dr. Florian Köhler für die XRD Messungen mit ausgiebiger Diskussion. Ich danke Jürgen Radde für seine Bemühungen den Laser wieder ans Laufen zu bringen. Ich danke Joachim Kirchhoff für die Zell Depositionen und anschließende Diskussion, Markus Hülsbeck für Raman Messungen sowie Auswertung und das immer bereitwillige zur Verfügung stellen von dringend benötigten optischen Komponenten.

Neben den oben genannten geht mein besonderer Dank an Jan Flohre, Jan Mock, Paolo Cadiz Bedini, Chao Zhang sowie Jan Philipp Becker. Vielen Dank für die schöne gemeinsame Zeit im - aber auch ausserhalb des Institutes. Ich hoffe wir verlieren uns nicht aus den Augen.

Auf Seiten 4JETs möchte ich mich vor Allem bei Thomas Melle, Kai Haesser, Christian Fuhs und Armin Reiss bedanken. Ihr habt mir erst gezeigt was ein "Laser" ist und wie man einen richtigen Laboraufbau macht. Ganz besonders danke ich Thomas für sein immer offenes Ohr und seine immer dreckige Lache.

Ich danke meinen Eltern für ihren fortwährenden Beistand in Rat und Tat, ihre immer helfenden Hände sowie fürs Korrekturlesen.

Vor Allem aber danke ich meiner Frau Miriam für die ständige Unterstützung: seelischer Art, zeitlicher Art aber auch wissenschaftlicher Art. Vielen Dank für wiederholtes alleiniges Bändigen unseres Sohnes, wenn es mal wieder länger gedauert hat. Vielen Dank fürs Zuhören in harten Phasen und konstruktive Kritik. Danke, dass du an meiner Seite bist.

Am meisten jedoch danke ich meinem Sohn Emil. Du hast mich immer wieder daran erinnert, was die wirklich wichtigen Dinge im Leben sind!



Band / Volume 346

**Design eines hocheffizienten Festoxid-Brennstoffzellensystems mit integrierter Schutzgaserzeugung**

M. Engelbracht (2016), 190 pp

ISBN: 978-3-95806-189-7

Band / Volume 347

**On model and measurement uncertainty in predicting land surface carbon fluxes**

H. Post (2016), xviii, 135 pp

ISBN: 978-3-95806-190-3

Band / Volume 348

**Bipolarplattenmaterialien für Polymer-Elektrolyt-Membran Elektrolyse**

M. Langemann (2016), I-III, 189, IV-XVIII pp

ISBN: 978-3-95806-192-7

Band / Volume 349

**Modellbasierte Ansteuerung räumlich ausgedehnter Aktuator- und Sensornetzwerke in der Strömungsregelung**

M. Dück (2016), XIII, 153 pp

ISBN: 978-3-95806-193-4

Band / Volume 350

**TRENDS 2015 – Transition to Renewable Energy Devices and Systems**

ed. by D. Stolten and R. Peters (2016), 200 pp

ISBN: 978-3-95806-195-8

Band / Volume 351

**Dual Phase Oxygen Transport Membrane for Efficient Oxyfuel Combustion**

M. Ramasamy (2016), VIII, 136 pp

ISBN: 978-3-95806-196-5

Band / Volume 352

**Transport, co-transport, and retention of functionalized multi-walled carbon nanotubes in porous media**

M. Zhang (2016), VII, 112 pp

ISBN: 978-3-95806-198-9

Band / Volume 353

**Untersuchungen zur Luftqualität in Bad Homburg**

C. Ehlers, D. Klemp, C. Kofahl, H. Fröhlich, M. Möllmann-Coers und A. Wahner (2016), IV, 93 pp

ISBN: 978-3-95806-199-6

Band / Volume 354

**Herstellung thermisch gespritzter Schichten  
mit optimierten Spannungseigenschaften**

M. Mutter (2016), VI, 142, VII-XXII, xxvi pp

ISBN: 978-3-95806-200-9

Band / Volume 355

**Entwicklung selbstheilender Wärmedämmschichten**

D. Koch (2016), X, 120 pp

ISBN: 978-3-95806-201-6

Band / Volume 356

**Betriebsstrategien für Brenngaserzeugungssysteme  
zur Anwendung in HT-PEFC-Hilfsstromaggregaten**

D. Krekel (2017), IX, 265 pp

ISBN: 978-3-95806-203-0

Band / Volume 357

**Korrosion metallischer Bipolarplatten in  
Hochtemperatur-Polymerelektrolyt-Brennstoffzellen**

V. Weißbecker (2017), viii, 194 pp

ISBN: 978-3-95806-205-4

Band / Volume 358

**Realistic Bandwidth Estimation in the Theoretically  
Predicted Radionuclide Inventory of PWR-UO<sub>2</sub> Spent  
Fuel Derived from Reactor Design and Operating Data**

I. Fast (2017), XI, 129 pp

ISBN: 978-3-95806-206-1

Band / Volume 359

**Light Trapping by Light Treatment**

Direct Laser Interference Patterning for the Texturing of Front Contacts  
in Thin-Film Silicon Solar Cells

T. Dyck (2017), vi, 172, XI pp

ISBN: 978-3-95806-208-5

Weitere **Schriften des Verlags im Forschungszentrum Jülich** unter  
<http://www.zwb1.fz-juelich.de/verlagextern1/index.asp>



**Energie & Umwelt /  
Energy & Environment  
Band / Volume 359  
ISBN 978-3-95806-208-5**

